Understanding the Effects of Ion and Neutron Irradiation on Tungsten



Robert Abernethy

Wolfson College

University of Oxford

A thesis submitted for the degree of

Doctor of Philosophy

Michaelmas Term 2018

Abstract

Tungsten will be an important material inside future fusion reactors. However, replicating the neutron irradiation that it will be exposed to in that environment is currently impractical. As a result ion irradiation is being used to extend the dose and temperature range. Irradiation hardening data from past experiments show a discrepancy between the results of these two irradiation species.

This work involves the first direct comparison between ion irradiation and neutron irradiation of tungsten, carried out at fusion relevant temperatures to a dose of 1.6 dpa. The materials from these irradiations have been examined to investigate the induced microstructural changes. Irradiation hardening measurements were carried out using nanoindentation and a model applied to correlate this with the defects observed. This has provided critical insight into neutron irradiation induced hardening at fusion relevant temperatures and shown that the discrepancy between ion and neutron irradiation hardening can be significantly reduced by accounting for the effect of transmutation.

The change in brittle to ductile transition (BDT) caused by neutron irradiation of single crystal tungsten has been fully characterised. These results show that the BDT temperature has increased by 500 K, yet activation energy has remained constant at 1.0 eV and activation volume at 5 b^3, strongly suggesting that the controlling mechanism remains kink-pair nucleation of screw dislocations. Investigations into the BDT in polycrystalline tungsten have shown anomalous strain rate dependence, with micro-cantilever testing showing grain boundary embrittlement.

Micro-pillar compression has also been applied to the ion irradiated W and W-1.4Re in order to acquire additional mechanical properties from ion irradiation experiments. Results from this experiment have shown that strain burst behaviour is strongly enhanced by ion irradiation of W-1.4Re, indicating that irradiation induced rhenium precipitation is changing dislocation behaviour. By comparison, displacement damage caused by ion irradiation of pure W appear to have a small effect on micro-pillar deformation.

Acknowledgements

First of all I would like to thank my principal supervisor, Dr David Armstrong, for making this project happen and for providing invaluable guidance and support for my research over the last four years. I'd also like to thank my co-supervisors, Dr Chris Hardie and Prof Steve Roberts, for their assistance and expertise that have contributed greatly to this work.

I am very grateful to my collaborators, who played critical roles in different aspects of the experiments at the heart of this thesis. They include Prof Peter Hosemann and his group who provided a warm welcome to Berkeley and taught me everything I know about micro-pillars, as well as Prof Hans-Christian Schneider and his colleagues at Karlsruhe Institute of Technology, who conducted excellent four-point bend experiments and demonstrated the value that collaborations can provide. Thanks also goes to Dr Mark Gilbert, Dr Lee Packer and Steve Bradnam at CCFE for sharing their knowledge of transmutation and taking the time to ensure the analysis in this work was as accurate as could be.

Many thanks also must go to the wonderful team in the Materials Research Facility at CCFE, not only for training me and technical assistance, but for the fantastic company you provided during my days there. Also to all the staff in the electron microscopy suite in Oxford for their teaching, patience and ability to fix just about anything.

I am very thankful to Jack Haley, Xiaoou Yi, Matt Lloyd, James Gibson and Anna Kareer for all the help they provided with TEM, APT and nanoindentation. Additionally, they and several others ensured I had good friends alongside me in the department. Thanks to Sarah Connolly, Edd Rowe, Glenn Jones and Helen Pratt for your companionship over the last four years.

Thank you to my family, to Laurence, Rikki, Jamie and Katrina without whose love and support I never would have made it this far, and to Liz, Doug and the Harpers for your encouragement and accepting me as part of your family.

Finally, to Rachel, your love has kept me going throughout the last four years. There is no chance that this would have all come together without you.

Preface

This thesis describes work carried out by the author at the University of Oxford under the supervision of Dr David Armstrong, Dr Christopher Hardie (Culham Centre for Fusion Energy) and Prof Steve Roberts. No part of this thesis has been previously submitted for a degree at this or any other university. All the work is original and where work from others has been included it has been clearly referenced and acknowledged in the text.

The work in this thesis was funded by EPSRC grant number EP/L01663X/1 and as part of the Fusion Centre for Doctoral Training, along with industrial CASE funding from Culham Centre for Fusion Energy.

Some work from this thesis has been reported at the following conferences and in the following publications:

Conferences

- 18th International Congress on Fusion Reactor Materials, Aomori, Japan, November 2017
- Universities' Nuclear Technology Forum 2017, Liverpool, April 2017
- European Student Divertor Research Workshop, Oxford, September 2016
- 4th International Workshop on Structural Materials for Innovative Nuclear Systems, Manchester, July 2016
- 2016 Materials Research Society Spring Meeting, Phoenix, USA, March 2016

Publications

- R.G. Abernethy (2017) Predicting the performance of tungsten in a fusion environment: a literature review, Materials Science and Technology, 33:4, 388-399, DOI: 10.1080/02670836.2016.1185260
- R.G. Abernethy, J.S.K.-L. Gibson, A. Giannattasio, J.D. Murphy, O.Wouters, S. Bradnam, L.W. Packer, M.R.Gilbert, M. Klimenkov, M.Rieth, H.-C.Schneider,

C.D. Hardie, S.G. Roberts, D.E.J. Armstrong (2019) Effects of neutron irradiation on the brittle to ductile transition in single crystal tungsten, Journal of Nuclear Materials, 527, 151799, DOI: j.jnucmat.2019.151799

- M.J. Lloyd, R.G. Abernethy, M.R. Gilbert, I. Griffiths, P.A.J. Bagot, D. Nguyen-Manh, M.P. Moody, D.E.J. Armstrong (2019) Decoration of voids with rhenium and osmium transmutation products in neutron irradiated single crystal tungsten, Scripta Materialia, 173, 96-100, DOI: 10.1016/j.scriptamat.2019.07.036
- M.J. Lloyd, R.G. Abernethy, D.E.J. Armstrong, P.A.J. Bagot, M.P. Moody, E. Martinez, D. Nguyen-Manh (2019) Radiation-induced segregation in W-Re: from kinetic Monte Carlo simulations to atom probe tomography experiments, European Physical Journal B, 92:241, DOI: 10.1140/epjb/e2019-100244-y

Contents

List of Figures **ii**

1 Introduction **1**
1.1 Tungsten for Fusion Power 1
1.2 Preparation of Tungsten for Testing 4
1.3 Radiation Damage in Tungsten 5
1.4 Novel Micro-Mechanical Testing Techniques 27
1.5 The Brittle to Ductile Transition in Tungsten 33
1.6 Research Goals 36

2 Materials and Irradiations **39**
2.1 Materials and Sample Preparation 39
2.2 Irradiations 40

3 Understanding Hardening Mechanisms in Irradiated Tungsten **44**
3.1 Introduction 44
3.2 Methods 45
3.3 Transmutation 54
3.4 TEM Examination of Irradiation Damage 57
3.5 Atom Probe Tomography 73
3.6 Nanoindentation 77
3.7 Correlating Irradiation Damage and Hardening 79
3.8 Discussion 82
3.9 Summary Table 96

4 Investigating Fracture Properties of Neutron Irradiated Tungsten **97**
4.1 Introduction 97
4.2 Methods 98
4.3 Results 102
4.4 Discussion 112
4.5 Summary 117

5 Micro-Pillar Compressions in Ion Irradiated Tungsten **119**
5.1 Introduction 119
5.2 Experimental 120
5.3 In-Situ Pillar Compression 122
5.4 Transmission Kikuchi Diffraction 133
5.5 Finite Element Modelling (FEM) 137
5.6 Discussion 141
5.7 Summary 145

6 Conclusions **146**
6.1 Effects of Neutron Irradiation on Single Crystal Tungsten 146
6.2 Developing Ion Irradiation of Tungsten 147
6.3 Moving to Real-World Materials 148
6.4 Future Work 148

References **150**

List of Figures

1.1 Image of JET with tungsten divertor (red arrows) and beryllium first wall (blue arrows). Reproduced from Eurofusion (CC BY) with arrows added. 4

1.2 Left: Evolution of damage cascades in tungsten, showing recoils with $E_{kin} > 10$ eV, coloured according to time (0-300 fs) after initial pka when recoil energy drops below 10 eV. Right: Same cascade after 40 ps, showing vacancy (blue) and interstitial (red) distributions [24] 7

1.3 TEM micrograph showing both acicular and circular precipitates formed by neutron irradiation of W-11Re at 1173 K. Reproduced from [55] by permission from Springer Nature. 11

1.4 Schematic of the evolution of the visible damage structure of pure W and WRe alloys irradiated with neutrons. Reproduced from [62] (CC BY NC ND). 12

1.5 TEM images showing the presence of rhenium and osmium containing precipitates in neutron irradiated tungsten (a) High angle annular dark field image (b) W EDX map (c) Re EDX map (d) Os EDX map. Reproduced from [66] (CC BY NC ND). 13

1.6 Bright field TEM images of voids formed by neutron irradiation of tungsten. Reproduced from [66] (CC BY NC ND). 14

1.7 Dislocation loop size distribution from in-situ irradiation of tungsten and W-5Re to 1.2 dpa using 150 keV W^+. Reproduced from [71] by permission from Elsevier. 15

1.8 Atom probe tomography of tungsten irradiated to 1 dpa in JOYO at 811 K showing the presence of rhenium precipitates. The concentration of rhenium across the APT sample was measured as 0.5 wt% Re. Reproduced from [74] by permission from Elsevier. 17

1.9 Atom probe tomography W-Re-Os alloys under self-ion irradiation to 33 dpa: (a) W-2Re irradiated at 573 K, (b) W-2Re irradiated at 773 K, (c) W-1Re-1Os irradiated at 573 K and (d) W-1Re-1Os irradiated at 773 K. Reproduced from [75] (CC BY). 18

1.10 Irradiation hardening of pure tungsten under neutron irradiation plotted against dose for JMTR, JOYO and HFIR irradiation campaigns. Reproduced from [84] by permission from Elsevier. 20
1.11 Irradiation hardening of pure tungsten under neutron irradiation plotted against dose for JMTR, JOYO and HFIR irradiation campaigns (Data taken from [60][85][86][61][87][88][89][62][84] 20
1.12 Irradiation hardening of pure tungsten under neutron irradiation plotted against predicted rhenium content for JMTR, JOYO and HFIR irradiation campaigns (Data taken from [60][85][86][61][87][88][89][62][84] 21
1.13 Irradiation hardening of pure tungsten under neutron irradiation plotted against dose for the HFIR irradiation campaign (Data taken from [61][86][87][88][89] 21
1.14 Nanohardness data from a range of ion irradiation experiments on pure tungsten (data taken from [31][32][92][93]) 23
1.15 Nanohardness data from a range of ion irradiation experiments on tungsten alloys (data taken from [31][32][75][93][94]) 23
1.16 Typical load-unload indentation data showing the key experimental quantities. Reproduced from [105] by permission from Cambridge University Press. 29
1.17 Example of a micro-cantilever. Reproduced from [120]. 32
1.18 Fracture surfaces of single crystal tungsten (a) at room temperature and (b) close to the brittle to ductile transition temperature. Reproduced from [131] by permission of Taylor & Francis. 34

2.1 A plot of dose against depth into sample for ion irradiation of W Single and W Re samples 41
2.2 Neutron spectrum from irradiation in HFR 42

3.1 EDS spectra from samples of known composition with fitted peaks showing method for calculating material composition 46
3.2 Images showing the process of creating a lift-out for TEM examination 47
3.3 A image of Kossel-Möllenstedt fringes showing the measurements for calculating sample thickness. The measurement labelled D corresponds to $2\theta_B$ and $\mathrm{d_i}$ corresponds to $\Delta\theta_i$ 48
3.4 Graph showing the plot used to calculate the thickness of the sample using $n_1 = 2$ 49
3.5 Images showing a void in over- and under-focus and the sizing method 50

3.6 Weak-bream, dark field images captured using the Digital Microscopy script [149] . . . 51
3.7 TEM image processing process: (a) align images in 3.6 into a stack and sum; (b) invert contrast; and (c) subtract background . . . 51
3.8 Loop counting process: (a) TEM image after processing; (b) apply threshold; and (c) fit ellipses . . . 52
3.9 Images used for estimation of error in loop counting by adjusting the threshold value: (a) Threshold = 164; (b) Threshold = 174; and (c) Threshold = 184; . . . 52
3.10 Histograms used for estimation of error in loop counting by adjusting the threshold value: (a) Threshold = 164; (b) Threshold = 174; and (c) Threshold = 184; . . . 53
3.11 Energy Dispersed X-ray Spectroscopy results for neutron irradiated tungsten single crystal showing the fitted peak for the tungsten and rhenium L_α energy . . . 55
3.12 Energy Dispersed X-ray Spectroscopy results for neutron irradiated tungsten single crystal showing the fitted peak for the Re L_α energy . . 55
3.13 TEM images of W Single unirradiated showing small black dot damage 58
3.14 TEM images of W-1.4Re unirradiated . . . 59
3.15 TEM images of W Single Ion showing dislocation strings and a high black dot population . . . 61
3.16 TEM images of W-1.4Re Ion with $\mathbf{g} = \pm 110$. The surface of the liftout is visible in the top left of (a), with the deposited platinum layer labelled. Only small black dot defects could be observed in this sample . . . 62
3.17 TEM images of W-1.4Re Ion with $\mathbf{g} = \pm 200$. The condition in (a) is strong dark-field . . . 63
3.18 TEM images of W Single Neutron under $\mathbf{g}=\pm 200$ . . . 65
3.19 TEM images of W Single Neutron under $\mathbf{g}=110$ . . . 66
3.20 Histogram of results from carrying out dislocation loop counting method on unirradiated samples . . . 68
3.21 Dislocation loop counts in W-1.4Re Ion with different imaging conditions 68
3.22 Dislocation loop counts in W Single Neutron with different imaging conditions . . . 69
3.23 Histograms showing the density of dislocation loops as a function of size for each of the irradiated samples . . . 69
3.24 Histograms showing the normalised distribution of defect sizes for each of the irradiated samples . . . 70

3.25 Under- and over-focus images for W Single neutron irradiated. Some voids are highlighted in red in (a) 71
3.26 Under- and over-focus images for W Single Ion 72
3.27 Under- and over-focus images for W-1.4Re Ion 72
3.28 Void size distribution for W Single Neutron (n = 50) 73
3.29 Isosurface plots of rhenium concentration in APT needles from W-1.4Re Ion 74
3.30 Isosurface plots of rhenium concentration in APT needles from W Single Neutron 75
3.31 APT maps of rhenium atoms identified as being inside clusters 76
3.32 Re concentration profile averaged around each identified cluster. $N_{clusters}$ = (a) 9 and (b) 5 77
3.33 Nanohardness results for unirradiated and irradiated samples between 200 - 1800 nm 78
3.34 Modulus measurements from nanoindentation for unirradiated and irradiated samples between 200 - 1800 nm 79
3.35 Hardening contributions from each defect type for irradiated samples . 81
3.36 Comparing the experimentally measured irradiation hardening with the prediction from the model 82
3.37 Images of dislocation loops in W irradiated to 1 dpa at 1073 K from [32]. Although some loops are clearly visible, the strong presence of thickness contours may be hindering the detection and accurate sizing of dislocation loops 84
3.38 log-log plot of dislocation loop density against loop size in number of point defects. The predicted power-law dependence would appear as a straight line. 85
3.39 log-log plot of dislocation loop density against loop size in number of point defects for TEM experiments (self-ion irradiated at 30 K) carried out by Yi, compared to results from MD models [70] 85
3.40 Images of voids in W-3Re irradiated to 1 dpa at 1073 K. The presence of voids is far from clear in this image and a through-focus series is not provided. The speckling observed across the image may be associated with surface defects depending on the out-of-focus conditions used. Reproduced from [32] (CC BY NC ND). 88
3.41 Void distribution from (a) W irradiated with neutrons to 1.67 dpa at 1173 K [this work] and (b) that determined by Tanno et al. [61] 90

4.1 Geometry of four-point bend setup. The load was applied such that the face with the pre-crack was in tension. Reproduced from [22] by permission from Taylor & Francis. 98
4.2 A graph of loading rate against depth for strain rate sensitivity nanoindentation 100
4.3 A graph showing the change in hardness with each strain rate jump. The first drop in strain rate occurred at 1400 nm 100
4.4 Process of making cantilevers using FIB 101
4.5 Hardness results from SRS indents in W, W-1.4Re and neutron irradiated W 102
4.6 The stress strain curves for four-point bend tests in neutron irradiated tungsten at four different strain rates, above and below the BDT temperature at each 103
4.7 The brittle to ductile transition temperature for neutron irradiated tungsten as a function of strain rate 104
4.8 The Arrhenius dependence of the brittle to ductile transition in unirradiated [131] and neutron irradiated tungsten 105
4.9 SEM fractography of unirradiated and neutron irradiated tungsten . . 106
4.10 High ductility observed in neutron irradiated sample tested at 823 K with a strain rate of 7 x 10^{-7} s^{-1} (above the BDT temperature). This sample showed a strain >10% before fracture 107
4.11 Stress strain curves from four point bend tests carried out on W Poly Neutron 108
4.12 SEM fractography of W Poly Neutron tested at 300 K 108
4.13 SEM fractography of W Poly Neutron tested at 573 K 109
4.14 Stress-strain curves from cantilever testing in W Neutron Poly 109
4.15 SEM images of cantilevers in W Poly Neutron after testing 110
4.16 EBSD maps of cantilevers 111
4.17 The BDT temperature measured before and after neutron irradiation across different BCC metals [174] [175] [176] 114

5.1 An example pillar after milling. The rings from milling using a sequence of decreasing currents can be seen around the base of the pillar. The arrow (a) indicates the height of the irradiated layer in ion irradiated samples. 121
5.2 Images showing the process of creating a pillar lift-out for Transmission Kikuchi Diffraction 122

5.3 Images taken from video recording of pillar compression of W Single Unirr alongside load versus time data from the test 123
5.4 Post-compression image of W Single Unirr 123
5.5 Images taken from video recording of pillar compression of W-1.4 Re Unirr alongside load versus time data from the test 124
5.6 Post-compression image of W-1.4Re Unirr 125
5.7 Images taken from video recording of pillar compression of W Single Ion sample alongside load versus time data from the test 125
5.8 Post-compression images of pillars in W Single Ion 126
5.9 Images taken from video recording of pillar compression of W-1.4Re irradiated sample alongside load versus time data from the test. This sample is shown twice due to the high variability in behaviour of pillars in this material 127
5.10 Images taken from video recording of pillar compression of W-1.4Re irradiated sample alongside load versus time data from the test. This sample is shown twice due to the high variability in behaviour of pillars in this material 128
5.11 Post compression SEM images of W-1.4Re Ion 129
5.12 Stress strain graphs for micro-pillar compressions of each sample 131
5.13 Mean flow stress for each sample measured at 3% (blue) and 10% (orange) strain 132
5.14 TKD results from post-compression imaging of a pillar from W Single Unirr 134
5.15 TKD results from post-compression imaging of a pillar from W-1.4Re Unirr 135
5.16 TKD results from post-compression imaging of a pillar from W Single Ion 136
5.17 TKD results from post-compression imaging of a pillar from W-1.4Re Ion 137
5.18 Finite element model of a cylindrical pillar showing near-uniform stress and plastic strain throughout the depth of the pillar 138
5.19 Finite element model of a pillar with 5° taper showing the stress and plastic strain concentrated at the top of the pillar 139
5.20 Finite element model of a pillar with 10° taper 140
5.21 Comparing indentation hardness (200 - 700 nm) with 3x the pillar flow stress at 10% strain 143

1 Introduction

1.1 Tungsten for Fusion Power

1.1.1 The Advantages of Fusion Energy

The World Health Organisation describes climate change as the greatest threat to human health in the 21st century [1]. The Paris Agreement aims to strengthen the worldwide response to climate change and keep global temperature rise this century well below 2 °C [2]. To achieve this goal, a dramatic reduction in anthropogenic carbon dioxide emissions is required [3].

Globally, carbon emissions are still increasing. Increasing gross domestic product (GDP) is providing improved standards of living across the world but this requires an increase in energy supply that results in greater carbon emissions [4]. To overcome this problem it is necessary for energy supply to move from fossil fuels to carbon neutral technologies.

Renewable energy sources such as solar and wind power will produce 20% of electricity across the European Union by 2020 and have successfully reduced carbon emissions across Europe [5]. However, there are challenges as grid penetration of variable renewables increases further due to the misalignment between peak energy production and peak demand [6].

One response to these challenges has been the proposal for increased nuclear power to reduce the need for variable renewables while continuing to lower carbon emissions. This strategy is being deployed in the UK with 16 GW of new build nuclear to be constructed by 2030 [7]. This strategy builds off 60 years of nuclear energy in the UK, during which time low carbon electricity has been supplied from 19 different nuclear power stations.

All nuclear power stations built to date rely on fission of heavy elements such as

uranium or plutonium. These reactions produce high levels of radiation and radioactive waste products. Fission power stations also have the risk of major accidents that release significant quantities of radioactive material and necessitate large scale evacuations. Accidents of this nature occurred at Chernobyl in 1986 and Fukushima in 2011 [8].

Fusion has the capability to move nuclear energy away from these problems. Careful reactor design and materials selection would result in no long term radioactive waste [9]. Fusion is intrinsically safer than fission, as a runaway reaction is impossible. The safety case for fusion reactors is being designed around a no-evacuation criterion. This means that in the event of an accident, even the areas directly adjacent to the site would not need to be evacuated and the public would not be exposed to dangerous levels of radiation [10]. Another advantage is that the fuels for fusion reactors, deuterium and lithium, are plentiful and the highly energetic fusion reaction uses very little fuel. Therefore the potential energy from fusion is practically limitless.

These advantages make nuclear fusion very attractive as an energy source. However, there are significant technological challenges to overcome before fusion energy can be realised. One of these is developing materials that can be used to produce components with an acceptable lifetime within the fusion environment [11]. This is particularly challenging in the region of the fusion divertor, where the plasma is brought into contact with the wall of the reactor to extract waste products [12].

1.1.2 The Fusion Divertor

The current leading design for potential fusion reactors is the divertor configuration tokamak. Examples of this include the Joint European Torus (JET), which currently holds the record for fusion output at 16 MW [13], and ITER, an internationally-backed tokamak currently under construction that will be the first fusion reactor to achieve net energy production.

Tokamaks use high magnetic fields to confine a plasma at 150 million kelvin. At this temperature deuterium and tritium ions can overcome electrostatic repulsion and fuse together releasing energy (see equation 1.1).

$$ {}^{2}_{1}\mathrm{D} + {}^{3}_{1}\mathrm{T} \rightarrow {}^{4}_{2}\mathrm{He} + {}^{1}_{0}\mathrm{n} + 17.6\ \mathrm{MeV} \tag{1.1} $$

Helium produced from the reaction must be extracted, otherwise it will inhibit the fusion reaction, and other particles (such as deuterium and tritium ions) will also drift outside the confined plasma volume. In divertor configuration tokamaks, the divertor is used to absorb energy and trap these particles. This exposes the divertor to very high heat fluxes (around 10 MW m^{-2}) so material selection is limited to those with a high melting point and good thermal conductivity [12].

In addition to the heat flux, the impact of energetic particles from the plasma can cause sputtering and erosion. If sputtered particles enter back into the plasma radiative losses from electron transitions in high atomic number (Z) material will result in cooling of the plasma. To maximise performance this loss of energy must

be minimised and so either low Z material (e.g. carbon) must be used or a material with a high sputtering energy.

The fusion reaction produces highly energetic (14.1 MeV) neutrons. Neutrons are not confined by the magnetic field, and interact with the structure of the reactor, causing radiation damage and activating the structural materials. Structural materials within the reactor must be radiation resistant to prevent failure and low activation materials will be used to prevent the production of long lived radioactive waste. Activation depends on the element and isotope of the original material and so certain elements are excluded from being used in a fusion reactor [14]. Suitable low activation elements include carbon and tungsten.

This combination of extremely high heat fluxes, plasma erosion and neutron irradiation is unique to fusion. Fission reactors produce high levels of neutron irradiation, but the materials commonly used do not fulfil the low activation criterion and there is no region of a fission reactor that experiences heat fluxes like those seen by the fusion divertor. This makes developing divertor materials a unique challenge, where only limited research has been carried out so far.

Carbon fibre composites were tested as a divertor material in the Joint European Torus (JET). They are made of low Z material and have high heat conductivity along the fibre axis and so seemed the optimal choice [15]. However, chemical erosion due to reactions between the carbon tiles and hydrogen from the plasma led to more rapid erosion than anticipated and concerns over the potential for tritium retention within the reactor. In order to minimise the risk from accident at a fusion reactor the tritium level must be carefully controlled and tritium retention must be minimised [16]. The carbon wall at JET was replaced with a tungsten divertor and beryllium first wall (see figure 1.1), both of which showed significantly reduced erosion [17].

Tungsten was selected as a replacement for carbon due to its high energy threshold for sputtering (E_{th} = 200 eV for Deuterium) and low erosion rate in the fusion environment [16, 18]. It has been successfully used as the divertor material for multiple fusion experiments, such as ASDEX and JET [12, 19]. As a result of this success, and due to the lack of suitable alternatives for fusion reactors, it has been selected as the divertor material for ITER [18]. It is also currently the leading candidate material for the divertor in demonstration tokamak power stations (so-called DEMOs) [20].

The use of tungsten for the fusion divertor comes with a range of challenges [21]. These are primarily due to its high brittle to ductile transition temperature (BDTT) [22]. This causes low temperature brittleness, which makes manufacturing of tungsten components a significant challenge [23]. There are also concerns over how radiation damage will affect the properties of tungsten and the consequences of this for its use in the fusion environment [24].

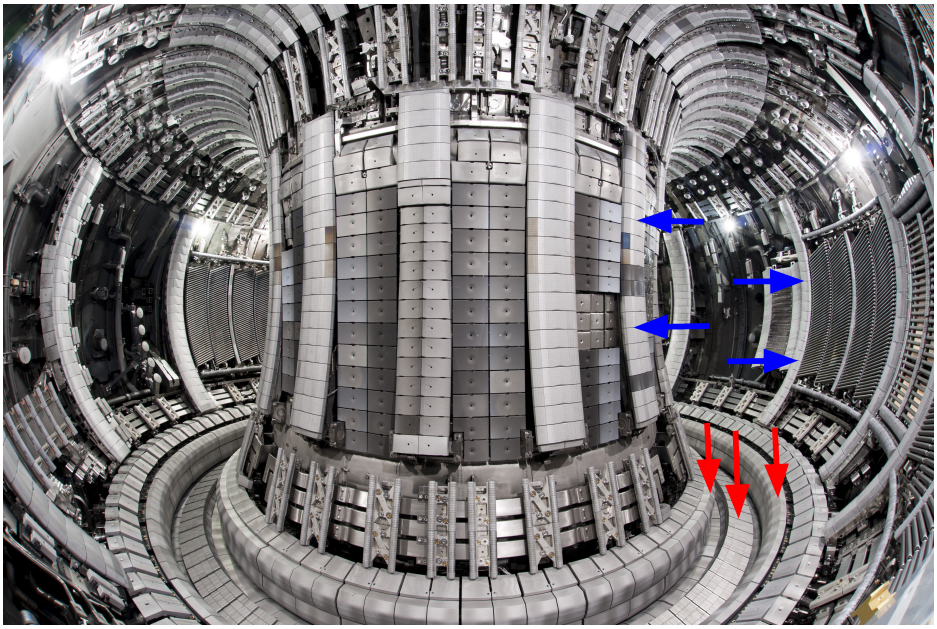

Figure 1.1: Image of JET with tungsten divertor (red arrows) and beryllium first wall (blue arrows). Reproduced from Eurofusion (CC BY) with arrows added.

1.2 Preparation of Tungsten for Testing

Tungsten is most commonly prepared via a powder metallurgy route [25]. This involves pressing into a mould and then sintering at high temperature (> 2300 K). A thermomechanical treatment is then usually applied, typically hot-rolling (T > 1500 K) into sheets, although cold-rolling to improve ductility is becoming increasingly popular [26]. These thermomechanical processes result in an anisotropic grain structure and an increased dislocation density. Metallurgical preparation (grinding and polishing) for indentation and microscopy or notching prior to mechanical testing contribute to further changes in microstructure.

In order to restore a "normal" microstructure within the material, some form of heat treatment is required. The lowest level of which is stress-relief. This removes any residual stress that is present in the material after processing. Stress relaxation in tungsten occurs rapidly (within 1 hour) at 1200 K [27], and these conditions are commonly used to prepare tungsten samples for scientific studies.

At temperatures above those used for stress-relief, recovery and recrystallisation begin to occur. During recovery the stored energy within the material is reduced by dislocations rearranging themselves to a lower energy configuration [28]. This process can result in the formation of low-angle boundaries and is marked by a decrease in dislocation density and softening of the material. Beyond this stage (at higher temperatures or longer time) complete recrystallisation can occur. Recrystallisation is characterised by the production of grains with very low dislocation densities and

grain growth. Further softening occurs and recrystallisation has been shown to result in embrittled tungsten [29]. Experiments that held heavily cold-worked tungsten at 1600 K showed that recovery occurred over a time period of 1-10 hours, followed by recrystallisation over 10-25 hours [30].

The heat treatment used to prepare tungsten for testing mechanical properties and studying radiation damage varies between authors. For example, tungsten annealed at 1673 K for 24 hours was used by Armstrong et al. [31], which would cause extensive recovery and potentially some recrystallisation, whereas a 20 minute treatment at 1173 K was used by Hwang et al. [32], which will only allow for stress-relief of tungsten and no recovery. These studies carried out similar experiments but observed starkly different results, as discussed in section 1.3.3.2.

1.3 Radiation Damage in Tungsten

Neutron irradiation causes transmutation of tungsten, primarily to rhenium and osmium, alongside displacement damage that results in dislocation loop and void formation. A plethora of techniques have been deployed to develop an understanding of the effects of this damage. These range from atomistic scale modelling [24] to mechanical tests on material exposed to a fission neutron fluence [33]. However, due to the complexity of the consequences of neutron damage there is still much to be understood [21].

There is not currently a high flux, fusion neutron source available so predictions of how tungsten will change under irradiation from 14.1 MeV neutrons must be made by a combination of computational modelling and experiments using irradiation techniques currently available. The best experimental proxy for fusion neutrons currently available is neutron irradiation within a fission reactor, although self-ion irradiation can also play a valuable role. Predicting the performance of tungsten in a fusion environment will rely on careful analysis of available experimental data from these irradiations and applying advanced modelling techniques to extrapolate these results to fusion conditions.

1.3.1 Modelling of Radiation Damage

Marian et al. [24] recently carried out a review of the recent advances in modelling and simulation of tungsten in a fusion environment. This review highlighted the broad range of modelling carried out, from transmutation calculations to molecular dynamics of cascade formation, and showed that there has been significant progress in recent years. The areas of modelling most relevant to this project are included here.

1.3.1.1 Transmutation

Modelling of transmutation of tungsten due to neutron irradiation is well-established and is capable of predicting the activation [34] and composition changes of tungsten [35] within a fusion environment and under other neutron irradiation experiments [36].

	Concentration (at%)
Tungsten	94.0
Rhenium	3.8
Osmium	1.4
Tantalum	0.8
Helium	34 appm
Hydrogen	76 appm

Table 1.1: Modelled elemental composition of tungsten after five years in a fusion power plant [35]. The concentrations are presented in atomic % (at%), except helium and hydrogen, which are shown in atomic parts per million (appm)

The most accurate model to date for these calculations is FISPACT-II [37], which has been designed to take neutron cross-section data from the European Activation File. The input data is typically calculated using MCNP (a Monte Carlo N-Particle code used for modelling neutron transport) [38], to give the neutron spectrum. FISPACT can then calculate the transmutation of all isotopes present, giving both an end composition and activity for the irradiated material.

The most important reactions for tungsten in a fusion environment are neutron multiplication (n,2n) or neutron capture (n, γ) followed by β decay to produce rhenium. Rhenium then undergoes similar reactions to form osmium. The consequence of these reactions is that pure tungsten is expected to fall to only 94 atomic % (at%) within five years in a fusion power plant [35] (the full predicted composition is given in table 1.1). Reliable predictions of transmutation are dependent on an accurate neutron spectrum and the inclusion of self-shielding effects within the model. In order to predict transmutation in DEMO, reactor design parameters are required.

1.3.1.2 Displacement Damage

Compared to the modelling of transmutation, understanding the effects of displacement damage from neutron irradiation of tungsten is far more complicated and attempts to accurately model these effects are still under development. The key difficulty lies in the range of time and length scales that are important for providing accurate predictions. A consequence of this is that no single computational modelling technique is capable of covering all areas so multi-scale modelling is required [24].

The first stage of modelling displacement damage is the neutron-tungsten interaction. An energetic neutron will interact with a single tungsten atom, called a primary knock-on atom (PKA). The PKA will be displaced from its lattice site by a neutron of sufficient energy and, provided the PKA has energy greater than the displacement energy, will displace nearby atoms from their lattice sites, causing a displacement cascade. A single neutron can interact multiple times, producing multiple PKAs, typically with a large spacing relative to the size of the displacement cascade.

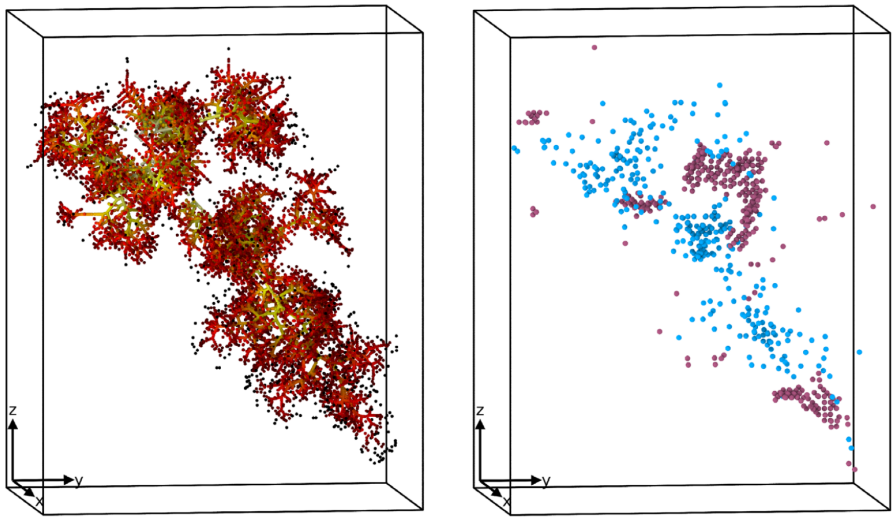

Figure 1.2: Left: Evolution of damage cascades in tungsten, showing recoils with E_{kin} > 10 eV, coloured according to time (0-300 fs) after initial pka when recoil energy drops below 10 eV. Right: Same cascade after 40 ps, showing vacancy (blue) and interstitial (red) distributions [24]

These early stage interactions have been most successfully modelled by molecular dynamics (MD). Models produced during the 1990s verified the formation of displacement cascades in metals under neutron irradiation and improved the understanding of radiation damage [39]. In particular, cascades were shown to result in a high density of interstitials and vacancies but that the majority of these Frenkel pairs annihilate with each other within a very short time period after the cascade forms (figure 1.2) [40]. Those that don't were shown to go on to form the larger defects that can be detected experimentally.

In order to provide predictions of the defects formed by these cascades, density functional theory (DFT) models are necessary. These are extremely small scale models (typically tens to hundreds of atoms) that are used to calculate the respective energies of different defect configurations, thus allowing the most stable defects to be determined.

Unfortunately DFT calculations must be carried out with an effective temperature of 0 K and only predict the equilibrium state. This leads to differences between models and experiments due to the highly non-equilibrium state of a displacement cascade. For example, Gilbert et al. [41] successfully matched the minimum size for vacancy loop defects in iron, but also predicted a similar phenomenon of a minimum loop size in tungsten, where this was not observed experimentally. The difference was explained as a result of low vacancy diffusivity in tungsten causing the material not to reach equilibrium conditions on experimental time frames.

This initial annihilation of dislike defects and grouping of like defects into larger defect clusters in the cascade is dynamic annealing and typically occurs over very short

time periods (« 1 s). This process occurs at all temperatures, although it is enhanced by higher temperatures [42]. Since the initial microstructure around a defect is far from equilibrium, high energy defects (such as small dislocation loops and vacancy clusters) are able to form during dynamic annealing. The formation of prismatic dislocation loops from large clusters of point defects has been demonstrated using MD [43].

MD models, informed by potentials calculated using DFT, have recently been used to match the observations of transmission electron microscopy experiments [44]. These showed that $\mathbf{b} = \langle 100 \rangle$ and $\mathbf{b} = 1/2\langle 111 \rangle$ dislocation loops of both self-interstitial atoms and vacancies form in the cascade debris. The most common loop type formed in BCC metals is $\mathbf{b} = 1/2\langle 111 \rangle$ [45], although $\mathbf{b} = \langle 100 \rangle$ can also form during cascade collapse.

A further recovery process, thermal annealing, occurs over much longer time processes and is mediated by the diffusion of atoms and defects. During this process the energy of the system continues to decrease through processes such as dislocation loop and void growth, and the continued annihilation of dislike defects. There is modelling evidence that $\mathbf{b} = 1/2\langle 111 \rangle$ can combine to form $\mathbf{b} = \langle 100 \rangle$ loops [46]. This process relies on mobility of dislocation loops and so occurs during thermal annealing. This pathway to $\mathbf{b} = \langle 100 \rangle$ loop formation may explain why a higher proportion of $\mathbf{b} = \langle 100 \rangle$ loops are observed in experiments than during models of cascades, where time frames are typically very limited.

The elastic interaction between dislocation loops can result in loop rafting. Kinetic Monte Carlo models have shown that the 1D motion of glissile interstitial loops can result in positions where the loop-loop elastic interaction lowers the overall energy [47]. These loops can then be trapped in these positions unless there is sufficient time and temperature for 3D climb to occur. Loop rafting can be observed using TEM through which chains of dislocation loops in the same plane and of similar orientation are imaged. Rafting has previously been observed in ion irradiated tungsten [48].

Radiation-induced chemical segregation is driven by coupling of diffusion fluxes of defects and alloying elements [49], and so also occurs during thermal annealing. The large difference in time scale between dynamic and thermal annealing processes mean that modelling them using a single technique is all but impossible, so multi-scale modelling techniques are required.

Once accurate multi-scale modelling techniques are developed, they will provide a key advantage of having the potential to be extended away from the experimental conditions to simulate the damage induced by a 14.1 MeV fusion neutron, which we cannot currently use for experimental irradiations. The models also give an understanding of the annealing processes, too small in length- or time-scale to be observed experimentally, that determine the evolution of a material under irradiation, including the formation of defects that cannot be observed directly but that can affect mechanical properties, such as small vacancy clusters [50].

1.3.1.3 Calculating Displacement Damage Level

The Kinchin-Pease model can be used to calculate the approximate amount of displacement damage in displacements per atom (dpa), which is a measure of the number of displaced atoms divided by the total number of atoms in the irradiated volume. This model calculates the average number of atoms displaced by a PKA of energy E_p. It assumes that the collisions between atoms are elastic hard sphere collisions; that a minimum amount of energy, E_d is required to displace an atom; the maximum neutron energy is a cut-off energy E_c caused by electron stopping; and that atoms are randomly distributed, ignoring the effects of crystal structure. From these assumptions it can be derived that the average number of atoms displaced per PKA is [51]:

0 if $E_p < E_d$
1 if $E_d < E_p < 2E_d$
$E_p/2E_d$ for $2E_d < E_p < E_c$
$E_c/2E_d$ for $E_p \geq E_c$

This type of model is used by FISPACT to calculate displacement damage alongside the transmutation calculations. For FISPACT calculations a displacement energy of 55 eV is used for tungsten.

1.3.1.4 Combined Effects of Transmutation and Displacement Damage

One very difficult area in modelling tungsten, that has gained increasing attention in recent years, is predicting the irradiated microstructure that forms as a result of the interaction between transmutation products and displacement damage. These interactions primarily occur on length- and time-scales too great for MD models, so kinetic Monte Carlo (KMC) or mean field rate theory (MFRT) models must be deployed.

KMC modelling was carried out by Suzudo and Hasegawa [52], the main result of this work was a prediction that rhenium and osmium would reduce the number of surviving point defects following a cascade, due to the effect of the transmutation elements on the mobility of interstitial defects. MFRT simulations carried out by Huang et al. [53] was able to simulate the defects formed and used micro-mechanical correlations to estimate the hardening levels from defect accumulation. These results predicted that hardening would be dominated by rhenium precipitate formation in multiple irradiation scenarios.

Accurately predicting rhenium precipitate formation, however, is difficult. The precipitates form at rhenium concentrations much lower than would be predicted by the phase diagram. As a result the conclusion is drawn that radiation induced precipitation is occurring. This phenomenon is not well understood as it encompasses non-equilibrium thermodynamics interacting with complex kinetics.

Recent DFT modelling [54] has shown that it may be a consequence of the high density of interstitial defects, but this is only the first stage in producing a model that can predict the rate of formation on a large enough scale to be validated experimentally. Further modelling efforts are likely to focus on this area, which will be essential

for developing a model describing the effects of fusion neutron irradiation on the mechanical properties of tungsten.

The ultimate aim of this modelling will be to predict what defects will form under neutron irradiation in a fusion environment and how these will effect the properties of tungsten. This work will provide valuable data points in the form of defects formed under neutron and ion irradiation, and how these correlate to irradiation hardening of tungsten. Particularly, ion irradiation induced hardening with and without the presence of rhenium will be examined, allowing the importance of radiation induced precipitation to be identified.

1.3.2 Microscopy of Radiation Damage in Tungsten

Like modelling, experiments on radiation damage in tungsten cover a very large scale range. From high resolution microscopy that can observe defect formation on a nanometre scale to macroscopic engineering tests that probe the mechanical properties following irradiation.

The finest scale experiments use transmission electron microscopy (TEM) or atom probe tomography (APT) to probe the defects formed by irradiation. There are three key types of defects observed: dislocation loops, voids and transmutation product clusters or precipitates. Each of these contribute to the properties of irradiated tungsten and each affects the formation of the others, making a thorough understanding of the post-irradiation microstructure essential.

1.3.2.1 TEM of Neutron Irradiated Tungsten

Fission neutrons are the best proxy for fusion neutrons as they can induce similar transmutation and displacement damage, although at different rates. There have been a number of TEM experiments carried out on neutron irradiated tungsten since the earliest experiments 50 years ago. These studies have primarily focused on radiation induced precipitation and void formation, with little reporting of dislocation loop size, density or distribution in the microstructure .

Early studies carried out in the 1970s and 1980s characterised both precipitates (figure 1.3) [55] and void lattices [56] formed by neutron irradiation of tungsten and tungsten-rhenium alloys. Tungsten-rhenium alloys were of particular interest due to their use as thermocouples within reactors, where decalibration occurred due to radiation induced precipitation. These early results showed that void formation was suppressed in tungsten-rhenium alloys relative to pure tungsten, resulting in significantly reduced irradation swelling [57].

It is difficult to know the full conditions from these early experiments, since fluences are only provided as total fluence and proportion $E > 1$ MeV and dpa calculations were not carried out (the dpa only came into common usage after 1991 [58]). Transmutation calculations were provided but given the recent advances in modelling of transmutation

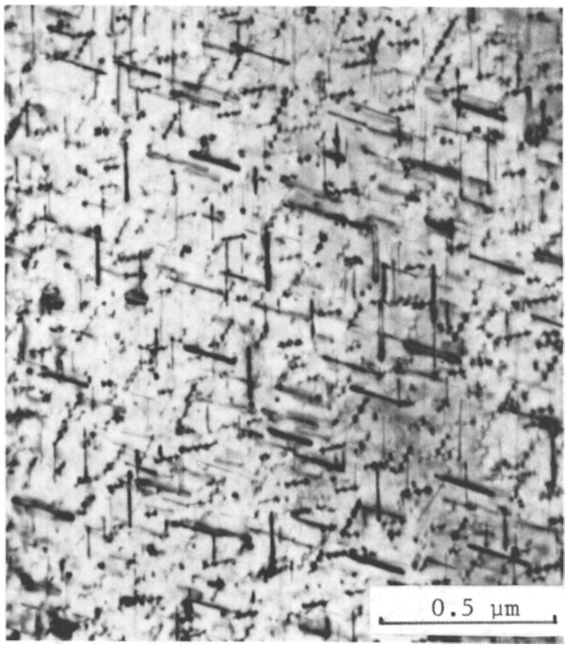

Figure 1.3: TEM micrograph showing both acicular and circular precipitates formed by neutron irradiation of W-11Re at 1173 K. Reproduced from [55] by permission from Springer Nature.

and the strong dependence on an accurate neutron spectrum it is difficult to know if these are correct, especially since no experimental validation was carried out. However, the experiments do provide valuable information with regards to peak swelling temperature (between 850 and 1200 K [57] and the formation of rhenium precipitates (as shown in the TEM micrograph in figure 1.3), enhanced at high temperatures (> 1100 K) and by greater rhenium content [55].

More recent investigations into neutron irradiated tungsten began after it was proposed as a divertor material for fusion reactors during the 1990s [18]. Following this, numerous irradiations were carried out in the USA and Japan using a range of test reactors.

Work by Nemoto et al. [59] used the Fast Flux Test Facility and showed that both χ and σ phase precipitates formed during neutron irradiation of W-26Re at a range of temperatures and damage levels between 2 and 11 dpa. This contradicted the results of Williams et al. [55], where only χ phase was observed. This is potentially due to the limited imaging techniques used by Williams et al. that resulted in only larger precipitates, that had formed at temperatures above 1300 K, being characterised.

This work was followed by irradiations in the Japan Materials Testing Reactor (JMTR) [60], JOYO [61] and the High Flux Irradiation Facility (HFIR) [33]. The results from TEM observations from these experiments for temperatures between 773 and 1073 K and damage levels up to 11 dpa are summarised by Hasegawa et

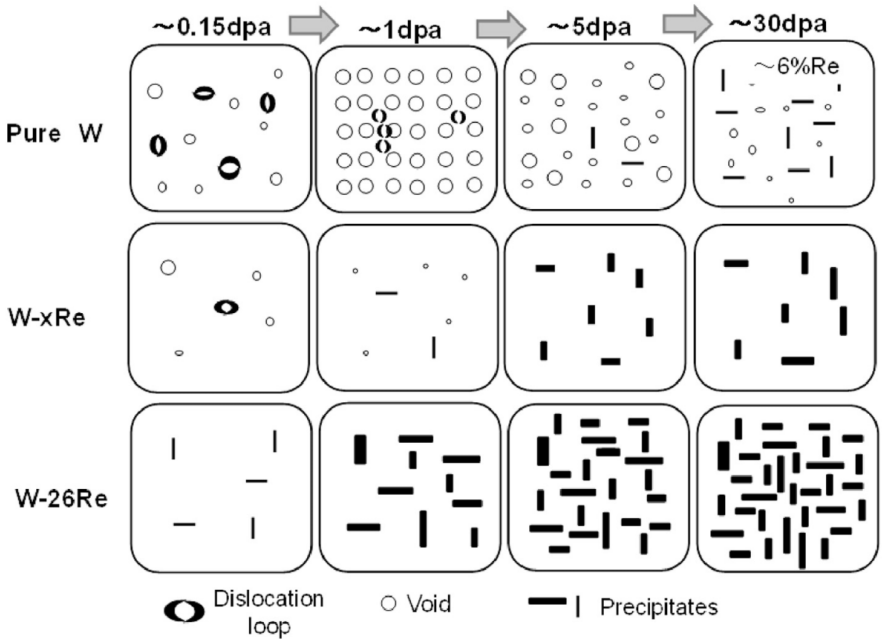

Figure 1.4: Schematic of the evolution of the visible damage structure of pure W and WRe alloys irradiated with neutrons. Reproduced from [62] (CC BY NC ND).

al.[62]. While the variation in neutron spectrum between the reactors results in a range of transmutation per dpa rates, a rough summary of the damage types observed under irradiation is given in figure 1.4 [62].

JOYO is a sodium-cooled fast reactor. As a result it has the lowest proportion of thermal neutrons out of all the irradiation facilities and so causes the lowest level of transmutation. TEM of pure tungsten irradiated to 1.5 dpa at 1023 K showed void lattice formation [63] similar to that reported by Sikka et al. [56]. Although Tanno et al. did not calculate the transmutation from irradiation in JOYO, it was later calculated by Hasegawa et al. [62] and found to be 1.5 wt% Re and 0.05 wt% Os at 1.5 dpa. This calculation, however, has not been experimentally verified. The irradiation of W-xRe alloys in JOYO demonstrated the suppression of void formation with increasing rhenium content, with far fewer voids observed even at 5 wt% Re.

The transmutation per dpa caused by irradiation in HFIR is significantly greater, resulting in 9.2 wt% Re and 5.0 wt% Os at 1.0 dpa. This deviates significantly from the predicted transmutation rate within a fusion environment, which is close to 1 wt% Re per dpa [64], although this varies depending on location within the reactor and assumptions made during modelling. The result of this different spectrum is that significantly more precipitates and fewer voids were observed following irradiation in HFIR.

The irradiation temperatures from JMTR, JOYO and HFIR experiments reach a maximum of 1073 K. By comparison Zinkle and Ghoniem [65] predict the operating window of tungsten in a fusion reactor to be between 1073 and 1573 K. The only recent

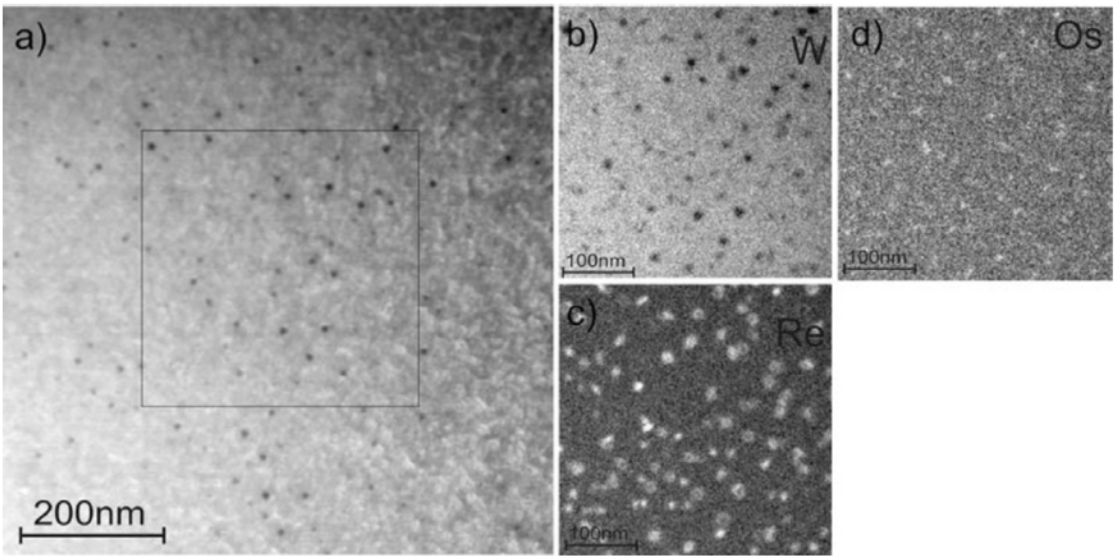

Figure 1.5: TEM images showing the presence of rhenium and osmium containing precipitates in neutron irradiated tungsten (a) High angle annular dark field image (b) W EDX map (c) Re EDX map (d) Os EDX map. Reproduced from [66] (CC BY NC ND).

irradiation carried out at temperatures within this window was carried out at the High Flux Reactor in the Netherlands. TEM of this material was carried out by Klimenkov et al. [66] and showed the presence of both voids and precipitates (see figures 1.5 and 1.6). The same neutron irradiated material has been examined in this work.

One area that has not been extensively studied in neutron irradiated tungsten is dislocation loop sizes and densities. Although Hasegawa's schematic (figure 1.4) indicates that dislocation loops should be present in pure tungsten irradiated to 1 dpa and there have been many irradiations carried out to similar conditions, there has not been extensive reporting of them. He et al. [60] carried out the most thorough characterisation of dislocation loops with size distributions given for irradiation to 0.15 dpa in JMTR at 873 and 1073 K. They found that increasing temperature reduced loop count in pure tungsten and that the inclusion of 3 wt% Re significantly reduced loop size without increasing loop density. One important factor in this work is the lack of transmutation analysis. As a result the initial compositions provided may be different to the post-irradiation composition since the transmutation rate of tungsten in JMTR is approximately 8% Re / dpa [62]. Additionally, no weak-beam dark-field TEM work was carried out, which is considered superior for imaging small dislocation loops [67].

1.3.2.2 TEM of Ion Irradiated Tungsten

The cost of an irradiation campaign, variability in spectrum, inaccuracies in monitoring temperature and the challenges in handling active material all make neutron irradiations

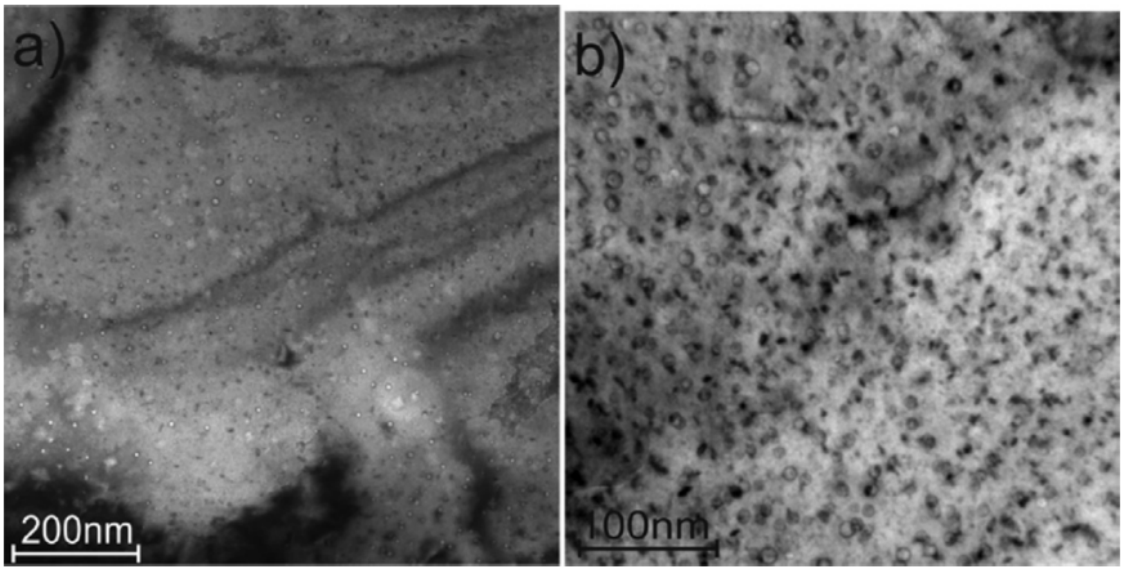

Figure 1.6: Bright field TEM images of voids formed by neutron irradiation of tungsten. Reproduced from [66] (CC BY NC ND).

difficult and limit repeatability of any given study. Self-ion irradiation can also be used as a proxy for neutron irradiation with several advantages. Tungsten ions are accelerated towards the target material with energies up to tens of MeV. Upon impacting on the material their behaviour is somewhat analogous to that of a PKA during neutron irradiation.

The advantages of this technique are that it does not induce radioactivity in the target material and irradiations to > 1 dpa can be conducted in hours rather than months. However, there are still questions as to the accuracy of the technique in replicating neutrons.

The implanted ion remains in the material and the number implanted is typically enough to affect the balance of vacancies and interstitials produced by displacement damage. The high dose rate, while an advantage in reducing time taken to do the experiment, may significantly alter irradiation effects and variation in dose rate in ion implantation experiments has been found to change the behaviour of iron and iron-chromium alloys under irradiation [68]. Finally ion implantation does not cause transmutation, although this can be used as an advantage by allowing separation of displacement damage and transmutation effects in radiation hardening.

Comparisons between ion and neutron irradiation are essential for greater understanding of these issues, and corrections must be made before ion irradiation can be considered a useful predictive tool for the fusion environment. These issues notwithstanding much can be learned from ion irradiation, particularly for informing and validating computational models.

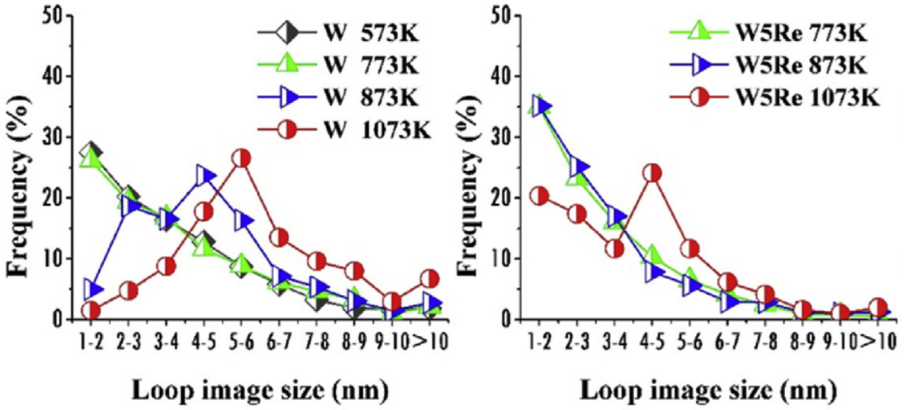

Figure 1.7: Dislocation loop size distribution from in-situ irradiation of tungsten and W-5Re to 1.2 dpa using 150 keV W^+. Reproduced from [71] by permission from Elsevier.

The most comprehensive work using TEM to study ion irradiation damage in tungsten has been carried out by Yi with several papers published covering a range of temperatures, alloy compositions and both in-situ and ex-situ irradiations [69][70][71].

Yi's work was the first to show the existence of $\mathbf{b} = \langle 100 \rangle$ dislocation loops in tungsten [69], a result that was later matched by MD modelling [44]. The proportion of loops of $\mathbf{b} = 1/2\langle 111 \rangle$ type in pure tungsten was around 60% for irradiation at room temperature and increased with temperature up to close to 100% at 1073 K. Additionally around 50% of $\mathbf{b} = 1/2\langle 111 \rangle$ loops were interstitial type at 773K (the remainder were vacancy type) increasing to 70% at 1073 K [71].

The primary variations with temperature were in loops density and size distribution. Loop density decreased from 1×10^{23} at 573 K to 3×10^{22} at 1023 K for in-situ irradiation of tungsten to 1.2 dpa using 150 keV W^+. There was also an increase in average loop size with increasing temperature, as shown in figure 1.7 [71]. This increase in average loop size was offset by decreasing loop density between 30 and 1073 K. The total concentration of point defects retained in loops was reported to have decreased by a factor of 17.

Figure 1.7 also shows the effect of rhenium content on dislocation loop distribution. It is clear from this that rhenium suppresses loop growth, especially at higher temperatures, with a far lower proportion of loops > 6 nm observed when rhenium was present. This also caused a slightly higher loop count in W-5Re than W and a greater proportion of the loops were $\langle 100 \rangle$ type. Rhenium did not have a significant effect on the ratio of interstitial to vacancy loops.

Ferroni et al. [72] carried out an annealing experiment on tungsten ion irradiated to 1.5 dpa at 773 K. This showed that dislocation loops began to coalesce and grow at around 1073 K on an hour timescale. At the same temperature and timescale, 1-2 nm voids formed. Upon reaching a temperature of 1673 K, nearly all dislocation

loops had been annealed out of the sample and voids had reached a mean diameter of 4 nm at a density of 10^{22} m^{-3}.

Voids were not reported by Yi under ion irradiation at temperatures up to 1073 K, however, 1-2 nm voids were imaged by Hwang et al.[32] in W and W-3Re under self-ion irradiation at 1073 K. In this work the voids are not very clear on the micrographs and over- and under-focused images, of the kind provided by Ferroni et al., are not shown. The conclusion that voids are present under irradiation at this temperature, and particularly the density provided of 7.1×10^{22} m^{-3} at 1 dpa may be somewhat questionable since surface defects in TEM foils can often appear void-like.

1.3.2.3 Atom Probe Tomography of Tungsten

There are relatively few atom probe tomography (APT) studies of irradiated tungsten. An early study by Herschitz and Seidman [73] showed the presence of radiation induced precipitation in W-10Re alloy after neutron irradiation to 8.6 dpa at 850 - 950 K with a size of 6 nm and density of 10^{22} m^{-3}.

Hwang et al.[74] demonstrated the presence of rhenium precipitates in initially pure tungsten irradiated to 1 dpa at around 800 K in JOYO (as shown in figure 1.8) and HFIR. The transmutation of tungsten under these irradiation conditions was measured as 0.5 % Re and 4.0% Re, 0.8% Os respectively. These measurements were very different to the calculations performed using FISPACT. This difference could arise due to the small sample size of APT (only one needle appears to have been characterised for each condition) or inaccuracies in the model due to approximations in the neutron spectrum or failing to account for self-shielding.

The spacing of precipitates in the tungsten irradiated in JOYO matched the spacing of features that had been identified as voids during TEM characterisation of the material [63], before it was understood that significant transmutation would occur during irradiation of tungsten in JOYO. It is unclear whether these are rhenium shells around voids or simply precipitates that had been misidentified.

The only other recent studies have been carried out on ion irradiated material. The most relevant of these is the work by Xu et al. [75] on W-Re and W-Re-Os alloys and Armstrong et al. [31]. Xu et al. showed rhenium precipitation for W-2Re and W-1Re-1Os for irradiation to 33 dpa at 573 K and 773 K as shown in figure 1.9. The work by Armstrong et al. is striking for the lack of precipitation up to 13 dpa at 573 K in W-5Re, as Hwang et al. [74] showed precipitate formation at 1 dpa under neutron irradiation. This suggests that ion irradiation does not replicate the precipitation behaviour of rhenium in tungsten. Xu et al. only irradiated to 33 dpa and showed that higher temperature increased the size of precipitates and that osmium clustered preferentially in these conditions.

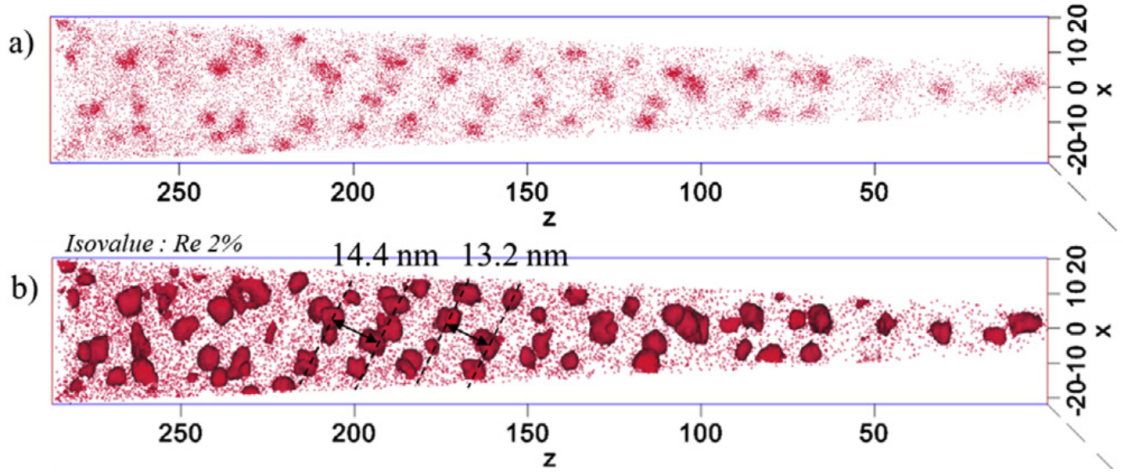

Figure 1.8: Atom probe tomography of tungsten irradiated to 1 dpa in JOYO at 811 K showing the presence of rhenium precipitates. The concentration of rhenium across the APT sample was measured as 0.5 wt% Re. Reproduced from [74] by permission from Elsevier.

1.3.2.4 Comparing Ion and Neutron Irradiation Through Microscopy

Ion irradiation has been most successfully deployed to match the formation of dislocation loops observed under neutron irradiation. The work by Yi et al. [71] on W and W-5Re self-ion irradiated to 1 dpa matches the results found by He et al. [60] in W and W-3Re irradiated to 0.15 dpa to a reasonable degree. Yi observed approximately double the density of loops (most likely due to the higher damage level) and the loop size distribution is similar for both W and W-xRe. Given the few studies in neutron irradiated tungsten that analyse dislocation loops this is the best comparison that can be made.

With regards to void and precipitate formation, ion irradiation matches neutron irradiation far less well. If voids have been observed from ion irradiation, they are certainly much smaller < 2 μm compared to 5 nm diameter for irradiation to 1 dpa at 1073 K [32]. The APT results show the stark contrast in damage needed to induce precipitate formation with precipitates forming at < 1 dpa in neutron irradiated material but not until > 10 dpa in ion irradiated tungsten.

1.3.2.5 Explaining the differences between ion and neutron irradiation

There are several possible reasons for the differences observed between ion and neutron irradiation. The first is the very large difference in dose rate between the techniques. Armstrong et al. [31] and Xu et al. [75] carried out irradiations at approximately 8 x 10^{-4} dpa / s whereas neutron irradiation is usually carried out at dose rates of approximately 10^{-7} [60][66][76]. The effect of dose rate on irradiation damage in tungsten is unknown [77] but Mansur [78] describes a theoretical basis for an

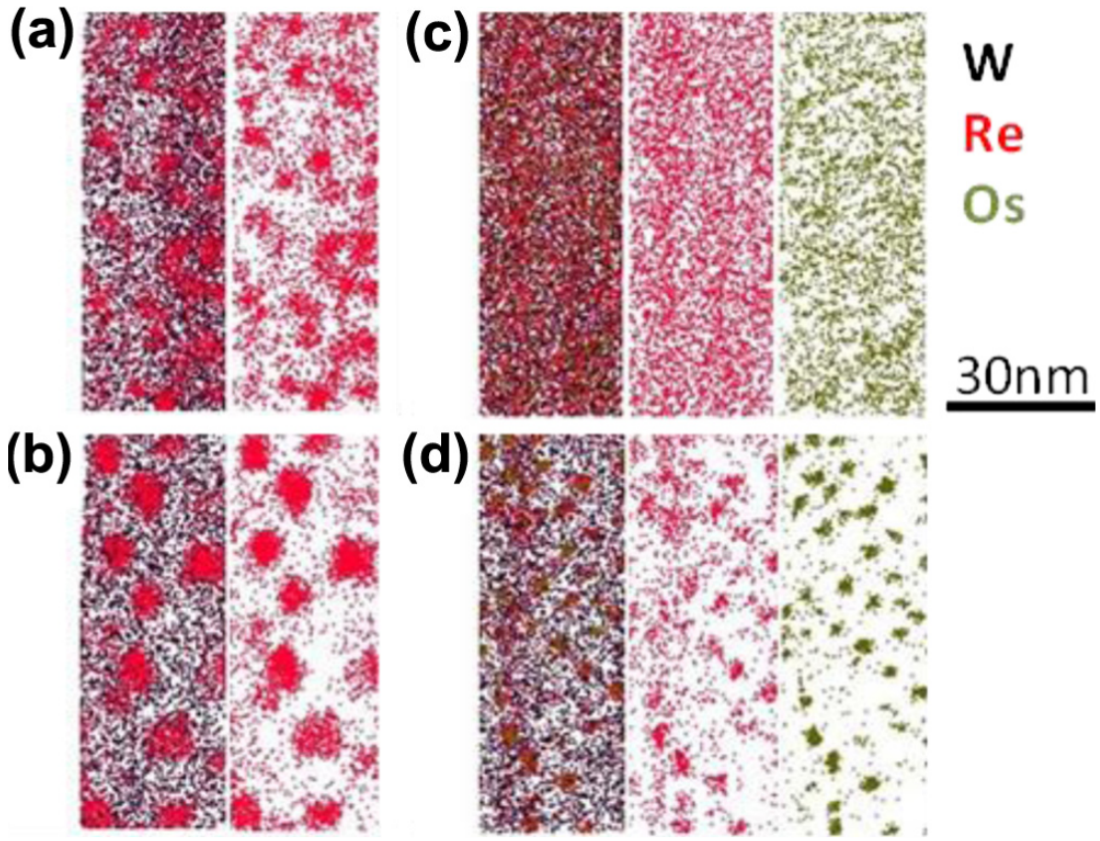

Figure 1.9: Atom probe tomography W-Re-Os alloys under self-ion irradiation to 33 dpa: (a) W-2Re irradiated at 573 K, (b) W-2Re irradiated at 773 K, (c) W-1Re-1Os irradiated at 573 K and (d) W-1Re-1Os irradiated at 773 K. Reproduced from [75] (CC BY).

equivalence between lower dose rate and higher temperature for comparing ion and neutron irradiation. Given that higher temperatures have been shown to promote void and precipitate formation in tungsten it is possible that the high dose rate of ion irradiation is suppressing this behaviour. Evidence for this exists in Fe-Cr where lower dose rate ion irradiation was shown to favour α' precipitate formation [79].

This difference in dose rate also gives rise to a change in the type of annealing occurring in each material. The rapid introduction of damage caused by ion irradiation results in predominantly dynamic annealing. In comparison, samples are held at high temperature for a long time during neutron irradiation, this allows thermal annealing to occur. This difference may explain the suppression of radiation-induced segregation during ion irradiation compared to neutron irradiation [80].

A second potential cause of these differences is a difference in vacancy population after ion and neutron irradiation. The vacancy population in ion irradiated material may be reduced as self-ion irradiation implants an excess of interstitials into the

material. This is particularly an issue in tungsten as the low penetration depth of even high energy ions means that the material being analysed is often at or near the Bragg peak (as is the case in [75] and [31]), where the implanted ions come to rest. This excess of implanted interstitials has been shown to suppress void formation in iron [81].

The vacancy population in neutron irradiated material may also be increased by gas production. (n,α) reactions produce helium impurities, which are attracted to and stabilise vacancies produced by irradiation. This process has been shown to contribute strongly to void formation [82] [83], particularly in steels. However, this effect in tungsten is expected to be less significant than in other materials because gas production from neutron irradiation is relatively low. For example He production in tungsten is $\approx$ 30 times lower than that in iron under fusion spectrum neutron irradiation [35]. This effect is reduced further under irradiation with fission spectrum neutrons, the result is gas production rates well below 1 appm / dpa. It is thus unlikely that hydrogen and helium production are making a significant contribution to the differences observed between ion and neutron irradiated tungsten.

1.3.3 Mechanical Properties Change With Irradiation

The radiation induced microstructural defects detected using microscopy have an impact on the macroscopic properties of tungsten, such as thermal conductivity and mechanical properties. It is these changes in properties that will influence how tungsten is used in fusion reactors. While the thermal properties of tungsten are vital, this project is focused on the mechanical properties and how they change under irradiation.

1.3.3.1 Neutron Irradiation Studies

The material irradiated in JMTR, JOYO and HFIR has been tested using Vickers micro-indentation, as well as TEM examination. The results from these micro-hardness tests are presented in figure 1.10 [84]. Despite the large variation in neutron spectrum and temperature, the trend is remarkably consistent, although the log scale for each axis should be noted.

Data for this graph, and data from publications published since it was produced, has been replotted on a linear access in figure 1.11. These results show a hardening level of approximately 4 GPa at 1 dpa, possibly reaching saturation at 7 GPa. There is obviously a very large range of scatter, due to the variation in spectra and temperature. Unfortunately, neutron irradiation results are rarely repeated due to the cost in time and resources to carry out an irradiation campaign. As a result, the effect of spectrum or temperature is difficult to determine.

The main influence of the reactor spectra is a large range of transmutation rates from 0.8 % Re / dpa for JOYO to 9.2 % Re / dpa for HFIR [62]. For comparison radiation hardening is plotted against predicted composition in figure 1.12. These transmutation rates are loose approximations, and the higher the Re content the less

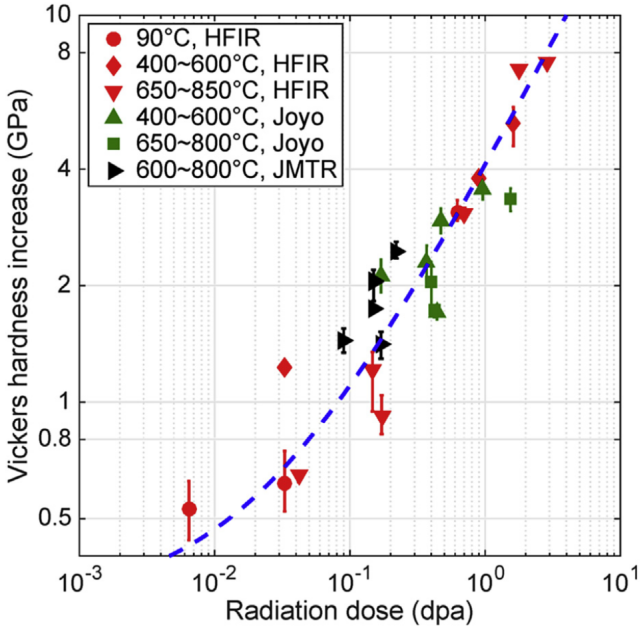

Figure 1.10: Irradiation hardening of pure tungsten under neutron irradiation plotted against dose for JMTR, JOYO and HFIR irradiation campaigns. Reproduced from [84] by permission from Elsevier.

accurate they are likely to be as Re transmutes to Os under neutron irradiation.

Figure 1.13 shows the results only for HFIR, separated by temperature. Unfortunately no clear trend for the effect of temperature on hardening can be observed in this case. Overall the neutron irradiation hardness data provides little information that could be used to predict the behaviour of tungsten in a fusion environment. Outside of the JOYO experiments, which reach a maximum of 1.5 dpa and account for a small proportion of the irradiations, the transmutation to damage ratio is much greater than will be expected in a fusion environment. Additionally, irradiation conditions have not been repeated so it is difficult to estimate the expected variation in irradiation hardening.

1.3.3.2 Ion Irradiation and Mechanical Properties

An alternative to neutron irradiation is necessary to attempt to mitigate some of these issues. Although ion irradiation has several key differences to neutron irradiation, the time taken to carry out an experiment is greatly reduced. The lack of transmutation during ion irradiation allows greater control over composition, allowing a more systematic investigation into the effects of dose, irradiation temperature and transmutation products. However, the most significant issue with ion irradiation of tungsten for mechanical testing is the limited penetration depth. The high stopping power of tungsten means that even high energy irradiation ($>$ 10 MeV) only penetrates

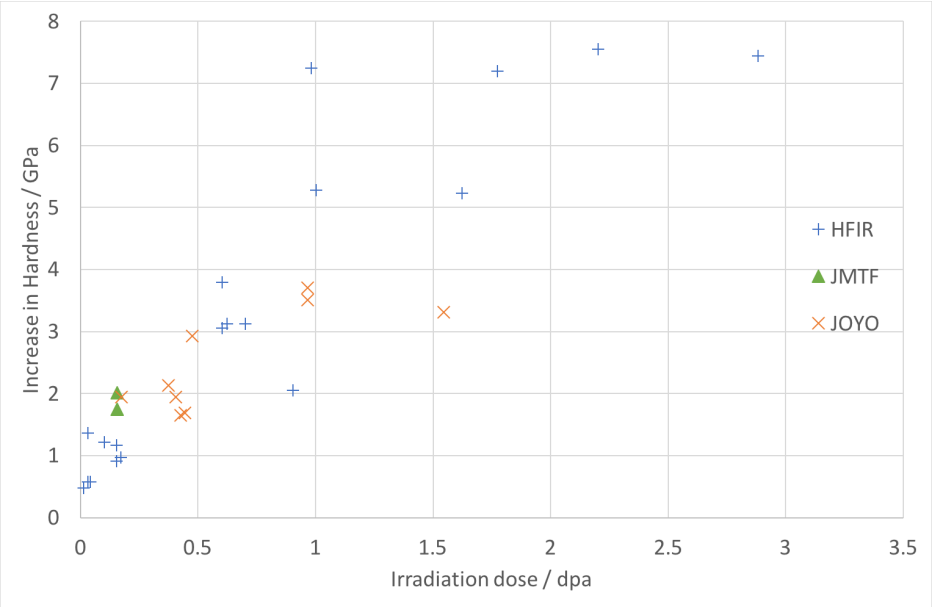

Figure 1.11: Irradiation hardening of pure tungsten under neutron irradiation plotted against dose for JMTR, JOYO and HFIR irradiation campaigns (Data taken from [60][85][86][61][87][88][89][62][84]

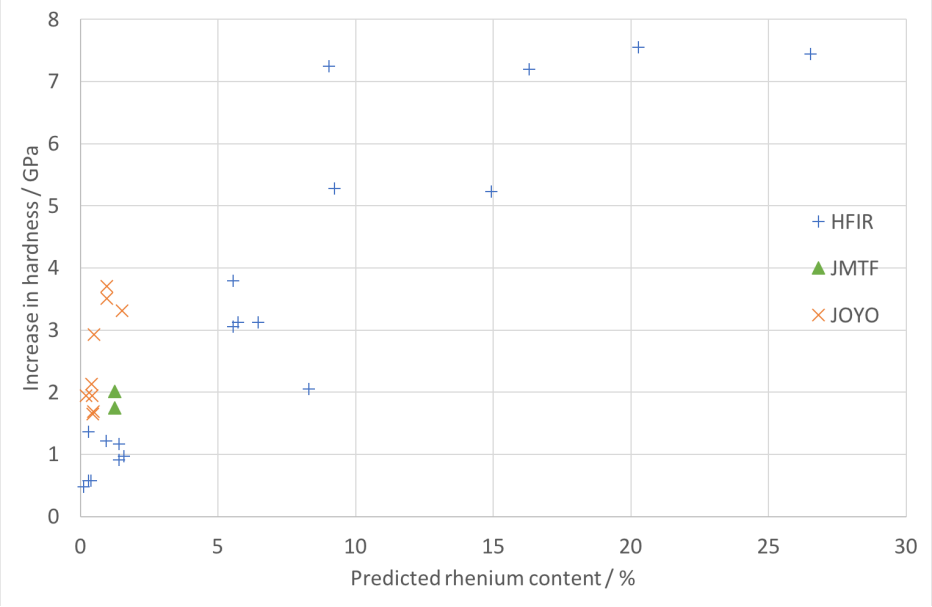

Figure 1.12: Irradiation hardening of pure tungsten under neutron irradiation plotted against predicted rhenium content for JMTR, JOYO and HFIR irradiation campaigns (Data taken from [60][85][86][61][87][88][89][62][84]

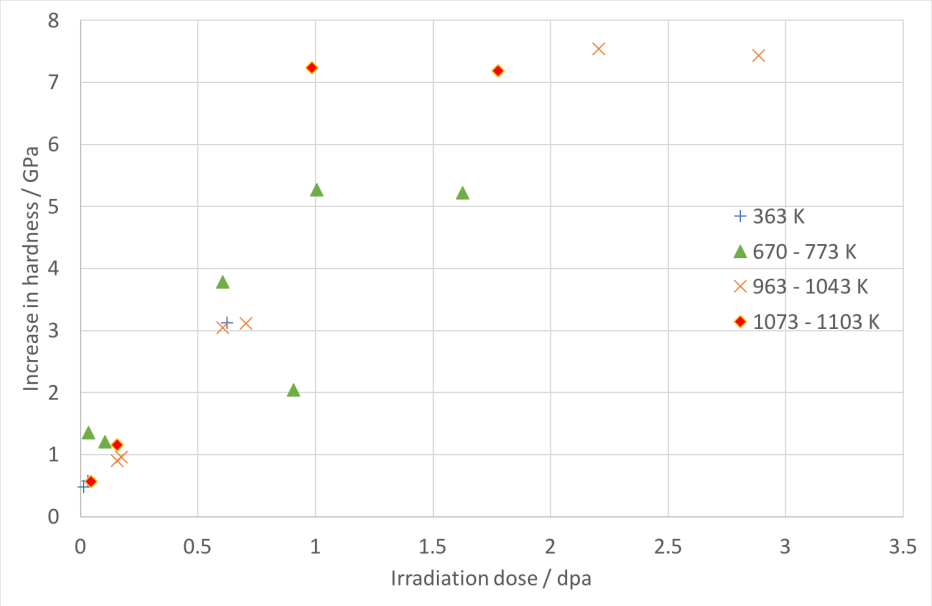

Figure 1.13: Irradiation hardening of pure tungsten under neutron irradiation plotted against dose for the HFIR irradiation campaign (Data taken from [61][86][87][88][89]

Author	Ion type	Energy / MeV	Temperature / K	Rate / dpa s^{-1}
Khan	$Re^{+/2+}$,$W^{+/2+}$	1,2,4	673	1×10^{-3}
Zhang	Fe^{3+}	6.4	573 / 773	4×10^{-4}
Xu	W^{+}	2	573 / 773	2×10^{-4}
Hwang	W^{6+}	18	773 / 1073	3×10^{-4}
Armstrong	W^{+}	2	573	8×10^{-4}

Table 1.2: Tungsten alloy ion irradiation conditions for results shown in figures 1.14 and 1.15

a few μm, limiting the range of mechanical tests that can be carried out.

The most common mechanical test for ion irradiated tungsten is nanoindentation. This allows for hardness data, similar to that from tests on neutron irradiated tungsten, to be acquired from a test depth in the hundreds of nanometres. Test volumes in this range show a 'size effect', whereby smaller test volumes show high hardness, but this can be accounted for either through Nix-Gao analysis [90] or comparison to the variation with depth in the unirradiated material [91].

Figure 1.14 shows the nanohardness data for several different ion irradiation experiments on pure tungsten. There is no clear trend between authors, with Hwang et al. [32] reporting hardening of almost 3 GPa that saturates at 1 dpa, while Armstrong et al. [31] and Khan et al. [93] reported hardening of 1 - 1.5 GPa at doses $>$ 30 dpa. The conditions for these ion irradiations are shown in table 1.2 but no correlation between hardening behaviour observed and temperature, ion energy

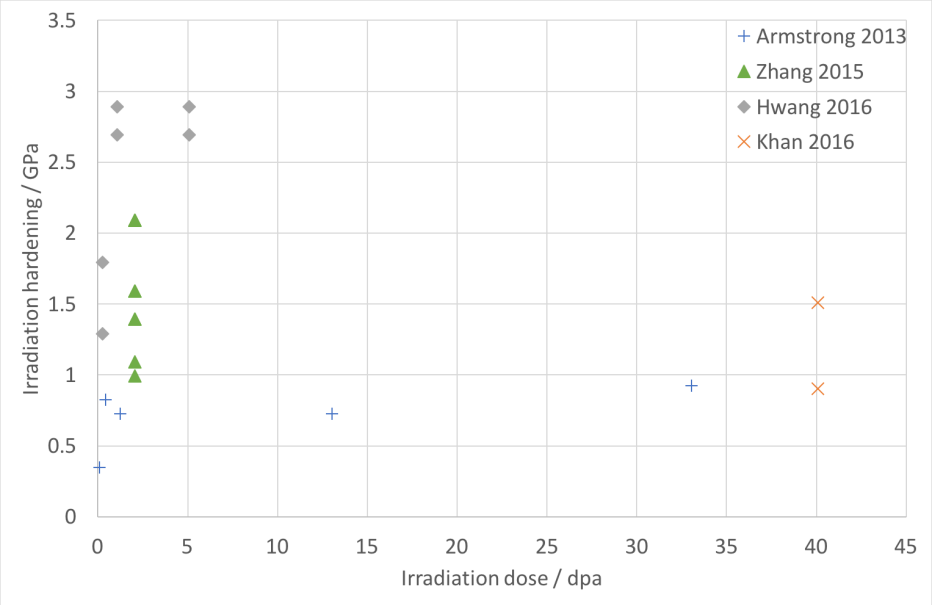

Figure 1.14: Nanohardness data from a range of ion irradiation experiments on pure tungsten (data taken from [31][32][92][93])

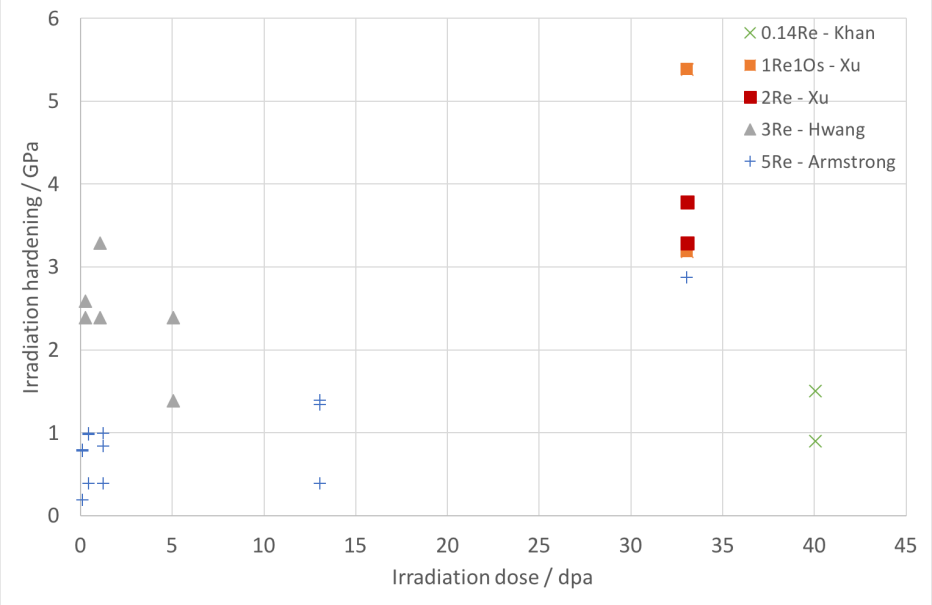

Figure 1.15: Nanohardness data from a range of ion irradiation experiments on tungsten alloys (data taken from [31][32][75][93][94])

or dose rate could be determined.

Figure 1.15 shows the nanohardness data for ion irradiation experiments on W-xRe and W-xRe-yOs alloys. This data shows a stronger trend for increasing hardness with increasing dose, with the exception of Khan [93], where only low levels of rhenium were implanted during the experiment. Comparing figures 1.14 and 1.15, the strong contribution of rhenium and osmium to irradiation hardening of tungsten becomes apparent, especially at higher doses.

The results from Zhang et al. [92] and Armstrong and Britton [95] demonstrate the importance of initial microstructure on irradiation hardening. These experiments showed, in W and W-5Re respectively, that increased initial hardness, due to grain structure or higher dislocation densities, reduced the irradiation hardening effect. This appears to be the best explanation for the differences in results between authors, as there was a wide variety of manufacturing and sample preparation techniques used.

In particular Hwang et al. [32] used W and W-3Re produced by powder processing and hot rolling, followed by a 20 minute anneal at 1173 K. These are stress-relief conditions and will not induce recovery. As a result excess dislocations from production and metallographic preparation are likely to still be present and may have contributed to the high hardening at low dose observed.

This issue of variation in preparation technique and initial microstructure has led to strong variations in results from both neutron and ion irradiation. The grade of tungsten that will be used in DEMO has not yet been chosen and different production routes are still being developed [96], so there is no standard tungsten grade that is representative of what will be used in future fusion reactors. This has led to recent neutron irradiation experiments on single crystal tungsten [97] [86]. While this material has different properties to the polycrystalline material that would be used in a fusion reactor, results from this can be used to establish baseline behaviour. The effect of grain boundaries can then be determined separately and the optimum microstructure for tungsten for fusion identified.

1.3.3.3 Comparing Ion and Neutron Irradiation Through Micro-Mechanics

The results from ion and neutron irradiation of tungsten are strikingly different. Firstly, it is apparent that self-ion irradiation of tungsten does not cause hardening in excess of 3 GPa even at doses in excess of 30 dpa. Comparatively, neutron irradiation can cause this level of hardening at 1 dpa.

Hardening of more than 4 GPa is only observed in neutron irradiation during which high levels of transmutation occur. As such, it is reasonable to assume that transmutation to rhenium and osmium, and subsequent precipitation, is responsible for high levels of irradiation hardening. The lack of transmutation in ion irradiation then explains why irradiation hardening in pure tungsten is limited to < 3 GPa.

Even when ion irradiation of W-xRe-yOs alloys is carried out to replicate the transmutation effect, levels of hardening similar to neutron irradiation are not seen

until very high dose levels. This is likely due to the delayed onset of precipitate formation during ion irradiation as describe in section 1.3.2.4.

This failure of ion irradiation to replicate the effects of neutrons are somewhat worrying. However, there has not been a concerted effort to match a particular neutron irradiation experiment. Differences in material types and preparation, testing techniques and irradiation conditions prevent a direct comparison of the two techniques.

1.3.4 Correlating Microstructural Changes and Irradiation Hardening

One key area for improving the understanding of irradiation damage in tungsten is a model capable of correlating microstructural changes with the observed increase in hardness. The irradiation-induced defects observed using microscopic techniques (dislocations loops, voids and precipitates) act as obstacles to dislocation motion. As a result, a greater stress is required to move dislocations and so a higher hardness is observed from indentation experiments.

Building a direct link between irradiation hardening and the microstructural defects present is critical for extrapolating from existing neutron and ion irradiation data to better predict the behaviour of tungsten in service. It would also help identify the importance of differences between the results from ion and neutron irradiation. Currently work on this area in tungsten is limited. There have been some attempts to correlate hardening and rhenium precipitation for neutron irradiated tungsten [61], however, only one recent paper has attempted to correlate the full array of radiation defects (loops, precipitates and voids) with irradiation hardening [98].

There are two well established model for the contribution of irradiation-induced defects to hardening [99]. The first is the dispersed barrier model. This is based of the geometrical considerations established by Orowan [100] (and so may also be referred to as an Orowan model) that predict the stress required for a dislocation to bypass an obstacle by bowing around it. An additional term (barrier strength factor) is added in order to accommodate the consideration that obstacles to dislocation motion are not perfectly hard barriers (i.e. dislocations may cut through obstacles rather than always bowing around them) [51]. This term varies between different obstacle types and sizes, and currently must be empirically established, although advanced computational models may eventually allow the determination of these obstacle strengths from first principles. A formula that can be used for calculating strengthening contribution based off this model is shown in given in equation 1.2.

$$\Delta\sigma = M\alpha\mu b(Nd)^{1/2} \tag{1.2}$$

$\Delta\sigma$ = Increase in yield stress / Pa
M = Taylor factor
μ = shear modulus / Pa

b = Burgers vector / m
N = defect density / m^{-3}
d = defect spacing / m

An alternative model was established by Friedel, Kroupa and Hirsch [101]. This model considered the situation where the effective spacing between obstacles is greater relative to the planar geometric spacing due to a lower degree of dislocation bowing prior to the point where the dislocation is able to separate from the barrier. This modified the dependence of the strengthening contribution on size and density of obstacles relative to the Orowan formulation. The contribution to strengthening from weak obstacles based off the Friedel-Kroupa-Hirsch model is given in equation 1.3.

$$\Delta\sigma = \frac{1}{8} M \alpha \mu b d N^{2/3} \tag{1.3}$$

$\Delta\sigma$ = Increase in yield stress / Pa
M = Taylor factor
μ = shear modulus / Pa
b = Burgers vector / m
N = defect density / m^{-3}
d = defect spacing / m

Hu et al. [98] used a barrier strengthening model of the form given in equation 1.4 and barrier strength factors (α) given in table 1.3. They considered Orowan and Friedel-Kroupa-Hirsch (FKH) models and found that the Orowan model produced a better fit of experimental data in all cases. To convert from increase in yield stress to increase in hardness, a factor of 3.2 was used, based off analysis by Busby [102], and a Taylor factor of 3.06 was used in this case (as is suitable for equiaxed BCC material [103]). Additionally they compared linear and root-sum square superposition laws for hardening from different obstacles. Both gave similar results but root-sum square superposition was considered to be more accurate in the majority of cases. Their model underestimated hardening for intermediate doses (1-4 dpa) in HFIR and JMTR irradiations, this was considered to be a consequence of "invisible" defects (voids and precipitates that are too small to be observed by TEM).

$$\Delta H_V = 3.2 M \alpha \mu b (N d)^{1/2} \tag{1.4}$$

ΔH_V = Increase in Vickers Hardness / Pa
M = Taylor factor (3.06)
μ = shear modulus / Pa
b = Burgers vector / m
N = defect density / m^{-3}
d = defect spacing / m

The values of barrier strength given in table 1.3 were derived by examining hardening in a select set of irradiated tungsten samples. A sample was irradiated to 0.03 dpa at 363 K. Due to the short duration of this irradiation, transmutation was negligible and

	Loops	Voids / nm				Precipitates
		1-2	2-3	3-4	>4	
Barrier strength factor α	0.15	0.25	0.3	0.35	0.4	0.6

Table 1.3: Barrier strength factors for radiation defects in tungsten

so the hardening contribution from rhenium clusters could be ignored. This sample was then annealed for one hour at a range of temperatures (773 - 1573) to produce a range of loop and void densities (the loop density peaked after annealing at 773 K whereas void density was highest after annealing at 1273 K). The loop and void size and densities were measured after each anneal, as was the increase in hardness. From this the contribution to hardening from dislocation loops and small voids could be individually determined and so the barrier strength factors for dislocation loops and voids could be established. The barrier strength factors for precipitates and large voids were established using a similar method on samples irradiated to higher doses. The values determined fit well with the best current understanding of hardening by irradiation defects; that dislocation loops and small vacancy clusters act as weak obstacles to dislocations, whereas large voids and precipitates act as strong barriers to dislocation motion [99].

This model provides the most considered attempt to correlate radiation defects and hardening from any work on tungsten. By comparison, there has been very little work of this nature in ion irradiated material. Xu et al. [75] used a very different model to determine the hardening contribution of rhenium precipitates in ion irradiated W-Re alloys. This found a very low strengthening contribution, likely due to the extremely small size of precipitates in that experiment (< 5 nm). This analysis also failed to consider any contribution to hardening from dislocation loops as no TEM analysis was carried out.

One factor of note in this Orowan model given above is that no distinction is made between hardening contributions from $\langle 100 \rangle$ and $\mathbf{b} = 1/2\langle 111 \rangle$. Atomistic modelling suggests that the hardening caused by loops in BCC materials is dominated by $\mathbf{b} = 1/2\langle 111 \rangle$ type loops, when both types are present [104]. However, there are frequently large uncertainties in determining the proportion of loop type present and inconsistencies between authors. Therefore further modelling to better understand the effect of different loop types on mechanical properties and an improved systematic approach to loop classification are likely to be required before the distinct contribution from each type of dislocation loop can be accurately determined.

Nowhere in the literature has a single model been used to compare hardening from neutron and ion irradiation. Completing an analysis of both ion and neutron irradiated material will allow for better comparison of the hardening effects of the irradiation types and may provide significant insight into the observed differences between ions and neutrons.

1.4 Novel Micro-Mechanical Testing Techniques

Both neutron and ion irradiation produce limited volumes of irradiated material. Neutron irradiation campaigns are expensive, time-consuming and handling large quantities of active material is difficult. Thus there is a desire to maximise the mechanical data that can be acquired from the smallest possible volume of material. Ion irradiation is limited by penetration depth with typical length scales being a few microns. As a result there is a drive to develop new techniques that acquire more mechanical data from a limited volume.

1.4.1 Nanoindentation

Nanoindentation is the most well developed of these, and its results have been used extensively above. This technique was first described by Oliver and Pharr in 1992 [105], and has been developed significantly since [106]. It is designed to sample a smaller volume than traditional micro-indentation and has improved instrumentation to provide continuous load and displacement data. This allows for calculation of hardness and modulus as a function of depth. This capability was initially developed for thin films, where the testing depth is on the same order of scale as the thickness of the material to be tested. Ion implantation produces a layer of irradiated material that is directly analogous to this situation.

Nanoindents can be performed quickly and much of the data analysis is automated, allowing relatively large data sets (>20 indents) to be acquired. This allows for accurate results with low statistical errors. Standard nanoindentation used the load-unload method described by Oliver and Pharr [106]. Typical results from this method and the key experimental quantities (peak load (P_{max}), peak displacement (h_{max}), final displacement (h_f) and unloading stiffness (S)) are shown in figure 1.16.

The contact area for the indent can be calculated from the displacement and an area function (which must be calculated empirically for each nanoindentation tip). Hardness at maximum indentation depth can then be calculated from peak load and displacement. Measurement of the initial unloading stiffness, S, allows for calculation of the modulus of the indented material, after taking into account the stiffness of the indenter tip.

Since the development of nanoindentation, a size effect where hardness appeared to increase with decreasing indentation depth became apparent. This effect was observed on a range of materials in the early 1990s [107] [108] and subsequently a mathematical fit for the size effect was produced by Nix and Gao [90]. However, attempting a Nix-Gao fit to indentation data from indents parallel to the irradiation data can produce false results, due to the variation in damage profile along the depth of the indent [91] so additional care must be taken when analysing results of this nature.

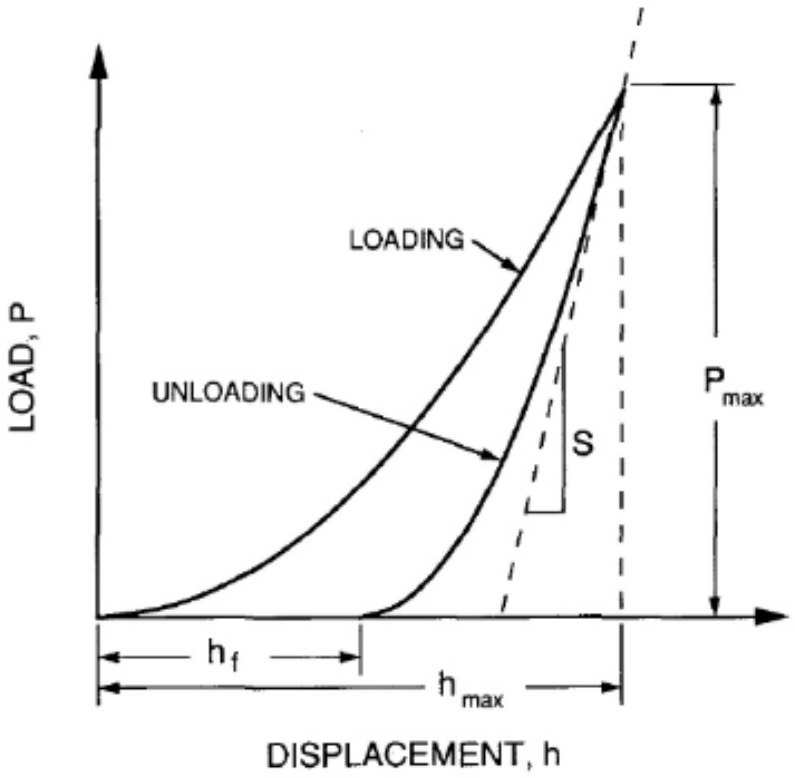

Figure 1.16: Typical load-unload indentation data showing the key experimental quantities. Reproduced from [105] by permission from Cambridge University Press.

1.4.1.1 Developments in Nanoindentation

Recently, continuous stiffness measurement (CSM) has been deployed on nanoindenters. This applies a small oscillation at a high frequency ($\approx$ 40 Hz) so that hardness and stiffness can be continuously measured throughout the depth of the indent [109]. This is particularly beneficial for studying ion irradiated material, where the damage level may vary across the depth of the indent. The depth at which unirradiated material below the irradiated layer can be identified and a better estimate of the size effect within the irradiated layer can be determined.

CSM also facilitates strain rate sensitivity indentation (SRS). SRS has been applied to materials with unusual microstructures such as nano-grained nickel [110] and nano-twinned copper [111] in order to elicit information about changes in deformation mechanism. In particular SRS has the capability to measure the activation volume of dislocation motion. This activation volume is of interest as it can provide information about the rate controlling mechanisms of plastic deformation in BCC metals [112]. This is of particular interest in tungsten, where the rate controlling mechanism of dislocation motion will control the BDTT (see section 1.5).

The relation between strain rate sensitivity and activation volume arises from the energy required for a dislocation to cross a barrier. Analysis has shown that, by calculating the thermal and mechanical components of this energy, the strain rate can be found to be related to the stress by the equations [113]:

$$\epsilon = \epsilon_0 e^{\frac{-E_a}{kT}} \tag{1.5}$$

$$E_a = E_k - \tau V \tag{1.6}$$

ϵ = Experiment strain rate (s^{-1})
ϵ_0 = Reference strain rate (s^{-1})
E_a = Experimental activation energy (J)
k = Boltzmann constant (J K^{-1}))
T = Temperature (K)
E_k = Energy for dislocation motion (J)
τ = Stress on dislocation (Pa)
V = Activation volume for dislocation motion (m^3)
The activation volume can then be calculated by [114]:

$$m = \frac{\partial \ln \sigma}{\partial \ln \epsilon} \tag{1.7}$$

$$V = \frac{\sqrt{3}kT}{m\sigma_f} = \frac{\sqrt{3}kT}{3m.H} \tag{1.8}$$

m = strain rate sensitivity
σ_f = flow stress
H = Hardness ($\approx 3\sigma_f$)
These formulations were used by Maier et al. [115] to determine the activation volume for deformation in single crystal (5.5 - 7 b^3) and ultra-fine grained tungsten ($\approx$ 6 b^3), where b = magnitude of the Burgers vector. Further development of SRS may allow it to be applied to the investigation of changes in deformation behaviour following irradiation. Significant increase or decrease of the strain rate sensitivity of a material may be indicative of a change in deformation mode as observed in the nanostructured materials above.

1.4.1.2 Limitations of Nanoindentation

There are, however, several significant issues arising from reliance on nanoindentation for mechanical test data. The first is the highly anisotropic and somewhat unknown stress state that occurs beneath an indent that results in a strong strain gradient and potentially different deformation mechanisms to bulk plasticity [116][117]. This factor is highly microstructure dependent so no general rule can be easily applied. Instead nanoindentation data is often compared to traditional mechanical testing data through

an assumed linear relationship between hardness and yield stress. As a result several complications around the real stress state under an indent are ignored.

Further issues with nanoindentation arise when testing ion irradiated materials. Kiener et al. [118] illustrate several of these complications. Indentation can be carried out either parallel to the implantation direction, in which case any variation in damage level with depth (as often arises from ion irradiation) can have an unknown impact on the results since the volume sampled by nanoindentation is complex [119]. The alternative is nanoindentation into a surface perpendicular to the irradiation direction, however, as Kiener found, this can complicate the results. It is difficult to avoid damaging the second surface during irradiation so metallographic preparation has to be carried out after irradiation. The result is that work hardening is introduced into the surface resulting in a higher measured hardness, which could result in an overestimate of irradiation hardening. Additionally the width of the indentation plastic zone is comparable to the length scale of the irradiation depth, so variations in dose could still affect the results.

Tungsten has a higher stopping power than most other materials so even high energy ($>$ 10 MeV) self-ion irradiation only penetrates a few μm into the material. Nanoindentation is typically carried out to depth of 2 μm, which results in a indent area of 100 μm^2. Since the plastic zone is approximately 3$\times$ larger than the indent, this can easily exceed the size of the irradiated volume from ion irradiation.

These limitations are driving a movement towards micro-mechanical tests for ion irradiated material [94] [118]. Micro-pillar compression or micro-cantilevers produce a better defined stress state over a known volume and so are potentially beneficial for providing results that can be more fully understood. Albeit at the cost of more complicated preparation routes that increase the cost and time required for experiments.

1.4.2 Micro-Cantilevers

Manufacture and testing of micro-cantilevers has been adopted in recent years thanks to the developments in focused ion beam microscopes (FIB). Using a FIB, gallium ion beams can be used to mill away material leaving structures that can be used for mechanical tests. The micro-cantilever is a thin beam, typically of triangular, rectangular or pentagonal cross-section attached to bulk material at one end (see figure 1.17). A load can be applied to the free end using a nanoindenter resulting in a stress state similar to a conventional cantilever test, and load-displacement data can be acquired. Using the geometry of the cantilever, stress-strain curves can be calculated. This can then be used to calculate yield stress, elastic modulus or fracture stress if the cantilever is broken during the test.

These values can be more useful than those acquired using nanoindentation [94], with fracture data in particular typically being inaccessible from nanoindentation. However, manufacturing cantilevers is relatively time-consuming and access to FIBs is often limited and expensive. As a result, data sets from micro-cantilever tests are

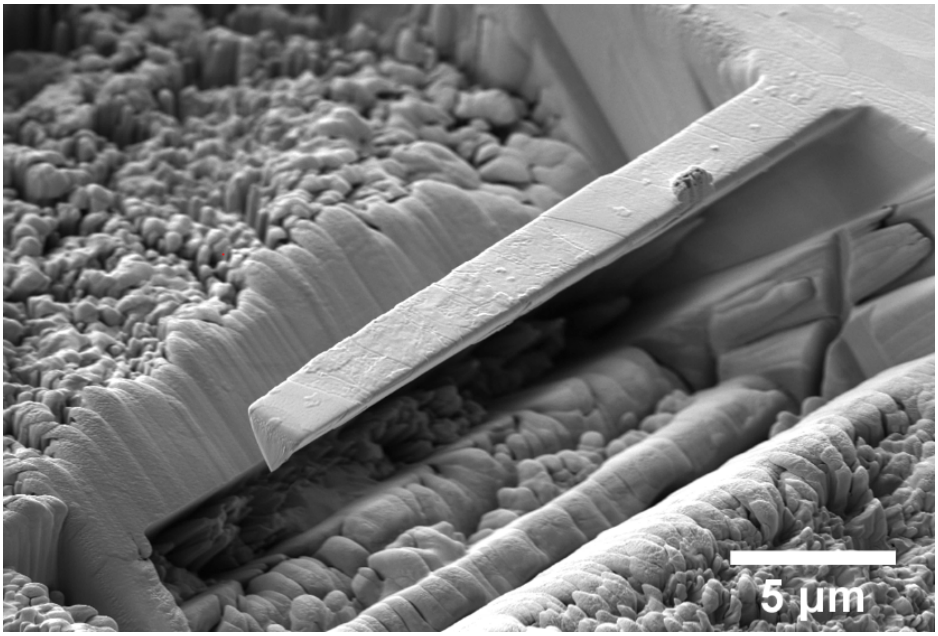

Figure 1.17: Example of a micro-cantilever. Reproduced from [120].

generally small and have relatively large errors.

Lessmann et al. [121] used micro-cantilevers to probe the fracture behaviour of self-passivating tungsten alloys before and after irradiation. These results showed a small shift in fracture stress after irradiation to 0.7 and 7 dpa (an apparent initial decrease followed by an increase), however, all the data set for each condition shows overlap with all other conditions and no calculation of changes in fracture strain following irradiation was presented. The unirradiated material also showed large inhomogeneity with significant variation in fracture toughness. As a result the observed changes may be an artefact of statistical variation.

1.4.3 Micro-Pillars

Micro-pillars are mostly produced in a similar way to micro-cantilevers, using FIB. One advantage of micro-pillars over micro-cantilevers is that milling is only required in one direction to produce an approximately cylindrical pillar. This allows increased automation of the process and so greater numbers of pillars can be produced more easily. Micro-pillars can have diameters ranging from a few hundred nm to several microns and usually have a length a few times this diameter.

Micro-pillar compression produces a simple stress state, comparable to that achieved from bulk compression tests of materials, although the small-scale can result in vastly different material behaviour [122]. This simple stress state allows for calculation of the active slip system during experiments [123]. Combining this with ion irradiation has the potential to provide significant insight into the effects of irradiation damage on

individual slip systems, particularly if in-situ testing can be carried out [124]. Kim et al. [125] successfully carried out micro-pillar compression on tungsten pillars below $1\mu m$ in diameter and showed the size dependence of the flow stress.

Micro-pillar compression has been successfully applied to ion-irradiated materials by several authors [124] [126] [127]. These results consistently show irradiation hardening but also show variations in strain-burst behaviour following irradiation, with some results showing that irradiation damage enhanced strain-bursts and others showing strain-burst inhibition. Cui et al. [128] carried out dislocation dynamic modelling to investigate this behaviour and found that loading mechanism as well as defect density affected whether strain burst behaviour was promoted or inhibited by irradiation. This result suggests that additional information regarding the interactions of dislocations with irradiation defects in tungsten can be acquired from observing strain-burst behaviour in micro-pillar compressions.

1.5 The Brittle to Ductile Transition in Tungsten

One critical parameter for designing a fusion reactor using tungsten is the BDTT. Above the BDTT tungsten has sufficient mechanical properties to be used as a structural material, however, its brittle behaviour at low temperatures is a severe disadvantage [129]. It not only hinders manufacturing of tungsten but may also impact the lifetime of tungsten components under the thermal cycling that will occur during pulsed operation of DEMO [20].

The BDTT of tungsten cannot be given as a single value, as it depends on microstructure [130] and testing conditions, particularly strain rate [22]. The relation between BDTT, strain rate and temperature can be described using the same equations used to relate strain rate, stress and activation volume above:

$$\epsilon = \epsilon_0 e^{\frac{-E_a}{kT}} \tag{1.9}$$

$$E_a = E_k - \tau V \tag{1.10}$$

ϵ = Experiment strain rate (s^{-1})
ϵ_0 = Reference strain rate (s^{-1})
E_a = Experimental activation energy (J)
k = Boltzmann constant (J K^{-1}))
T = Temperature (K)
E_k = Energy for dislocation motion (J)
τ = Stress on dislocation (Pa)
V = Activation volume for dislocation motion (m^3)

The most comprehensive characterisation of the BDTT was carried out by Giannattasio and Roberts [131]. This work carried out four-point bend tests on notched single

crystal and polycrystalline samples at a range of strain rates and temperatures. For each strain rate a transition temperature was identified through the increasing fracture toughness up to a sharp transition to ductile behaviour. The difference in behaviour between low temperature and close to the BDTT can be seen in figure 1.18.

Through Arrhenius analysis of the dependence of BDTT on strain rate, Giannattasio and Roberts found the experimental activation energy for the brittle to ductile transition to be close to the theoretical kink pair formation energy of 1.75 eV for $\{112\}$ screw dislocations [132].

Tarleton and Roberts [133] carried out dislocation dynamics modelling that showed the controlling process for the brittle to ductile transition was the motion of dislocations away from the crack tip, that can enable crack tip blunting. Further analysis by Giannattasio et al. [22] characterised the activation volume associated with the process through the kink-pair model proposed by Ackermann et al. [134] and found it to be 19 b^3, where b is the magnitude of the Burgers vector. The activation volume is of particularly interest here as it is a measure of the relationship between stress and dislocation mobility, a relationship that will impact the measurement of the characteristic energy of the BDTT.

The work by Giannattasio et al. [22] showed the strong impact of impurities on the activation energy of the brittle to ductile transition. In particular the results showed that 99.97% pure sintered tungsten (with 100 appm Mo and 30 appm Fe and C) had a BDTT 90 K higher than pure (99.99%) W and an experimental activation energy of 1.45 eV compared to 1.0 eV for pure W.

Dislocation dynamics modelling predicted a linear dependence of BDTT on activation energy. As a result radiation damage will cause the BDTT to increase due to impurities produced by transmutation as well as the displacement damage that decreases the mobility of dislocations. This makes a thorough understanding of radiation damage in tungsten and the effect it has on the brittle to ductile transition critical for its application in fusion reactors.

This characterisation of the brittle to ductile transition has been questioned by recent work produced by Swinburne et al. [135]. This work shows that with microstructures above a well-defined length scale, a single kink activation energy would be expected. This correlates with the experimental values determined for a range of BCC materials, without modifying the activation energy based upon the stress on dislocations.

1.5.1 Effect of Radiation Damage on the Brittle to Ductile Transition in Tungsten

At present, macroscopic tests are required for determining the BDTT of a material. As a result ion irradiated material cannot be used, and neutron irradiation must be carried out. A consequence of this, and the high cost of neutron irradiation, is that only limited analysis of the brittle to ductile transition in irradiated tungsten has been carried out. The results from studies that have carried out ductility tests on

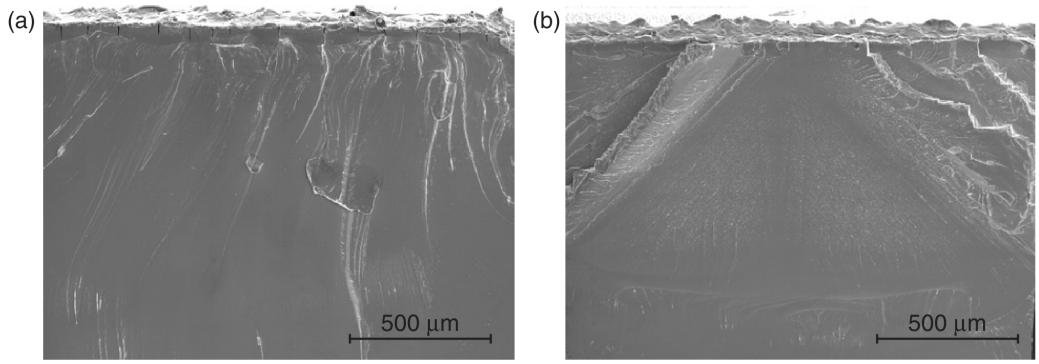

Figure 1.18: Fracture surfaces of single crystal tungsten (a) at room temperature and (b) close to the brittle to ductile transition temperature. Reproduced from [131] by permission of Taylor & Francis.

neutron irradiated tungsten are presented in table 1.4.

All the tests were carried out in uniaxial tension, except for Krautwasser where three-point bend tests were used. Where possible a BDTT has been inferred from the results by assuming that fracture before 5% strain are indicative of brittle behaviour in tensile tests. From this assumption and the data available it was possible to determine the minimum BDTT in the work by Rau [136] and Gorynin [137], but no ductile tests were shown for these conditions and so the maximum BDTT in these cases could not be established. Steichen [138] showed brittle and ductile tests so a range for the BDTT could be established.

The full paper written by Krautwasser could not be accessed but the abstract that was available provided details of the testing technique (three-point bend) and the observed increase in BDTT.

The most recent of these studies was carried out in 1992 but the dose in dpa was not provided. It is very difficult to extrapolate from these to the effects of fusion irradiation on tungsten, especially since the irradiation temperatures are all significantly below the predicted operating window for tungsten in the fusion environment.

The results from Krautwasser and Steichen indicate relatively modest increases in the BDTT. This contrasts with Rau, where a sizeable increase at a low fluence was observed, and Gorynin who observed a significantly higher BDTT after irradiation. The lack of consistency between these results make it clear that further irradiations and tests to establish the post-irradiation BDTT are required. Furthermore, these experiments provide little insight into the underlying mechanism that controls the BDT. Improving our understanding in this area is critical to extrapolating results from fission neutron irradiation to fusion conditions.

The results do show how even low dose irradiation increases the BDTT significantly. It has thus been assumed that tungsten will become brittle following low dose irradiation [140]. This conclusion is workable for ITER but due to the challenging temperature

Table 1.4: Inferred increases in BDTT from previous mechanical tests on neutron irradiated tungsten

Reference	**Neutron Fluence(s) / m^{-2} (E > 0.1 MeV)**	**Irradiation Temperature/K**	**Inferred BDTT / K**
Krautwasser [139] (abstract only)	5.6 x 10^{25}	525-575	Increased by 70 (13.7 / 10^{24} n up to 5 x 10^{24})
Steichen [138]	5 x 10^{25} 9 x 10^{25}	648 648	505 - 700 K 505 - 700 K
Rau [136]	2.7 x 10^{24}(thermal) 3.8 x 10^{23}(E>1MeV)	343	>673 K
Gorynin [137]	1.5 x 10^{26} (no threshold energy)	773	>773 K

range for DEMO, ductile tungsten components have been proposed [141]. The high neutron irradiation level in DEMO means that a better understanding of the neutron irradiated BDTT in tungsten is required if it is to be used in this way and this will rely on computational models fitted to experimental results.

The work by Swinburne et al. [135] attempted to predict the effect of radiation damage on the BDTT. The conclusion of their work is that a reduction in the scale of microstructure due to irradiation would result in a transition from single kink activation energy to double kink. An approximate doubling of the BDTT would then be expected. This was found to be the case for a range of experiments on ferritic-martensitic steels. However, no verification of the change in activation energy was available.

The Swinburne model contrasts with an alternative proposed by Li et al [142]. This model suggests that the brittle to ductile transition temperature is increased due to the apparent dislocation velocity being reduced by the presence of defects. In this model, dislocations have to cross-slip in order to pass radiation induced defects, increasing the path length that a dislocation must glide to accommodate an applied strain. This model would expect the BDT temperature to increase without changing the activation energy, since cross-slip of screw dislocations has the same activation energy as slip along the original glide plane.

Two key experimental results that could help distinguish which of these models accurately describes the mechanism responsible for the increase in BDTT with irradiation are: (1) a more accurate determination of the increase in BDTT under neutron irradiation and (2) finding the activation energy associated with the post-irradiation BDT, similar to the work by Giannattasio and Roberts on unirradiated tungsten [131]. A doubling of the BDTT activation energy following irradiation would provide evidence for the Swinburne model, whereas a relatively small increase in BDTT and no change in activation energy would suggest that the Li model is accurate.

1.6 Research Goals

Based upon the literature reviewed above three key research goals have been identified for this work, as discussed in the sections below.

1.6.1 Improving our Understanding of the Effects of Neutron Irradiation on the BDT of Tungsten

As discussed in section 1.5, the BDT of tungsten is a critical design parameter for future fusion devices. In spite of this, our understanding of the effects of irradiation damage on the BDT are extremely limited and as a result we have no method of predicting what the BDT temperature of tungsten will be in service. This work aims to improve our understanding through four-point bend tests of neutron irradiated tungsten at a range of strain rate in a similar manner to that carried out by Giannattasio et al. on unirradiated tungsten [22].

This will not only provide another data point for BDT temperature vs dose but also measure the effect of irradiation on the activation energy of the BDT. This will give greater insight into how radiation damage affects the BDT and thus provide better capability for predicting the BDT following irradiation at different temperatures and doses than can be achieved currently. In particular, there are competing models for the cause of increase in BDT temperature in BCC metals following irradiation. These models can be distinguished by measurement of the activation energy associated with the BDT following irradiation.

1.6.2 Understanding the Differences Between Ion and Neutron Irradiation

Sections 1.3.3.3 and 1.3.2.4 highlight the significant differences between the mechanical and microstructural changes that result from ion and neutron irradiation. These differences pose a significant barrier to the development of ion irradiation as a proxy for neutrons, a technique that is being relied on to speed up the development of materials for the fusion environment. The discrepancies that arise from ion and neutron irradiation in tungsten are currently difficult to analyse as there has been no systematic attempt to match ion irradiation results to those produced by neutron irradiation.

This work will thus be the first to deliberately attempt to replicate a particular neutron irradiation experiment in tungsten through ion irradiation, critically matching the transmutation level as well as the dose and temperature. This may alleviate some of the apparent differences between ion and neutron irradiation while highlighting others. From this basis alterations could then be made to future ion irradiation campaigns in order to achieve better comparison to neutron irradiation.

1.6.3 Developing Testing Techniques Appropriate for Use on Ion Irradiated Material

Even if ion irradiation can be made to better replicate neutrons, testing techniques currently developed for ion irradiated material leave a lot to be desired. Micro-cantilever testing is still in early stage of development, particularly with regards to acquiring fracture properties from ion irradiated material [121]. Micro-pillars have been successfully applied to other ion irradiated material and unirradiated tungsten. Using it to test ion irradiated tungsten is a logical step and can be expected to provide useful information regarding the effects of irradiation on the plastic behaviour of tungsten.

Carrying out new applications of these techniques will aid the development of a pool of mechanical testing methods suitable for application to ion irradiation. This is another crucial area for the development of ion irradiation as a technique that can be used as a surrogate for neutrons.

2
Materials and Irradiations

Seven different samples were examined for this work. These were from three different as-received materials: single crystal tungsten, polycystalline tungsten and arc-melted tungsten 1.4wt% rhenium. Three different conditions were then studied: unirradiated, neutron irradiated and ion irradiated. The sections below detail the sourcing of these materials and the irradiation conditions used.

2.1 Materials and Sample Preparation

Commercially pure tungsten single crystal (W Single) and polycrystalline tungsten (W Poly) were acquired from Metal Crystals and Oxides, Cambridge, UK in the form of a 100 mm long x 10 mm diameter rods. The polycrystalline material had a distinct texture with grains elongated in the rolling direction to give large grains of approximately 100 x 10 μm, with a sub-grains approximately 20 x 2 μm.

"Matchsticks" were cut from W Single and W Poly for neutron irradiation by A Giannattasio and J Murphy according to the recipe given in [131]. These were 1 x 1 x 11 mm with sides cut along the $\langle 100 \rangle$ directions. Following electropolishing in 0.5 % NaOH, the matchsticks were notched using a sharp edge in a spark erosion machine for a few seconds at room temperature. This produced pre-cracks of 60 μm, composed of a 20 μm wedge notch and sharp pop in cracks of approximately 40 μm. In the W Single the pre-cracks were along $\{100\}$ directions. In W Poly the notch was orientated perpendicular to the rolling direction. This process was carried out prior to neutron irradiation.

W Single samples prepared in this work for ion irradiation were cut from the cross-section of the rod, exposing a (100) face. These samples were then ground using silicon carbide paper to a 2500 grit finish, followed by 3 μm diamond paste and polished

using 40 nm colloidal silica. Following this metallographic preparation the samples were annealed at 1673 K for 24 hours. These samples were used for ion irradiation.

Tungsten - 1.4 wt% rhenium (W-1.4Re) samples were prepared using arc melting. Arc melting gave a grain size > 1 mm. After arc melting they were cut, ground, polished and annealed in the same manner as W Single.

2.2 Irradiations

Ion irradiation was performed on W Single and W-1.4Re samples. Neutron irradiation was carried out on W Single and W Poly.

2.2.1 Ion Irradiation

Ion irradiation was carried out on JANNuS (Joint Accelerators for Nano-science and Nuclear Simulation) at CEA Saclay using a 3 MV Pelletron accelerator (Épiméthée). The samples were irradiation using W^{9+} ions accelerated to 24 MeV. Aluminium degrader foils of 0.8, 2 and 3 μm thickness were used to give a flat irradiation profile. The ion flux was an average of 7.0 x 10^{14} W^{9+} m^{-2} s^{-1} for a period of 11580 s. The irradiation was carried out at 1073 K.

2.2.1.1 Calculating Damage Using SRIM

The damage profile for the implantation was calculation using SRIM-2008 using the quick (Kinchin-Pease) cascade option as recommended by Stoller [143]. A displacement energy of 68 eV was used to maintain comparability between the ion irradiation results presented here and elsewhere in the literature. The damage level was calculated by the number of vacancies produced, provided by the SRIM output VACANCY.txt in units of angstrom^{-1} ion^{-1}. The calculation to convert this output to dpa, using the ion fluence Φ and atoms m^{-3} n is given in equation 2.1.

$$N_{dpa} = \frac{N_{SRIM} \times 10^{10} \times \Phi}{n} \tag{2.1}$$

The damage profile from the irradiation is given in figure 2.1. This shows that a profile with an average dose of 1.6 dpa up to 1 μm was achieved through the ion irradiation at a dose rate of 1.4×10^{-4} dpa s^{-1}. Microstructure examination was carried out within 1 μm of the surface. The damage level remained above 1.2 dpa up to a depth of 2 μm. This is the limit of the depth investigated through micro-mechanical testing.

2.2.2 Neutron Irradiation

W matchsticks were irradiated for 208 full power days in the High Flux Reactor (HFR), Petten at 1173 K under the Extremat II campaign. The neutron flux was 6.8 x 10^{18}

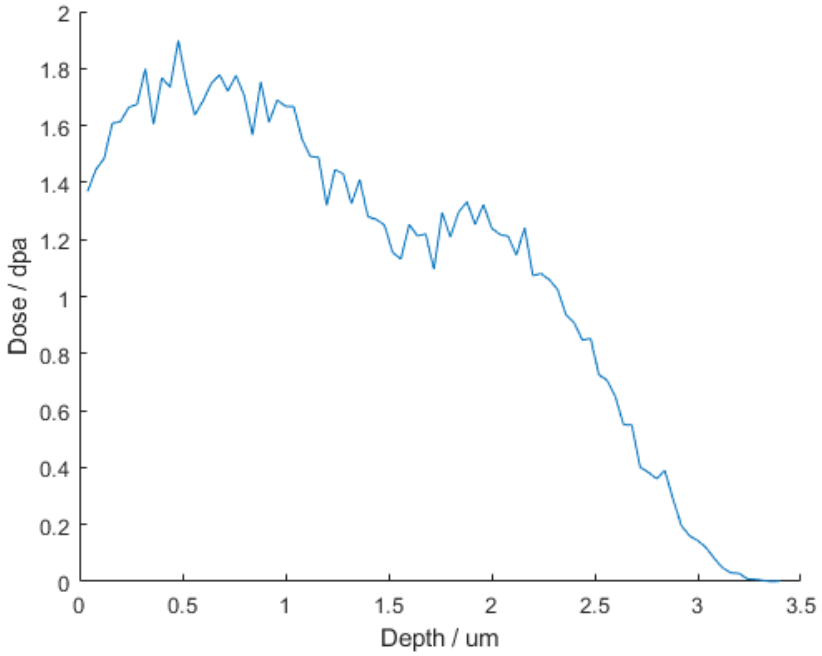

Figure 2.1: A plot of dose against depth into sample for ion irradiation of W Single and W Re samples

m^{-2} s^{-1} (3.2 x 10^{18} m^{-2} s^{-1} E > 0.1 MeV) for the first location (148 full power days) and 6.6 x 10^{18} m^{-2} s^{-1} (3.2 x 10^{18} m^{-2} s^{-1} E > 0.1 MeV) for the second location (60 full power days). The average energy spectrum of the neutron flux is shown in figure 2.2. FISPACT II [37] calculations were carried out by M Gilbert using a displacement energy of 55 eV, showing that the irradiation resulted in 1.67 dpa at a dose rate of 9×10^{-8} dpa s^{-1}. A lower displacement energy was used for FISPACT calculations than SRIM following specific advice based upon computational modelling [144]. Experiments using SRIM showed that a 68 eV displacement energy resulted in approximately 15% lower dpa than a 55 eV displacement energy for 24 MeV W irradiation.

The calculations also predicted transmutation to 1.4 wt% Re and 0.1 wt% Os. MCNP [38] modelling was carried out by Stephen Van der Marck, Nuclear Research Group, Petten. This showed that the irradiation spectrum had a much lower thermal flux than is usual for HFR. This was due to a neighbouring experiment that had high thermal neutron absorption. This resulted in less transmutation to rhenium and osmium than would otherwise be expected. Despite this reduction in thermal neutrons, the spectrum was much lower energy and transmutation rate much higher than would be expected in a fusion environment. The transmutation rate in this experiment was approximately 1 % Re per dpa, compared to 0.05-0.09 % Re per dpa predicted for DEMO [53]. Transmutation rates for other neutron irradiations of tungsten vary from 0.1 % per dpa in the JOYO fast reactor, Japan, to 3.4 %

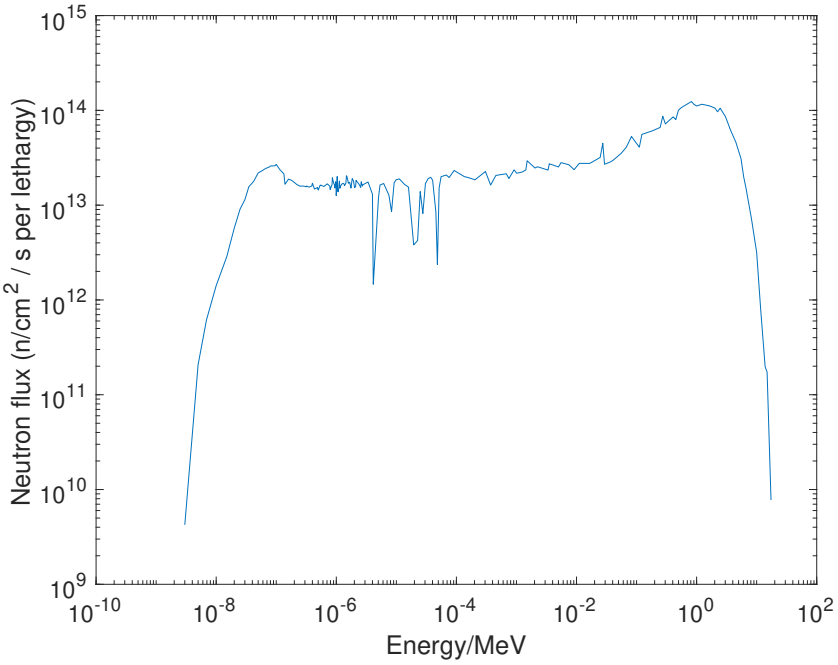

Figure 2.2: Neutron spectrum from irradiation in HFR

per dpa in HFIR, Oak Ridge, USA [53].

The materials were prepared for neutron irradiation by A. Giannattasio and J.D. Murphy while at the University of Oxford. The samples were not annealed prior to neutron irradiation, but the high irradiation temperature will result in stress-relief. Given the long time period for neutron irradiation, it is possible that recovery occurred as well. However, recovery of tungsten under these conditions has not been studied and the full time-temperature dependence of recovery and recrystallisation of tungsten is not well established.

Recrystallisation experiments have been used to determine the maximum operating temperature for tungsten in a fusion environment [30]. The model based on these experiments showed that extensive recrystallisation would be expected to occur at 1270 - 1370 K over a time period of two years. From this it reasonable to anticipate that significant recovery would be expected to occur during 273 days at 1173 K. The annealing conditions used prior to ion irradiation (24 hours at 1473 K) should have produced a similar degree of recovery so that the underlying microstructure (excluding irradiation damage) is comparable between the ion and neutron irradiated samples. Unfortunately, from currently available data it is not possible to quantify this any further.

A comparison experiment could be carried out by annealing tungsten samples for 273 days at 1173 K to establish the effect of in-reactor annealing on the underlying microstructure but this would require an extended amount of time available for the experiment and the rapid oxidation of tungsten at these temperatures means that

carefully controlled annealing conditions would be required. It was not possible to carry out such an experiment during this project.

3

Understanding Hardening Mechanisms in Irradiated Tungsten

3.1 Introduction

Hardness measurements have been commonly used to measure irradiation damage in tungsten, with a large array of neutron irradiation conditions having been tested with microhardness testing [86] and nanoindentation applied to ion irradiated tungsten [31]. These irradiation experiments have also investigated the microstructural changes in tungsten, however, efforts to correlate microstructure changes and irradiation hardening are in their nascency [24] [53]. Furthermore there is a significant gap between the results in neutron and ion irradiation hardening and further work is required to establish an understanding of the differences between them.

In order the understand to changes in mechanical properties induced by irradiation, an accurate measurement of the changes in microstructure is required. This has been carried out through use of energy-dispersive X-ray spectroscopy to measure transmutation and transmission electron microscopy of defects including dislocation loops and voids. Atom probe tomography has been applied in order to investigate the clustering of rhenium. The irradiation hardening measured has been correlated to the observed changes in microstructure through an irradiation hardening model similar to that described by Hu et al. [98].

3.2 Methods

Several different microscopy techniques have been deployed in this project to develop an understanding of how ion and neutron irradiation has altered the microstructure of W Single and W-1.4Re. These have used a range of scanning electron microscopes (SEM), transmission electron microscopes (TEM) and focused ion beam (FIB). While some of the more basic techniques are now standard, others are still being developed. This latter category are described below.

3.2.1 SEM Techniques

SEM can be used to investigate materials down to the sub μm scale. The microscopes used to do this work are mostly standard equipment available commercially, however, new methods for using these microscopes are constantly being explored and developed.

3.2.1.1 Energy Dispersive X-ray Spectroscopy of Tungsten Alloys

Energy dispersive X-ray spectroscopy (EDS) is a commonly used method for mapping the microstructure of alloys. Allowing the composition of different phases within an alloy to be easily measured. The application in this project is slightly more unusual, that of measuring the composition of an unknown alloy. Therefore care had to be taken to ensure the measurements were as accurate as possible, especially given the relatively low proportion of alloying elements present and the small difference in X-ray emission energies between the elements of interest. The SEM used for EDS in this work was a Tescan Mira 3 with an Oxford Instruments X-Max 80 EDS detector.

EDS spectra were measured from the neutron irradiated tungsten and the arc melted W-1.4Re alloy. L_α emission peaks were used due to their convenient energy values, located at 8.40 keV for W and 8.65 keV for Re, and acceptable separation between peaks. The M emission peaks were considered to overlap too much to be usable and K peaks for these elements are beyond the energies of standard SEM.

A background count assumed to be linear in energy between 8 and 9 keV was calculated and subtracted. A Gaussian peak was then fitted to 8.2-8.6 keV in order to calculate the tungsten count, and to 8.6-8.7 keV to calculate the rhenium count. Emission spectra for W and the arc-melted W-1.4Re are shown in figure 3.1 to show how these peaks appear in practice. The ratio between the peak sizes was calculated and assumed to be equal to the tungsten to rhenium ratio in the material. This was then converted to composition. Repeating these measurements on multiple arc-melted samples gave a standard deviation of 0.1% Re.

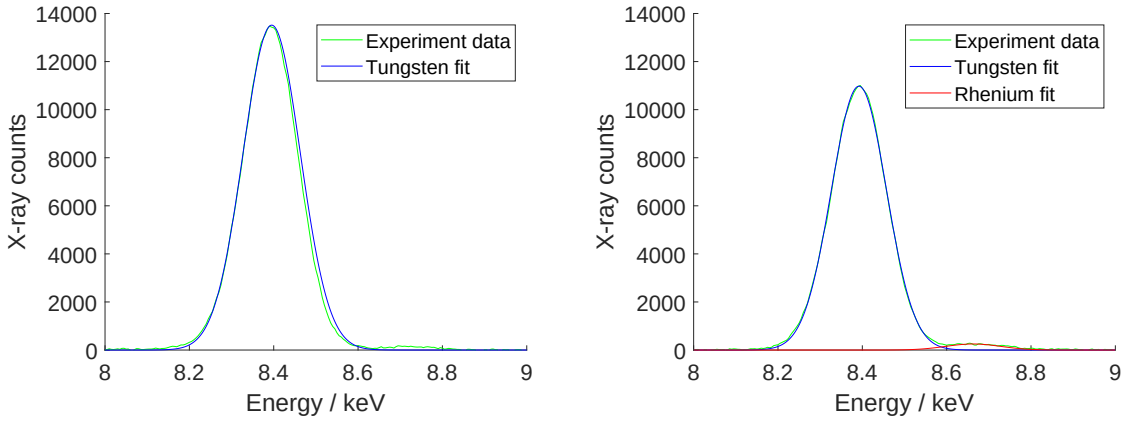

(a) W Single **(b)** W-1.4Re

Figure 3.1: EDS spectra from samples of known composition with fitted peaks showing method for calculating material composition

3.2.2 TEM Techniques

SEM is limited to a resolution > 100 nm for most applications. Given the very fine length scale ($\sim$ 1 nm) of defects present in tungsten following both ion and neutron irradiation, TEM was used in order to achieve higher resolution imaging. The techniques used for studying radiation damage are niche and still being developed, therefore they are described here. The particular defects being investigated in irradiated tungsten are voids and dislocations loops of $\mathbf{b} = \langle 100 \rangle$ and $\mathbf{b} = 1/2\langle 111 \rangle$ types. The TEM used in this work was a JEOL 2100 operated at 200 kV.

3.2.2.1 FIB Lift-Out Preparation for TEM

The shallow irradiation depth present in ion irradiated materials makes preparation of samples through electropolishing difficult. Additionally the electropolishing preparation technique is destructive and uses significant volumes of material. In order to allow for both mechanical testing and TEM of the same material, TEM samples were instead prepared using FIB lift-out method. This reduced the area of material required to around 40 x 40 μm. FIB lift-out is also the preferred method for preparing TEM samples from neutron irradiated material as electropolishing of active samples would produce significantly greater volumes of radioactive waste, something to be avoided if possible.

The FIB lift-out method is shown in figure 3.2, the energy of the beam used for the process is 30 kV unless otherwise stated. A platinum protective layer was deposited over the volume to be examined using the gas injection system (GIS) and a 240 pA beam. Trenches were then milled from either side using 16 nA ion beam. The lift-out volume was thinned and undercuts were made using a 2 nA beam. FEI Helios and Zeiss Auriga dual-beam FIB microscopes with micro-manipulator needles

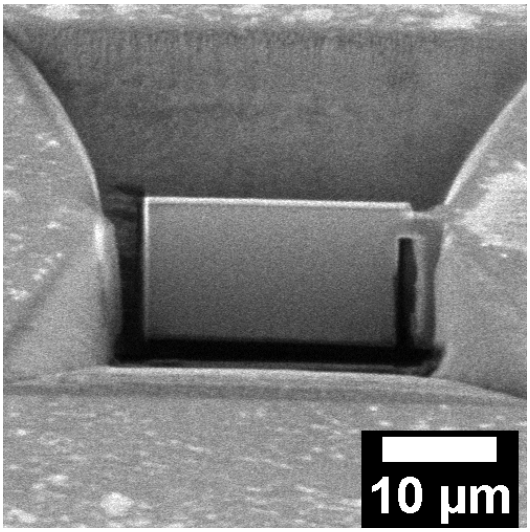

(a) Lift-out with top coated in Pt and sides cut away

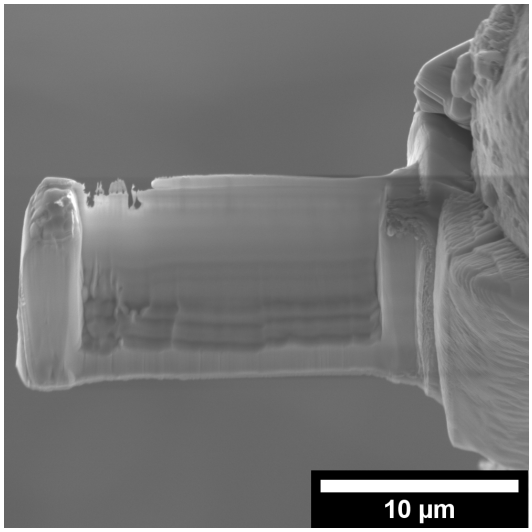

(b) Lift-out attached to grid and thinned to transparency

Figure 3.2: Images showing the process of creating a lift-out for TEM examination

for in-situ lift-out were used in this work.

The micro-manipulator needle was attached to the lift-out using Pt deposition before the undercut was completed to free the lift-out from the bulk sample. The sample was exchanged for a TEM grid and the lift-out was attached using Pt deposition. A window within the lift-out was then thinned using a succession of decreasing beam currents, with the lift-out at 2° to the incident beam in order to avoid milling of the Pt protective layer. The final thinning and cleaning of the sample was carried out using a 2 kV, 200 pA beam at 45° until the lift-out was transparent under a 10 kV electron beam.

In order to ensure that the maximum amount of FIB damage was removed from the lift-out, flash polishing was carried out. This involved placing the TEM grid with the lift-out in 0.5% NaOH solution and applying a 10 V electric current for 50 ms. Molybdenum TEM grids were used for this purpose and platinum tipped tweezers were used to hold the grid. The samples were then cleaned in methanol and plasma cleaned using a Fischione 1020 Plasma Cleaner for 120 s in order to remove any remaining solvent.

A similar FIB lift-out method was used to prepare samples for atom probe tomography. This method was similar to that described by Saxey et al. [145]. The key changes from TEM to APT sample preparation were that the sample was lifted out onto a silicon coupon rather than a TEM grid, the sample was thinned into a sharp needle shape, and no flash polishing step was carried out.

3.2.2.2 Foil Thickness Measurements

Foil thickness measurements were carried out using the convergent beam method described by Williams and Carter [146]. This involves investigating the Kossel-

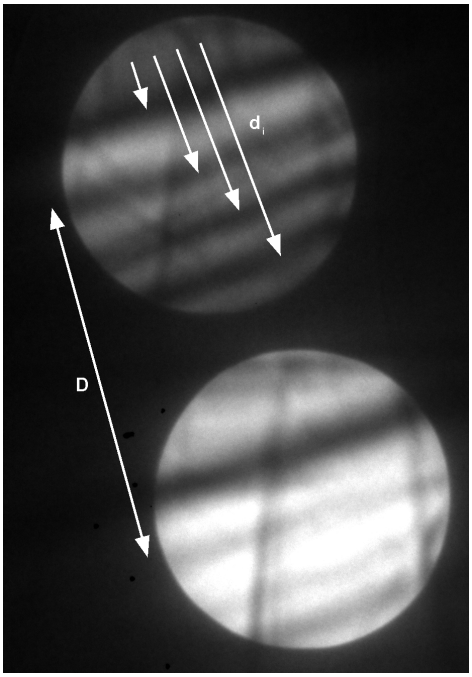

Figure 3.3: A image of Kossel-Möllenstedt fringes showing the measurements for calculating sample thickness. The measurement labelled D corresponds to $2\theta_B$ and d_i corresponds to $\Delta\theta_i$

Möllenstedt fringes under a strong two-beam condition. The spacing between the ith dark fringe and the bright central fringe can be used to calculate the deviation s_i using equation 3.1. The method for experimentally determining the factors introduced in equation 3.1 is given in figure 3.3. A JEOL 2100 TEM was used in this work.

$$s_i = \lambda \frac{\Delta\theta_i}{2\theta_B d^2} \tag{3.1}$$

$$\frac{s_i^2}{n_k^2} + \frac{1}{\xi_g^2 n_k^2} = \frac{1}{t^2} \tag{3.2}$$

Once s_i has been calculated, the thickness can be calculated from equation 3.2 where ξ_g is the extinction distance and n_k is an integer assigned a value using the method detailed below. From this equation plotting $\frac{s_i^2}{n_k^2}$ against $\frac{1}{n_k^2}$ should give a straight line of gradient $-\frac{1}{\xi_g^2}$ and intercept $\frac{1}{t^2}$. To investigate this n_k is first assigned a value of 1 for the first fringe, 2 for the second fringe etc. The graph is then plotted.

If a straight line of negative gradient is given then the values of n_k used is taken to be correct. If this is not the case then it indicates that the minimum thickness is greater than ξ_g. In this case each value of n_k is increased by one and the graph is replotted. A minimum of three visible dark fringes is necessary to utilise this method. n_1 was found to equal 2 for the sample shown in this example and the thickness was calculated as 49 nm.

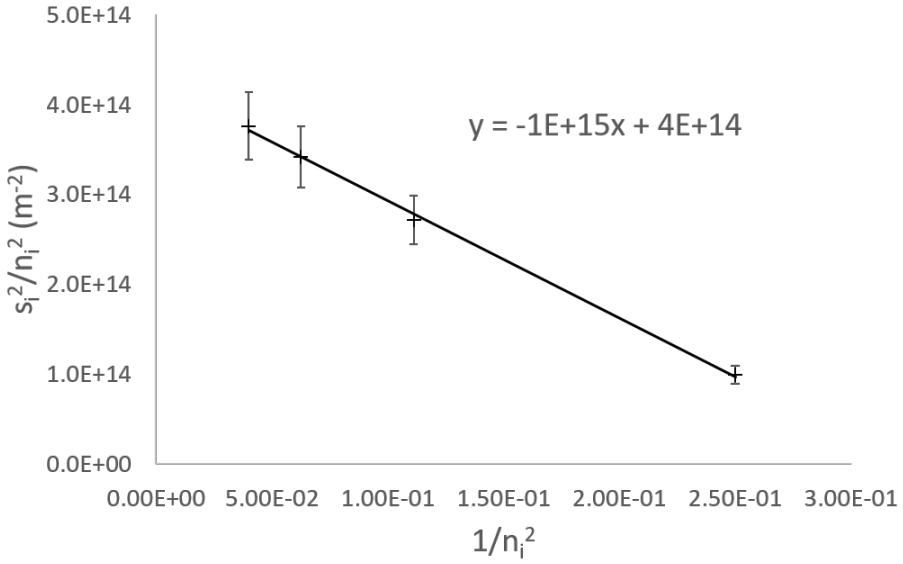

Figure 3.4: Graph showing the plot used to calculate the thickness of the sample using $n_1 = 2$

Sample	Thickness / nm
W Single Unirr	120 ± 12
W-1.4Re Unirr	116 ± 15
W Single Ion	95 ± 9
W-1.4Re Ion	72 ± 12
W Single Neutron	48 ± 6

Table 3.1: Measured thicknesses of the samples included in this work

For this work all Kossel-Möllenstedt patterns were imaged using a $\mathbf{g} = 112$ condition in order to have good separation between the diffraction disks. The method described was applied to each sample examined in this chapter and thickness measurements ranged between 50 and 120 nm, the thicknesses are shown in table 3.1.

3.2.2.3 Void Analysis

An electron beam passing through a void will pass through less material than a parallel beam that does not. This will cause a difference in structure-factor contrast and so large voids can be readily imaged in kinematical bright-field conditions. However, for smaller voids (< 5 nm), this contrast may be weak. Passing through a voids causes also a phase-shift in electrons relative to those that pass through adjacent crystal. This effect will produce phase contrast so in an out-of-focus TEM image Fresnel fringes will be visible around voids [147].

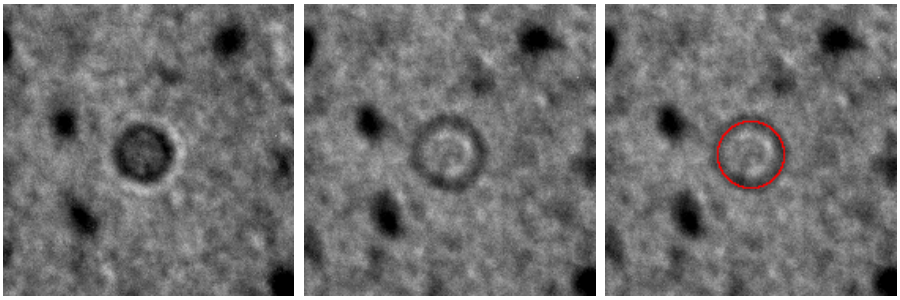

(a) 1000 nm overfocus **(b)** 1000 nm underfocus **(c)** Size measurement

Figure 3.5: Images showing a void in over- and under-focus and the sizing method

Voids were imaged and sized using the out-of-focus techniques described by Jenkins and Kirk [67]. Images were taken in a two-beam kinematical-bright field condition with the sample in focus and at ± 1000 nm in order to investigate the presence of voids in the material. The under- and over-focused images were compared in order to identify the location of voids. By aligning the images using ImageJ [148], voids could more easily identified by the change in contrast between under- and over-focused images. It should be noted that a bright-field images taken away from strong diffraction conditions (rather than in the two-beam condition used here) would have been better for imaging of voids with this method.

The imaged voids were then measured using the first dark Fresnel fringe in the under-focused image in order to give an accurate measurement of the size as recommended by Jenkins and Kirk. The under-focused image is used due to the high clarity of the Fresnel fringe. The discussion by Jenkins and Kirk considers calculations of the size of the dark fringe relative to the size of the void. These calculations found that the inside of the first Fresnel fringe gave a small over-estimate of size for small voids, within 10% for voids >2 nm. This was considered the most accurate method for this work given the small size of the voids identified. Circles were manually fitted to this fringe in ImageJ and the void diameters recorded. This process is shown in figure 3.5. Voids < 5 nm in size are difficult to measure using this method and the sizing becomes inaccurate at this scale. Below 2 nm voids are almost impossible to identify and so voids of this size were not considered.

3.2.2.4 Loop Counting

Weak-beam dark-field images were used to image and size dislocation loops as recommended by Jenkins [67]. These were captured using $\mathbf{g} = \pm 200$ and ± 110, typically at 4-5 $\mathbf{g}$ with $s \neq 0$. The images were captured using a Digital Microscopy script written by Haley [149]. This varied the deviation parameter by up to 0.02 nm^{-1} and processed the beam in a circle. The result is ten micrographs each captured using a slightly different deviation parameter, as shown in 3.6. The exposure time for each micrograph was 5 s.

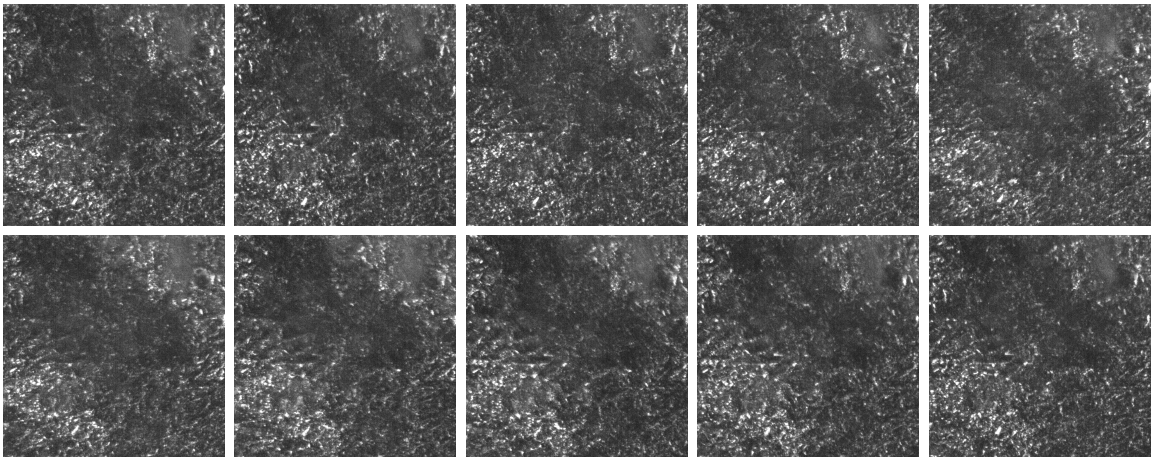

Figure 3.6: Weak-bream, dark field images captured using the Digital Microscopy script [149]

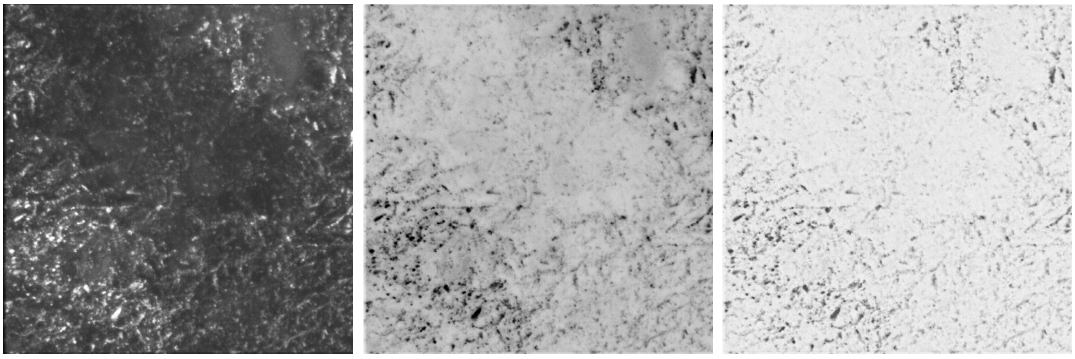

(a) **(b)** **(c)**

Figure 3.7: TEM image processing process: (a) align images in 3.6 into a stack and sum; (b) invert contrast; and (c) subtract background

These micrographs can then be aligned using ImageJ [148], to give a micrograph with enhanced contrast for dislocation loops and reduced background noise. The micrographs are shown with inverted contrast as this was found to give a clearer depiction of defects (dark defects against a light background). This process is shown in figure 3.7.

Loop counts were carried out using ImageJ and the method described by Yi [70]. This involves thresholding the image to convert from grey scale to binary. Ellipses are then automatically fitted to the defects visible in the image. These were then binned into 1 nm sizes based upon the major axis of the fitted ellipse. This method works well for "black dot" type defects where dislocation loops show little to no internal contrast. This was true of most the loops observed in this work. An example of these steps is shown in 3.8.

Some issues arise when trying to size loops < 4 nm diameter as the contrast for these loops will be weaker and so loops may be undersized or missed completely if < 1

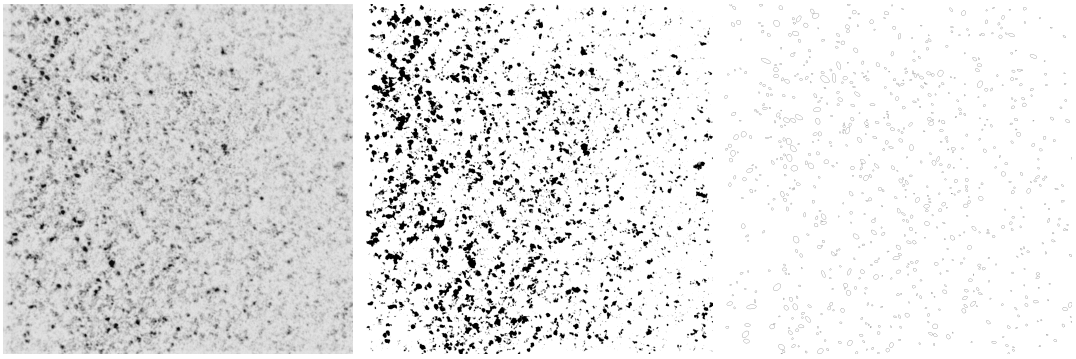

(a) **(b)** **(c)**

Figure 3.8: Loop counting process: (a) TEM image after processing; (b) apply threshold; and (c) fit ellipses

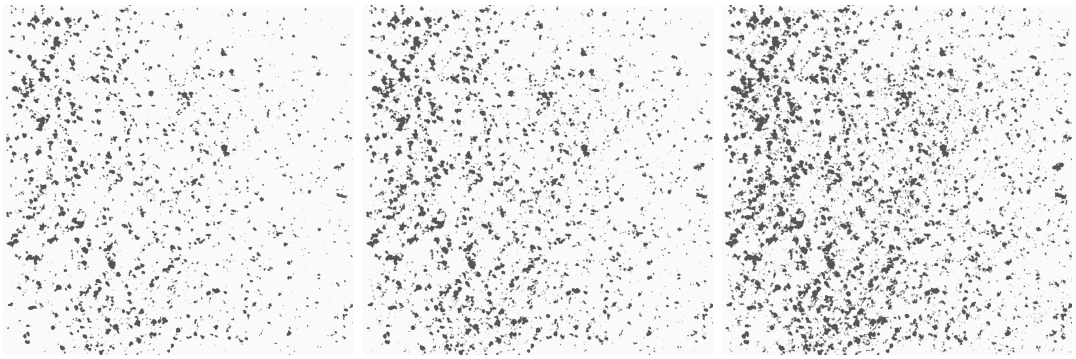

(a) **(b)** **(c)**

Figure 3.9: Images used for estimation of error in loop counting by adjusting the threshold value: (a) Threshold = 164; (b) Threshold = 174; and (c) Threshold = 184;

nm. As a result no loops below 1 nm were considered. In order to estimate the error in number density of loops and mean size, the background noise in an area considered to contain no loops was measured. This gave a typical background noise level of 20 (out of 256 on an 8 bit grey scale). The loop count was then repeated with the threshold set at $\pm$ 10 from the original value, as shown in figure 3.9. Repeating the loop counting method on using each of these thresholds gave the histograms shown in figure 3.10. These distributions were used to calculate the error in loop density and mean loop size. This process was carried out using one imaging condition from each sample in order to establish a representative error. The error calculated using this method was significantly larger than the calculated errors in sample thickness, or the apparent loop density in the unirradiated samples, and so was considered the dominant error in loop density measurements for the purpose of further analysis.

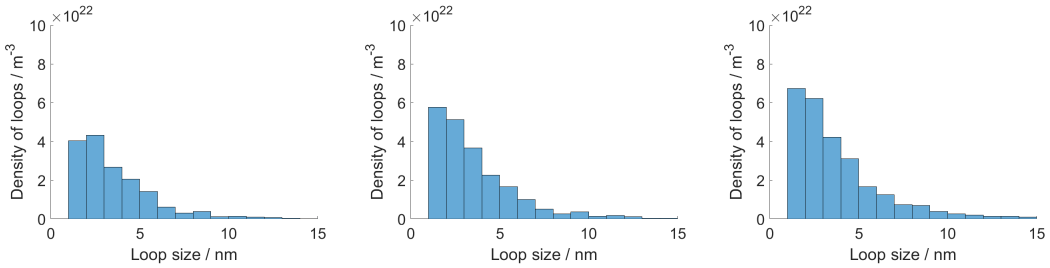

Figure 3.10: Histograms used for estimation of error in loop counting by adjusting the threshold value: (a) Threshold = 164; (b) Threshold = 174; and (c) Threshold = 184;

3.2.2.5 Loop Type Analysis

Previous study of ion irradiated tungsten has shown that $\mathbf{b} = 1/2\langle 111\rangle$ and $\mathbf{b} = \langle 100\rangle$ are produced [150]. Analysis of this type relies on the visibility criteria of loops under different imaging conditions. Dislocation loops can only be observed in TEM due to diffraction contrast. By carefully selecting the diffraction condition used for imaging, different types of loops will be visible or invisible. The important criteria for this is that only loops where the dot product of the g-vector ($\mathbf{g}$) (which describes the diffraction condition) and the Burgers vector of the dislocation loop ($\mathbf{b}$) does not equal zero will be visible. A common set of diffraction conditions used for this analysis in tungsten are ± 110 and ± 200.

The value of $\mathbf{g.b}$ is given for each of the combinations of $\mathbf{g} = \pm 110$, $\mathbf{g} = \pm 200$, $\mathbf{b} = 1/2\langle 111\rangle$ and $\mathbf{b} = \langle 100\rangle$ are given in table 3.2. The work by Yi et al. used images of individual loops under multiple conditions to confirm the Burgers vector of each loop. This is a highly specialised technique that it was not possible to replicate in this work. Instead the overall loop density was measured under each diffraction condition and conclusions were drawn from these values.

For example two thirds of $\mathbf{b} = \langle 100\rangle$ loops are visible under $\mathbf{g} = \pm 110$ conditions, whereas only one third are visible under $\mathbf{g} = \pm 200$ conditions. Therefore if the loop density observed under $\mathbf{g} = \pm 110$ conditions was twice the loop density observed under $\mathbf{g} = \pm 200$ conditions then the conclusion could be made that almost all the loops are of $\mathbf{b} = \langle 100\rangle$ type and that the total loop density is $\frac{3}{2}\times$ the loop density observed under $\mathbf{g} = \pm 110$ conditions.

3.2.3 Nanoindentation

Two types of nanoindenter (nanoindenter XP and nanoindenter G200) were used in this work. Indentation was carried out using continuous stiffness measurement (CSM) mode. This applies a small oscillation (typically 2 nm at 39 Hz) to the indent, allowing for the elastic modulus and hardness of the material to be measured constantly.

	$\mathbf{g} = 110$	$\mathbf{g} = \bar{1}\bar{1}0$	$\mathbf{g} = 200$	$\mathbf{g} = \bar{2}00$
$1/2[111]$	1	-1	1	-1
$1/2[11\bar{1}]$	1	-1	1	-1
$1/2[1\bar{1}1]$	0	0	1	-1
$1/2[1\bar{1}\bar{1}]$	0	0	1	-1
$[100]$	1	-1	2	-2
$[\bar{1}00]$	-1	1	-2	2
$[010]$	1	-1	0	0
$[0\bar{1}0]$	-1	1	0	0
$[001]$	0	0	0	0
$[00\bar{1}]$	0	0	0	0

Table 3.2: **g.b** for diffraction conditions used for weak-beam dark-field imaging of defects. Only defects with $\mathbf{g.b} \neq 0$ will be visible in each image

This allows for faster and more accurate measurements than load-unload tests due to the reduced effect of thermal drift.

The usual conditions for nanoindentation were 2 μm deep indents at a strain rate of 0.05 s^{-1}. The strain rate for nanoindentation is given in equation 3.3 where h is the indentation depth, $\dot{h}$ is the indentation speed, and $\dot{\varepsilon}_{nanoindentation}$ is the nanoindentation strain rate. The depth over which materials parameters were calculated varied depending on the material being tested due to the shallow penetration of the ion irradiated volume.

$$\dot{\varepsilon}_{nanoindentation} = \frac{\dot{h}}{h} \tag{3.3}$$

3.3 Transmutation

3.3.1 Energy Dispersive X-ray Spectroscopy

The transmutation caused by neutron irradiation was measured using energy dispersive X-ray spectroscopy (EDS) as described in section 3.2.1. The X-ray counts from the L_α emission were estimated by subtracting the background counts (approximated to a linear dependence on energy) and fitting peaks around the tungsten (8.40 keV) and rhenium (8.65 keV) L_α energies. The proportion of rhenium was then calculated by comparing the area under the fitted peaks. The experimental result and the fitted curves are shown in figures 3.11 and 3.12. This analysis showed that the material had transmutated to 1.5 wt% Re. The presence of osmium (L_α = 8.91 keV) could not be detected from this technique.

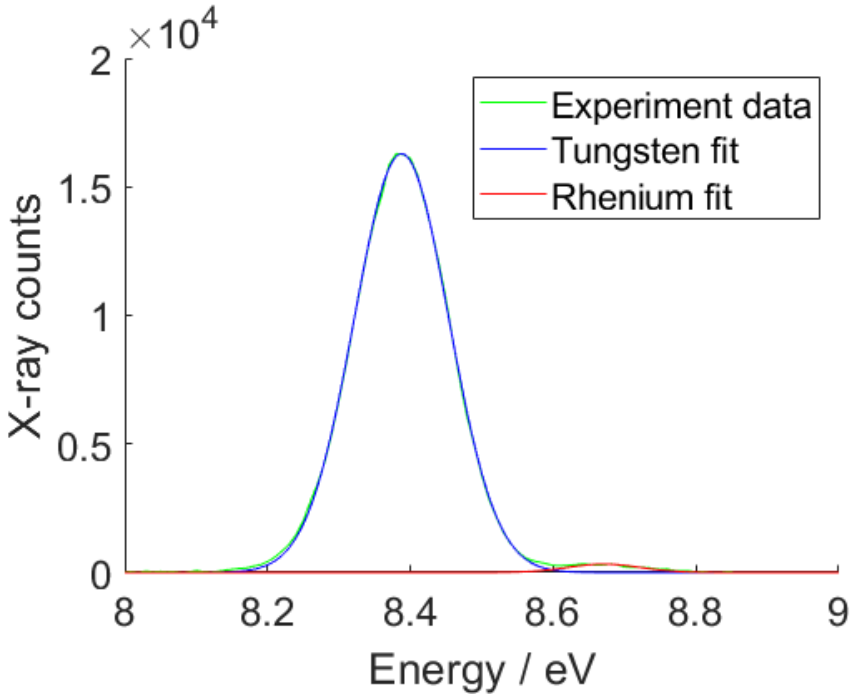

Figure 3.11: Energy Dispersed X-ray Spectroscopy results for neutron irradiated tungsten single crystal showing the fitted peak for the tungsten and rhenium L_α energy

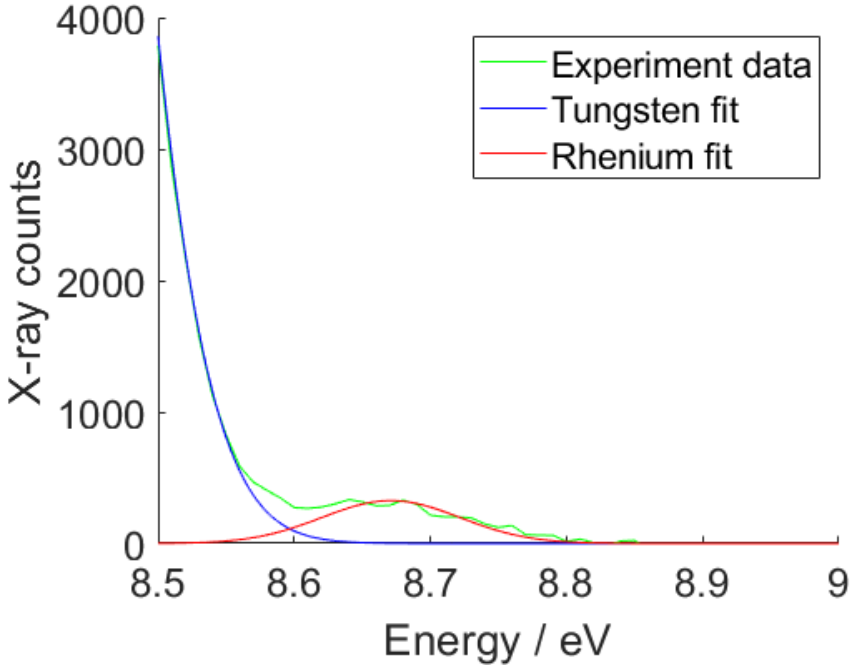

Figure 3.12: Energy Dispersed X-ray Spectroscopy results for neutron irradiated tungsten single crystal showing the fitted peak for the Re L_α energy

Element	Concentration (atomic %)
W	98.5
Re	1.4
Os	0.1
Ta	0.02
He	0.015 appm
H	0.003 appm

Table 3.3: Modelled elemental composition of tungsten after irradiation to 1.67 dpa in HFR, Petten

3.3.2 FISPACT Modelling

The transmutation was also modelled using FISPACT-II [37] by Mark Gilbert, Culham Centre of Fusion Energy, UK. This model used a spectrum calculated using MCNP by Steven van der Marck, Nuclear Research Group, Petten, Netherlands. This calculation had to take into account the location within the reactor and other experiments present in order to achieve an accurate spectrum. FISPACT predicted a transmutation to 1.4 wt% Re and 0.1 wt% Os. This rhenium content matches that measured by EDS and the low level of osmium could not be detected with the EDS equipment available. FISPACT calculations also showed very low production of hydrogen and helium from this irradiation (< 1 appm). A summary of the composition predicted by FISPACT is shown in table 3.3.

The FISPACT model also gave predictions of sample activity. For this, the appropriate cooling period after irradiation was also included. These results were then compared to gamma spectroscopy measurements.

3.3.3 Gamma Spectroscopy

Gamma spectroscopy of the sample was carried out in the ADRIANNA laboratory by Steve Bradnam and Lee Packer, Culham Centre for Fusion Energy. The measurements were made using a Small Anode Germanium detector. These measurements detected peaks at 99 keV and 137 keV. These peaks corresponded to Re-187 and Re-187m respectively. The measured activity of these isotopes is shown in table 3.4 and compared to the values calculated using FISPACT.

These measurements were carried out nine years after the irradiation so more active, shorter half-life isotopes have mostly decayed away. This includes the majority of Re-186 produced from the irradiation. The residual activity of Re-186 is being fed by the decay of Re-186m. This is why the measured activity of the isotopes is very similar.

Both Re-186 and Re-186m are formed predominantly by Re185(n,γ) with Re-186 having a cross-section approximately $10^3\times$ greater. As a result measuring the cross-section for formation of Re-186m during irradiation is difficult as it is a substantially

Isotope	Half-life / s	Modeled activity / Bq g^{-1}	Measured activity / Bq g^{-1}
Re-186	3.2 x 10^5	95 ± 7	187 ± 2
Re-186m	6.3 x 10^{12}	95 ± 7	200 ± 9

Table 3.4: Modeled activities compared to those measured using gamma spectroscopy

smaller than the Re-186 with a nearly identical energy dependence. As a result the nuclear data source (EXFOR) used for FISPACT modelling has a large uncertainty for the cross-section of Re-186m. This is the most likely cause of the large difference between the predicted activity from the FISPACT model and the measured value from gamma spectroscopy. This error is unlikely to affect the accuracy of the transmutation prediction as the total amount of Re-186m accounts for only 0.000015% of the rhenium production during the irradiation.

3.4 TEM Examination of Irradiation Damage

The post-irradiation microstructure of the ion and neutron irradiated materials was examined using transmission electron microscopy (TEM) to features that contribute to hardening including dislocation loops and precipitates. The samples were prepared for TEM using FIB lift-out and flash electropolishing as described in section 3.2.2.1.

The sample thickness was measured through the techniques described in section 3.2.2.2. This was essential for calculations of void and loop density. The thickness of the samples examined ranged between 50 and 120 nm.

3.4.1 Imaging Dislocation Loops

Weak-beam dark-field imaging was used to image the dislocation loops present in the ion and neutron irradiated materials as described in section 3.2.2.4. The figures below include images from each sample.

3.4.1.1 Unirradiated Samples

Images were taken from unirradiated samples and loop counts performed in order to give a background count for what defects were expected in the pre-irradiation microstructure and any imaging artefacts or remnants of damage from the sample preparation process. The defects present were analysed in the same manner as the irradiated samples in order to give a background level for the dislocation loop counts. The loop count results are presented together in section 3.4.2. These defects were most likely introduced through the focused ion beam preparation method.

W Single unirradiated (figure 3.13) was imaged near a (002) pole with $\mathbf{g} = \pm 110$ (4-5 $\mathbf{g}$) and had a thickness of 100 nm. The images taken from this sample show small black dot damage present throughout up to a few nanometres in size. No large defects

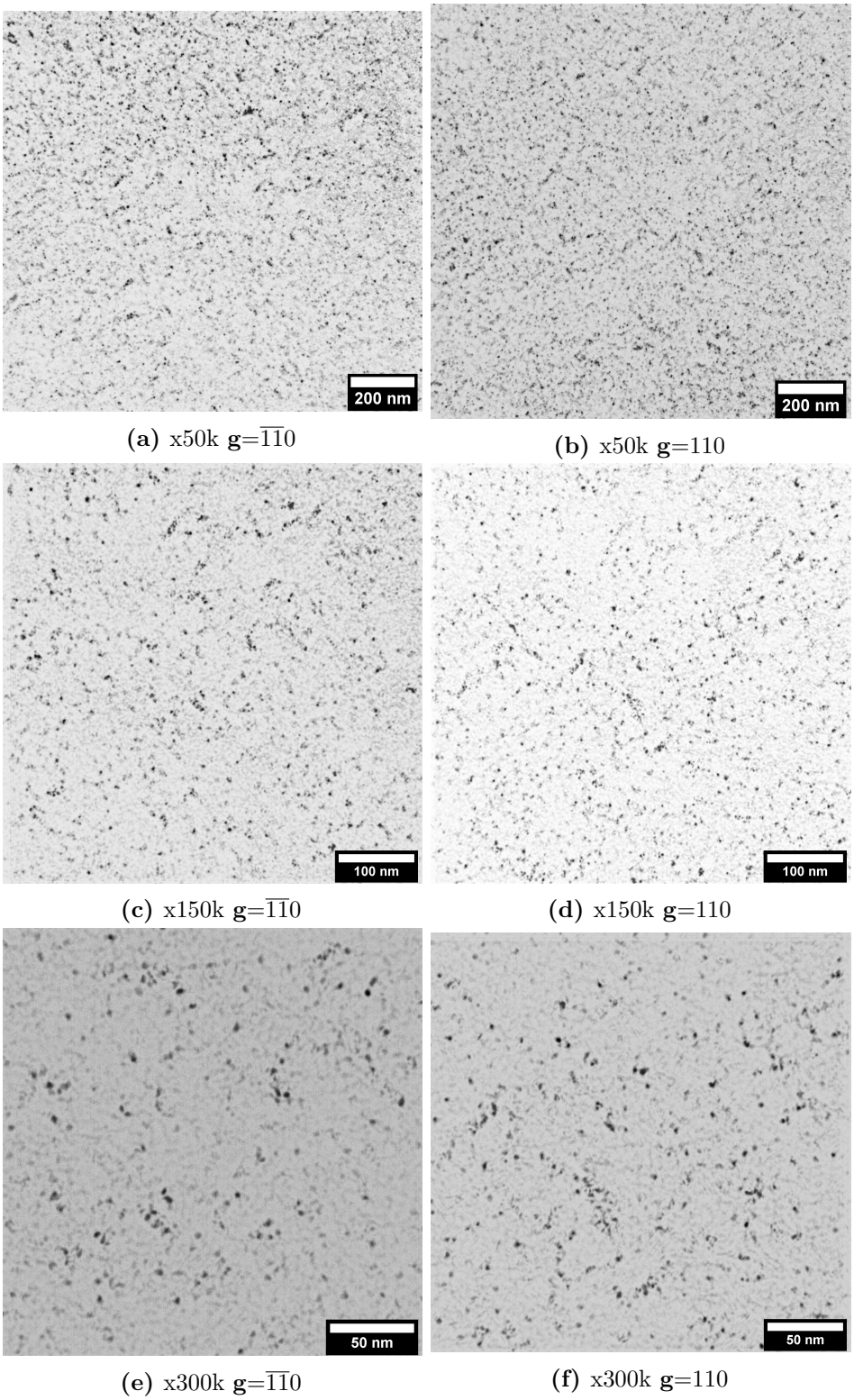

(a) x50k **g**=$\overline{1}\overline{1}0$ **(b)** x50k **g**=110

(c) x150k **g**=$\overline{1}\overline{1}0$ **(d)** x150k **g**=110

(e) x300k **g**=$\overline{1}\overline{1}0$ **(f)** x300k **g**=110

Figure 3.13: TEM images of W Single unirradiated showing small black dot damage

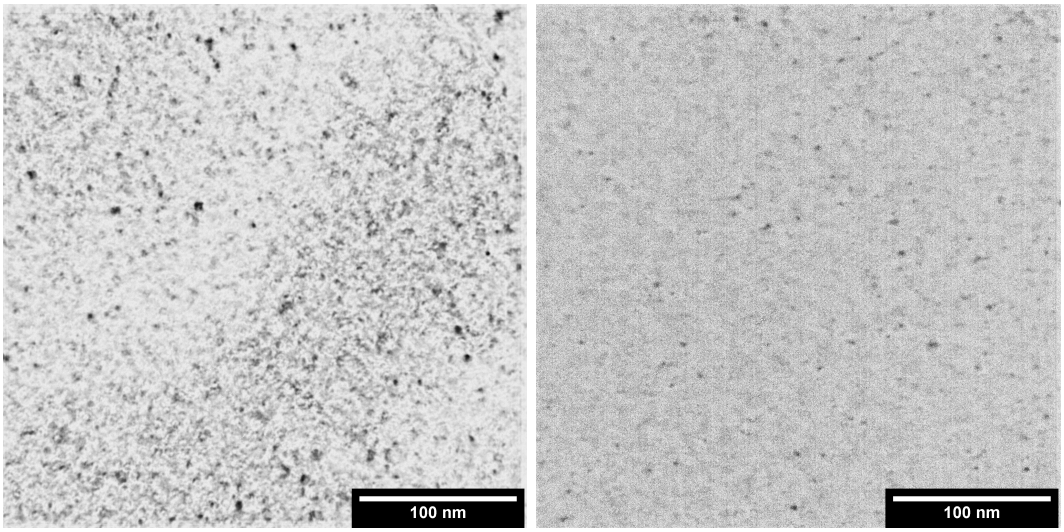

(a) x250k **g**=$\overline{1}10$ **(b)** x250k **g**=110

Figure 3.14: TEM images of W-1.4Re unirradiated

were observed and the background dislocation count appears to be very low, as would be expected after the annealing process. These images provide a good idea of the background against which radiation damage in the irradiated samples is to be measured.

W-1.4Re unirradiated (figure 3.14) was imaged near a (002) pole with $\mathbf{g} = \pm 110$ (4-5 **g**) and had a thickness of 120 nm. The thickness of this liftout means that the images acquired are of limited quality.

3.4.1.2 Ion Irradiated Samples

The images below show the radiation damage observed in self-ion irradiated W Single and W-1.4Re samples.

Figure 3.15 shows images from W Single Ion taken imaged near a (002) pole with $\mathbf{g} = \pm 110$ (4-5 **g**). These images show defects in significantly high density than the unirradiated samples. In addition to black dot defects, there appears to be some linear defects, although these are weaker in contrast. Similar loop rafts were observed by Xiaoou Yi in ultra-high purity tungsten under ion irradiated at 1023 K [70].

The visible loops generally appear similar to those observed by Yi in commercially pure tungsten irradiated to 1.4 dpa at 773 K [151]. The only significant difference is the additional rafting, suggesting that this is encouraged by higher temperature irradiation.

Yi found that the vast majority of defects in tungsten after irradiation above 750 K were interstitial $1/2\langle 111\rangle$ type loops. Due to the **g.b** invisibility criterion, this suggests that only half the loops present in the material will be visible in images taken with $\mathbf{g} = \pm 110$ (see table 3.5). The aim of this work was not to carry out replicate analysis of nature and orientation as this was comprehensively covered by

	$\mathbf{g} = 110$	$\mathbf{g} = \overline{1}\overline{1}0$	$\mathbf{g} = 200$	$\mathbf{g} = \overline{2}00$
$1/2\langle 111\rangle$	1	-1	1	-1
$1/2\langle 11\overline{1}\rangle$	1	-1	1	-1
$1/2\langle 1\overline{1}1\rangle$	0	0	1	-1
$1/2\langle 1\overline{1}\overline{1}\rangle$	0	0	1	-1

Table 3.5: g.b for diffraction conditions used for weak-beam dark-field imaging of defects. Only defects with $\mathbf{g.b} \neq 0$ will be visible in each image

Yi. Rather an overall dislocation loop density was calculated for each sample in order to inform hardness calculations in section 3.7.

W-1.4Re Ion appears to only show small black dot type damage but at a very high density in well imaged regions. The sample was imaged in both $\mathbf{g} = \pm 110$ and $\mathbf{g} = \pm 200$ conditions. The variation in image signal makes it difficult to tell by eye if there is any difference in loop population between the imaging conditions so further discussion on the dominant type of loop present is in section 3.4.2.

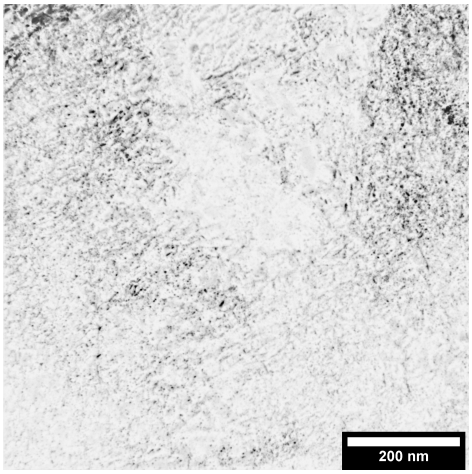

(a) x100k **g**=$\overline{1}\overline{1}0$

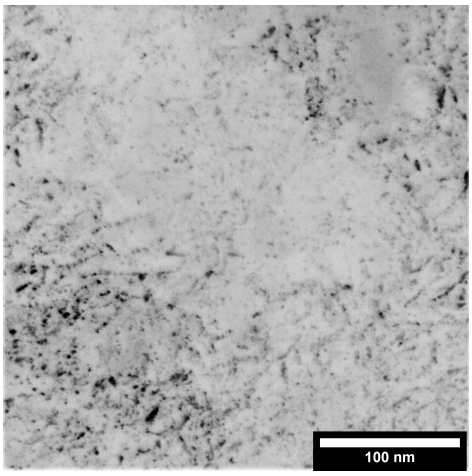

(b) x250k **g**=$\overline{1}\overline{1}0$

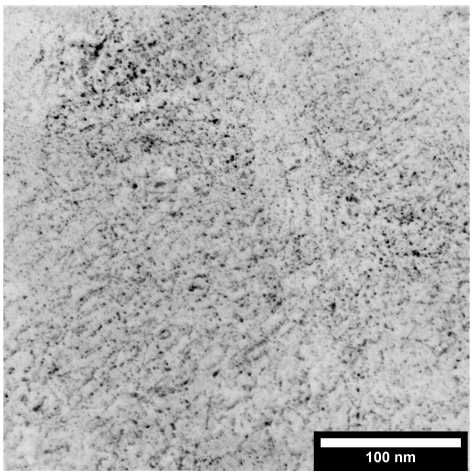

(c) x250k **g**=110

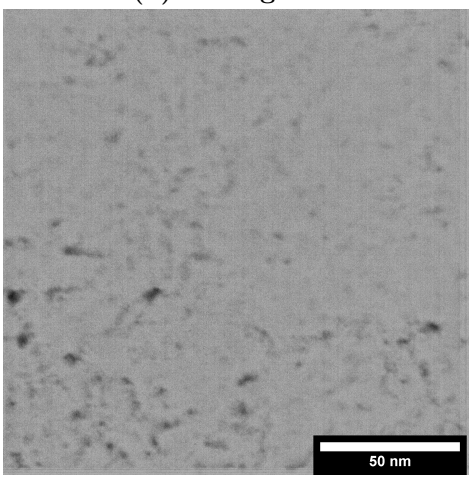

(d) x500k **g**=$\overline{1}\overline{1}0$

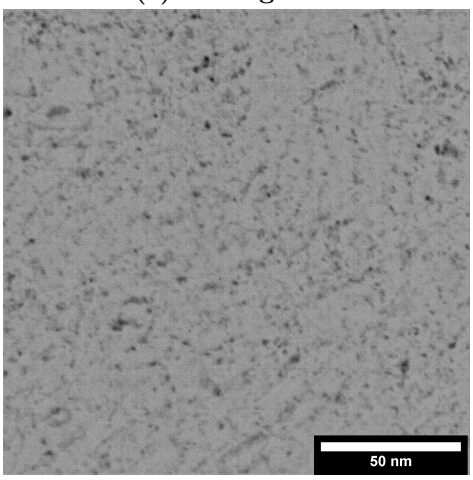

(e) x500k **g**=110

Figure 3.15: TEM images of W Single Ion showing dislocation strings and a high black dot population

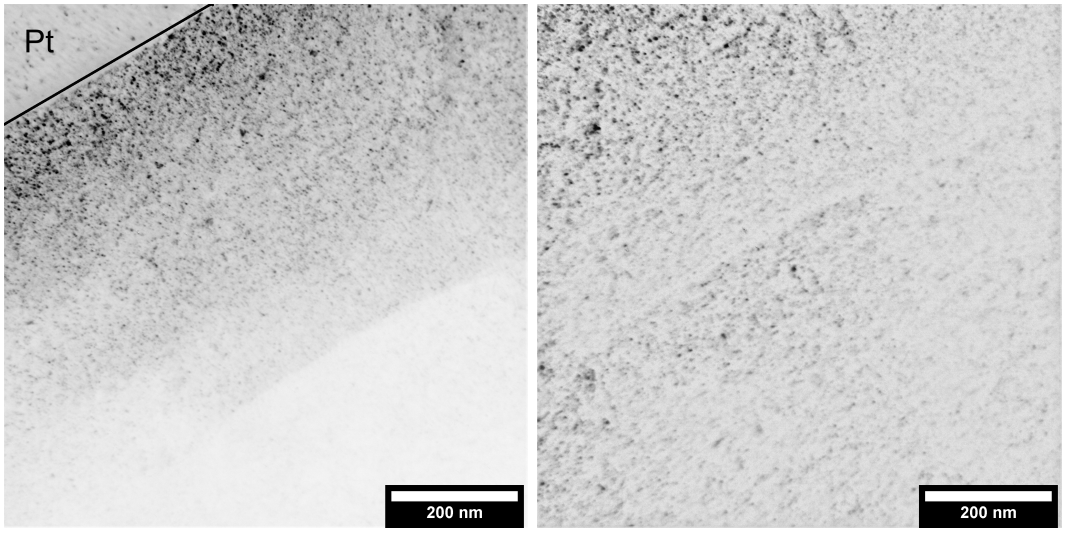

(a) x100k **g**=$\overline{1}\overline{1}0$ **(b)** x100k **g**=110

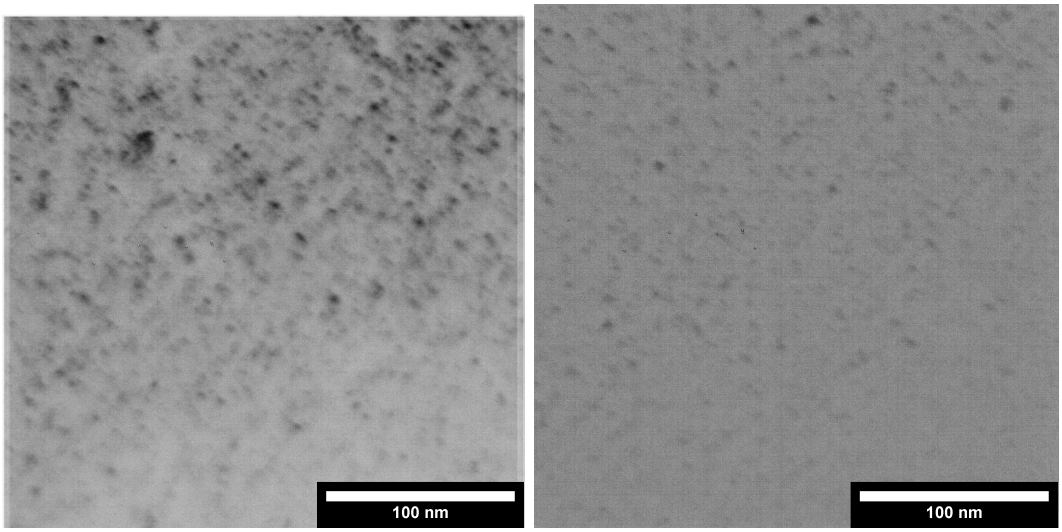

(c) x300k **g**=$\overline{1}\overline{1}0$ **(d)** x300k **g**=110

Figure 3.16: TEM images of W-1.4Re Ion with **g** = ±110. The surface of the liftout is visible in the top left of (a), with the deposited platinum layer labelled. Only small black dot defects could be observed in this sample

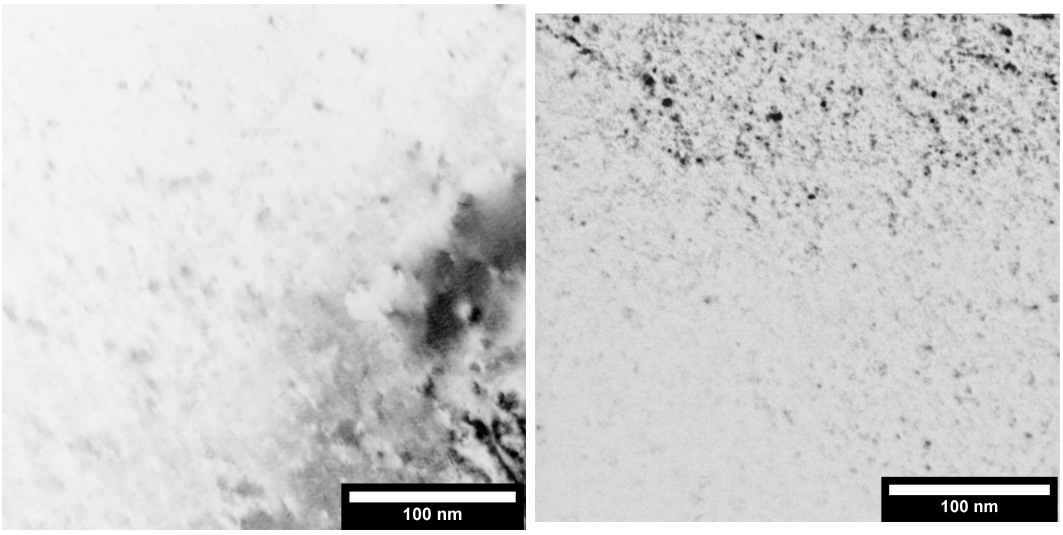

(a) x250k **g**=$\bar{2}$00 **(b)** x250k **g**=200

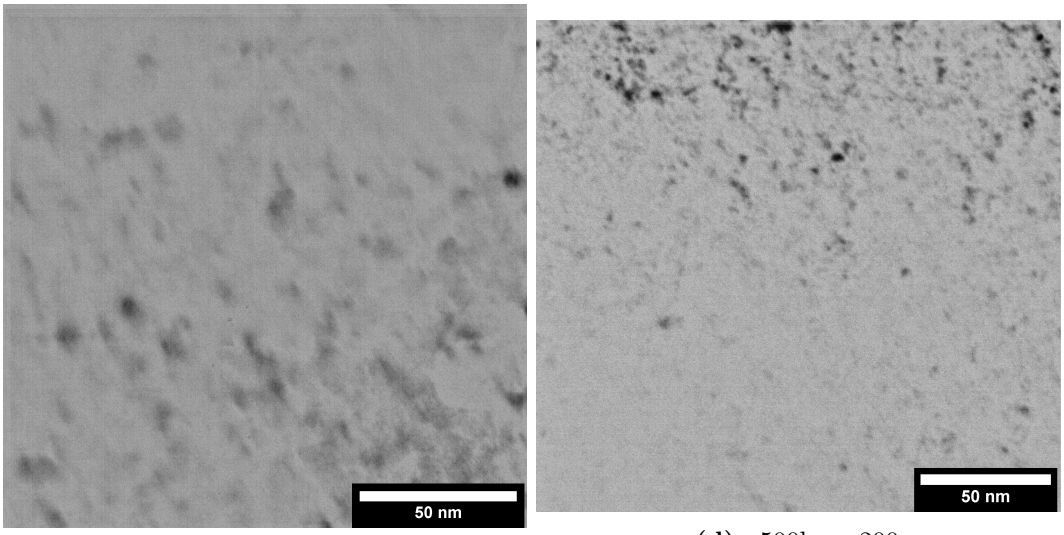

(c) x500k **g**=$\bar{2}$00 **(d)** x500k **g**=200

Figure 3.17: TEM images of W-1.4Re Ion with **g** = ±200. The condition in (a) is strong dark-field

3.4.1.3 Neutron Irradiated Sample

Images of the neutron irradiated sample were taken in three weak-beam dark-field conditions $\mathbf{g}=\pm 200$ and $\mathbf{g}=110$. The sample was 50 nm thick. Only black dot damage was visible. There appeared to be approximately double the amount of damage present in the $\mathbf{g}=\pm 200$ compared to $\mathbf{g}=110$. This suggests that the loops present are of $1/2\langle 111\rangle$ type as expected.

Small loop defects were also found in clusters, possibly around pre-existing defects, after neutron irradiation at 573 K by Van Renterghem and Uytdenhouwen [152]. These were characterised as all being of $1/2\langle 111\rangle$ nature.

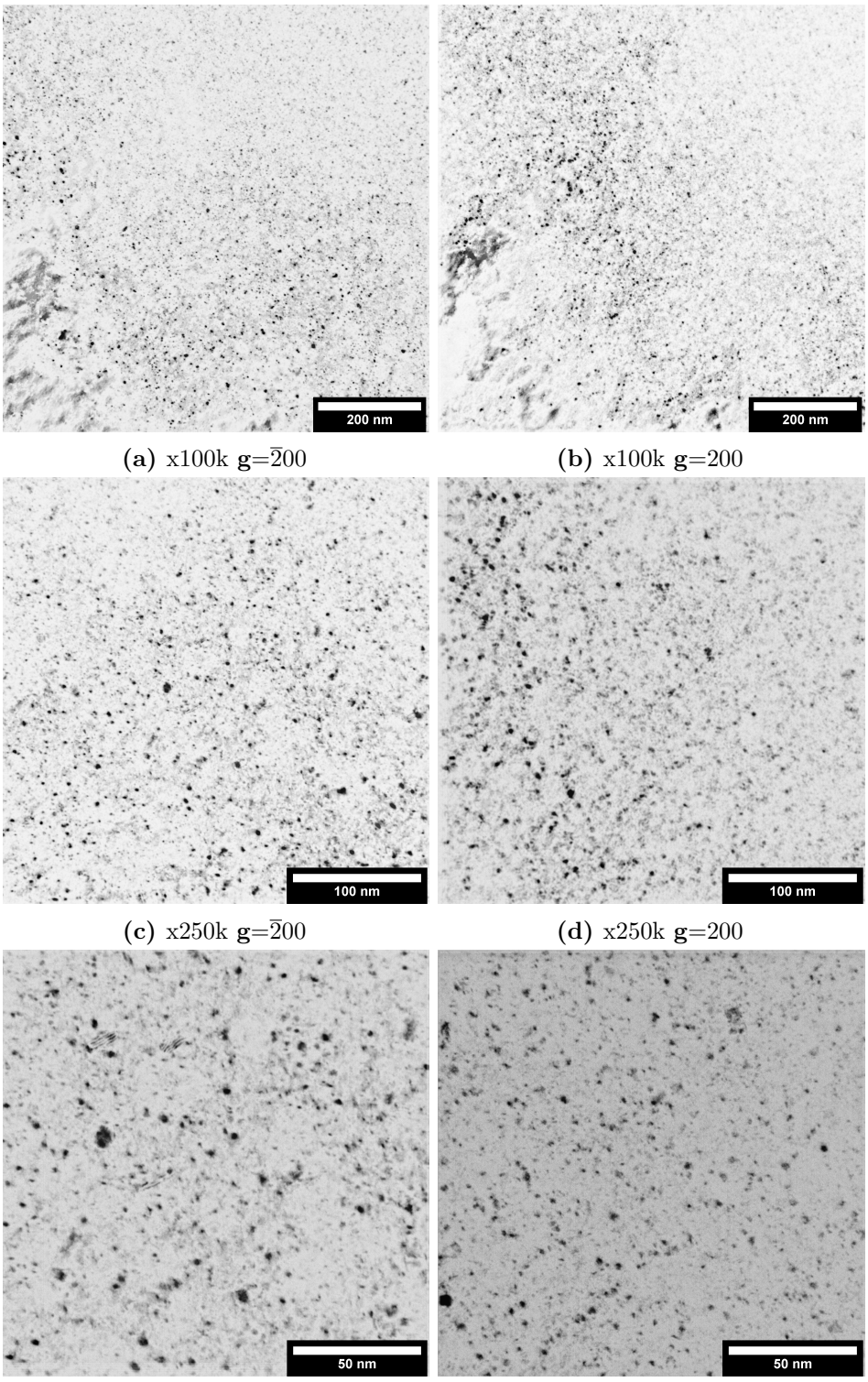

(a) x100k **g**=$\bar{2}$00 **(b)** x100k **g**=200

(c) x250k **g**=$\bar{2}$00 **(d)** x250k **g**=200

(e) x500k **g**=$\bar{2}$00 **(f)** x500k **g**=200

Figure 3.18: TEM images of W Single Neutron under **g**=±200

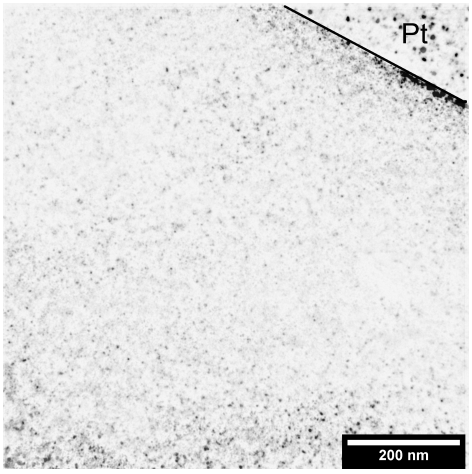

(a) x100k **g**=110

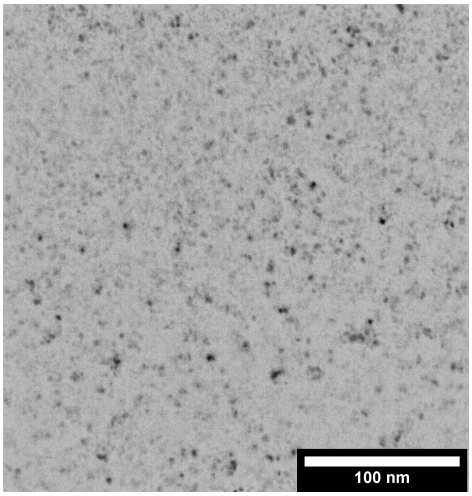

(b) x250k **g**=110

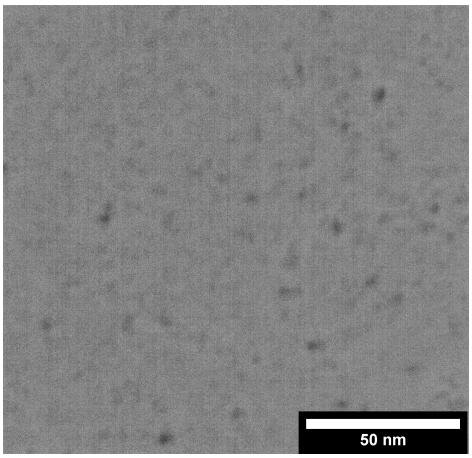

(c) x500k **g**=110

Figure 3.19: TEM images of W Single Neutron under **g**=110

3.4.2 Dislocation Loop Counts

Dislocation loop counts were made from images with $250,000 - 300,000\times$ magnification. This allowed for a balance of clear images and good defect separation. The counts were taken from well-imaged areas for each sample using the method described in section 3.2.2.4.

Figure 3.20 shows the defect measurements for the unirradiated W Single and W-1.4Re samples. These show very low defect densities as expected, dominated by defects below 5 nm. It was concluded from this that the FIB preparation route is not significantly affecting the loop density counts below.

These images from unirradiated samples highlight some of the difficulties in achieving accurate dislocation loop counts, especially for loops < 5 nm in size, as there is a background of defects that appear following the preparation route used in this study. However, while qualitatively similar in appearance, these background defects are of a smaller size at a significantly lower density than those induced by radiation damage, as shown by the comparison of dislocation loop counts in this section. Since the error in loop count calculated by varying the intensity threshold was calculated to be much more significant than the density of defects in the unirradiated samples, no subtraction of background defects from the dislocation loop counts for irradiated samples was carried out.

In figures 3.21 and 3.22, loop density counts from different imaging conditions are compared for W-1.4Re Ion and W Single Neutron respectively. Both of these sets of counts show approximately twice as many loops under $\mathbf{g}$=200 relative to $\mathbf{g}$=110, confirming that the dominant loop type is $\mathbf{b} = 1/2\langle 111 \rangle$. For the comparison of loop counts in different materials below, $\mathbf{g}$=200 counts will be used where possible and $\mathbf{g}$=110 counts will be doubled.

The histograms below show the size-density distribution of defects for each irradiated sample in figure 3.23 and the normalised distribution in figure 3.24. Comparing the W Single and W-1.4Re ion irradiated samples shows the strong effect that rhenium has on the defects formed during irradiation. W-1.4Re Ion has a significantly higher defect density, but predominantly at smaller sizes. W Single Ion has a lower total density of loops but at a greater average size, possibly associated with the rafting behaviour observed within the micrographs 3.15.

This difference in distribution agrees with the results found by Yi [69]. In that work it was found that the presence of rhenium resulted in a greater density of defects. An explanation was provided that rhenium pinned dislocation loops, reducing their ability to annihilate with defects of the opposite character.

W Single Neutron has a very similar distribution and density of loops to W-1.4Re Ion. This is surprising given that the neutron irradiated sample has spent 208 days at 1173 K during the irradiation, while the ion irradiated material was only at irradiation temperature for a few hours. However recent object kinetic monte carlo modelling aimed at predicting TEM observable defect formation in tungsten under irradiation

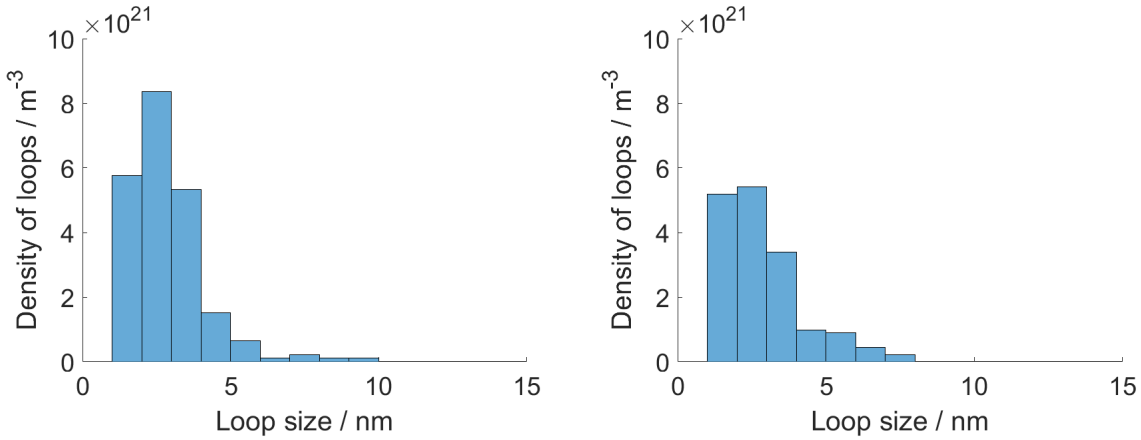

(a) W Single Unirradiated **(b)** W-1.4Re Unirradiated

Figure 3.20: Histogram of results from carrying out dislocation loop counting method on unirradiated samples

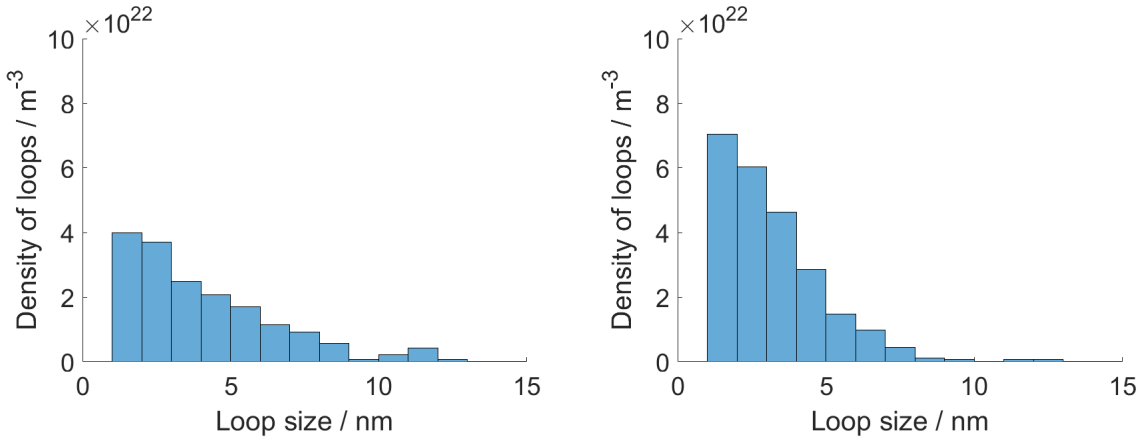

(a) **g**=110 (n = 247) **(b)** **g**=200 (n = 585)

Figure 3.21: Dislocation loop counts in W-1.4Re Ion with different imaging conditions

predicts that moderate levels of interstitial elements and rhenium from transmutation will suppress self-interstitial atom mobility [153]. The result of this is that loop size from neutron irradiation is not expected to have a strong temperature dependence, with an average defect size of a few nm under irradiation between 573 and 1023 K. This result appears to be confirmed in these experiments, where only the pure tungsten shows significant loop growth to above 10 nm.

One of the purposes of measuring the dislocation loop density and size is to provide data for the irradiation hardening model used in section 3.7. For this, total loop density and mean loop size is required from each sample. This data is shown in table 3.6.

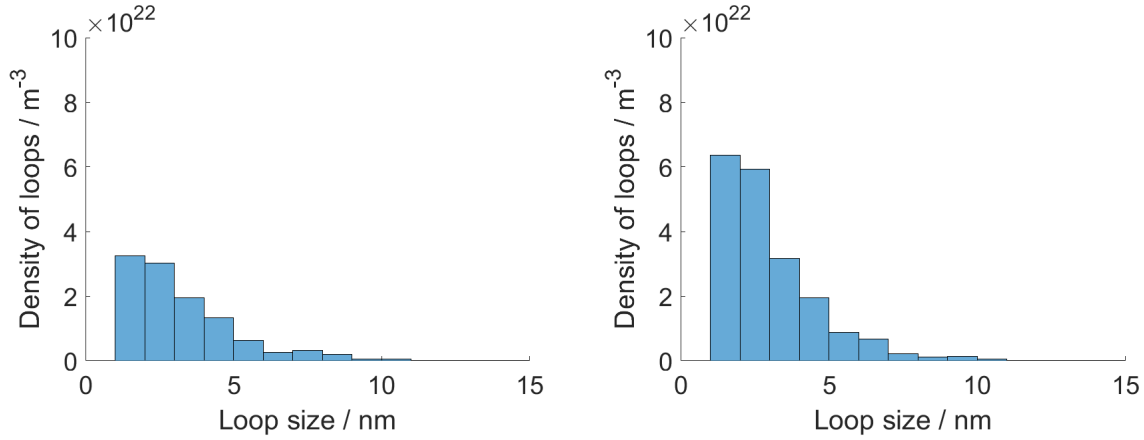

(a) **g**=110 (n = 625) **(b)** **g**=200 (n = 1294)

Figure 3.22: Dislocation loop counts in W Single Neutron with different imaging conditions

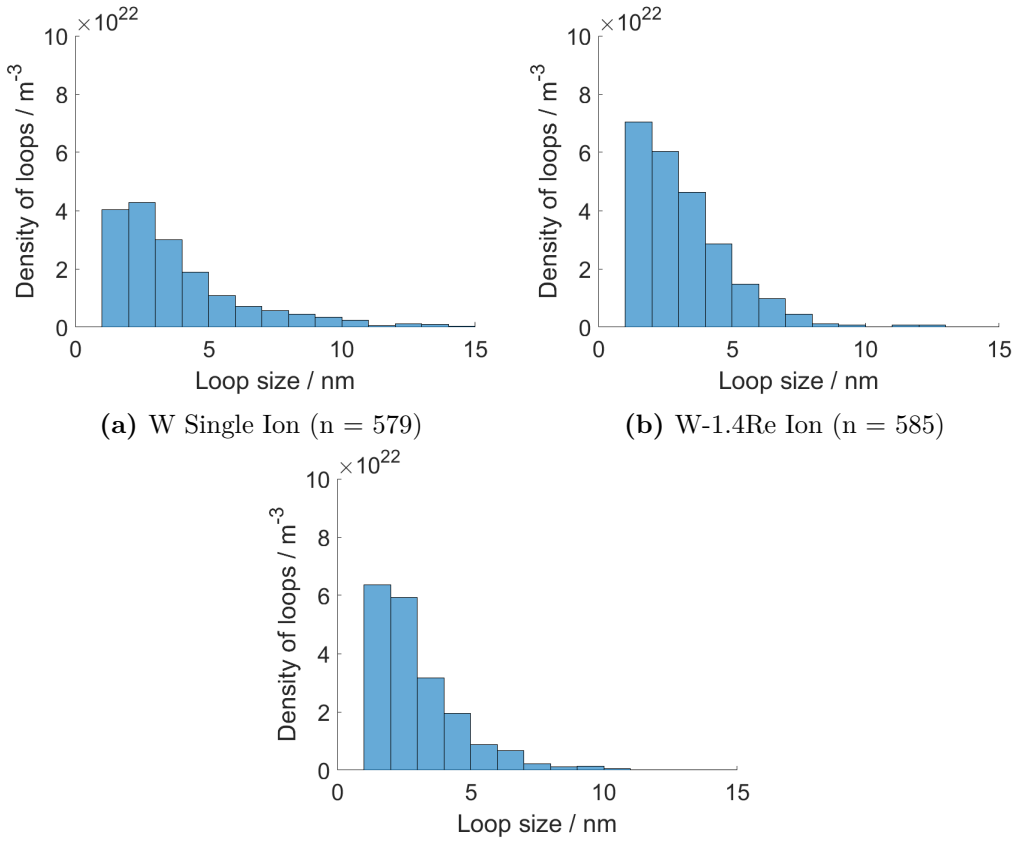

(a) W Single Ion (n = 579) **(b)** W-1.4Re Ion (n = 585)

(c) W Single Neutron (n = 1294)

Figure 3.23: Histograms showing the density of dislocation loops as a function of size for each of the irradiated samples

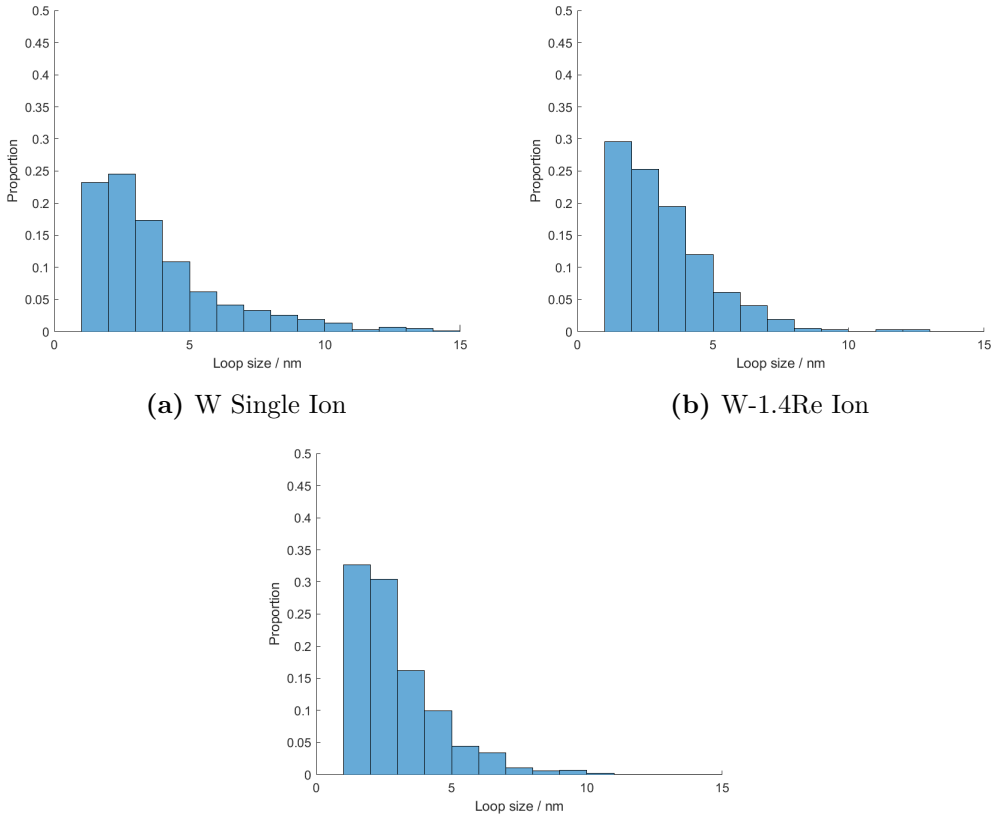

(a) W Single Ion

(b) W-1.4Re Ion

(c) W Single Neutron

Figure 3.24: Histograms showing the normalised distribution of defect sizes for each of the irradiated samples

Sample	Loop size / nm	Density / 10^{22} m^{-3}
W Single Ion	4.2 ± 0.3	17 ± 3
W-1.4Re Ion	3.2 ± 0.2	24 ± 3
W Single Neutron	3.0 ± 0.2	19 ± 4

Table 3.6: Dislocation loop mean diameter and number density for the irradiated samples

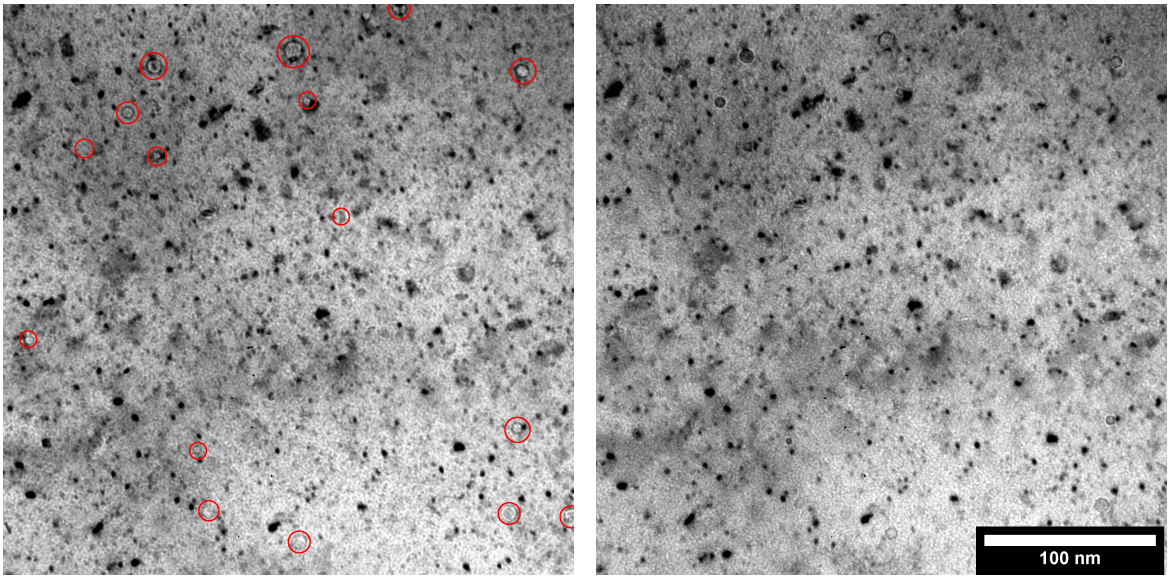

(a) -1000 nm **(b)** 1000 nm

Figure 3.25: Under- and over-focus images for W Single neutron irradiated. Some voids are highlighted in red in (a)

3.4.3 Imaging Voids

Over- and under-focused images taken in bright field conditions were used to attempt to identify voids in the material. These images are shown in figures 3.25, 3.26 and 3.27 for each of the irradiated samples. Voids could be clearly identified in the neutron irradiated material 3.25, however any voids present in the ion irradiated material were too small to be readily identified with the techniques available. The voids present in the neutron irradiated material were measured using the technique described in section 3.2.2.3 and the results are plotted in figure 3.28. The voids were measured as having a mean size of 5.4 nm $\pm$ 0.4 and number density of 6.4×10^{21} m^{-3} $\pm$ 0.6×10^{21}.

Animated gifs of figures 3.25, 3.26 and 3.27 are available at `https://drive.google.com/drive/folders/1X_EmteOuz7arZcIe8qBarwZ2_2RIqXaK?usp=sharing`.

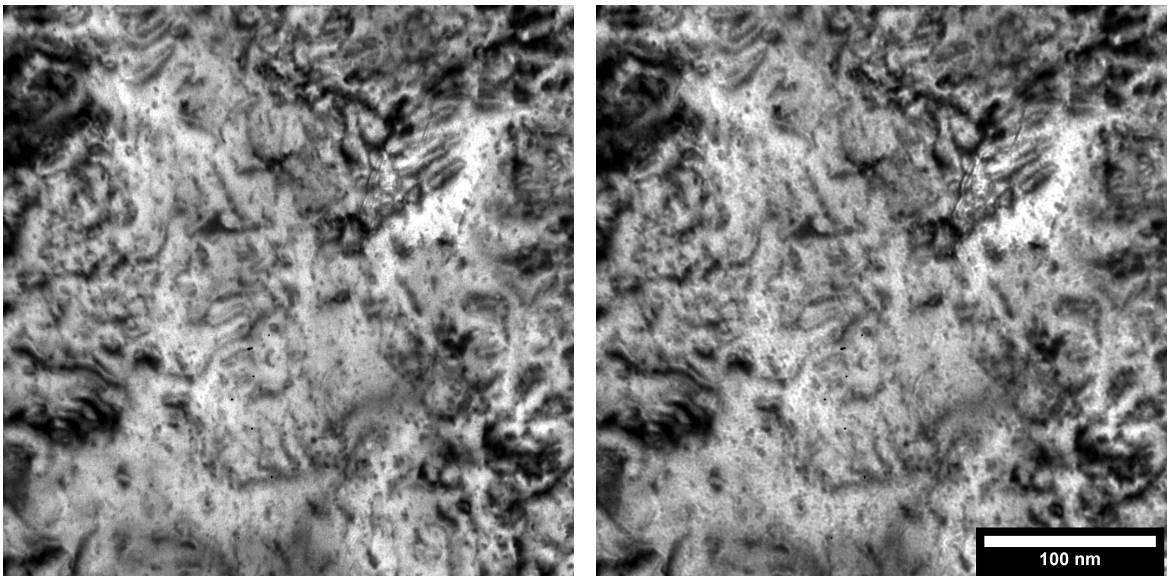

(a) -1000 nm **(b)** 1000 nm

Figure 3.26: Under- and over-focus images for W Single Ion

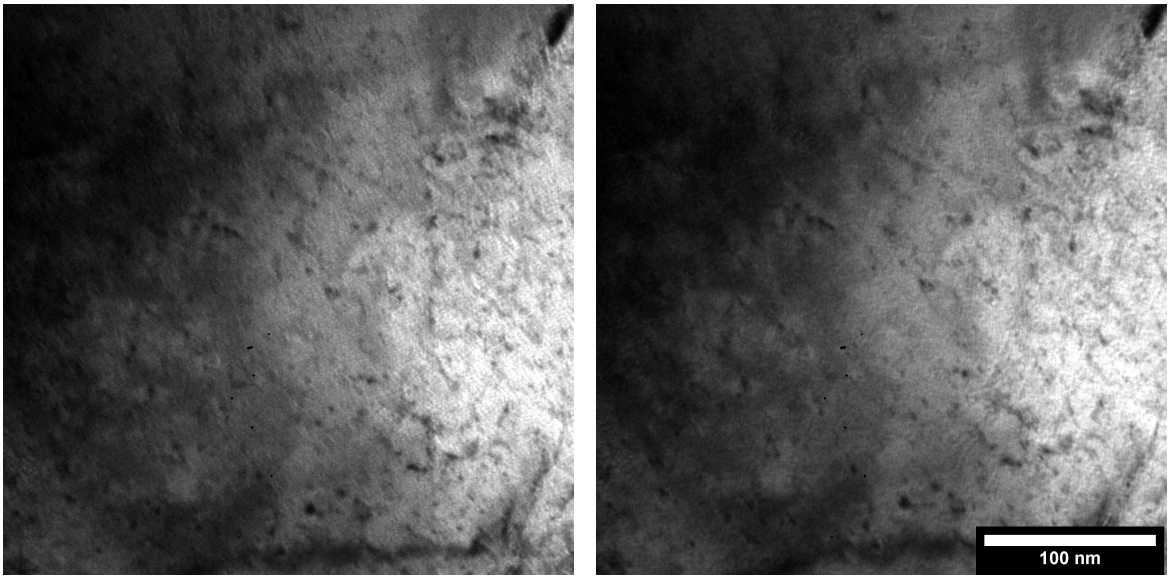

(a) -1000 nm **(b)** 1000 nm

Figure 3.27: Under- and over-focus images for W-1.4Re Ion

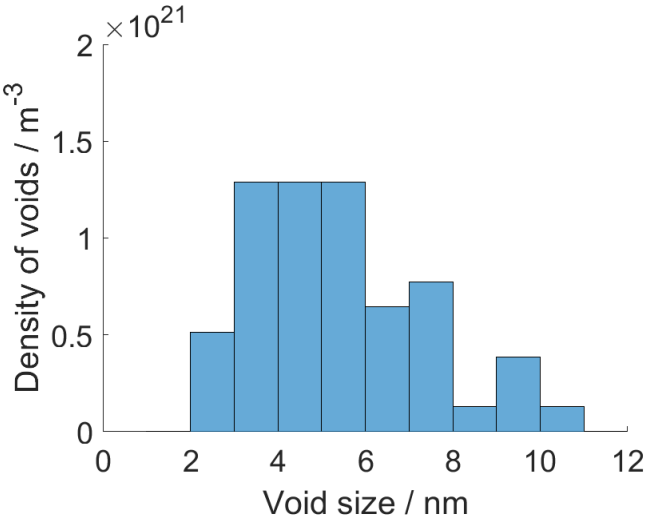

Figure 3.28: Void size distribution for W Single Neutron (n = 50)

3.5 Atom Probe Tomography

Atom probe tomography (APT) of the ion irradiated W-1.4Re sample and the W Single neutron irradiated was carried out by Matthew Lloyd, University of Oxford. This author assisted with sample preparation and FIB lift-out for the W Single Neutron. The results are included here due to their relevance to section 3.7.

Figures 3.29 and 3.30 show isosurface plots for W-1.4Re Ion and W Single Neutron for 3%, 5% and 10% rhenium. These show that although rhenium has clustered in both materials, the diffuseness of the clusters varies between the samples.

W-1.4Re Ion shows a large network of interconnected clusters when analysed with 3% isosurfaces. A 5% isosurface shows small precipitates spread throughout the needle with a maximum radius of around 5 nm. The attempt to fit a 10% isosurface is shown in figure 3.29c, no significant clusters were observed with concentrations above 10%.

W Single Neutron shows a far more consistent distribution with increasing % Re. This shows several large clusters were present within the needle, each with a high rhenium concentration such that their size does not change significantly going from 3% Re to 10% Re.

Isosurface analysis is not considered best practice for APT but was included here due to the clarity provided regarding the differences between W-1.Re Ion and W Single Neutron. Best practice for cluster analysis in dilute solute alloys uses the maximum separation algorithm. This was applied to produce figure 3.31, which shows the atoms contained within identified clusters in W-1.4Re Ion and W Single Neutron.

Figure 3.32 shows the variation in rhenium concentration averaged around each cluster for W-1.4Re and W Single Neutron. This shows that the peak concentration is above 28%, the point at which σ phase is expected to form. By comparison, the large

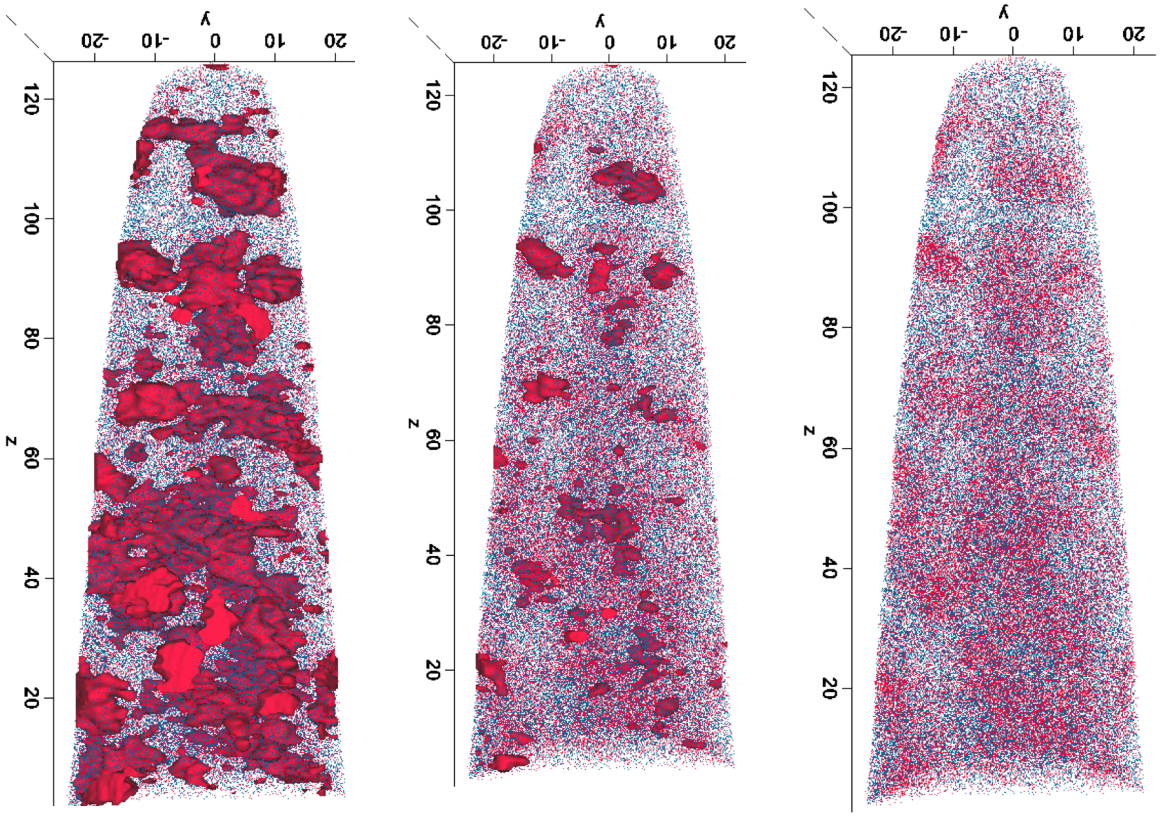

(a) 3% Re Isosurface **(b)** 5% Re Isosurface **(c)** 10% Re Isosurface

Figure 3.29: Isosurface plots of rhenium concentration in APT needles from W-1.4Re Ion

number of small clusters identified in W-1.4Re Ion means that the mean concentration only reaches 2.5 % Re, and quickly decays down to the background level.

One of the aims of this analysis was to provide information for the hardening model described in section 3.7. This model requires radius and number density measurements. The radius of each clusters was found by measuring the volume of the cluster and calculating the radius of a sphere of equal volume. The mean radius of the clusters in each sample was calculated, as was the standard error of the mean. These are presented along with the number density of clusters for each sample in table 3.7 and are used in the hardening model.

These results show that using the standard maximum separation algorithm for analysis for APT produces results that identify a significantly greater volume of cluster in W-1.4Re Ion than in W Single Neutron. The isosurface and concentration plots show that the clusters in W Single Neutron have a significantly higher peak concentration and the concentration drops to background levels at a greater distance from the cluster centre, yet the average cluster size was determined to be smaller than W-1.4Re Ion. This highlights some issues with using maximum separation algorithm and the

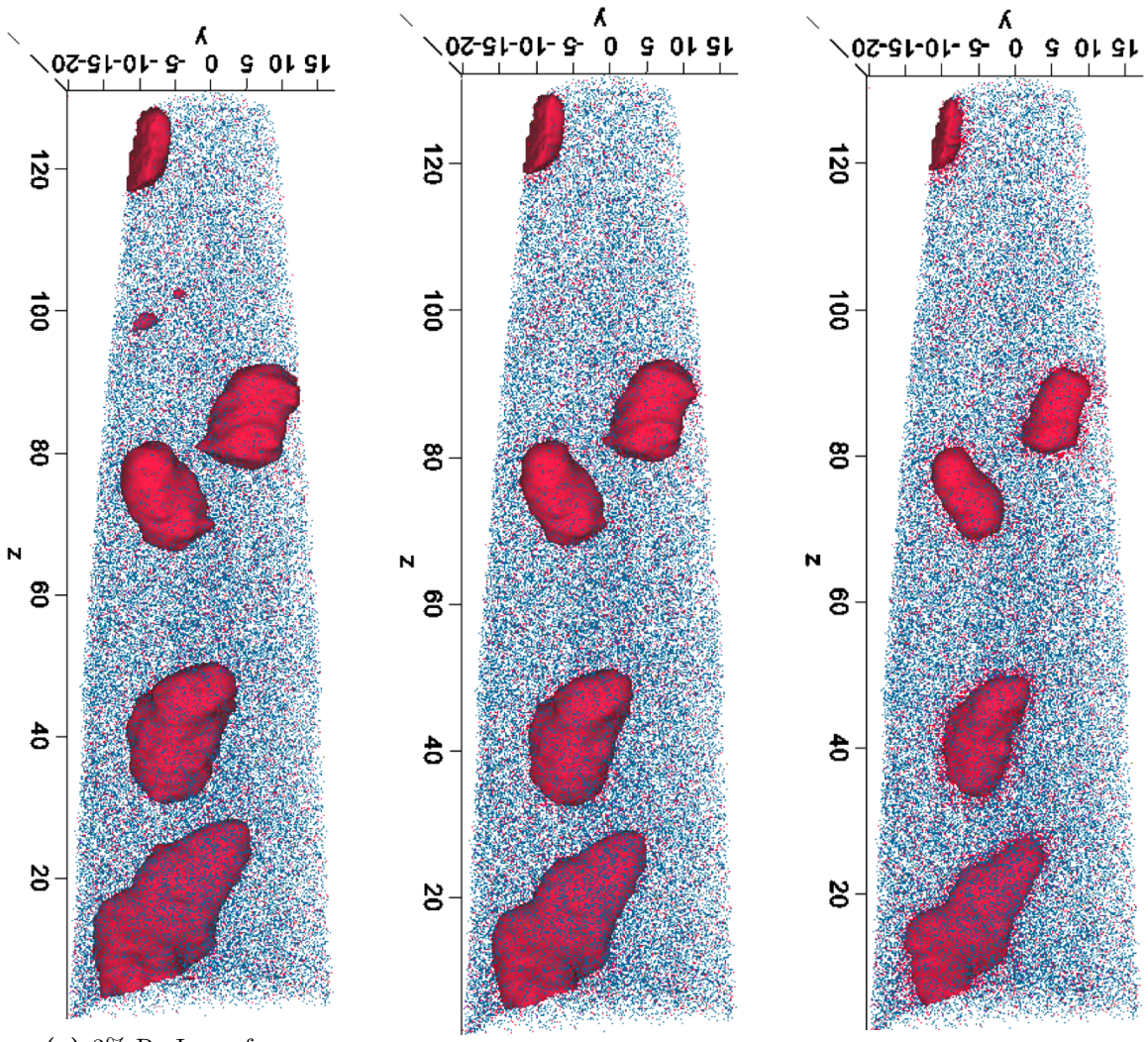

(a) 3% Re Isosurface **(b)** 5% Re Isosurface **(c)** 10% Re Isosurface

Figure 3.30: Isosurface plots of rhenium concentration in APT needles from W Single Neutron

simplicity of the hardening model used in section 3.7, where only size and number density are considered and not any dependence on concentration within the cluster. This is discussed further in section 3.8.3.

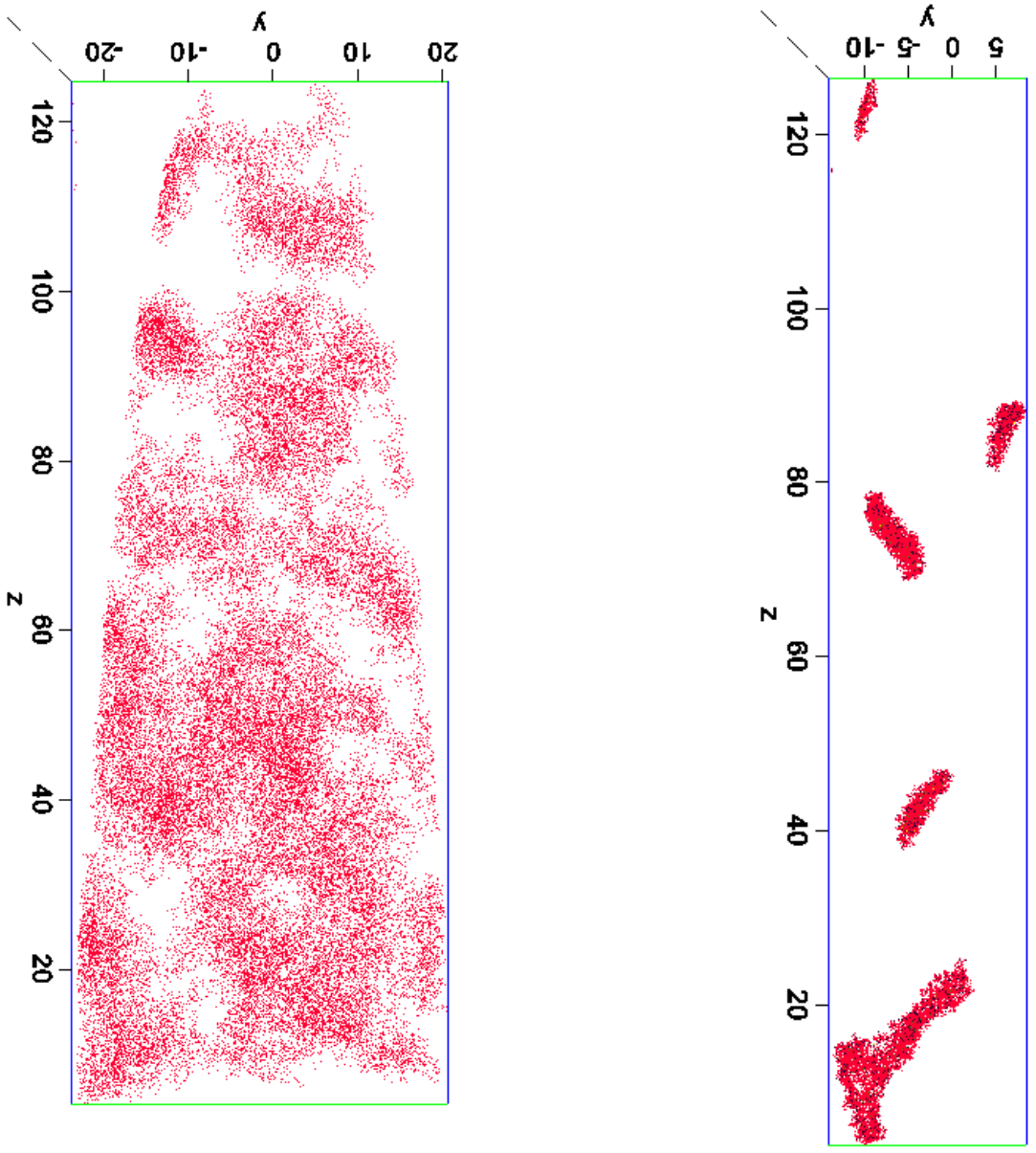

(a) W-1.4Re Ion

(b) W Single Neutron

Figure 3.31: APT maps of rhenium atoms identified as being inside clusters

Table 3.7: Rhenium cluster size, with standard error, and number density results from APT analysis. $N_{clusters}$ indicates the number of clusters measured in each sample

Sample	$N_{clusters}$	Cluster Radius / nm	Number Density / x10^{22} m^{-3}
W-1.4Re Ion	9	8.0 ± 2.6	7.8 ± 0.9
W Single Neutron	5	3.5 ± 1.0	5.4 ± 1.1

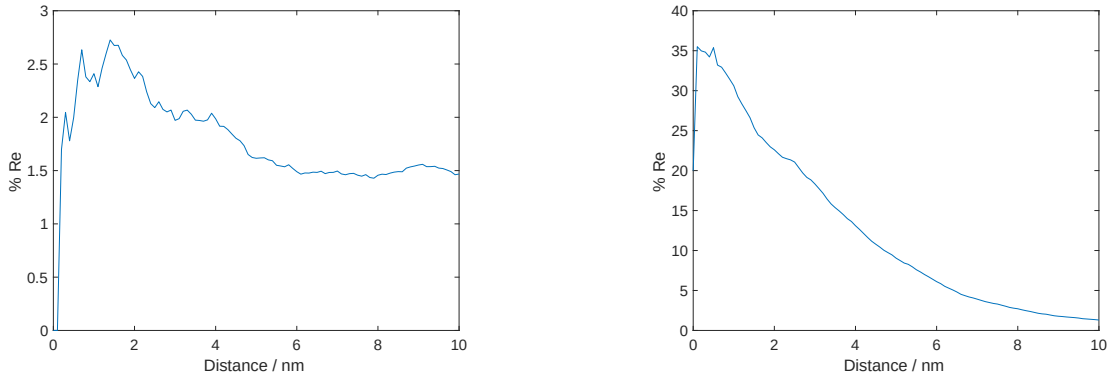

(a) W-1.4Re Ion **(b)** W Single Neutron

Figure 3.32: Re concentration profile averaged around each identified cluster. $N_{clusters}$ = (a) 9 and (b) 5

3.6 Nanoindentation

The results of nanoindentation of the ion and neutron irradiated samples are shown in figure 3.33. The hardness of the ion irradiated samples tends towards the unirradiated hardness at depths greater than the irradiation layer as expected. The hardness of the neutron irradiated samples continues to be greater than the unirradiated material at all depths. As a result, the irradiation hardening was calculated between 200 - 700 nm to allow comparison between all samples. The calculated irradiation hardening values are shown in table 3.8.

Figure 3.34 shows the calculated modulus data for each of the samples. These results are largely consistent with all samples showing a modulus between 400 and 450 GPa throughout the depth of the indent. This consistency of measured modulus with increasing depth indicates that the indenter tip calibration used for these indents was accurate. The modulus values between 200 - 700 nm were calculated in the same manner as the hardness values. These showed that the difference in modulus between samples was no greater than 10 GPa, which is the error expected from the technique.

Table 3.8: Hardness of unirradiated and irradiated samples from nanoindentation between 200 and 700 nm

Sample	Hardness (GPa)	Irradiation Hardening (GPa)
W Single Unirradiated	5.8 ± 0.2	
W-1.4Re Unirradiated	5.9 ± 0.4	
W Single Ion	6.6 ± 0.3	0.8 ± 0.4
W-1.4Re Ion	7.7 ± 0.4	1.8 ± 0.6
W Single Neutron	8.0 ± 0.2	2.2 ± 0.3

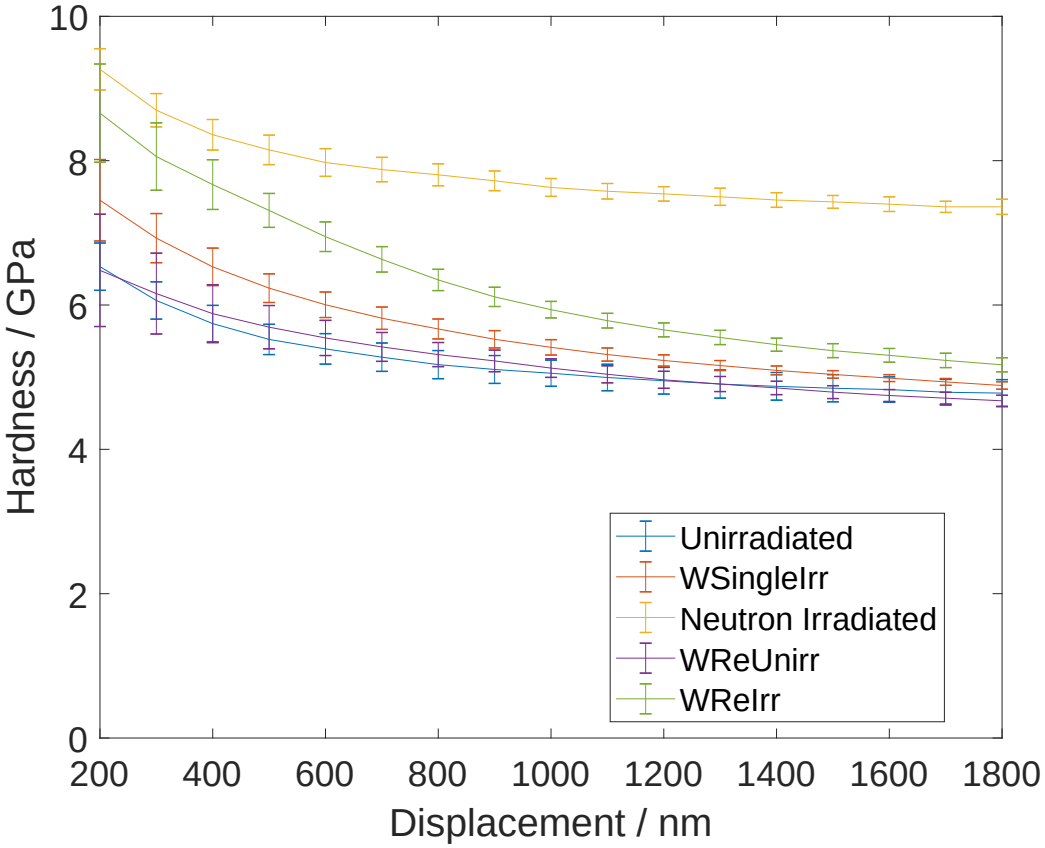

Figure 3.33: Nanohardness results for unirradiated and irradiated samples between 200 - 1800 nm

Table 3.9: Modulus of unirradiated and irradiated samples from nanoindentation between 200 and 700 nm

Sample	Modulus (GPa)
W Single Unirradiated	420 ± 10
W-1.4Re Unirradiated	410 ± 20
W Single Ion	420 ± 10
W-1.4Re Ion	430 ± 10
W Single Neutron	430 ± 10

It was therefore considered that irradiation had not induced any changes in modulus.

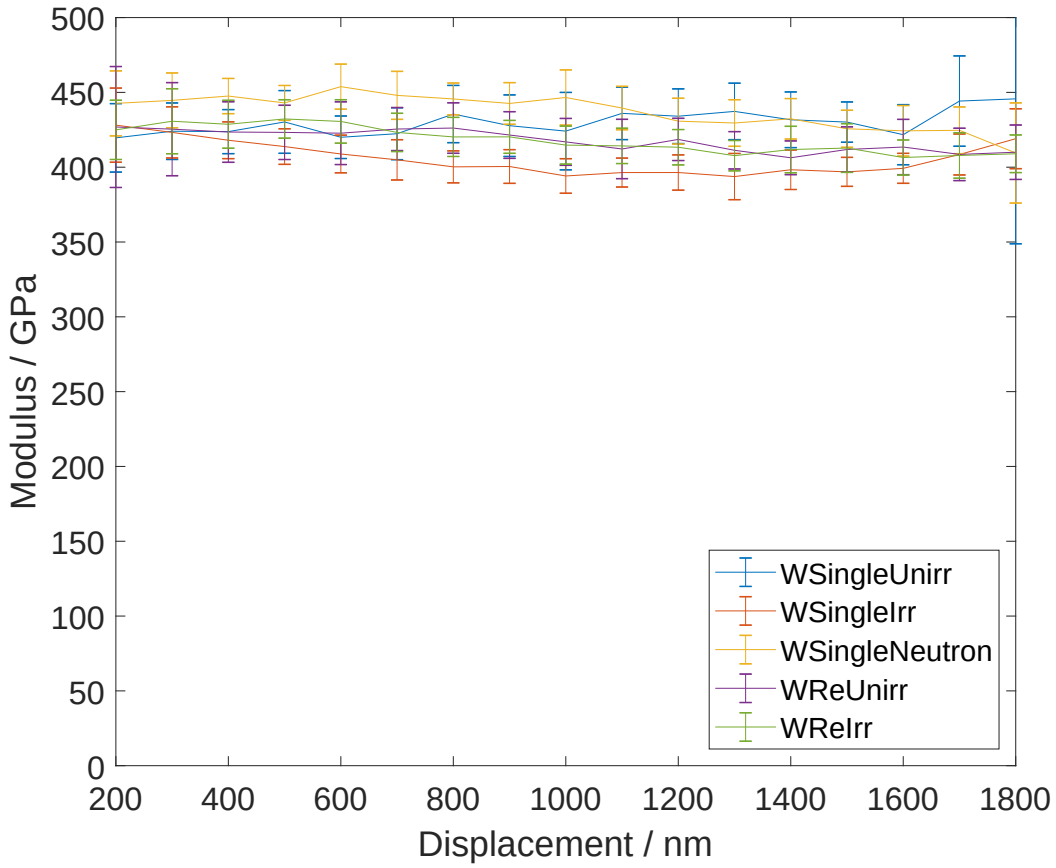

Figure 3.34: Modulus measurements from nanoindentation for unirradiated and irradiated samples between 200 - 1800 nm

3.7 Correlating Irradiation Damage and Hardening

Correlating the irradiation damage observed using TEM and irradiation hardening measured using nanoindentation has been carried out on various materials to varying success [99]. For strong obstacles, such as voids and precipitates, a dispersed barrier model (equation 3.4) is considered most appropriate and was used. For weaker obstacles such as dislocation loops, a Friedel-Kroupa-Hirsh (FKH) model (equation 3.5) was used. The model considers the hardening from $\mathbf{b} = 1/2\langle 111 \rangle$ and $\mathbf{b} = \langle 100 \rangle$ dislocation loops to be equivalent. There is some evidence that $\mathbf{b} = 1/2\langle 111 \rangle$ loops dominate the hardening in irradiated BCC metals [104], however, this has not been confirmed experimentally nor demonstrated for tungsten. As a result it was considered best practice in this work to consider both loops types as equal. Furthermore, from the

Table 3.10: Defect cluster barrier strengths for irradiation induced defects in tungsten [98]

Defect	Defect barrier strength (α)
Dislocation loops	0.15
Voids (< 2 nm)	0.25
Voids (2-3 nm)	0.3
Voids (3-4 nm)	0.35
Voids (> 4 nm)	0.4
Precipitates	0.6

TEM techniques used in this work it was not possible to confirm the presence of $\mathbf{b} = \langle 100 \rangle$ dislocation loops. Further modelling and experimental work would be required for the hardening contribution from different loop types to be identified.

$$\Delta\tau = \alpha\mu b(Nd)^{\frac{1}{2}} \tag{3.4}$$

$$\Delta\tau_{DL} = \frac{1}{8}\mu b d N^{\frac{2}{3}} \tag{3.5}$$

α = defect cluster barrier strength (see table 3.10)
μ = shear modulus
b = burgers vector
N = Number density / m^{-3}
d = Defect diameter / m

The increase in yield stress due to irradiation defects can be calculated using equation 3.6, this is then multiplied by a factor of 2.74 to give the increase in hardness [154].

$$\Delta\sigma_y = M\sqrt{\Delta\tau_{DL}^2 + \Delta\tau_V^2 + \Delta\tau_C^2} \tag{3.6}$$

M = Taylor Factor ($\sqrt{3}$ for single crystal)

This model can be applied directly using the microstructure characterisation in this chapter. The resultant contributions to hardening, prior to root-square-summation, are shown in figure 3.35. Irradiation hardening contributions from each defect type are given, along with the calculated errors, in table 3.11. These individual contributions were then summed using the root-square-summation as indicated by equation 3.6. The results of this summation, broken down by contribution from each defect type, are compared to the experimental hardening values in figure 3.36. The model appears to give accurate hardening predictions for W Single Ion and W Single Neutron. However, there is a poor correlation between prediction and result for W-1.4Re Ion. The reason for this is discussed in section 3.8.5.

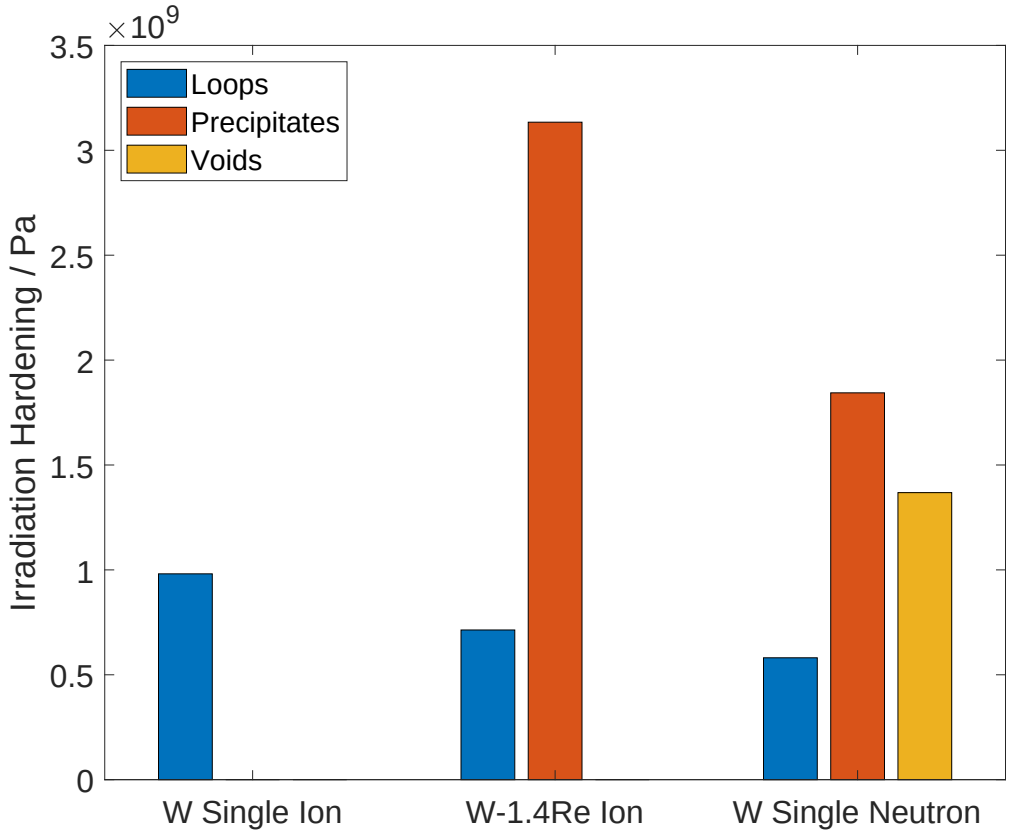

Figure 3.35: Hardening contributions from each defect type for irradiated samples

Table 3.11: The calculated individual contribution to irradiation hardening from each defect type and the resultant total irradiation hardening as calculated by root-square-summation

Irradiation hardening / GPa	W Single Ion	W-1.4Re Ion	W Single Neutron
Dislocation loops	1.0 ± 0.2	0.7 ± 0.1	0.6 ± 0.1
Precipitates	0	3.1 ± 0.7	1.8 ± 0.7
Voids	0	0	1.4 ± 0.2
Root-square-summation	**1.0 ± 0.2**	**3.2 ± 0.7**	**2.4 ± 0.7**

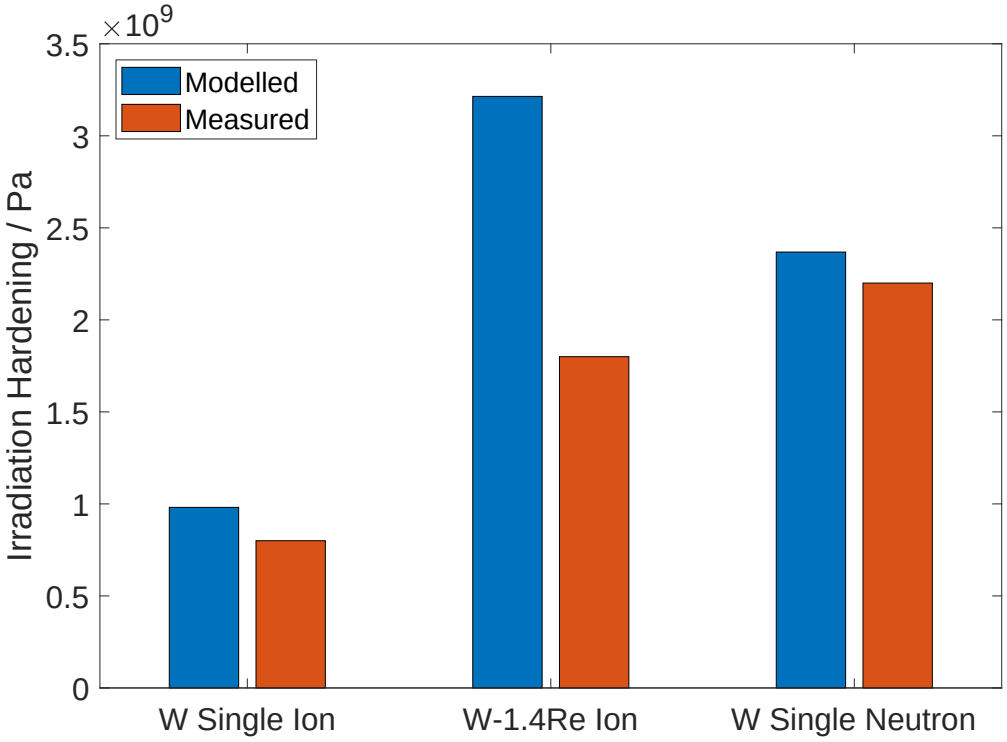

Figure 3.36: Comparing the experimentally measured irradiation hardening with the prediction from the model

3.8 Discussion

The results from each of the techniques above is discussed in this section and compared to literature results for similar experiments.

3.8.1 Dislocation Loop Density

Two primary authors have carried out dislocation loop counts on self-ion irradiated tungsten and W-Re alloys, Hwang [32] and Yi [151] [70]. The results are shown in tables 3.12 and 3.13 alongside the count from W Single Ion and W-1.4Re Ion.

3.8.1.1 Ion Irradiated Tungsten

The average loop size found in this work for self-ion irradiated tungsten agrees well with those determined by Yi (2 MeV W^+) [150] and Hwang (18 MeV W^{6+}) [32], as shown in table 3.12. The results acquired by Yi at 573 and 773 K suggested that the average loop size increased with temperature and dose, yet both this work and Hwang found a smaller average loop size at 1073 K. This may have been due to the

FIB lift-out process used in both this work and that by Hwang that results in small defects as shown in section 3.4.1.1. Another possibility is that the technique used for taking dark-field images in this work, using the beam procession script, reduces the background noise, and hence increases the number of small defects that can be identified. These differences combine with the difficulty in systematic imaging of very small loop (< 2 nm), as a result the average size may be misleading and distributions have also been compared for some cases.

The loop density measured in this work was significantly higher than that observed by Yi or Hwang. Hwang captured images using $\mathbf{g} = 110$ conditions, and does not mention having accounted for the **g.b** invisibility criterion. It is therefore possible that only half the loops present may have been imaged and counted. The difference between this work and Yi could then be accounted for by either the FIB lift-out process, although the relatively low dislocation count from unirradiated samples prepared through FIB lift-out would suggest that this is not having a large impact.

Yi [150] demonstrated that the proportion of loops > 4 nm increased with increasing temperature in ion irradiated tungsten. The maximum value determined by Yi was 45 % ± 10 of loops > 4 nm irradiated to 1.2 dpa at 1023 K. The value determined in this work was 35 % ± 7. These values agrees within the error bounds, but suggest that temperatures above 1023 K during irradiation are not contributing significantly to loop growth.

One notable difference between this work and that carried out by Hwang, is the very low proportion of large loops ($\approx 20\% > 4$ nm) found by Hwang, and the almost complete absence of loops > 7 nm. As discussed below, Yi et al. [70] suggested that there is a limit on the maximum size of defects that corresponds to the maximum cascade size. However, this depends on ion energy and Yi used lower ion energy than Hwang and found larger defects. This suggests that the lack of large loops detected by Hwang may be due to the imaging technique. The high density of thickness bands can be easily observed in figure 3.37 and this may be hindering accurate loop size determination. In general, the total number of defects analysed is not given, and so the reliability of the size distributions of loops and voids determined is unknown.

Yi [151], Zhang [155] and Hasenhuetl [156] all observed dislocation loop rafting in self-ion irradiated tungsten under a wide range of temperatures and doses. This agrees with the rafting observed in W Single Ion in this work.

The density of dislocation loops is expected to have a power-law dependence on the number of point defects contained within the loop [70]. This power-law dependence would appear as a straight line on a log-log plot of dislocation loop density against defect size in number of point defects (N). The results from the samples investigated in this work are shown on such a graph in figure 3.38. It is clear from this figure that the power-law dependence is not observed experimentally for loops > 1000 or < 100 point defects in size. This matches the results shown by Yi [70] 3.39. The deviation at small dislocation loop sizes was accounted for by defects being difficult to detect using TEM. The deviation from a power law dependence at high defect

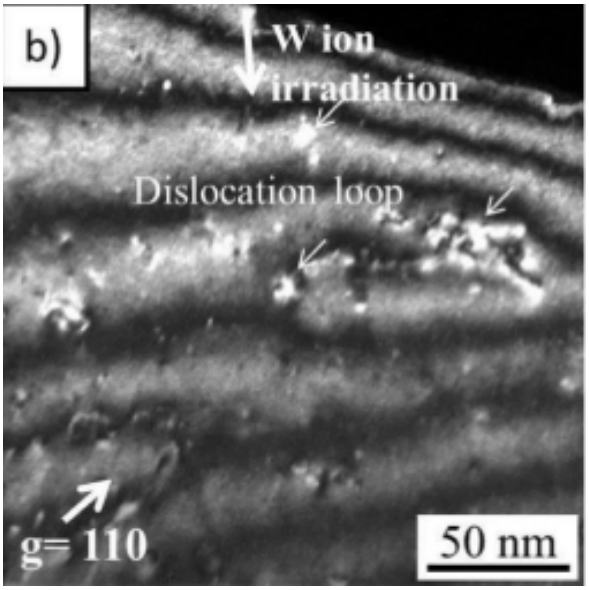

Figure 3.37: Images of dislocation loops in W irradiated to 1 dpa at 1073 K from [32]. Although some loops are clearly visible, the strong presence of thickness contours may be hindering the detection and accurate sizing of dislocation loops

Table 3.12: Dislocation loops density in self-ion irradiated commercially pure tungsten [70] [32]

Ion	Dose / dpa	Temperature / K	Loop size / nm	Density / 10^{22} m^{-3}
2 MeV W^+	0.5	573	3.4	4.5
2 MeV W^+	1.5	573	3.2	8.0
2 MeV W^+	0.5	773	3.1	3.0
2 MeV W^+	1.5	773	3.8	5.0
2 MeV W^+	4.5	773	3.8	5.0
18 MeV W^{6+}	1.0	1073	3.3	6.1
18 MeV W^{6+}	5.0	1073	3.0	6.0
This work	1.6	1073	3.2	19

sizes was considered to be a result of the maximum loop size produced by a cascade being limited by the implanted ion energy.

Yi analysed samples prepared exclusively by electropolishing and irradiated at very low temperatures and the predicted power-law dependence was only determined to be accurate over a narrow range. It is therefore unsurprising that in this work, where FIB lift-out was necessary to prepare the samples and a high irradiation temperature was used, the results show a high scatter and the power-law dependence cannot be confirmed.

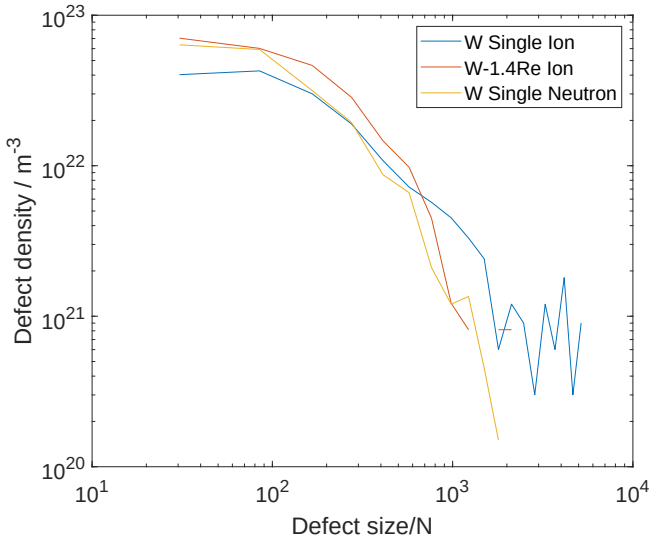

Figure 3.38: log-log plot of dislocation loop density against loop size in number of point defects. The predicted power-law dependence would appear as a straight line.

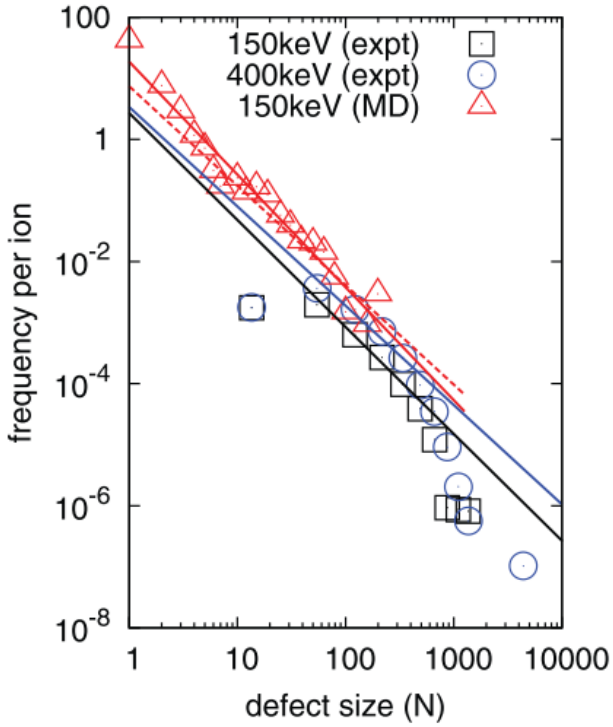

Figure 3.39: log-log plot of dislocation loop density against loop size in number of point defects for TEM experiments (self-ion irradiated at 30 K) carried out by Yi, compared to results from MD models [70]

Table 3.13: Dislocation loops density in W-xRe alloys [70] [32]

Ion	% Re	Dose / dpa	Temp / K	Loop size / nm	Density / 10^{22} m^{-3}
2 MeV W^+	5	0.5	573	2.3	9.0
2 MeV W^+	5	1.5	573	2.9	9.0
2 MeV W^+	5	0.5	773	2.6	3.0
2 MeV W^+	5	1.5	773	3.0	5.0
2 MeV W^+	5	4.5	773	3.5	5.0
18 MeV W^{6+}	3	1.0	1073	3.6	3.8
18 MeV W^{6+}	3	5.0	1073	3.0	3.9
This work	1.4	1.6	1073	3.0	24

3.8.1.2 Ion Irradiated W-xRe

Hwang and Yi observed opposing effects from the inclusion of rhenium under self-ion irradiation of tungsten. Yi observed a decrease in dislocation loop size and increase in dislocation loop density for W-5Re compared to commercially pure tungsten, while Hwang observed very similar loop sizes and a sharp decrease in loop density in W-3Re. This work found the same result as Yi for irradiation of W-1.4Re with a slight decrease in loop size and an increase in loop density. It is particularly noticeable from the graphs in section 3.23 that the number of loops $>$ 10 nm is higher for W Single Ion than W-1.4Re Ion.

There are a number of features of the work by Hwang that make the conclusions questionable. Firstly, the material was only annealed at 900 °C for 20 minutes to relieve stresses after rolling. Ferroni et al. [72] showed that damage in tungsten was only annealed out after one hour above 1100 °C. Secondly, although dark-field imaging has been applied by Hwang, the micrographs (see figure 3.37) provided show the edge of the sample, without any platinum protective layer remaining, and dense thickness fringes, indicating that the thickness of the sample varies significantly across the image. This would make acquiring an accurate volumetric number density for dislocation loops difficult. Finally, as mentioned above, no explicit method has been used in order to account for the **g.b** invisibility criterion.

This leads to the conclusion that the result from this work and that found by Yi reflects the true effect of rhenium on loop formation in tungsten. These results shows that the presence of rhenium suppresses loop growth and mobility. While there is significant modelling work on the mobility of rhenium in tungsten, there is little regarding the effect of rhenium on the mobility of dislocation loops. This is possibly an underestimated effect that may have significant impact on the thermal recovery of tungsten following neutron irradiation.

The proportion of loops greater than 4 nm can again be compared between this work and that carried out by Yi [150]. As mentioned above, Yi found an increasing proportion of large loops ($>$ 4 nm) at increasing temperature, reaching at 22 % *pm*

5 for W-5Re irradiated to 1.2 dpa at 773 K. This agrees well with the value of 26 % pm 5 for W-1.4 Re at 1073 K determined in this work. The lack of increase in proportion of large loops at high temperature provides further evidence that rhenium continues to suppress loop growth at high temperatures.

3.8.1.3 Neutron Irradiated Tungsten

Dislocation counts are given by Hu et al. [98] for a number of works on neutron irradiated tungsten, the results of which were used for the irradiation hardening model. The values of dislocation loops size and density vary between 2.9 - 12.2 nm and 0.1 - 4.7 x 10^{22} m^{-3}. However, none of the works cited [33] [60] [63] [157] use weak-beam dark-field imaging, which is best for carrying out dislocation loops counts [67]. Instead the focus of these papers is in void and precipitate identification. Only some of the citations provide micrographs of dislocation loops and these show a high density of defects, only a few of which are characterised as dislocation loops. As a result it is likely that the number of small dislocation loops is significantly underestimated and the average size of the loops may not be accurate.

Equally, in this work it was not possible to separate the defects identified as loops in W Single Neutron from precipitates. As a result the number of loops may be overestimated by up to 6 x 10^{22}. However, precipitates will only be visible if the strain field of the precipitate is anisotropic and so it is not possible to assume that the precipitates were imaged under the dark-field conditions used for loop counting. Ideally a control experiment would be carried out on tungsten containing rhenium precipitates introduced through metallurgical treatment but this is difficult to carry out as the irradiation induced precipitates formed in low rhenium content tungsten alloys are not expected to form from the phase diagram. Alternatively, high resolution chemical mapping could be used alongside dark-field imaging of the neutron irradiated samples, however, a TEM with sufficiently high resolution chemical mapping was not available for this work.

The lack of other weak-beam dark-field imaging of loops in neutron irradiated tungsten makes verification of the loop count from W Single Neutron difficult. This work appears to be the best imaging of dislocation loops in neutron irradiated tungsten available. The results here show that the dislocation loop distribution produced by neutron irradiation is very similar to that produced by ion irradiation of W-1.4Re. Notably, dislocation rafting is observed in W Single Ion but not W Single Neutron. These results suggest that the rhenium produced as a result of transmutation limits defect mobility from an early stage of irradiation, preventing both rafting and loop growth.

The results here disagree strongly with the model produced by Huang et al. [53], which predicted that loops above 2 nm would not form under neutron irradiation. The key result from this section is that dislocation loop distributions similar to those characterised in ion irradiated tungsten form under neutron irradiation. The impact

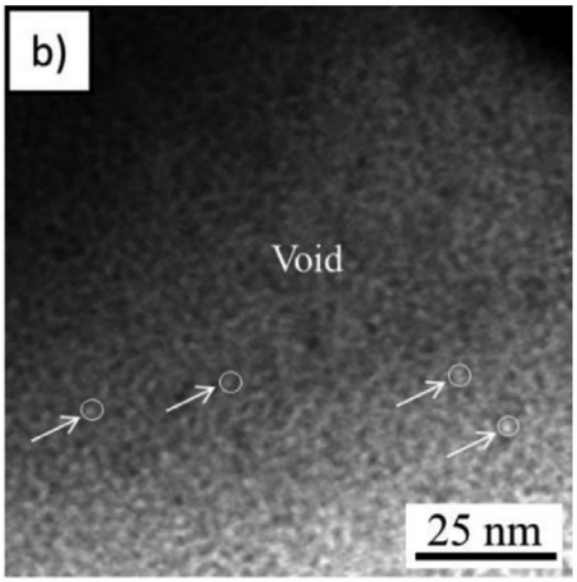

Figure 3.40: Images of voids in W-3Re irradiated to 1 dpa at 1073 K. The presence of voids is far from clear in this image and a through-focus series is not provided. The speckling observed across the image may be associated with surface defects depending on the out-of-focus conditions used. Reproduced from [32] (CC BY NC ND).

of this on hardness models for tungsten is discussed is section 3.8.5.

3.8.2 Void Counts

No voids were found in either of the ion irradiated samples in this work. This agrees with the observations made by Yi [151]. The only voids > 2 nm reported in self-ion irradiated tungsten were observed by Ferroni et al. [72] during annealing of an ion irradiated sample at 1373 K. This suggests that significantly higher temperatures than those used here are required to promote void growth. Small voids have been reported elsewhere [32] [152] but the over- and under-focus imaging technique used in those works is not suitable for measuring voids < 2 nm [67]. Additionally, ± focus values are not provided and surface defects can be made to appear void-like if large values of over- and under-focus are used. An image analysed by Hwang is shown in figure 3.40. The presence of voids in this image is far from clear and the imaging technique used is not described (e.g. ± focus conditions used). High resolution Scanning-TEM imaging using a high angle annular dark field detector of the samples irradiated in this experiment could be used to determine if small voids are present in the material but was not available for analysis of the ion irradiated samples. This type of analysis has been carried out by Klimenkov on the neutron irradiated samples examined in this work [66].

The average void size measured in this work using the over- and under-focused method was 5.4 nm. The minimum void size that could be identified with this technique

was 2 nm. Klimenkov [66] analysed the same material using high resolution STEM and found an average void size of 5 nm (also with a minimum size of 2 nm). The density of voids measured in this experiment (6.4 x 10^{21}) was higher than that measured by Klimenkov (2.5 x 10^{21}). Klimenkov analysed a larger sample volume resulting in a greater total number of voids counted, but it is possible that some voids were missed since the images appear to show voids with a similar density to those measured in this work. The technique by which voids were identified in the work by Klimenkov is not described and over- and under-focus images are not provided so the count method used in this work cannot be replicated.

The values reported by Hu et al. [98] for neutron irradiation above 1000 K vary between 7 x 10^{20} - 1.2 x 10^{23} for doses between 0.4 and 2.2 dpa, with no clear dependence on dose or temperature. This suggests large errors in some of the measurements made or a drastic difference in void production depending on the neutron energy spectrum. One clear difference in these counts is that some authors reported average void sizes of as low as 1.3 nm indicating that very small features are being included in the measurement, possibly erroneously. Without an accepted minimum void size for analysis, it is difficult to compare reported void densities across different irradiations.

Tanno et al. [63] reported a void lattice forming in W after irradiation to 1.54 dpa at 1023 K. It is clear that in this work no void lattice formed. The distribution of voids detected by Tanno is compared to that found in this work in figure 3.41. From this it can be clearly observed that the void size distribution for W irradiation to 1.67 dpa at 1173 K is very similar to that for 1.54 dpa at 1023 K. Some slightly larger voids were detected in this work, most likely due to the higher temperature, allowing for a greater degree of thermal annealing. This is a continuation of the dependence of void size on irradiation temperature observed by Tanno.

The model produced by Huang et al. [53] predicts no voids above 1 nm for fission neutron irradiation at 1073 K. The results presented here directly contradict that result.

It is clear from these results that heavy ion irradiation of tungsten fails to recreate the void production that occurs under neutron irradiation. There are several factors that may to contribute to this behaviour. Firstly, there is a significant dose rate difference between ion and neutron irradiation (10^3 in this work). As a result defects have a significantly reduced time to evolve over, so dynamic annealing will dominate under ion irradiation. Defect formation occurs rapidly during dynamic annealing so many small defects would be expected. There may be a high density of small, vacancy clusters in the ion-irradiated material that cannot be detected using standard TEM techniques [158]. In the neutron irradiated sample, there has been adequate time for significant thermal annealing to occur, this would enable small vacancy clusters to coarsen into the voids observed.

A second contributing factor may be the excess of implanted ions introduced by the irradiation. During this irradiation 1.5 x 10^{14} m^{-2} tungsten ions were implanted into the target. Due to the degrader foils used for this irradiation the Bragg stopping peaks were spread throughout the 2 μm irradiated layer leading to an approximately even

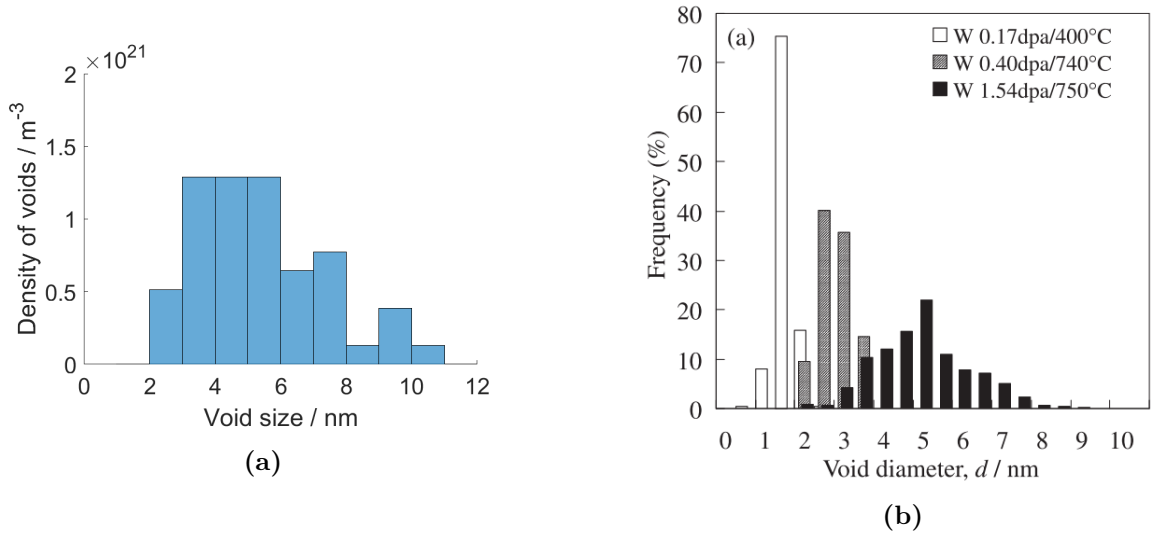

Figure 3.41: Void distribution from (a) W irradiated with neutrons to 1.67 dpa at 1173 K [this work] and (b) that determined by Tanno et al. [61]

distribution of implanted tungsten ions with depth. This leads to an excess number of tungsten atoms in the material of 7.5 x 10^{19} m^{-3} or approximately 10 appm. While this number is very small compared to the total number of interstitial-vacancy pairs created by the irradiation, it may be sufficient to influence the population of defects remaining after the annealing process that occurs in the material following irradiation; increasing the interstitial concentration and decreasing the vacancy concentration. A study that investigates the damage within an area of the Bragg stopping peak and an equally damaged area outside the Bragg stopping peak could provide more information on the effect of implanted interstitials. However, this is difficult to carry out in tungsten as the high stopping power of the material leads to a sharp Bragg peak with a damage profile that changes rapidly with depth.

Finally, there is the difference in gas production between ion and neutron irradiation. Ion irradiation only injects tungsten atoms into the material, whereas neutron irradiation causes the production of hydrogen and helium. This has a strong effect in some other materials, for example steels particularly under high energy neutron irradiation [83] where the hydrogen and helium concentration can reach 10s appm. However, in this experiment the hydrogen and helium production were low (« 1 appm) due to the neutron spectrum used and the small cross-sections for hydrogen and helium producing reactions in tungsten. As a result this was unlikely to be the cause of the difference in voids observed between ion and neutron irradiated material.

3.8.3 Rhenium Clusters

The APT results show the formation of some clusters in W-1.4Re Ion. The only other study of precipitation in tungsten under ion irradiation was carried out by Xu et al. [75] [159]. The precipitates identified in this work were larger but less numerous (8.0 nm, 7.8 x 10^{22} m^{-3}) than those reported by Xu for W-2Re irradiated to 33 dpa at 773 K (3.3 nm, 8.1 x 10^{22} m^{-3}). This work also shows the formation of rhenium precipitates at far lower doses than was previously observed (1.7 dpa rather than 33 dpa). This may be due to higher irradiation temperature, which has previously been observed to promote rhenium precipitation during neutron irradiation [62] and was a trend found by Xu under ion irradiation. However, the clusters found in this work were much weaker than those observed by Xu, with clusters having peak concentrations of 5 - 10 %, whereas Xu reached peak concentrations of 30% Re in W-2Re after irradiation to 33 dpa at 773 K.

The clusters are much clearer in W Single Neutron. The peak concentration of 30% in these clusters indicate that χ or σ phase precipitates could be forming, but it was not possible to determine this from the APT results. The clusters are too small to routinely analyse with TEM but high resolution TEM techniques may be able to determine their crystal structure.

Klimenkov also analysed rhenium clustering in this sample using STEM-EDX techniques. Klimenkov reported clusters with a number density of 5 x 10^{21} m^{-3} but did not report sizes [66]. The density detected using APT in this work was an order of magnitude higher at 5.4 x 10^{22} m^{-3}. The resolution of APT (atomistic) is higher than that of STEM (1 nm probe size) so it is possible that additional small clusters identified by APT were missed while analysing with STEM. Klimenkov only reported the cluster density with reference to its relation to void density. Given that the void density measured was lower than that found in this work, it may be that the corresponding cluster density is also under-reported.

The only precipitates included by Hu et al. [98] are from high temperature irradiation in HFIR, which causes significantly greater transmutation (9.2%Re per dpa) than other commonly used irradiation facilities (usually around 1%Re per dpa) due to the high thermal spectrum in HFR. Unsurprisingly the results from HFR indicate significantly larger precipitates 16 - 20 nm for irradiation above 1000 K. The number densities reported (3.6 - 4.8 x 10^{22}) were very similar to those found in this work. The lack of cluster analysis in other neutron irradiation studies relies on two factors. Firstly, a number of early studies from the group at Tohoku University incorrectly assumed that transmutation of tungsten under neutron irradiation would be negligible. Secondly, nearly all of these studies rely on TEM analysis of the microstructure, where the minimum detectable cluster size is significantly greater than that using APT.

The only other analysis of neutron irradiated tungsten using APT was carried out by Hwang et al. [74]. They found that FISPACT modelling systematically overestimated transmutation during irradiation. This is surprising given the good match between FISPACT modelling and experimental data found in this work. The difference found

Table 3.14: APT detected cluster size and density following neutron irradiation in various fission reactors [74]

Sample	% Re	% Os	Cluster size / nm	Cluster density / 10^{22} m^{-3}
W Single Neutron (HFR)	1.4	0.1	3.5	5.4
Hwang (JOYO)	0.5	0.0	3.3	6.1
Hwang (HFIR)	4.0	0.8	2.9	18.5

by Hwang may have been due to inaccurate spectrum information. In this work it was necessary to recalculate the spectrum for not only the position of the irradiation within the reactor but also for the precise conditions during neutron spectra were acquired.

Hwang analysed pure tungsten irradiation to 0.9 dpa at 800 K in two different reactors, HFIR and JOYO. The results are compared to this work in table 3.14. This work produced larger and fewer clusters than the irradiations analysed by Hwang. This is likely due to the elevated temperature at almost 400 K higher. This higher temperature will enhance the mobility of rhenium and may encourage clustering. It is interesting that the HFIR irradiation produced smaller clusters than either HFR or JOYO, despite the increased transmutation. It may be that osmium encourages the formation of many, small clusters rather than a few large clusters. Xu found under ion irradiation that osmium clustered preferentially to rhenium This could contribute to the difference seen as HFIR irradiation produced significantly higher Os levels than either JOYO or HFR.

Modelling by Huang [53] predicted clusters at 3 x 10^{23} m^{-3} following irradiation to 1 dpa in JOYO, which produces less transmutation than HFR. This clearly overestimates irradiation induced precipitation but the ability to produce models capable of replicating irradiation induced precipitation at all is a very recent development, so accuracy may improve in the near-term.

Although clusters were identified in both ion and neutron irradiated material in this work, there are clear differences in the nature of these precipitates. The maximum separation algorithm used identified large diffuse clusters in W-1.4Re Ion, while isosurface analysis shows that the volume with Re concentration above 5% are very small, and no volume reaches 10% Re. By comparison in W Single Neutron the analysis detected clusters that are easily observable by eye in the isosurface plots and have a peak concentration above 30%. There is a question as to how these different types of cluster will interact with dislocations and contribute to hardness. This is discussed in section 3.8.5.

This difference is most likely caused by the differences in dose rate and time at elevated temperature between ion and neutron irradiation. Hardie et al. [68] found that reducing the dose rate for ion irradiation of Fe-Cr alloys encouraged precipitate formation. A similar experiment on higher rhenium containing tungsten alloys could investigate if similar behaviour is observed in tungsten. However, the expectation that an experiment that holds the material at higher temperature for

longer under irradiation encourages cluster formation is a reasonable one as this will allow time for thermal annealing to occur. Since radiation induced segregation is driven by defect diffusion, it is expected to occur during thermal annealing. Recently developed models are capable of predicting rhenium cluster formation under neutron irradiation [53] and could be adapted to investigating the effect of dose rate and time at elevated temperature. This may provide valuable information on how to adapt ion irradiation to best replicate neutrons.

3.8.4 Irradiation Hardening

3.8.4.1 Hardening Caused by Ion Irradiation

As discussed in section 1.3.3.2, a broad range of irradiation hardening results have been reported for ion irradiation of tungsten. The results acquired here on W Single Ion agree with Armstrong [31]. The irradiation in that work was carried out at 573 K on polycrystalline tungsten. It is surprising that the higher irradiation temperature used in this work did not reduce the irradiation hardening, however single crystal tungsten has a lower initial hardness and this has been shown to result in higher irradiation hardening [95].

The only hardness measurements from ion irradiated single crystal tungsten are from Hasenhuetl et al. [156]. This irradiation used Fe^{3+} ions at 573 K. The result was irradiation hardening of 1.8 GPa at 1 dpa, significantly higher than that observed in this work. These results suggest that increasing irradiation temperature decreases hardening in tungsten, as would be expected.

The picture for ion irradiation of W-xRe is even more complicated than that for tungsten. The results acquired in this work show substantially higher hardening than the 1 GPa of hardening measured by Armstrong for self-ion irradiation of W-5Re at 573 K to 1.2 dpa [31]. This may be indicative of higher temperature increasing irradiation hardening in W-xRe. A range of studies have shown hardening > 2 GPa for ion irradiation of W-xRe to 33 dpa [31] [75] [159] and the work by Xu et al. showed that this was associated with rhenium cluster formation. As discussed in section 3.8.3, rhenium clusters have formed in W-1.4Re at lower doses than previously observed, likely because of the high irradiation temperature. This cluster formation is the best explanation for the increased hardening found in this work.

The consequence of this is that the hardening of tungsten in a fusion environment may be greater than predicted. Previous irradiations have all been conducted at temperatures below the operating temperature of tungsten in a fusion reactor, and received knowledge is that higher temperatures reduce irradiation hardening as is commonly observed in other materials. If higher temperatures enhance rhenium clustering, rather than assisting in annealing out radiation damage, then the irradiation hardening of tungsten in a fusion environment will be severe.

3.8.4.2 Hardening Caused by Neutron Irradiation

The hardening observed in W Single Neutron (2.2 GPa) was significantly lower than that measured by Tanno for irradiation in JOYO to 1.54 dpa at 1073 K (3.3 GPa) [61], which was the closest match in irradiation conditions found in the literature. This suggests that either irradiation hardening in tungsten has a strong dependence on temperature above 1000 K, spectrum differences between JOYO and HFR result in different hardening or that the change in indentation method results in different values of irradiation hardening.

The difference in indentation size will affect the hardness levels measured but it is difficult to interpret how (if at all) this would affect the irradiation hardening measured. Examining the hardness curves from nanoindentation the difference in hardness between W Single Unirr and W Single Neutron remains constant throughout the depth of the indent. This suggests that the irradiation hardening measured is independent of size.

The density of voids found by Tanno was significantly higher (12 x 10^{22} m^{-3}) than that found in this work. This is particularly relevant as Tanno also only considered voids $>$ 2 nm. The difference in void density may have been caused by irradiation temperature or neutron spectrum. The correlation between microstructural features and hardness is discussed in greater detail in section 3.8.5.

3.8.5 Modelling Irradiation Hardening in Tungsten

The model used in section 3.7 accurately predicts the expected irradiation hardening in W Single Ion and W Single Neutron. This is a significant result and explains why previous ion irradiations of tungsten have failed to match the irradiation hardening observed in neutron irradiated tungsten. Voids and precipitates dominate hardening in neutron irradiated tungsten and are both absent after ion irradiation of tungsten. As a result there is a significant difference in irradiation hardening between W Single Ion and W Single Neutron.

Previously, the closest match to neutron irradiation using ion irradiation was carried out on W-xRe irradiated to $>$ 30 dpa [31]. This was shown to correspond with the formation of rhenium clusters, which only occurred only above 13 dpa [75] [159]. Higher irradiation temperature has accelerated rhenium cluster formation in this work, so that clusters are seen at 1.6 dpa. However, these are weak clusters (with a peak concentration between 5 and 10 % Re) and their hardening impact is clearly overestimated by the simple model applied here, causing the poor match between model and experiment for W-1.4Re Ion. Some dependence of barrier strength on the concentration of rhenium in the cluster would be expected. Dislocation dynamics modelling could be carried out to investigate this relationship and may lead to more accurate interpretations of hardness results in future.

One striking factor from these results is that although W-1.4Re Ion and W Single Neutron showed similar irradiation hardening, it was caused by different underlying

defect densities. There are still significant differences between the effects of ion and neutron irradiation, even after transmutation has been accounted for. Both void and cluster formation are enhanced in neutron irradiation compared to ion irradiation. This is likely due to the large difference in dose rate. However, results here and elsewhere show that higher temperatures encourage clustering and void formation. This suggests that a temperature shift, similar to that proposed by Mansur [78] may bring the results from ion and neutron irradiation closer. Alternatively the sample could be held at high temperature after irradiation to allow for thermal annealing. These methods may allow ion irradiation to still function as a useful tool for predicting the performance of tungsten in a fusion environment.

Hu et al. [98] also applied an irradiation hardening model to several data sets acquired from irradiation of tungsten in HFIR, JOYO and JMTF [61] [33] [60] [63]. There are numerous issues with this data set as have been discussed above. Firstly, there is no weak-beam analysis of dislocation loops. This is likely to lead to an underestimate of the density of loops present. Secondly, the minimum size of void analysed varies between authors from 2 nm to < 1 nm. This leads to a larger variation in void density than is representative of the irradiations. Finally, transmutation was considered not to be a factor in early irradiations so cluster densities are not available for samples where significant transmutation would be expected.

Hu used a dispersed barrier model for dislocation loops rather than the FKH model used in this work and recommended by Zinkle [99]. A consideration of the FKH model was made but rejected due to underestimate of hardening for low dose irradiations, where dislocation loop hardening dominates. This underestimation was likely caused by the lack of weak-beam dark-field TEM analysis resulting in low dislocation loop counts, not inaccuracy in the FKH model.

Hu found that the model underestimated hardening between 0.4-1 dpa, particularly in samples irradiated in HFIR. This is probably caused by the lack of Re cluster analysis for these samples since transmutation under irradiation in HFIR is particularly high. The accurate correlation between predicted and measured hardness in W Single Neutron in this work suggests that APT is suitable for analysing cluster sizes and densities.

The hardening contribution from voids is likely to have been overestimated by Hu for several of the samples analysed, since voids below the size that can be accurately measured using standard TEM techniques were included. Several of the results from JOYO have the model overestimating hardness despite the lack of cluster analysis. These results also have very high reported void densities ($> 10^{23}$)

There are a number of other differences between this work and that carried out by Hu. Particularly, the results presented here are based off nanoindentation while Hu used microindentation. The lack of dependence of irradiation hardening on size observed by nanoindentation between 200 and 2000 nm depth suggests that this may not cause a discrepancy in results. There is also a difference in the conversion factors from yield stress to hardness. Hu used a factor of 3.2 based upon empirical analysis carried out by Busby [102] on a range of results from ferritic stainless steels. It is

unclear whether this analysis is accurate for tungsten, so the conventional 2.74 from Tabor theory was used in this work [154].

This work has highlighted some of the issues from previous analysis of neutron irradiated tungsten and demonstrated that, with accurate analysis, the irradiation hardening can be predicted from microstructure observation. This is a critical step towards a completely predictive model of irradiation damage and its effects [160].

For a completely predictive model of irradiation damage, a model that can accurately predict changes in microstructure caused by irradiation is also needed. The modelling carried out by Huang [53] attempts to do this, but is shown to be inaccurate for predicting loop and void formation by the results here. The predictions of cluster formation were relatively accurate and led to the conclusion that irradiation hardening levels in DEMO will be intolerable due to clustering. This work backs up that conclusion by demonstrating that cluster formation is the dominant effect in hardening of samples irradiated at fusion relevant temperatures.

3.9 Summary Table

The key results from this chapter are included in table 3.15. This includes the defect densities and mean sizes observed and the irradiation hardening measured.

Table 3.15: Key results from the study of irradiation hardening

	W Single Ion	W-1.4Re Ion	W Single Neutron
Dislocation loop density / 10^{22} m^{-3}	17 ± 3	24 ± 3	19 ± 4
Dislocation loop mean size / nm	4.2 ± 0.3	3.2 ± 0.2	3.0 ± 0.2
Precipitate density / 10^{21} m^{-3}		7.8 ± 0.7	5.4 ± 1.1
Precipitate mean size / nm		8.0 ± 2.6	3.5 ± 1.0
Void density / 10^{21} m^{-3}			6.4 ± 0.6
Void mean size / nm			5.4 ± 0.4
Irradiation Hardening / GPa	1.0 ± 0.2	3.2 ± 0.7	2.4 ± 0.7

4

Investigating Fracture Properties of Neutron Irradiated Tungsten

4.1 Introduction

This chapter investigates the effect of neutron-induced radiation damage on the fracture properties tungsten. In particular, the brittle to ductile transition in neutron irradiated single crystal tungsten was investigated and fully characterised using four-point bend tests at multiple strain rates and temperatures. This was accompanied by dislocation activation volume measurements using nanoindentation strain-rate sensitivity measurements. This allowed a full picture of the effect of neutron irradiation on the BDT of single crystal tungsten. This is critical information for demonstration fusion power plants, where the BDT of tungsten will control the minimum operating temperature and lifetime of divertor components [65], and may also affect end of life handling methods.

Although tungsten is likely to be the material used for plasma facing divertor components, the exact microstructure of the tungsten to be used is as yet unknown with manufacturing techniques still in development [21] and significant research going into ductilisation of tungsten through microstructure changes [96]. Investigating single crystal tungsten provides baseline information about the effects of neutron irradiation on the material. This knowledge can then be applied to assist in predictions of the behaviour of advanced tungsten materials.

Any engineering tungsten component will contain grain boundaries so investigations into the fracture properties of neutron irradiated polycrystalline tungsten were also made. The results from four-point bend tests showed highly anomalous results, so further tests were carried out using micro-cantilevers to probe grain boundary behaviour.

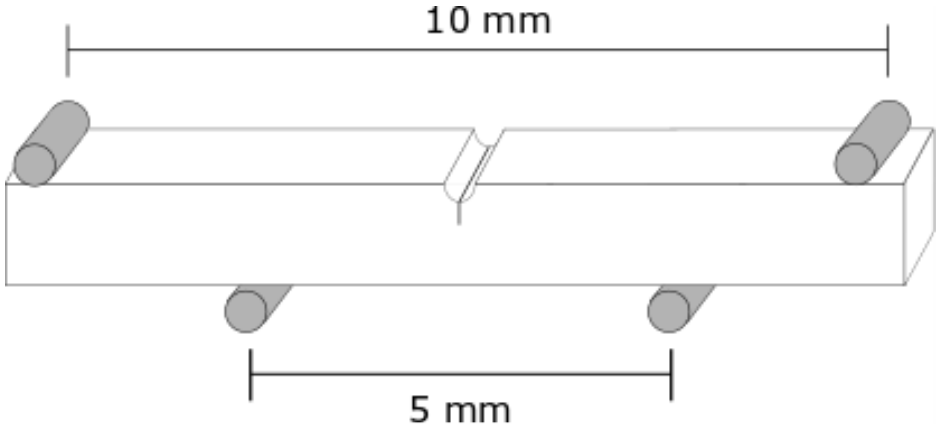

Figure 4.1: Geometry of four-point bend setup. The load was applied such that the face with the pre-crack was in tension. Reproduced from [22] by permission from Taylor & Francis.

4.2 Methods

The materials investigated in this chapter were primarily W Single and W Poly as described in section 2.1. These materials were investigated in the unirradiated state and following neutron irradiation, which is described in section 2.2. The testing techniques used were four-point bend test, multiple strain rate nanoindentation and micro-cantilever bend tests. Multiple strain rate nanoindentation was also carried out on W-1.4Re in order to characterise the impact of rhenium on the strain rate sensitivity of tungsten.

4.2.1 Four-Point Bend Tests

Four-point bend tests were carried out on neutron irradiated tungsten by H.C. Schneider and co-workers at Karlsruhe Institute of Technology (KIT), using the same method as Giannattasio et al [131]. The samples were tested on a four-point bend rig within a vacuum furnace at temperatures up to 1173 K and displacement rates between 0.0005 mm min^{-1} and 0.035 mm min^{-1}. This corresponded to strain rates between 3.5×10^{-7} and 2.5×10^{-5}.

$$\sigma = 3P\frac{(L-a)}{2wt^2} \tag{4.1}$$

Stress values were calculated from the load cell measurement (P) and equation 4.1. L (10 mm) and a (5 mm) are the outer and inner spans respectively and w and t are the sample width and thickness (both 1 mm) (see figure 4.1). The strain rate was found by assuming a modulus of 410 GPa and fitting the gradient of the elastic portion of the stress-strain curve region to this value. This was considered to be more accurate than calculating strain rate from the cross-head displacement

speed. Any sample that fractured before 5% strain was considered to be brittle and the BDT temperature was taken as being equal to the temperature of the lowest temperature ductile test. The gap between highest brittle temperature and lowest ductile temperature was 25 K for each strain rate.

Following four-point bend tests the samples were analysed using SEM fractography. This allowed verification of the precrack length and confirmation of brittle or ductile behaviour from the fracture surface. Fracture was observed to have occurred through cleavage along the (100) plane parallel to the precrack as expected.

Although this author did not carry out the four-point bend tests, they were responsible for selecting test conditions (temperature and displacement rate) and complete analysis of the results. A visit to KIT was undertaken in order to assist with SEM fractography of the samples and coordinate further testing.

4.2.2 Multiple Strain Rate Nanoindentation

The basic nanoindentation method is described in section 3.2.3. The work in this chapter focuses on using multiple strain rate indentation to investigate strain rate sensitivity (SRS) of tungsten in the unirradiated and neutron irradiated states.The shallow depth penetration of ion irradiation prevented SRS nanoindentation being carried out on any ion irradiated samples.

The applied strain rate can be varied throughout the depth of an indent (strain rate jump tests) and the apparent hardness measured for each strain rate using continuous stiffness measurements as described by Maier et al. [114]. In this experiment the strain rate was varied between 0.01 and 0.1 s^{-1}. In between each strain rate the hardness was measured at a base strain rate. This allowed for accurate calculation of the difference in hardness between the base strain rate and the strain rate being investigated. A typical loading rate profile for SRS indentation is shown in figure 4.2. Depths > 1 μm were used to minimise the size effect and ensure accurate comparison between hardness measured at base strain rate and the strain rate being investigated.

Typical hardness results are shown in figure 4.3. A clear decrease in hardness can be observed alongside each drop in strain rate, with a return to the base rate in between. This drop in hardness is added to the base strain rate hardness measured between 800 and 1000 nm in order to calculate a representative hardness for each strain rate. These results are then plotted on a log hardness versus log strain rate graph in order to calculate the strain rate sensitivity, m, as given by equation 4.2.

Changes in flow stress with strain rate have long been established as being a measure of the activation volume for thermally activated dislocation motion in BCC metals [161] and has been used to show the decrease in activation volume for nanograined tungsten [162]. The strain rate sensitivity can be related to flow stress through equation 4.3, where σ_f is the flow stress. This equation is converted to a dependence on hardness using the assumption that $H \approx 3\sigma_f$, a loose approximation as the constant can be considered to vary between 2.7 and 3.2, but more than sufficient for this case where

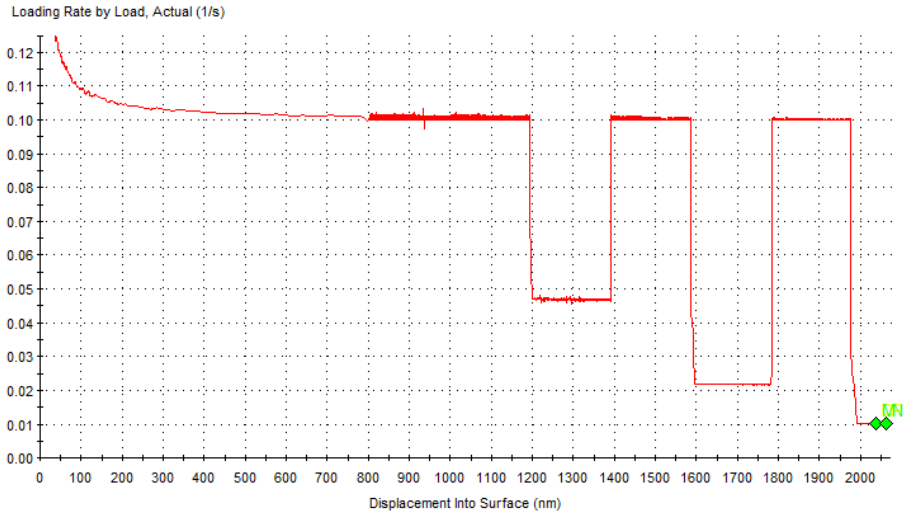

Figure 4.2: A graph of loading rate against depth for strain rate sensitivity nanoindentation

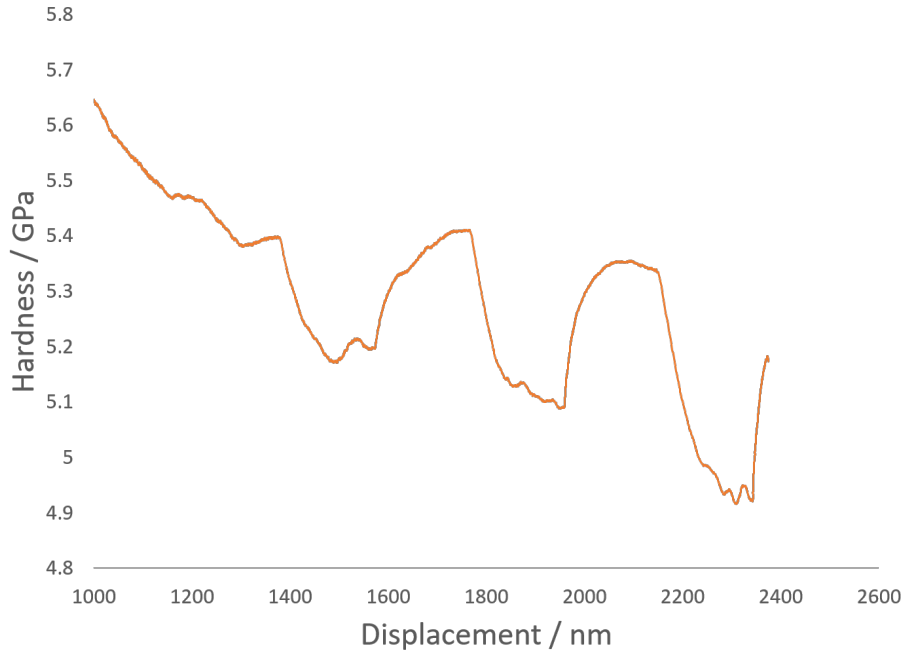

Figure 4.3: A graph showing the change in hardness with each strain rate jump. The first drop in strain rate occurred at 1400 nm

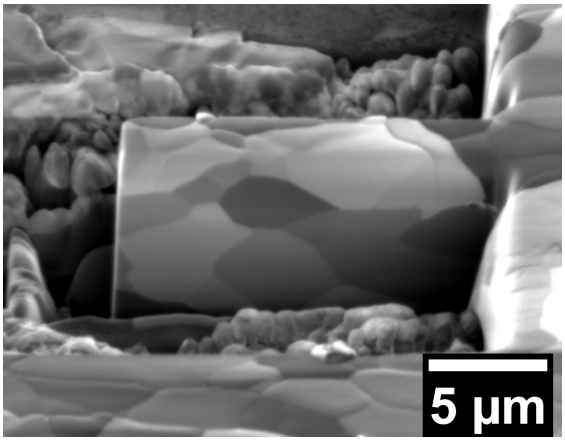

(a) Trenches cut around cantilever

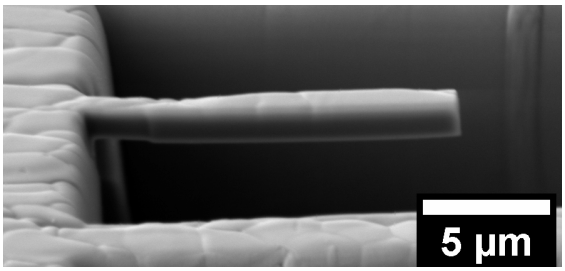

(b) Cantilever after undercuts have been made

Figure 4.4: Process of making cantilevers using FIB

m can vary by orders of magnitude between materials.

$$m = \frac{d\ln(H)}{d\ln(\dot{\varepsilon}_{nanoindentation})} \tag{4.2}$$

$$m = \frac{\sqrt{3}kT}{V.\sigma_f} \approx \frac{3\sqrt{3}kT}{V.H} \tag{4.3}$$

4.2.3 Micro-Cantilever Tests

Micro-cantilevers were produced in W Poly Neutron using FIB. The cantilevers were milled to a size of 15 x 3 x 2 μm, with the side faces at 45° to the top face. To achieve this, rough U-shaped trenches of 25 x 25 x 10 μm were cut around the cantilever using a 30 kV, 16 nA beam. The remaining material was reduced to the desired size and undercutting carried out using a 600 pA beam. Figure 4.4 shows the cantilever-making process. The precise width and length of the cantilevers was measured using SEM prior to testing.

These cantilevers were tested using an Agilent G200 Nanoindenter with a piezoelectric-controlled nano-positioning stage. This allows the cantilever to be scanned using very low load (0.2 μN) so that the indentation location can be accurately chosen. The cantilevers were tested to a displacement of 1000 nm with a displacement rate of 10 nm/s. Load and displacement data were then converted to stress-strain results using simple beam theory [163]. After testing the cantilevers were examined using SEM.

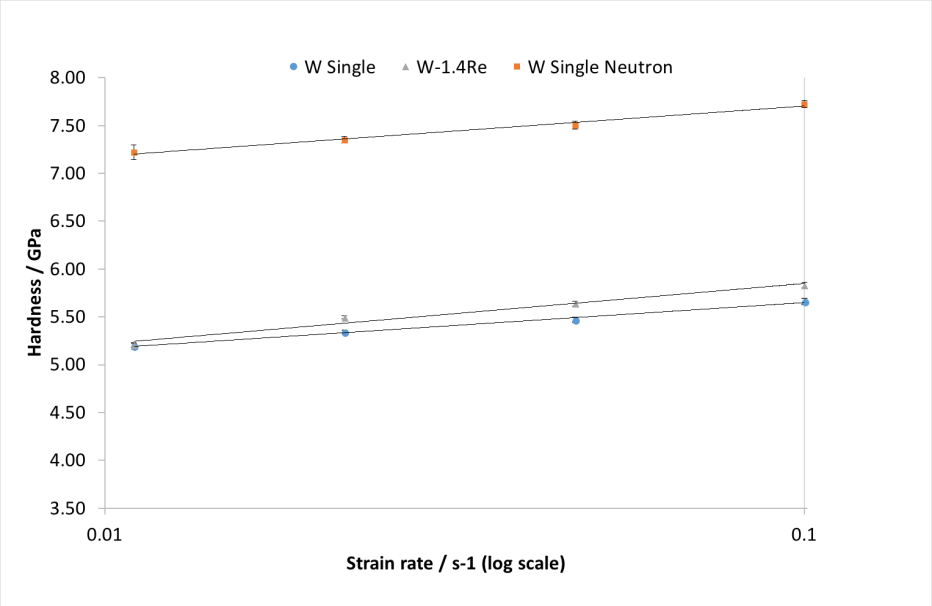

Figure 4.5: Hardness results from SRS indents in W, W-1.4Re and neutron irradiated W

	m	Activation volume / m^3	Activation volume / b^3
W	0.038	1.1 x 10^{-28}	5.6 ± 0.7
W-1.4Re	0.050	7.4 x 10^{-29}	4.0 ± 0.5
Neutron W	0.030	9.4 x 10^{-29}	4.6 ± 1.0

Table 4.1: Activation volumes for dislocation motion from SRS nanoindentation

4.3 Results

4.3.1 Strain Rate Jump Tests

The SRS nanoindentation measurements are presented in figure 4.5 for the unirradiated materials and neutron irradiated W. These results confirm the similar hardness measurements for the unirradiated W Single and W-1.4Re. The significant increase in hardness of W Single following neutron irradiation is also apparent. The data also shows that the strain rate sensitivity, m, of each material is similar. From m it is possible to calculate activation volumes for dislocation motion, using equation 4.3. The results of these calculations are presented in table 4.1.

These results show that there is a small difference in activation volume between W and W-1.4Re but there has been no significant change in the activation volume in the single crystal as a result of neutron irradiation.

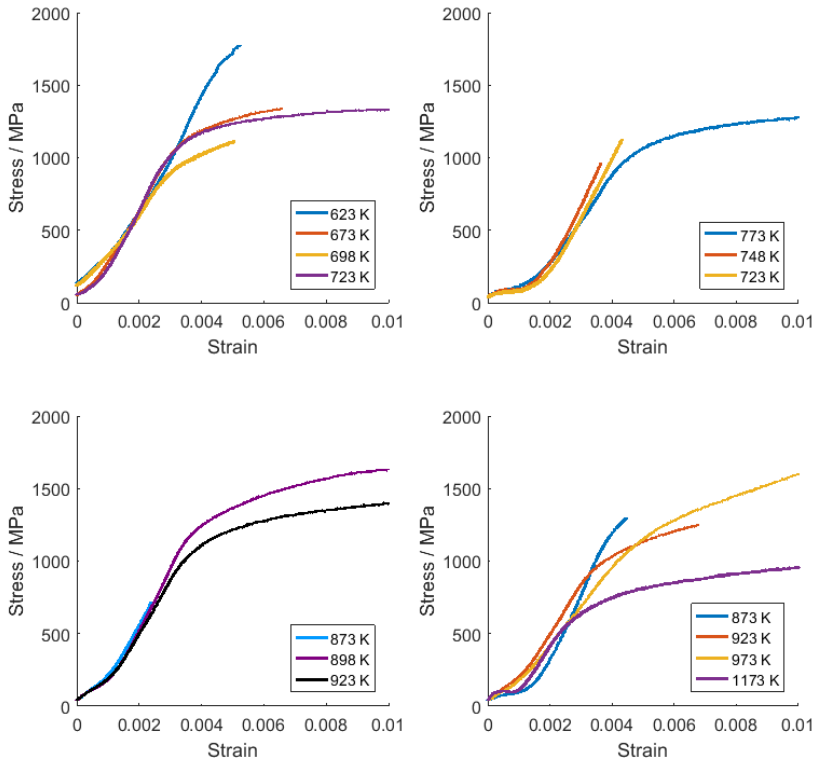

Figure 4.6: The stress strain curves for four-point bend tests in neutron irradiated tungsten at four different strain rates, above and below the BDT temperature at each

4.3.2 Four-Point Bend Tests in W Single Neutron

The results from the four-point bend tests of W Single Neutron are presented in figure 4.6. For each sample, a sharp transition from brittle to ductile behaviour (defined as $> 5\%$ strain before fracture) could be observed. The minimum temperature window between tests was 25 K and a complete transition was considered to have taken place within this window for each sample.

The BDT temperature was taken to be the temperature of the lowest ductile test. Figure 4.7 shows the BDT temperature at each strain rate for both the unirradiated and neutron irradiated tungsten. These results show that the BDT temperature has increased by $>$ 500 K at strain rates around 3 x 10^{-5} s^{-1}.

For unirradiated single crystal tungsten, the brittle to ductile transition was found to have an Arrhenius dependence of the form given in equation 4.4. From experiments this value of the activation energy, E_a, was found to be 1.0 [22]. The Arrhenius plot for neutron irradiated tungsten is shown in figure 4.8. This analysis showed that the activation energy for the brittle to ductile transition was 1.05 $\pm$ 0.3 eV .

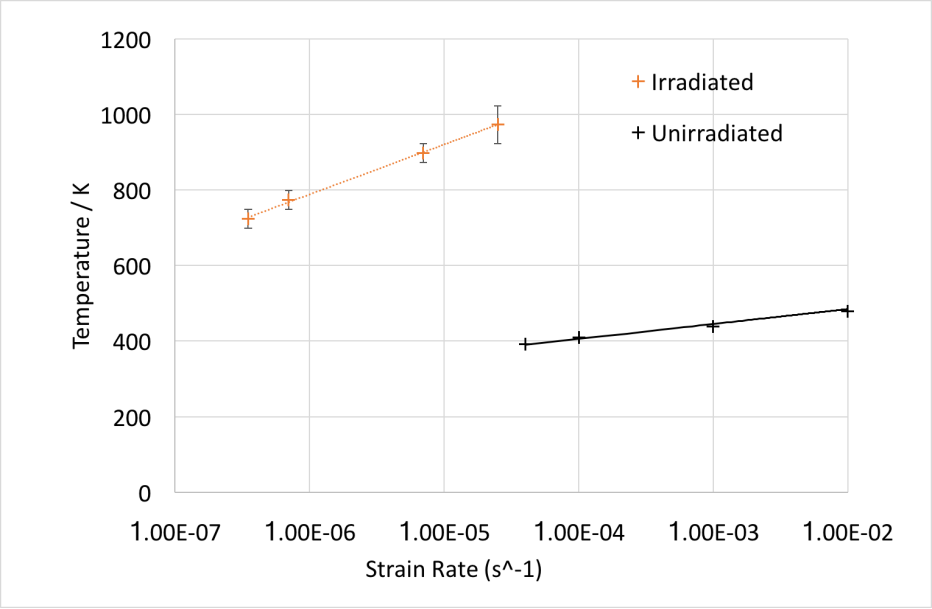

Figure 4.7: The brittle to ductile transition temperature for neutron irradiated tungsten as a function of strain rate

$$\dot{\varepsilon} = \dot{\varepsilon_0} e^{\frac{-E_a}{kT}} \tag{4.4}$$

4.3.2.1 Four-Point Bend Fractography

Figure 4.9 shows SEM images of the fracture surface of single crystal tungsten after four-point bend in a range of conditions. The images show the significant increase in dislocation activity as the test temperature is increased towards and past the BDT temperature. There is no significant change in the fracture surfaces after neutron irradiation. In both specimen types, at temperatures far below the BDT, fracture is by cleavage on the {001} plane, with little visible deformation, whereas at temperatures close to the BDT rough fracture surfaces with characteristic river lines are observed. Above the BDT temperature, fracture surfaces show significant macro-scale deformation; here fracture occurred at strains greater than 10 %.

The fractography also allows for verification of the pre-crack size in the samples. These measurements confirm that the pre-crack size was 40 - 60 μm, the same as that reported in the unirradiated samples. The SEM images show that at temperatures well below the BDTT limited, a smooth fracture surface is observed with few river lines. This indicates that there was very limited dislocation mobility as the crack propagated through the material, showing that the material was in the brittle regime due to limited dislocation mobility. By comparison, in the samples close to the BDTT a clear arrowhead pattern could be observed. This corresponds to the motion

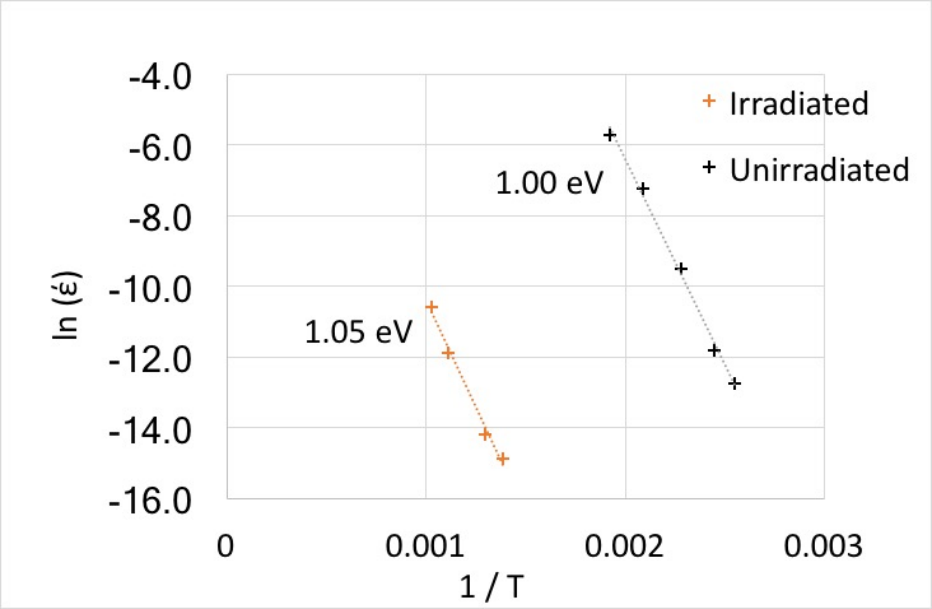

Figure 4.8: The Arrhenius dependence of the brittle to ductile transition in unirradiated [131] and neutron irradiated tungsten

of dislocations away from the intense stress at the crack tip with the lines of the arrowhead corresponding to the dislocation slip planes. This process has been modelled by Tarleton [133] in order to provide greater understanding of the BDT. The dislocation motion can shield the crack tip, and these patterns indicate that the material is on the border of the ductile regime.

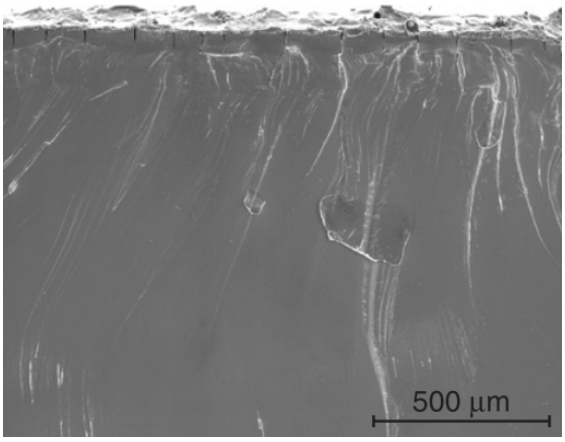

(a) Unirradiated tungsten showing low dislocation mobility at 77 K

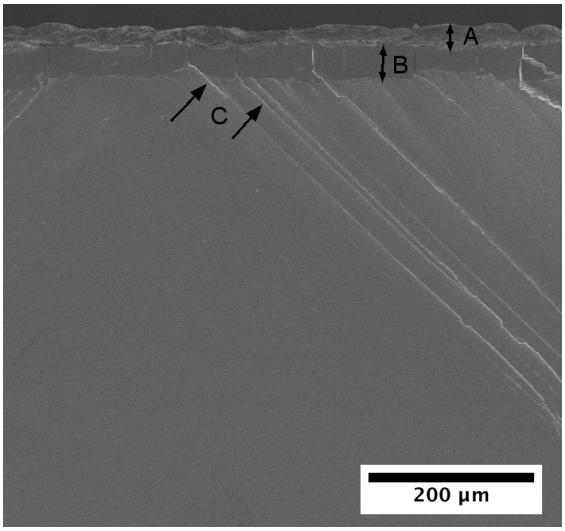

(b) Neutron irradiated tungsten showing low ductility for sample fracture at 473 K with a strain rate of 7 x 10^{-7} s^{-1}. The notch (A), precrack (B) and river lines (C) are labelled in this image

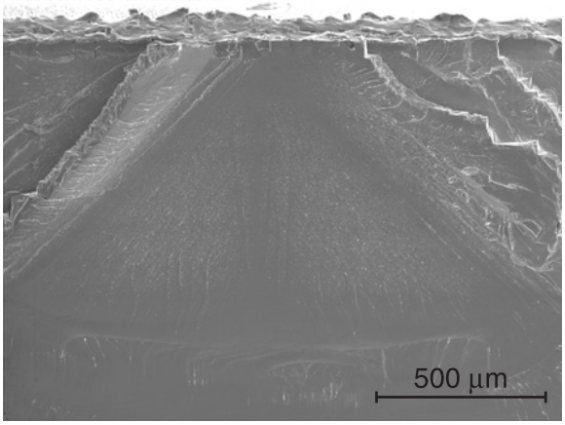

(c) Significant ductile work and faint arrowhead pattern observed in unirradiated sample fractured at 478 K (close to the BDTT)

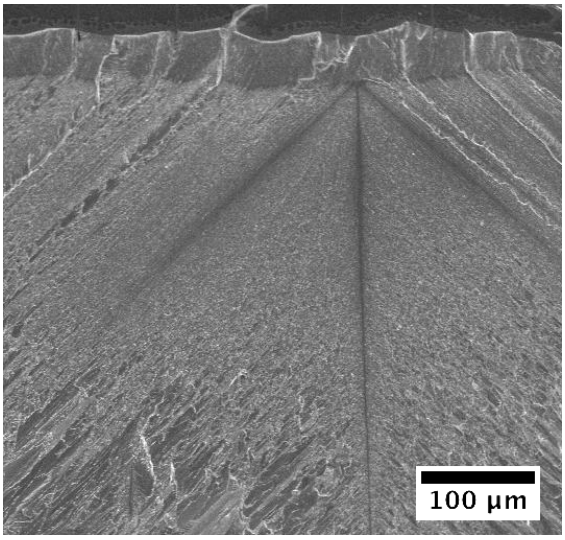

(d) Arrowhead pattern around crack nucleation point observed in neutron irradiated sample fractured at 723 K and a strain rate of 3.5 x 10^{-7} s^{-1} (close to the BDTT)

Figure 4.9: SEM fractography of unirradiated and neutron irradiated tungsten

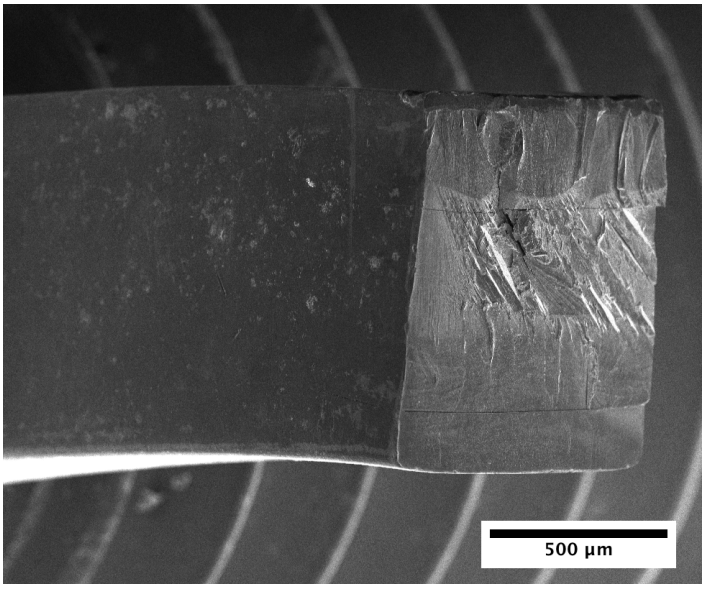

Figure 4.10: High ductility observed in neutron irradiated sample tested at 823 K with a strain rate of 7 x 10^{-7} s^{-1} (above the BDT temperature). This sample showed a strain >10% before fracture

4.3.3 Four-Point bend Tests in Polycrystalline Tungsten

The results from four-point bend tests on W Poly Neutron are shown in figure 4.11. The BDT temperature at $\dot{\varepsilon} = 3 \times 10^{-5}$ s^{-1} could be accurately identified as being between 503 and 573 K. Giannattasio [22] found that the BDT temperature for unirradiated polycrystalline tungsten was 390 K. This suggests that the increase in BDT temperature may be much lower in polycrystalline tungsten. However, tests on W Poly Neutron at a lower strain rate found that the material still showed brittle fracture at 623 K. This would suggest that the material is more brittle at lower strain rates, a very unusual result. Limited access to the testing equipment meant that no further tests could be conducted. As a result no estimate for activation energy of the BDT in W Poly Neutron was possible. Additionally, the result from one strain rate is not sufficient to determine the BDT temperature in W Poly Neutron, especially given the strange behaviour observed at the second strain rate.

Fractography from samples tested at 300 and 503 K with $\dot{\varepsilon} = 3 \times 10^{-5}$ s^{-1} are shown in figures 4.12 and 4.13. These show mixed trans- and inter-granular fracture, with increased inter-granular fracture at higher temperature. This is consistent with the result found by Giannattasio [131] who observed a transition from trans-granular fracture at 77 K to inter-granular at 419 K.

The non-flat fracture surfaces and non-linear cracks observed are both indications that cracks in this material are propagating easily along grain boundaries. The weakening of the grain boundaries following neutron irradiation may partially explain

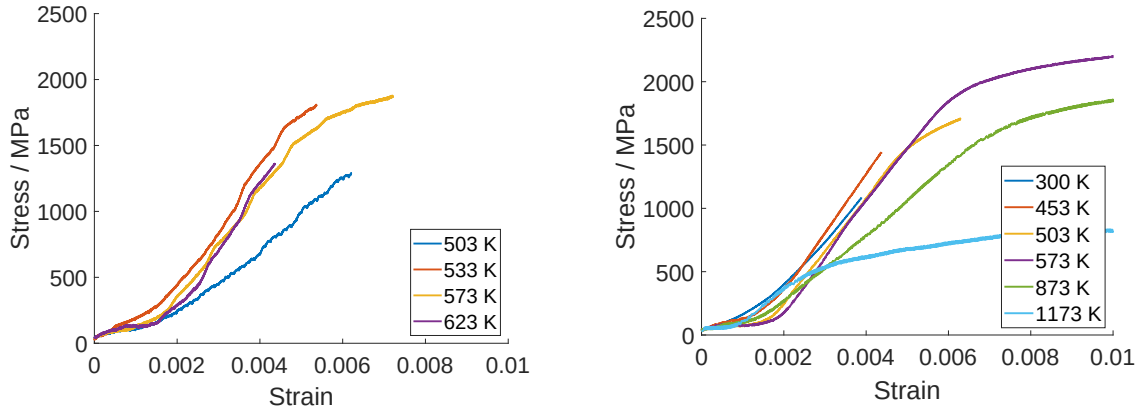

(a) $\dot{\varepsilon} = 8 \times 10^{-6}$ s^{-1} **(b)** $\dot{\varepsilon} = 3 \times 10^{-5}$ s^{-1}

Figure 4.11: Stress strain curves from four point bend tests carried out on W Poly Neutron

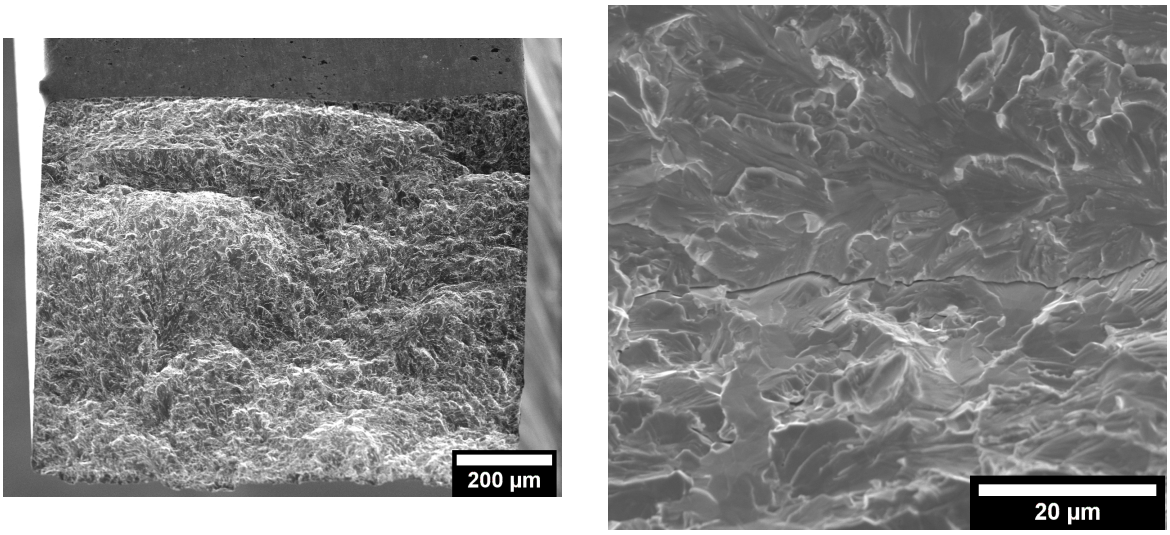

Figure 4.12: SEM fractography of W Poly Neutron tested at 300 K

the unusual strain rate response. To investigate this further micro-cantilevers were produced and tested in W Poly Neutron.

4.3.4 Micro-Cantilever Testing

Micro-cantilever tests were performed on W Poly Neutron in order to investigate the effect of neutron irradiated on the strength of grain boundaries in the material. Stress strain curves for the cantilever tests are presented in figure 4.14. From these curves it is apparent that two cantilevers, F and G, snapped during testing. While both of these cantilevers showed some ductility before fracture, it is highly unusual to observe fracture in tungsten cantilevers of this size and nature [120]. This suggests

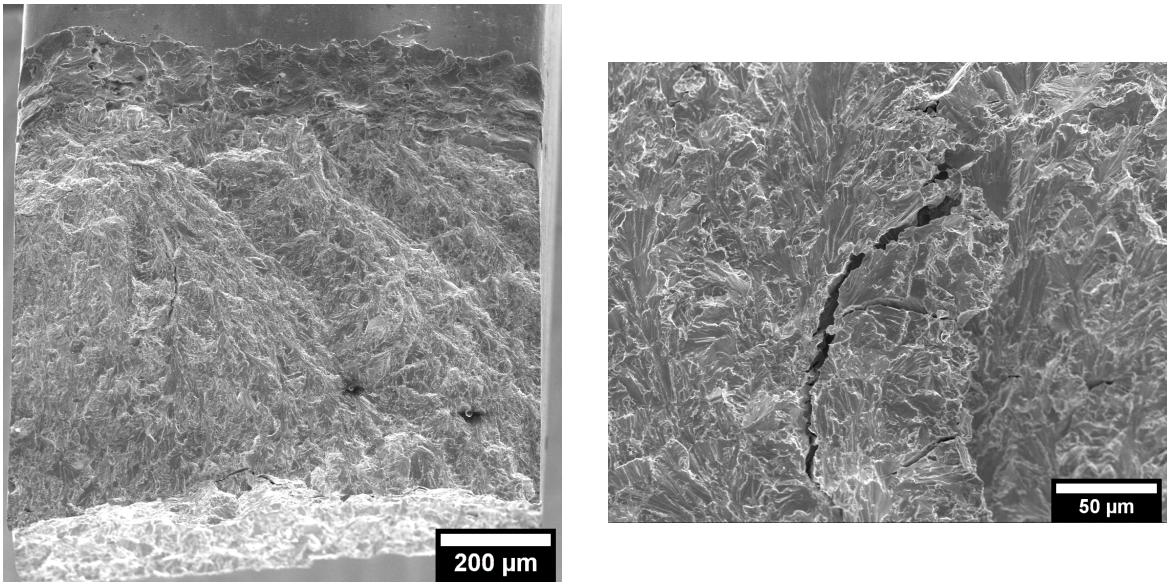

Figure 4.13: SEM fractography of W Poly Neutron tested at 573 K

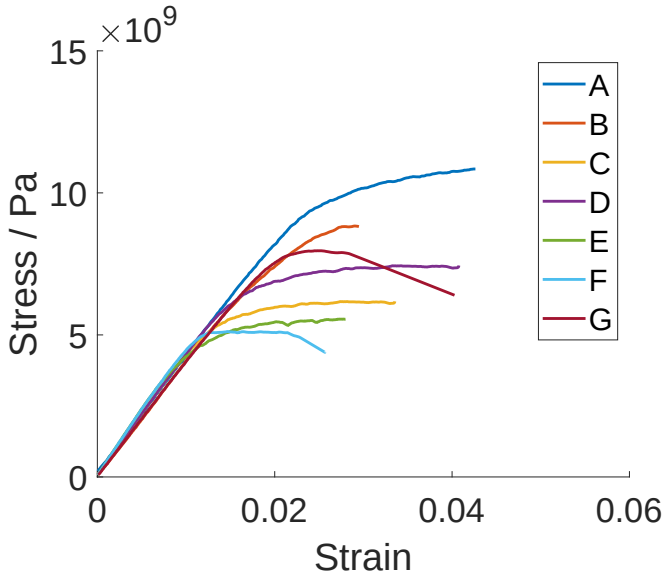

Figure 4.14: Stress-strain curves from cantilever testing in W Neutron Poly

that the room temperature brittleness of this material has increased significantly compared to unirradiated tungsten.

Post-test images are shown for several cantilevers, including F and G, in figure 4.15. These images show that the fracture observed in F and G occurred along boundaries near the base of the cantilever. EBSD maps including F and G are shown in figure 4.16. This shows that the boundaries where fracture occurred was a sub-grain boundary.

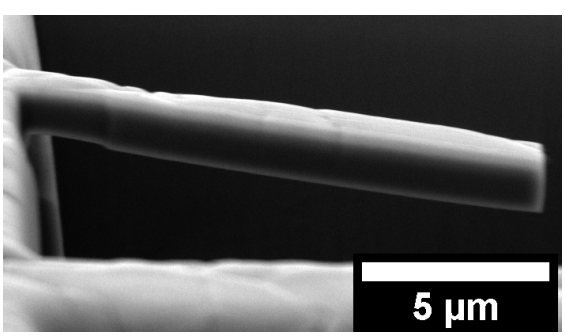

(a) A

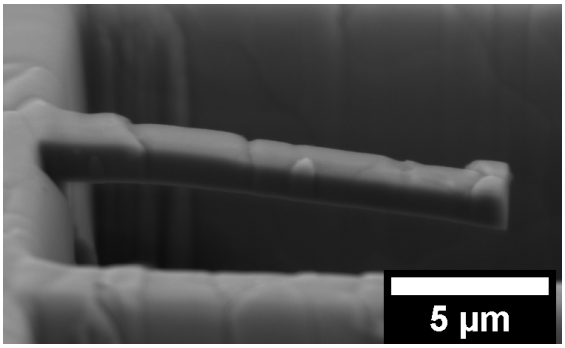

(b) C

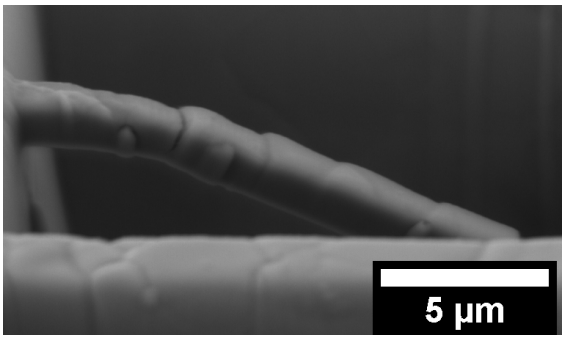

(c) F

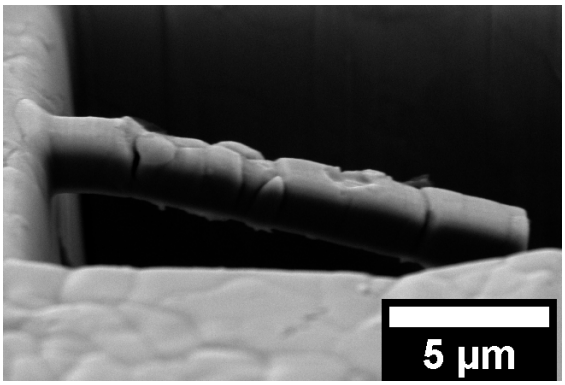

(d) G

Figure 4.15: SEM images of cantilevers in W Poly Neutron after testing

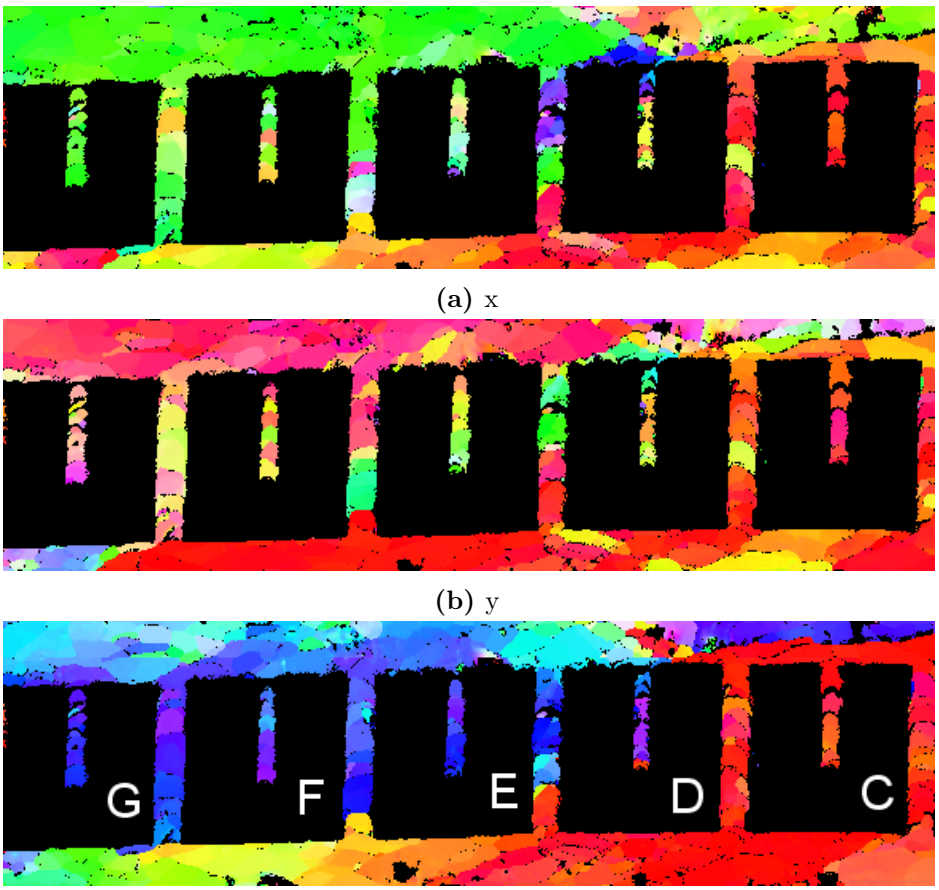

(a) x

(b) y

(c) z

Figure 4.16: EBSD maps of cantilevers

4.4 Discussion

4.4.1 SRS Nanoindentation

The strain rate sensitivity value ($m = 0.38$) for single crystal tungsten agrees well with literature values of $m = 0.4$-0.5 from large scale compression tests [164]. The activation volumes calculated by SRS also agree well those found by Brunner using tensile tests for room temperature testing of tungsten [165]. Futhermore, these results agree with the values of activation volume ($V = 6\ b^3$) calculated using strain rate jump tests by Maier at al. [115].

The activation volume appears to decrease with added rhenium. This coincides with a change in the screw dislocation core structure [166] and increasing ductility of tungsten with rhenium addition [167] [168]. Other routes for ductilising tungsten such as cold-rolling have also been shown to be assocaited with a decreased activation volume for dislocation mobility [162]. Further investigations on W-Re alloys using strain rate jump tests would be needed to prove conclusively that the observed change in activation volume was due to rhenium addition.

W Single Neutron appears to have an activation volume closer to the unirradiated single crystal than would be expected given the presence of 1.4 wt% rhenium. This may be associated with the clustering of rhenium as discussed in section 3.5. This cluster formation may leave the matrix depleted of rhenium, which could explain the higher observed activation volume.

4.4.2 Increase in BDT Temperature Following Neutron Irradiation in W Single

There is evidence from both the four-point bend mechanical results and the SEM fractography that the brittle to ductile transition temperature has increased very dramatically following neutron irradiation to 1.67 dpa. The four point bend tests give clear BDT temperature windows for each of the strain rates used. The BDT temperature is strain rate dependent, and so is the difference between unirradiated and irradiated BDT temperature so a single value is not representative of the increase. However, strain rates $\approx 3 \times 10^{-5}$ were investigated in both materials and showed a difference in BDT temperature of 500 K.

The fractography shows similar behaviour on fracture surfaces in unirradiated and irradiated tungsten, but at substantially higher temperatures for the irradiated material. This agrees with the very large increase in BDT temperature measured from the mechanical testing data, and shows that dislocation mobility is increasing as the BDT is approached in both the unirradiated and irradiated material.

The increase in BDT temperature in tungsten is compared to other experiments investigating fracture in neutron irradiated tungsten in table 4.2, reproduced from section 1.5.1. The results suggest a steadily increasing BDT temperature with increasing

Table 4.2: Inferred increases in BDTT from previous mechanical tests on neutron irradiated tungsten

Reference	**Neutron Fluence(s) / m^{-2} (E> 0.1 MeV)**	**Irradiation Temperature/K**	**Inferred BDTT / K**
Krautwasser [139] (abstract only)	5.6 x 10^{25}	525-575	Increased by 70 (13.7 / 10^{24} n up to 5 x 10^{24})
Steichen [138]	5 x 10^{25} 9 x 10^{25}	648 648	505 - 700 505 - 700
Rau [136]	3.8 x 10^{23}(E > 1 MeV)	343	>673
Gorynin [137]	1.5 x 10^{26} (no threshold energy)	773	>773
This work	1.2 x 10^{26} 1.67 dpa	900	700 - 1000

fluence. There is no evidence from this that the high irradiation temperature (close to expected service temperatures for tungsten components in DEMO) has any mitigating effect on the increase in BDT temperature caused by irradiation.

The samples were pre-cracked prior to irradiation and no annealing was carried out. As a result, a residual stress around the crack tip would be expected. The nature of the crack induced by electro-discharge machining (EDM), as in this work, is still under investigation across a range of materials [169][170]. An unirradiated sample was studied prior to testing using EBSD [171]. This showed that there was a large in-plane rotation either side of the crack, but critically there was no plastic zone ahead of the crack path. However, the pre-cracking was likely to have resulted in a residual compressive stress at the crack tip [172].

Pre-cracking by fatigue loading is the technique recommended by ASTM and ISO standards for fracture toughness tests as a sharp crack can be induced under carefully controlled conditions with a low Δ K [173]. However, this pre-cracking process can be very time consuming. The EDM technique used in this work is much quicker, allowing a greater number of samples to be prepared, but leads to an uncontrolled residual stress.

The compressive residual stress in the unirradiated sample is likely to have suppressed crack growth under the tensile loading conditions during four-point bending. As a result the measured fracture toughness may be greater than the true fracture toughness. This may also have increased the measured BDTT. The high temperature during neutron irradiation (1173 K) in this work would have relieved the stress present following EDM pre-cracking. Since the residual stress would have increase measured fracture toughness and decreased BDTT in the unirradiated sample, the increase in BDTT following neutron irradiation may have been underestimated but it is

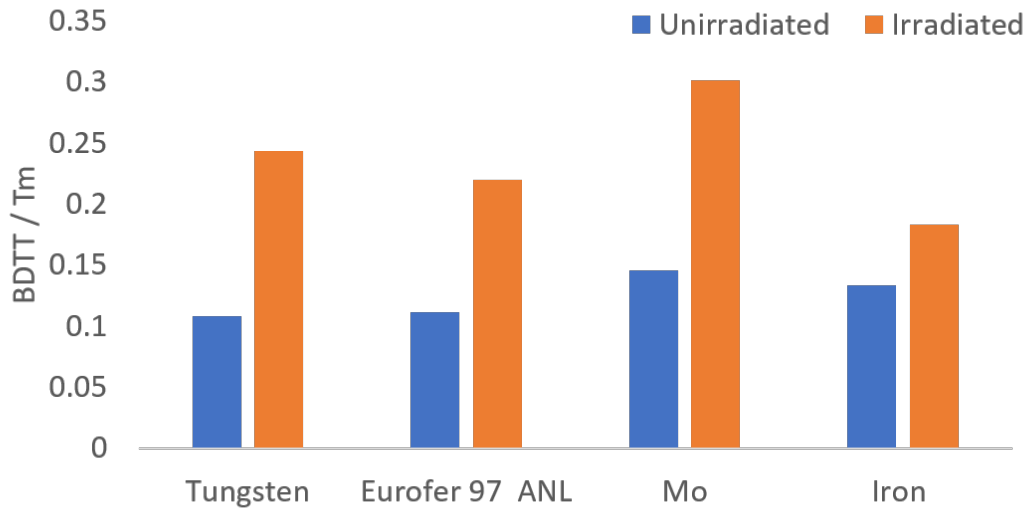

Figure 4.17: The BDT temperature measured before and after neutron irradiation across different BCC metals [174] [175] [176]

difficult to quantify by how much.

4.4.3 Comparison to other BCC metals

Figure 4.17 shows the brittle to ductile transition temperature in several BCC metals, normalised by melting temperature. The dose and temperature of irradiation varies between samples as shown in table 4.3 (with the only available data for pure iron in particular being high temperature or low dose). From this, a general trend can be seen to emerge. The BDT temperature for most BCC metals is around 0.1 T_m prior to irradiation and increases to 0.2 - 0.3 T_m after irradiation. The results for tungsten found during this work fit well with this picture.

The data from Gaganidze et al. [174] gives BDT temperature data for several reduced activation ferritic-martensitic steels irradiated at a range of temperatures. These results show that the increase in BDT temperature drops for irradiation temperatures of 623 K and above, or greater than 0.35 T_m. The equivalent homologous temperature in tungsten is 1300 K. This suggests that despite the high irradiation temperature in this work, a maximum increase in BDT temperature may still be being observed and that higher irradiation temperatures may result in a decrease in post-irradiation BDT temperature.

Table 4.3: Irradiation conditions for BDT temperature measurements in BCC metals

Material	Dose / dpa	Irradiation Temperature/K
Tungsten (this work)	1.67	1173
Eurofer 97 [174]	16.3	573
Molybdenum [175]	2.2	782
Iron [176]	0.13	673

4.4.4 Understanding the Effects of Neutron Irradiation on the BDT in Tungsten Single Crystal

Despite the large increase in BDT temperature following neutron irradiation, there is no appreciable change in activation energy. Further to this, activation volume measurements also show no significant change following neutron irradiation. Finally, the appearance of fracture surfaces near the BDT temperature, with characteristic 'river-lines', suggest that the mobility of dislocations is the same in both materials. All this suggests that the BDT is still controlled by dislocation mobility, and that this in turn is controlled by the same mechanism.

The analysis carried out by Giannattasio et al. [131] showed that this was kink-pair formation in 1/2 {112} screw dislocations, with an activation energy (2 H_k) of 1.75 eV [165]. This conclusion was confirmed through dislocation dynamics modelling by Tarleton and Roberts [133]. One key aspect of this analysis is the effect that stress has on the observed activation energy, as given by equation 4.5.

$$E_a = 2H_k - \tau V \tag{4.5}$$

The dislocation dynamics modelling carried out by Tarleton [133] found the stress on dislocations to be around 300 MPa, assuming an activation volume of 20 b^3. This assumed activation volume is significantly larger than that found in this work using SRS nanoindentation ($\approx$ 5 b^3). This difference may be due to the different loading conditions considered in each case. In particular, nanoindentation was carried out at room temperature and the applied stress around the sharp tip is very high. As a result it may be expected that the thermal contribution to dislocation motion is relatively low, and so large double kinks are less likely to form. By comparison, the four-point bend tests were carried out at low strain rates and high temperatures, so the thermal activation of dislocation motion would have been greater, resulting in a larger activation volume. Further experimental and modelling work is required to enhance our understanding of the mobility of screw dislocations around the BDTT and accurate interpretation of activation volumes from SRS nanoindentation.

Swinburne and Dudarev [135] postulate that the controlling mechanism for the BDT in unirradiated BCC metals is a single kink mechanism, rather than the often

cited double kink. They explain that the activation energy for kink mobility halves from $2H_k$ to H_k when the average dislocation length becomes greater than a stress and temperature-dependent critical length. The critical length for tungsten as a function of stress and temperature was not shown, and could not be calculated based upon the information provided, but for iron it ranges from 0.01 to 10 μm for temperatures of 200 - 500 K and stresses between 0 and 150 MPa. This compares to a dislocation spacing of 30 μm for a well-annealed dislocation density of 10^9 m^{-2}.

This leads to the prediction that the activation energy in unirradiated materials is representative of a single kink rather than double kink energy. Experimental values of $2H_k$ for tungsten vary between 1.75 and 2.06 eV. Density functional theory calculates a value of 1.54 eV [177]. The activation energy measured by Giannattasio [131] was 1.0 eV. This value can obviously fit with a single kink energy if the higher measurement of the kink pair energy is correct. On the other hand, the dislocation dynamics modelling by Tarleton [133] shows that this energy can agree with the lower calculations of $2H_k$ if the effect of stress acting on the dislocation is taken into account as in equation 4.5.

A key result of the work Swinburne and Dudarev is that the BDT temperature will approximately double following neutron irradiation. This is a result of the activation energy increasing from H_k to $2H_k$ as the length between obstacles in an irradiated material is likely to be significantly below the critical length. This result clearly agrees with the trend generally observed in figure 4.17. However, this would be expected to be accompanied by a doubling in the measurement of activation energy.

This work is the only measure of activation energy of the BDT in a BCC metal before and after neutron irradiation. The result found was that the activation energy did not change as a result of neutron irradiation. This leads to the conclusion that, although the BDT temperature has approximately doubled, the cause is not that postulated by Swinburne and Dudarev. The measurement of an activation energy of 1.05 eV after neutron irradiation suggests that this corresponds to a kink pair energy, with the difference accounted for by the stress acting on the dislocation.

If the explanation postulated by Swinburne and Dudarev is taken to not apply in this case, then another reason for the large increase in BDT temperature is required. From the microstructural observations in chapter 3, it is clear that there is a high density of obstacles than are impeding dislocation motion, causing irradiation hardening. In particular voids and precipitates are present in the material at a density of around 10^{22} m^{-3} and are likely to act as hard obstacles to dislocations. These defect densities could be used in the model proposed by Li and Robertson [142] in order to calculate the expected increase in BDTT and determine if this model is capable of explaining the very large increase in BDTT observed.

4.4.5 The Effect of Grain Boundaries on Fracture Properties of Neutron Irradiated Tungsten

The results from four-point bend tests on W Neutron Poly presented in section 4.3.3 show that grain boundaries are having a significant effect on the fracture properties of neutron irradiated tungsten and near the BDT temperature inter-granular fracture is dominating.

Based upon results from four-point bend tests at $\dot{\varepsilon} = 3 \times 10^{-5}$ s^{-1}, the BDT temperature in W Poly Neutron appears to be 350 K lower than that in W Single Neutron. This is highly surprising given the BDT temperature before irradiation was very similar [22]. However, given the lack of ductile tests at other strain rates, and the very strange strain rate dependence of fracture behaviour in W Poly Neutron, it is too soon to conclude what the true BDT temperature is.

The cantilever test results show that the grain boundaries in W Poly Neutron have become very brittle. Small, un-notched, triangular cantilevers of the kind used here do not fracture in unirradiated or ion irradiated tungsten [120]. Investigations into fracture properties of tungsten have used pentagonal or rectangular cantilevers with large pre-notches in order to achieve fracture [178].

TEM analysis of this material carried out by Klimenkov [66] shows significant rhenium segregation to the grain boundaries in this material. This is likely to be contributing to the significant increase in brittle behaviour of this material.

4.5 Summary

The brittle to ductile transition in neutron irradiated tungsten single crystal has been fully characterised using nanoindentation strain rate jump tests and four-point bend tests at multiple temperatures and strain rates. These results show that the BDT temperature has increased by around 500 K. However, there has been no significant change in activation energy or activation volume. This strongly suggests that the kink pair mechanism that has been shown to control the BDT in unirradiated tungsten is still the controlling mechanism.

The reason for this large increase in BDT temperature without a change in control mechanism is somewhat unclear, however, it is likely to be related to the voids and precipitates described in chapter 3. These defects will limit the total length of mobile dislocation and reduce the deformation propagated after each kink formation.

Preliminary results from four-point bend tests on neutron irradiated polycrystalline tungsten appear to show a smaller increase in BDT temperature. However, the BDT could only be identified at one strain rate and testing at a second strain rate showed that the BDT temperature had increased with decreasing strain rate. This highly anomalous behaviour may be explained to a certain extent by the embrittlement of grain boundaries, identified through micro-cantilever testing. Further experiments are required to

establish what effect grain boundaries will have on the BDT in real-world materials.

5

Micro-Pillar Compressions in Ion Irradiated Tungsten

5.1 Introduction

Ion irradiation can simulate the displacement damage effect of neutron irradiation at significantly lower cost and avoiding the production of radioactive material. Chapter 3 highlights some of the difficulties in replicating the full spectrum of effects from neutron irradiation with ions, but there is still significant value to be gained from the information ion irradiation provides and better designed experiments may achieve a closer match between ion and neutron irradiation.

One of the main limitations of ion irradiation is the limited damage depth, typically a few microns. This is particularly acute in tungsten due to its high stopping power relative to lighter elements. As discussed in section 1.4, this drives a desire for novel testing techniques that can provide information regarding the mechanical properties of a material from a small sample volume. Currently nanoindentation is capable of providing hardness and modulus data but values beyond this such as yield stress and fracture properties are desirable. Additionally, there is interest in observing how the material deforms under different stress states to those imposed by indentation.

This project investigates in-situ micro-pillar compression as a technique for performing micro-mechanical tests on ion irradiated layers. The pillar production and in-situ testing were carried out at University of California, Berkeley thanks to funding from the Fusion CDT and Santander Academic Travel Award that allowed three months to be spent there.

5.2 Experimental

5.2.1 Micro-Pillar Preparation and Testing

Micro-pillars were prepared using a dual-beam focused ion beam microscope (FEI Quanta). The pillars were milled using 30 kV Ga^+ beam with a succession of decreasing currents, from 16 nA for outer trenches down to finishing with a 240 pA beam. A height of 6 μm tall and a diameter of 2 μm were aimed for during production of the pillars but the exact height and width of each pillar was measured using SEM. The average width of the pillars was 1.9 $\pm$ 0.3 μm with a taper of approximately 5°. The pillars had to be produced within a few microns of the edge of the sample so that the pillar could be viewed side-on through a milled-away section. At least 6 pillars were produced in each sample. An example pillar is shown in figure 5.1.

The pillars were produced parallel to the milling direction. As a result the pillar contains both irradiated (2 μm depth) and unirradiated material. The alternative was to cut and prepare a second face in the already irradiated sample, but it was considered that damage induced during metallographic preparation may affect the results.In W Single Unirr and Irr the pillars were prepared with the length of the pillar orientated along $\langle 100 \rangle$. In WRe Unirr and Irr the pillars were not orientated along any particular direction. The impact of the pillar height exceeding irradiation depth is discussed in section 5.6.1.

5.2.1.1 In-situ Compression of Micro-Pillars

The pillars were tested in-situ within the FEI Quanta to allow imaging of the test from two directions. A hysitron P-85 picoindenter was used to perform the compression. The displacement rate was 10 nm s^{-1}. The hysitron was calibrated using an air indent before each sample was tested in order to calibrate any loading resistance from the indenter and a PID control was used to maintain the target displacement rate. The width and height of each pillar was measured using SEM and used to calculate engineering stress and strain for each pillar compression.

5.2.2 Transmission Kikuchi Diffraction of Compressed Pillars

Lift-outs were made from compressed pillars using a similar method to that for preparing samples for TEM examination 3.2.2.1.

The FIB lift-out method is shown in figure 5.2, the energy of the beam used for the process was 30 kV unless otherwise stated. A platinum protective layer was deposited over the pillar, extending to either side in order to produce a cuboid that could be lifted out, measuring approximately 2 x 2 x 20 μm, using the gas injection system (GIS) and a 240 pA beam. Trenches were then milled from either side using a 16 nA ion beam. The lift-out volume was thinned and undercuts were made using a 2 nA beam.

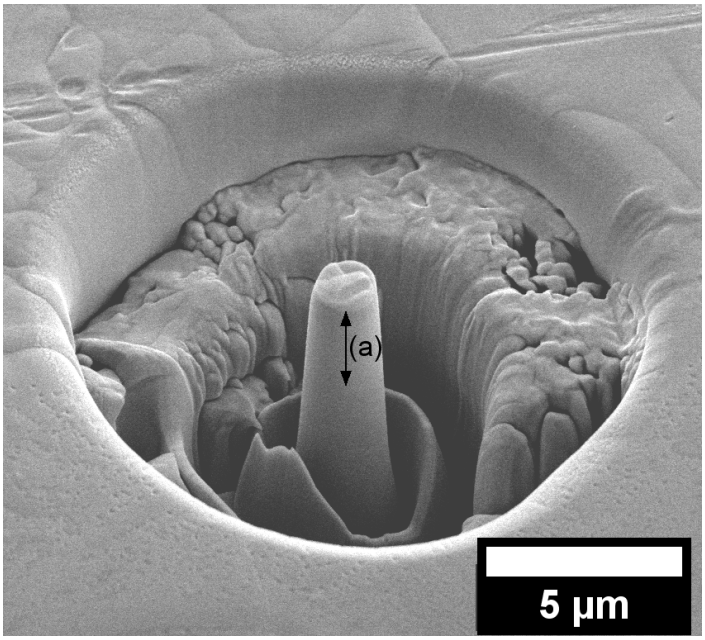

Figure 5.1: An example pillar after milling. The rings from milling using a sequence of decreasing currents can be seen around the base of the pillar. The arrow (a) indicates the height of the irradiated layer in ion irradiated samples.

A kliendiek micromanipulator needle was attached to the lift-out using platinum deposition before the undercut was completed to free the lift-out from the bulk sample. The sample was exchanged for a TEM grid and the lift-out was attached using platinum deposition. A window within the lift-out was then thinned using a succession of decreasing beam currents, with the lift-out at 2° to the incident beam in order to avoid milling of the platinum protective layer. The final thinning and cleaning of the sample was carried out using a 2 kV, 200 pA beam until the lift-out was transparent under a 10 kV electron beam.

These pillar lift-outs were then examined using a Zeiss Merlin FEG SEM with a Brucker EBSD system. The sample was mounted in a transmission Kikuchi diffraction holder with the cross-section of the pillar at 80° to the incident electron beam. With the sample mounted at this angle, forward scattered electrons were collected by the EBSD detector. Electrons that have exited the sample close to the Bragg condition relative to the crystal structure were diffracted resulting in Kikuchi bands [179]. These bands were indexed and used to determine the crystal orientation.

The orientation of the crystal was identified at each point in the cross-section and the misorientation across the sample was calculated using using MTEX [180]. The misorientation was indicative of strain within the material [181]. Advanced methods can be carried out to precisely quantify these strains but the main area of interest in this work was determining the location of strains in order to establish whether localised deformation had occurred.

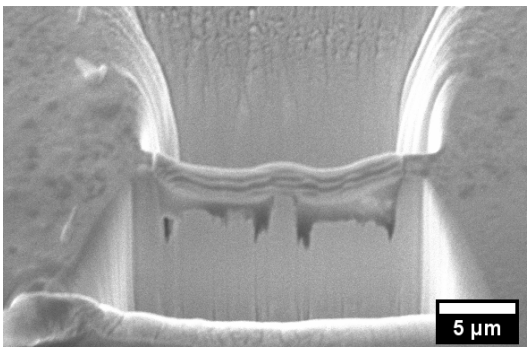

(a) Pillar with platinum layer deposited on top and trenches milled either side

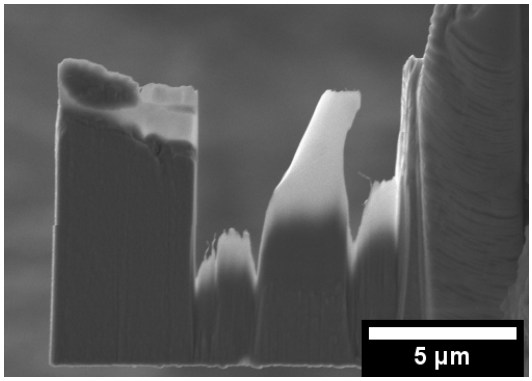

(b) Pillar attached to grid and thinned to transparency at 10 keV

Figure 5.2: Images showing the process of creating a pillar lift-out for Transmission Kikuchi Diffraction

5.3 In-Situ Pillar Compression

Micro-pillars were produced and tested in unirradiated and ion irradiated W single and W-1.4Re as described in section 5.2.1. At least five pillars were produced and tested for each sample. A small number of tests were stopped early due to the indenter hitting the edge of the tench around the pillar, but most were completed and provide complete loading and unloading curves. Images from the video recorded during pillar compression are presented below alongside load vs time graphs for each sample.

The pillars were tapered due to the FIB manufacturing process. The pillar was between 4 and 10°. This had the effect of concentrating stress and strain in the top portion of the pillar. Finite element modelling was used to investigate the extent of this effect and is discussed in section 5.5.

The W Single Unirr pillar images and graph (figure 5.3) show the initial elastic behaviour, a clear yield point and then steady plastic deformation. The continual increase in load after yield is likely due to the significant taper (around 10°) of this pillar. The initial contact between indenter and pillar is not completely flat. These two factors combined lead to large variability in the yield point observed in different samples. These errors decrease as strain increases due to the contact area between indenter and pillar becoming more constant. Section 5.3.1 discusses the accuracy of yield stress and flow stress measurements at different strains and how the testing data can be accurately interpreted.

Figure 5.4 shows an image of a pillar from W Single Unirr after compression. This image was taken as the indenter was retracting so the effect of vibration during scanning affects the image quality. However, a faint slip band can be observed to have formed, although the deformation localised along this band does not appear to be very large.

The W-1.4Re unirradiated pillar images show faint slips band appearing across at

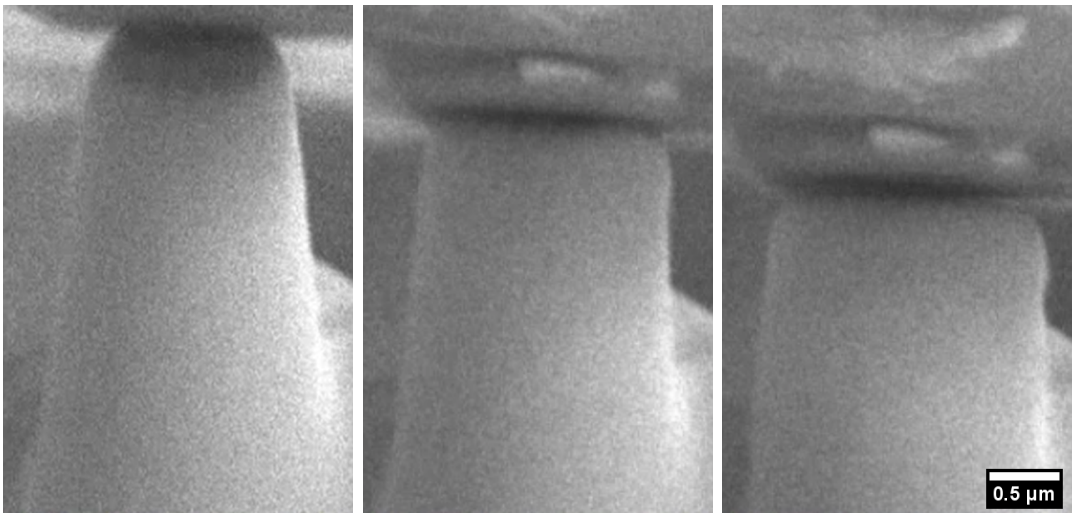

(a) t = 10 s **(b)** t = 60 s **(c)** t = 120 s

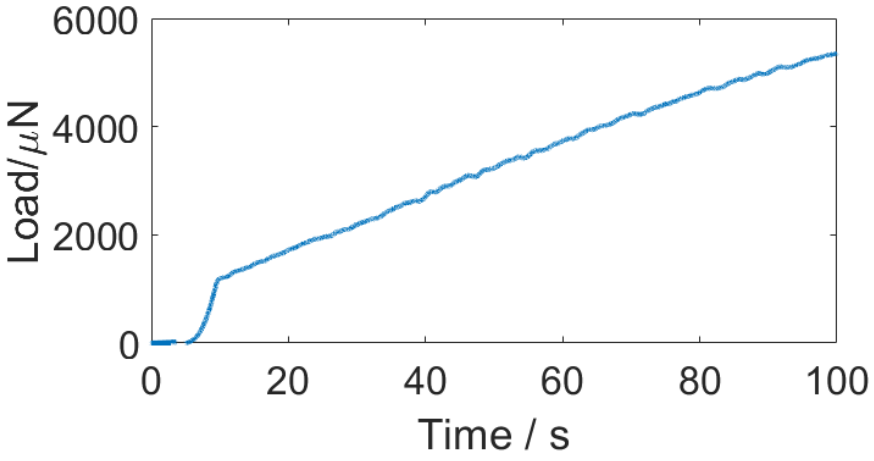

Figure 5.3: Images taken from video recording of pillar compression of W Single Unirr alongside load versus time data from the test

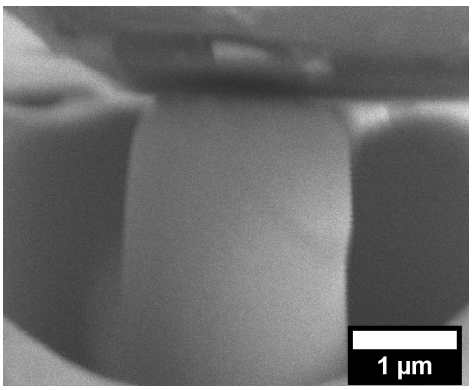

Figure 5.4: Post-compression image of W Single Unirr

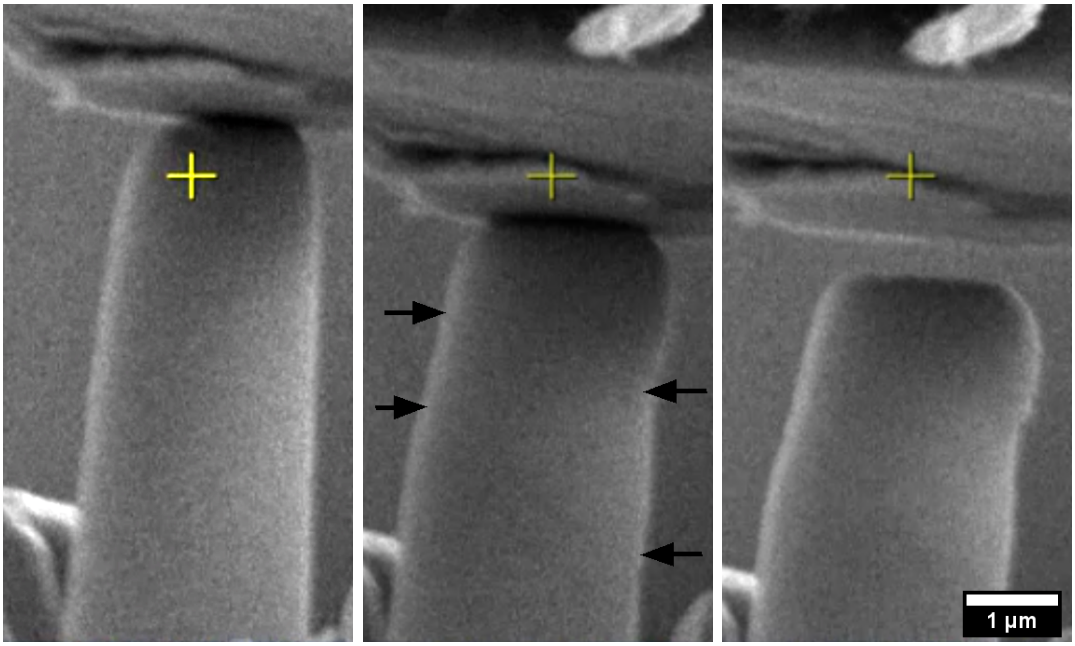

(a) t = 10 s **(b)** t = 60 s **(c)** t = 120 s

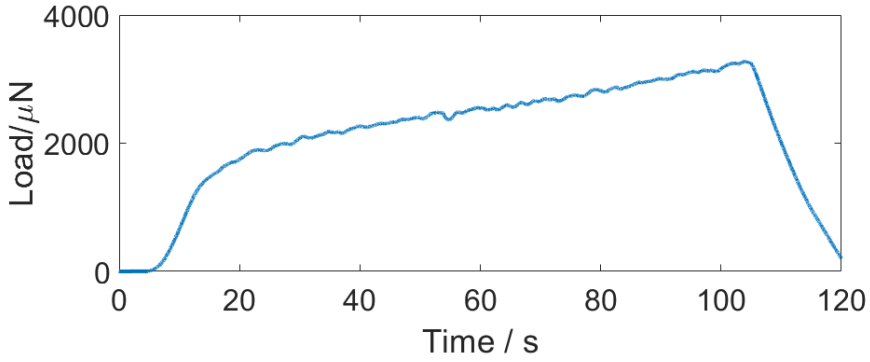

Figure 5.5: Images taken from video recording of pillar compression of W-1.4 Re Unirr alongside load versus time data from the test

depths of up to a few μm (highlighted by black arrows in figure 5.5. The appearance of these slip bands was gradual and were first noticeable around 30 s into the test. The post-compression images in figure 5.6 show three different pillars. In these, deformation along slip bands in multiple orientations can be observed. Again, no single slip band appears to show a large amount of deformation.

W Single Ion shows smooth deformation but increased slip band behaviour compared to the unirradiated samples (figure 5.7). No large load drops were observed in this sample during testing but larger slip bands were visible and appear to show more deformation localised to each band. This behaviour was very consistent as shown by the post-compression images in figure 5.8.

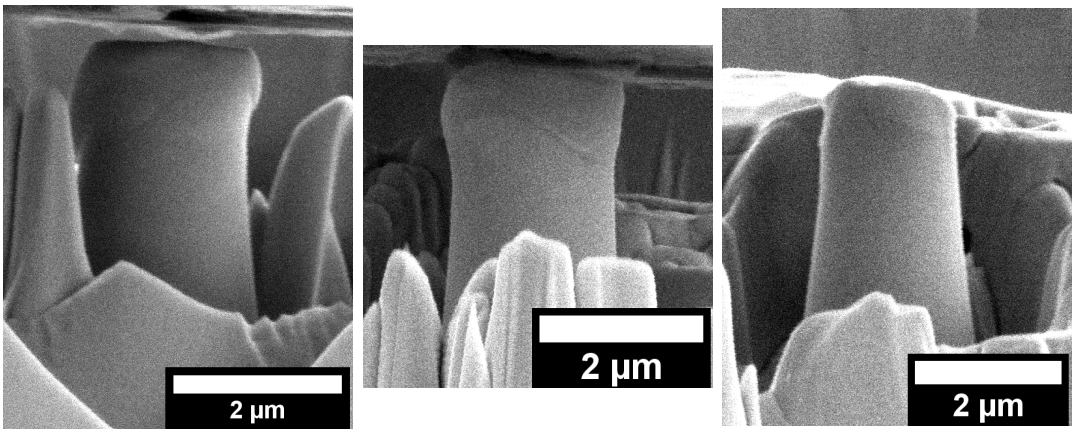

Figure 5.6: Post-compression image of W-1.4Re Unirr

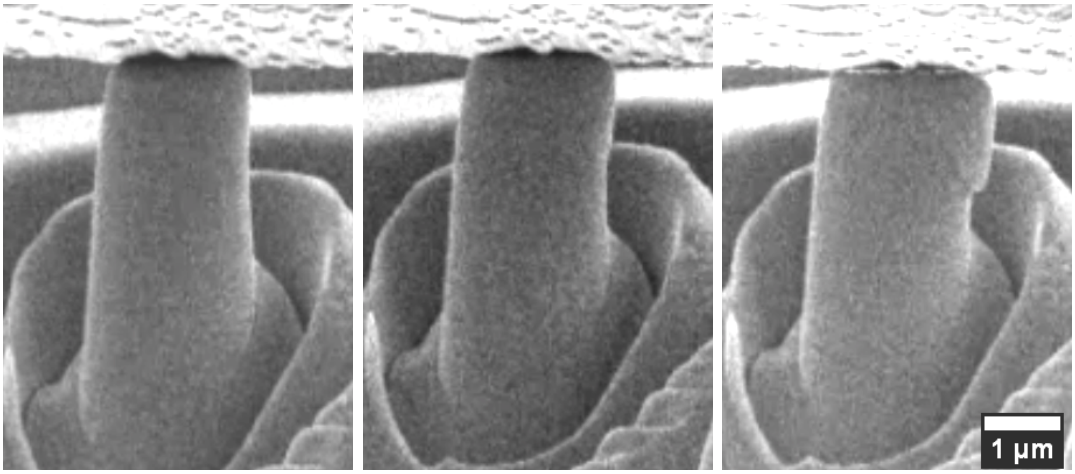

(a) t = 10 s **(b)** t = 60 s **(c)** t = 120 s

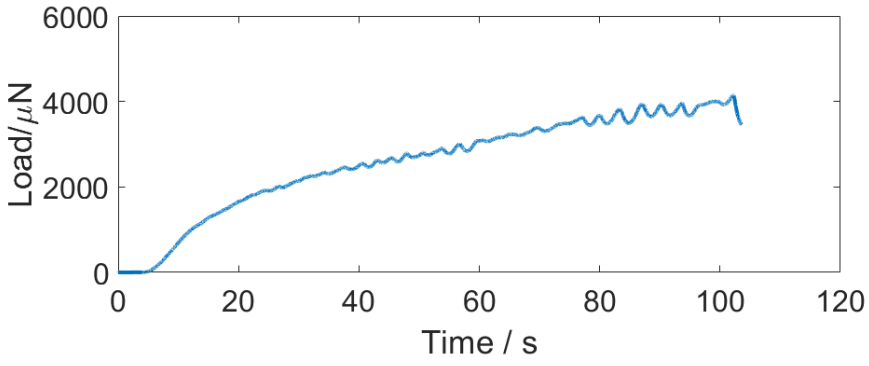

Figure 5.7: Images taken from video recording of pillar compression of W Single Ion sample alongside load versus time data from the test

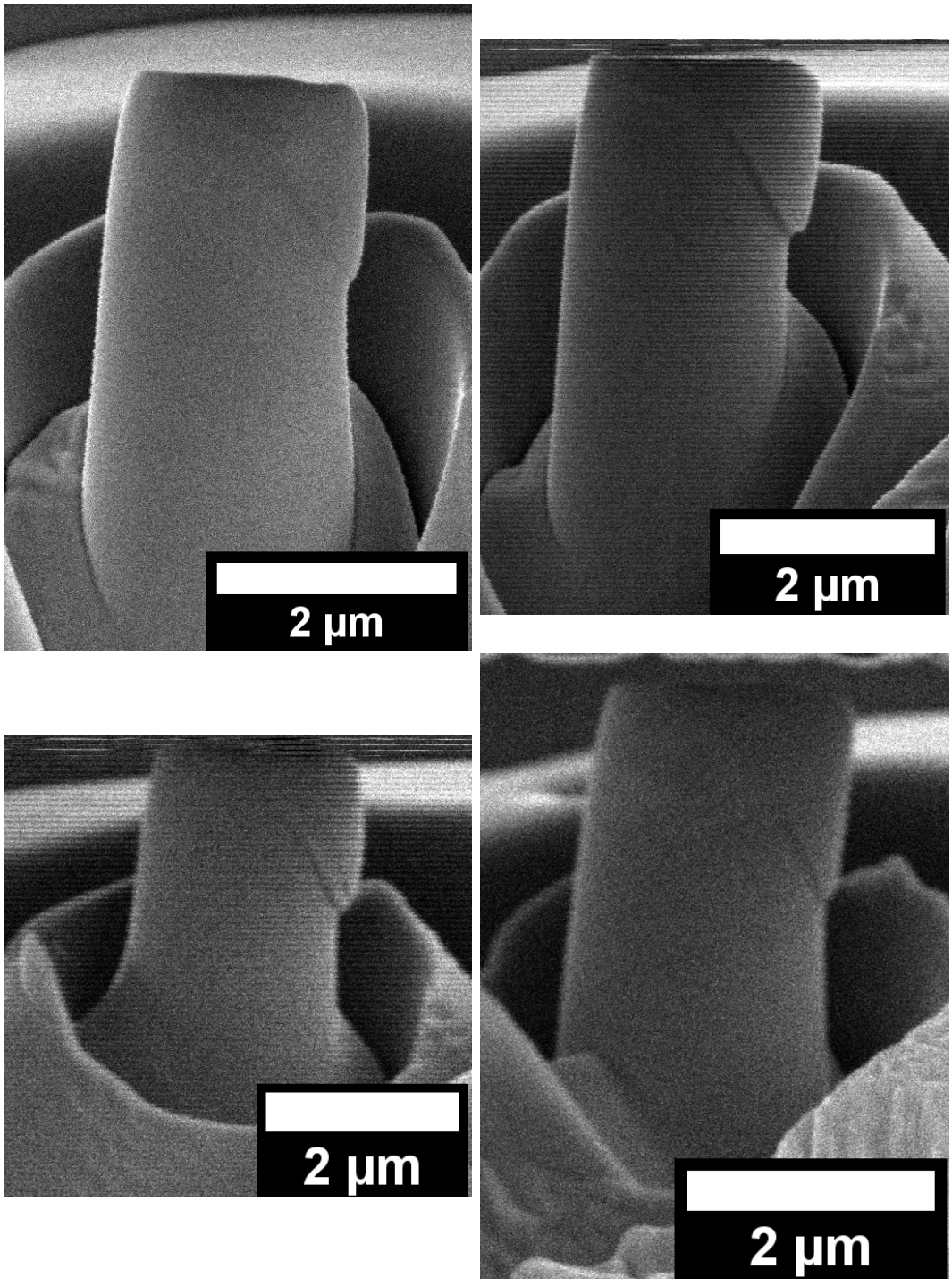

Figure 5.8: Post-compression images of pillars in W Single Ion

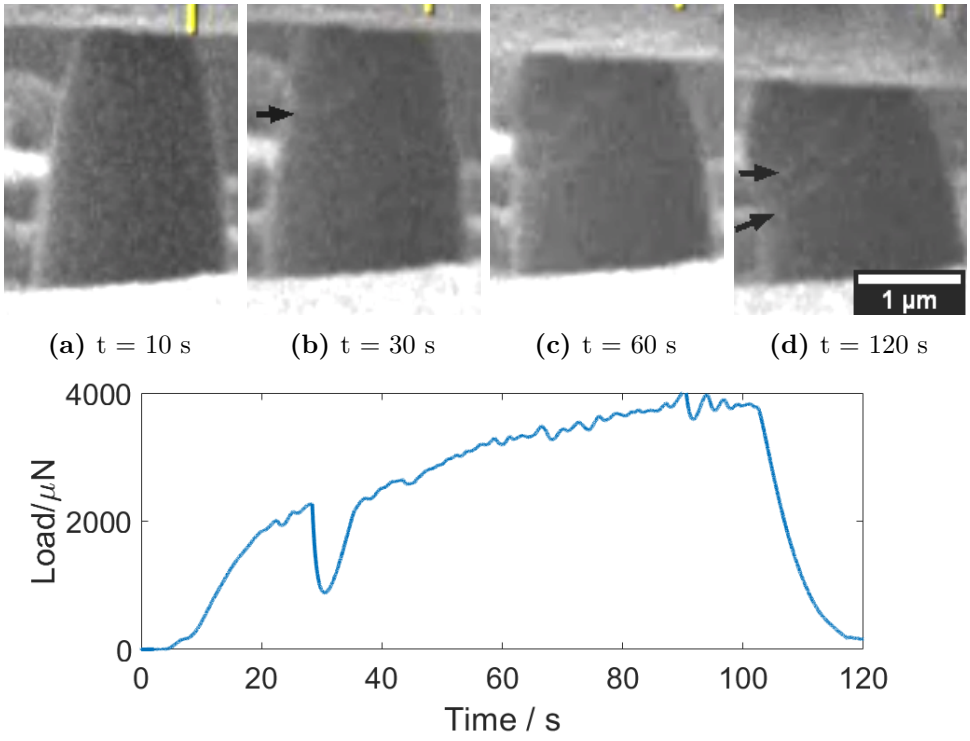

Figure 5.9: Images taken from video recording of pillar compression of W-1.4Re irradiated sample alongside load versus time data from the test. This sample is shown twice due to the high variability in behaviour of pillars in this material

W-1.4Re Ion showed distinctly different behaviour that varied from pillar to pillar so two images and graphs are included here (see figures 5.9 and 5.10). The first shows a steady increase in load until a single, large slip event occurred around 30 s (figure 5.9b). This event could be observed in the video as a slip band appears suddenly at the same time as the drop in load. This is indicative of a strain burst. The potential causes and importance of this behaviour is discussed in section 5.6.4. The second pillar from this sample shows an increase to a significantly high force before clear slips bands are observed to form, as shown in figure 5.10, corresponding to smaller drops in load than the first pillar. Some strain softening is observed to occur as well, with the flow stress decreasing after initial yield. This strain softening behaviour was observed in multiple pillars from this sample and in no other samples. Sharp clear bands showing large localised deformation can be observed in both of the pillars shown in figure 5.11. These demonstrate that deformation was more localised in this sample than any of the previous.

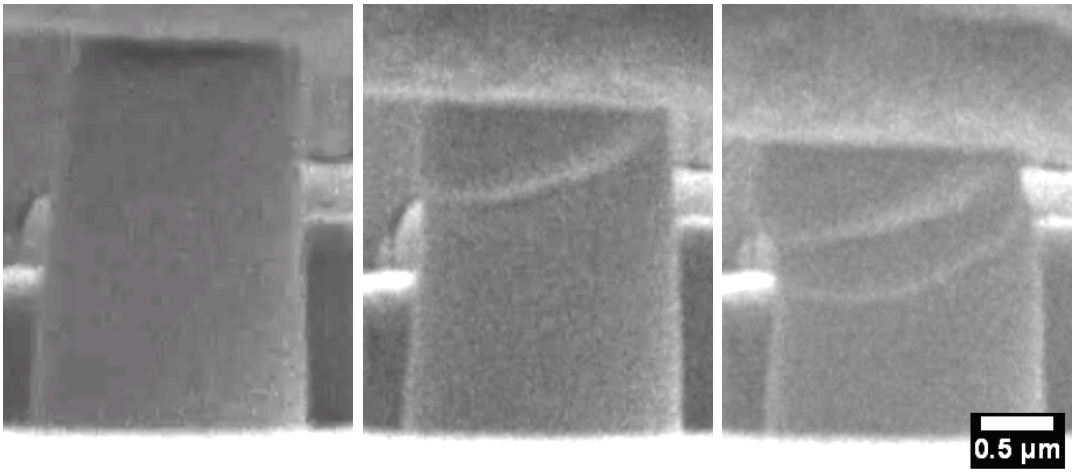

(a) t = 10 s **(b)** t = 60 s **(c)** t = 120 s

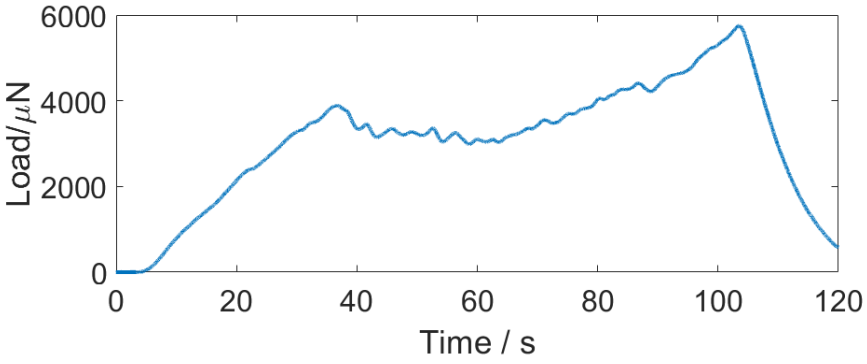

Figure 5.10: Images taken from video recording of pillar compression of W-1.4Re irradiated sample alongside load versus time data from the test. This sample is shown twice due to the high variability in behaviour of pillars in this material

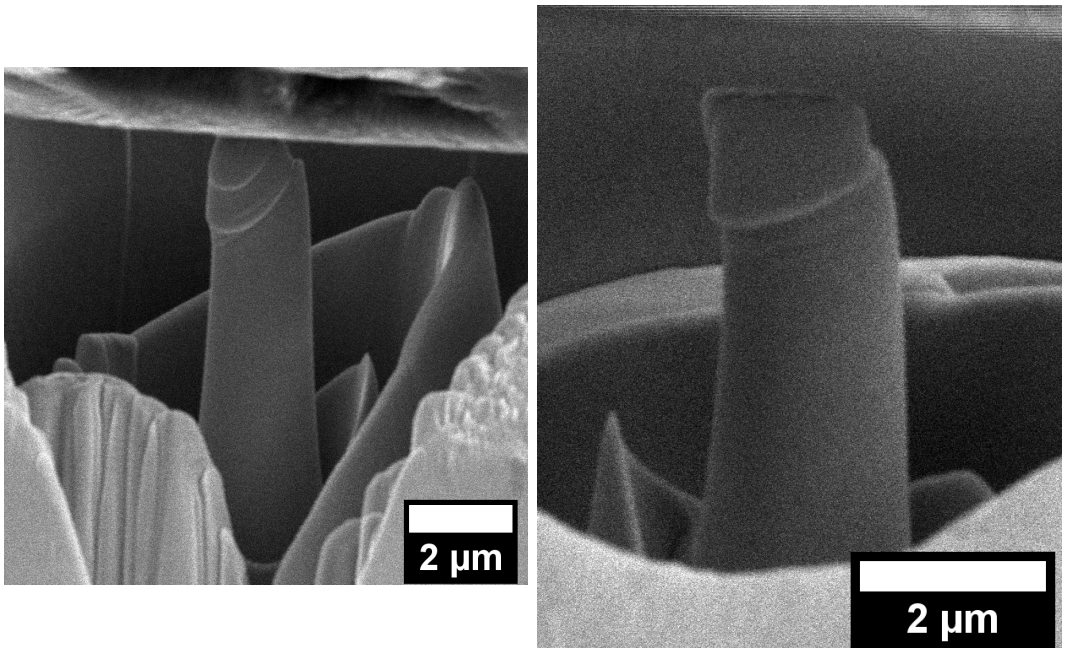

Figure 5.11: Post compression SEM images of W-1.4Re Ion

5.3.1 Stress Strain Data for Pillar Compression

The width and height of each pillar was measured for each sample prior to testing. These are then used to calculate the engineering stress and strain values. The yield stress was found to vary strongly between pillars in the same sample. This is likely to be due to initially poor contact between indenter and pillar, partly due to rounding of the top of the pillar during FIB milling. As a result yield stress is not calculated but instead flow stresses are used.

Graphs showing the calculated stress strain plots for each sample are presented in figure 5.12 and the mean flow stresses for each sample at 3 and 10 % strain are shown in figure 5.13. Due to the low initial contact area between indenter and pillar, the 3 % flow stresses are significantly lower than the 10% flow stress. By 10 % strain the indenter and pillar have formed good contact in all tests, resulting in a relatively low spread in flow stress values between pillars. This value was considered to be the best indicator of material properties.

Comparing the results for each sample, it is clear that the unirradiated materials show very similar behaviour. W Single Ion shows similar qualitative behaviour, but at slightly increased stress throughout the test. W-1.4Re Ion, however, shows substantially different behaviour. Not only does it have significantly higher flow stresses than the other samples but the stress strain curves show unusual features.

The first feature that becomes apparent is the variability between tests, with a very large spread in flow stress at all strains. This may be due to microstructural features within these samples that are non-homogeneously distributed on the scale of the pillars. The second feature is the drops in load during the test, that are most likely due to strain bursts. Small strain bursts can be seen in some pillars from each sample but only W-1.4Re irradiated showed drops > 10 % flow stress. This sample also showed work softening in several pillars, with flow stress decreasing with increasing strain, for at least some portion of the test. These unusual features are discussed in section 5.6.4.

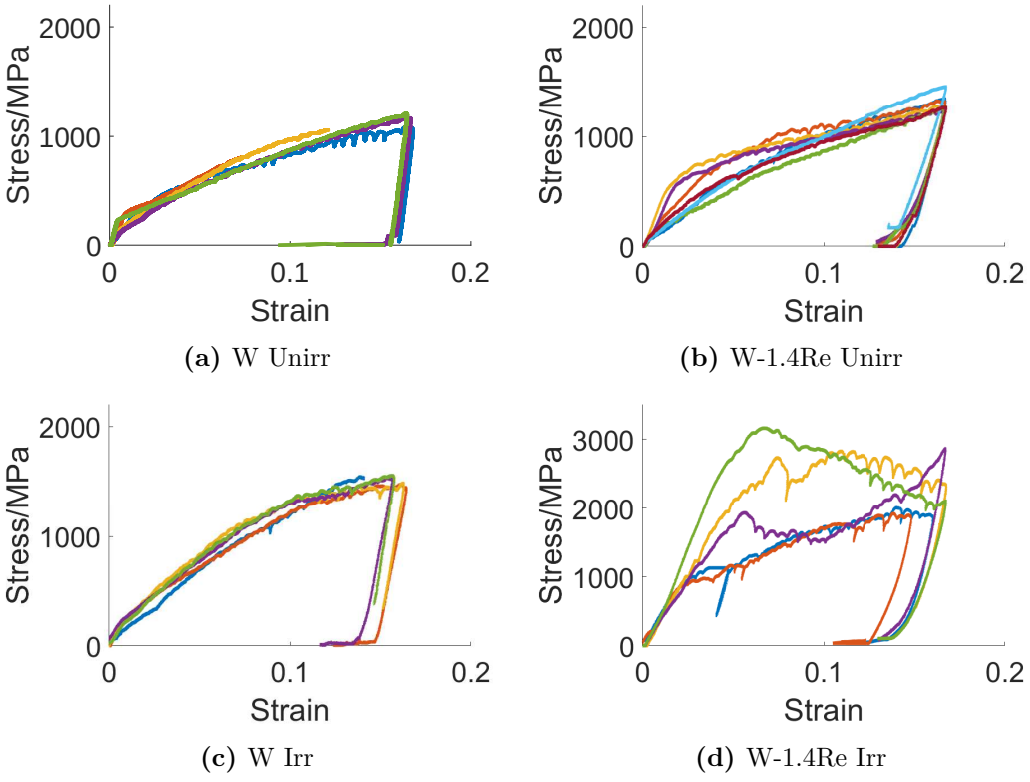

(a) W Unirr **(b)** W-1.4Re Unirr

(c) W Irr **(d)** W-1.4Re Irr

Figure 5.12: Stress strain graphs for micro-pillar compressions of each sample

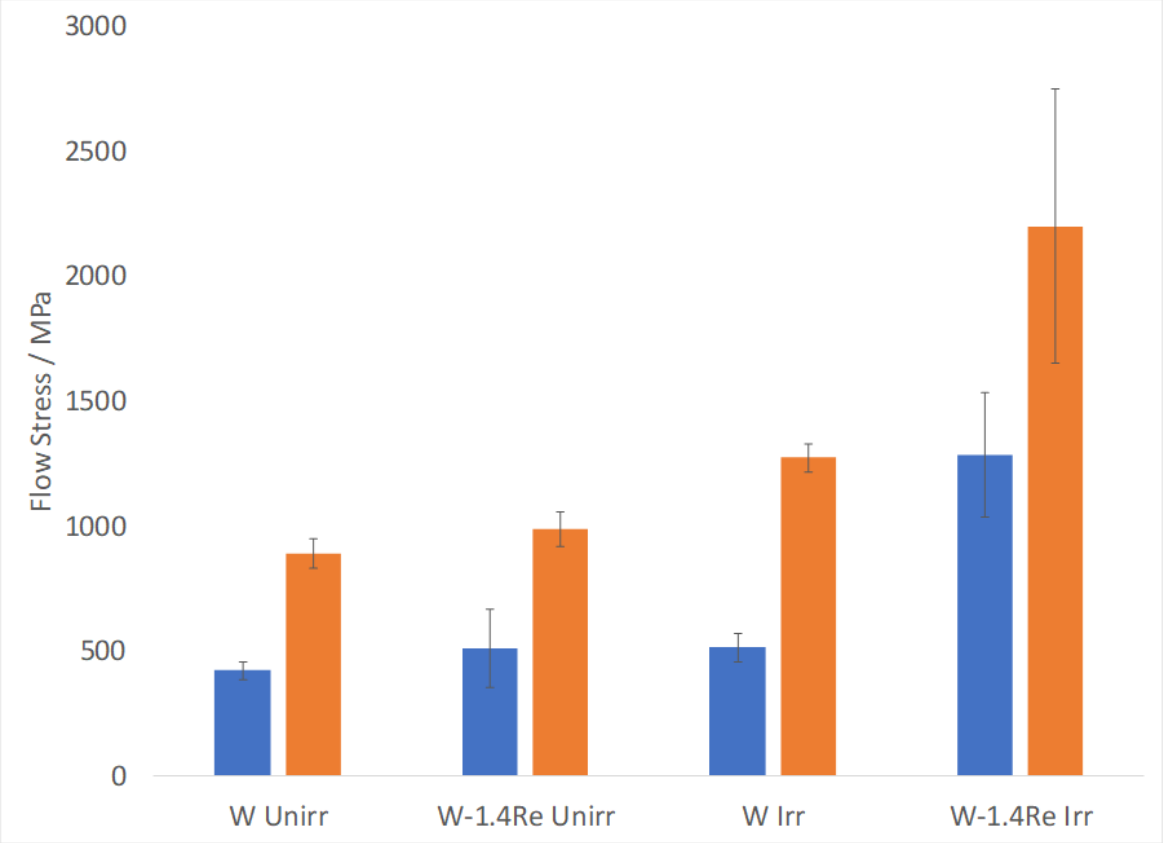

Figure 5.13: Mean flow stress for each sample measured at 3% (blue) and 10% (orange) strain

5.4 Transmission Kikuchi Diffraction

After compression, cross-section lift-outs of the pillars were made and analysed using TKD as described in section 5.2.2. This allowed for measurement of the misorientation induced by deformation. For each sample a map and a line scan of the misorientation is shown, alongside a SEM image showing the locations of the scans.

W Single Unirr (figure 5.14) shows high misorientation near the very tip of the pillar, then another jump in misorientation around 2 μm down the pillar. There is an area of low band contrast in between, where misorientation could not be measured, that may be indicative of slip bands in this region. While the misorientation does appear to be concentrated in two regions, these are each around 0.5 μm in length. The high change in misorientation between 2 and 3 μm corresponds to a section of the map that had a low success rate. This may indicate large amounts of localised deformation in this region.

W-1.4Re Unirr sample (figure 5.15) has curled up during the thinning process, leaving some uncertainty as the the extent of misorientation from deformation and that from the angling of the sample area with regards to the detector. However, the line scan was taken from the flatter side of the pillar and shows that the misorientation was concentrated in the top 1 μm of the pillar. A high number of slip bands can also be observed in both the misorientation map and the SEM image. These are associated with a gradual gradient on the line scan, suggesting that each of these slip bands contributes a small amount to the total misorientation.

The TKD scan of W Single Ion (figure 5.16) fails to show significant misorientation near the top of the pillar. This is surprising as the videos from during the testing of pillars and post-compression images on this sample show slip bands appearing in the top micron of the pillar. Unfortunately a second lift-out could not be made from this sample so it is unclear if this TKD scan is representative of all the pillars in this sample. The pillar overall shows much lower misorientation than the other samples, again the reason for this is unclear. It is possible that the low taper of this pillar has led to deformation much deeper than in other tests. Alternatively the top of the pillar may have been lost during lift-out preparation as no platinum is visible and the TKD map shows an unexpected shape along the top edge.

The W-1.4Re Ion line scan (figure 5.17) shows a very high misorientation gradient near the surface. The pillars on this sample were damaged in transit before TKD lift-outs could be produced. As a result the total deformation will be greater than that imposed during the test. This may explain the large drop in misorientation at one point along the pillar, which was not observed in the other samples.

The TKD scan does show that the deformation was concentrated near the top of the pillar, which matches the observations from the testing video and images. The total angle of misorientation is similar to that observed in W Single Unirr and W-1.4Re Unirr. This sample has a relatively high number of uncharacterised spots, possibly due to strong local deformation in these areas. There are also sharp jumps in the line scan. This is likely to be indicative of slip bands were large strain has occurred.

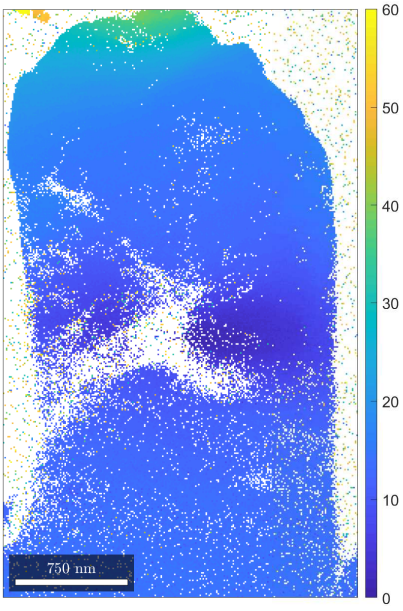

(a) Misorientation map, the colour bar indicates misorientation in degrees

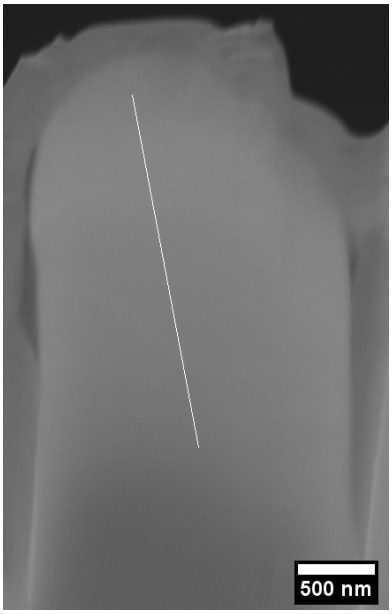

(b) SEM image showing locations of scans

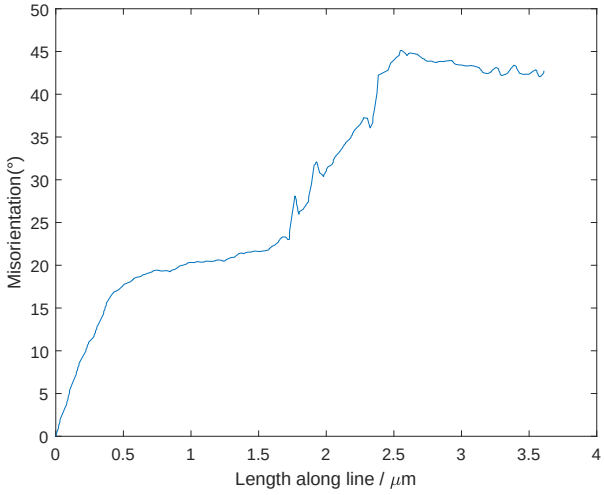

(c) Misorientation from line scan (location shown in (b))

Figure 5.14: TKD results from post-compression imaging of a pillar from W Single Unirr

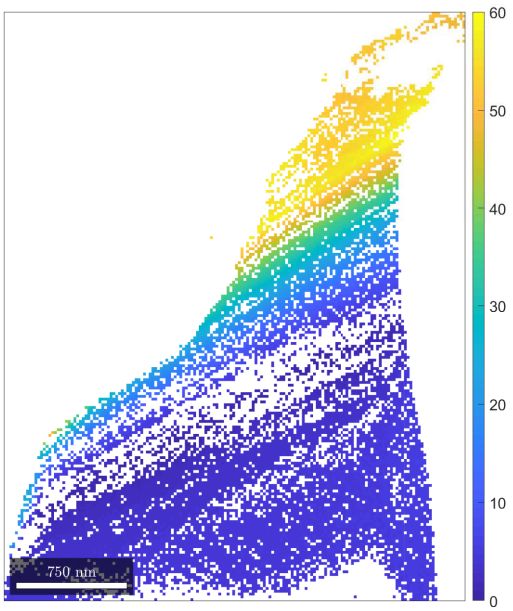

(a) Misorientation (°) map

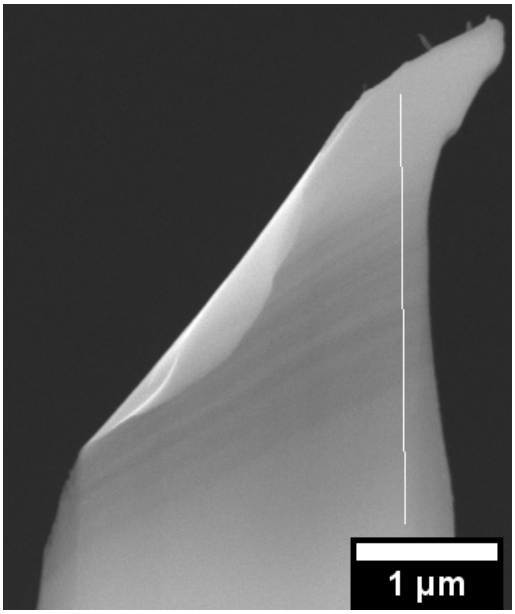

(b) SEM image showing locations of scans

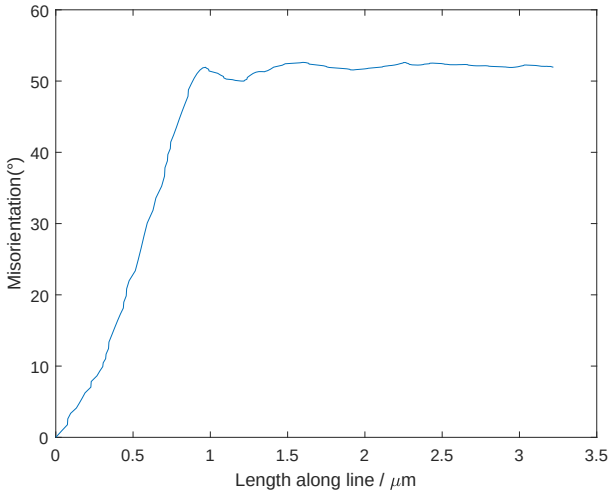

(c) Misorientation from line scan (location shown in (b))

Figure 5.15: TKD results from post-compression imaging of a pillar from W-1.4Re Unirr

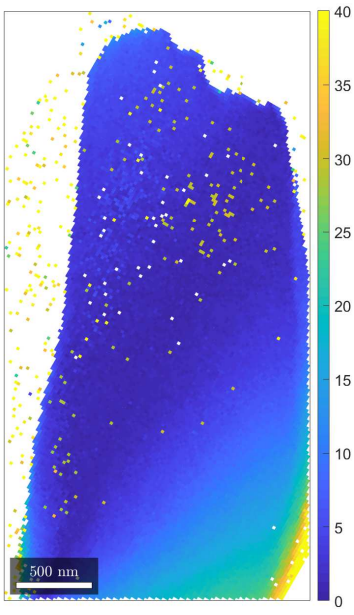

(a) Misorientation (°) map

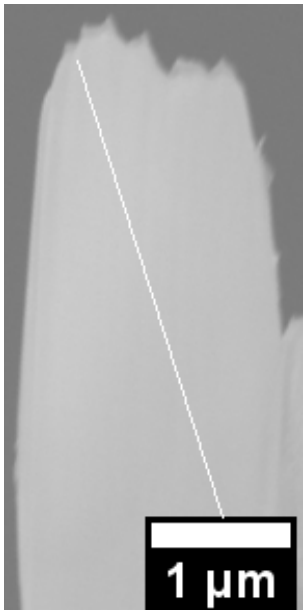

(b) SEM image showing locations of scans

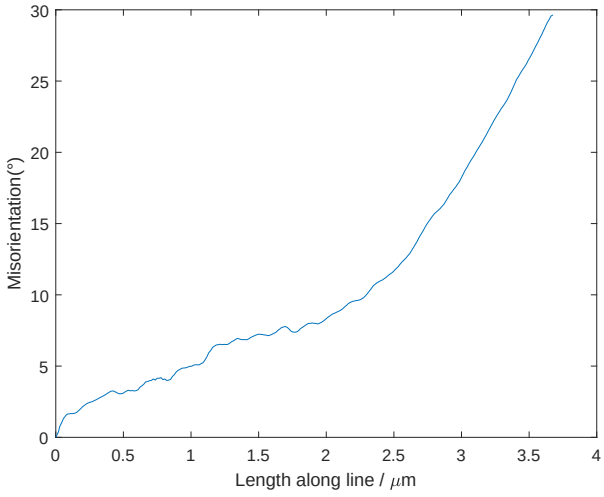

(c) Misorientation from line scan (location shown in (b))

Figure 5.16: TKD results from post-compression imaging of a pillar from W Single Ion

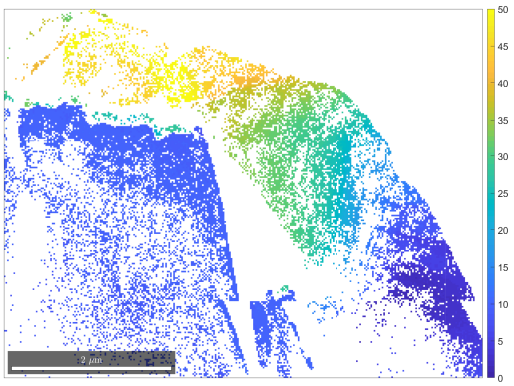

(a) Misorientation (°) map

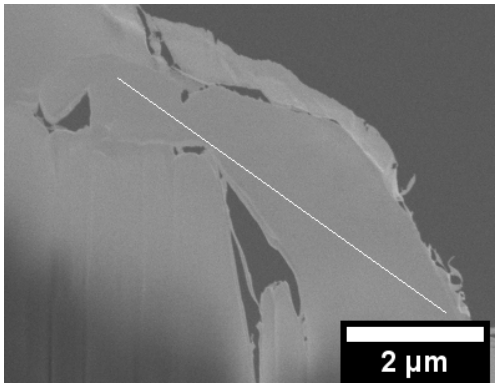

(b) SEM image showing area of scan

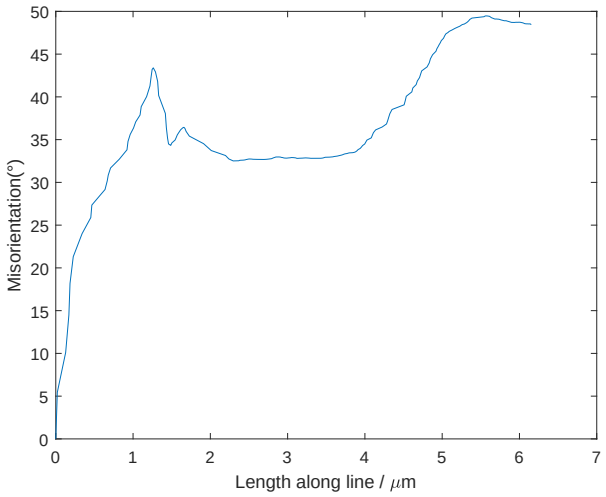

(c) Misorientation from line scan (location shown in (b))

Figure 5.17: TKD results from post-compression imaging of a pillar from W-1.4Re Ion

5.5 Finite Element Modelling (FEM)

Abaqus was used to produce finite element models of the tapered pillars in order to determine the effect that the taper had on the stress and strain distributions. Pillars were made with 0, 5 and 10 ° tapers. The pillar material was programmed with the elastic modulus and flow stress values as a function of strain for tungsten. It was anchored at the bottom of the pillar with no displacement or rotation allowed at this point. A uniform pressure was applied to its top surface. The stress and strain distributions from this model are shown for each taper angle in figures 5.18, 5.19 and 5.20.

These results show the expected result of increasing concentration in stress and plastic strain towards the top of the pillars as the taper angle increases. This is particularly important for this work as one of the key areas for investigation is the effect of irradiation damage on dislocation behaviour in tungsten. As a result it

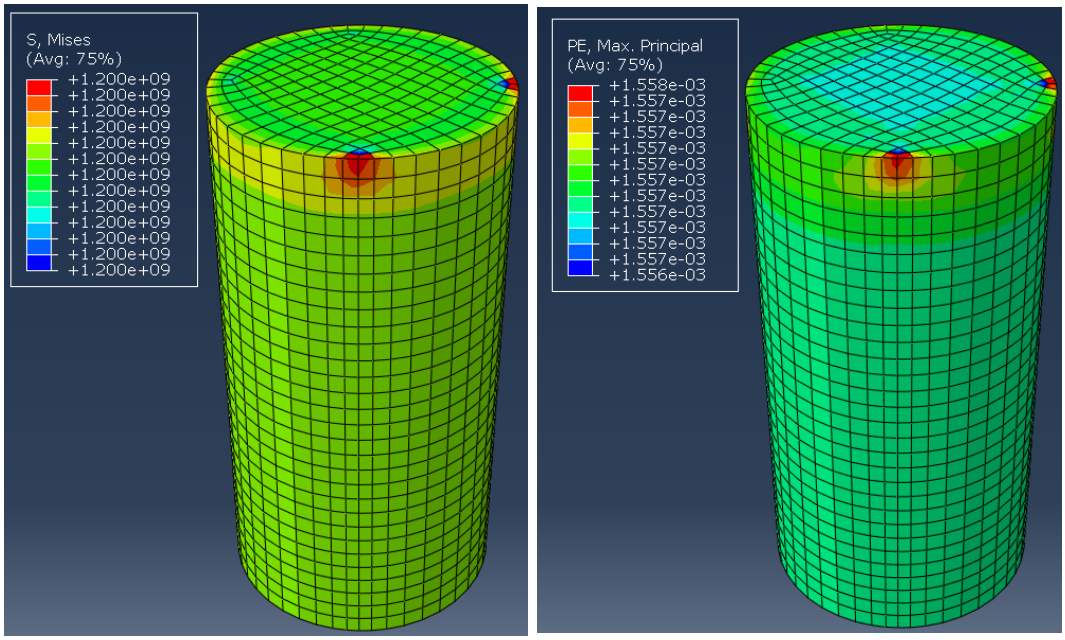

(a) Von Mises stress **(b)** Plastic Strain

Figure 5.18: Finite element model of a cylindrical pillar showing near-uniform stress and plastic strain throughout the depth of the pillar

is critical that the plastic deformation of the pillars was limited to the irradiated layer near the top of the pillar.

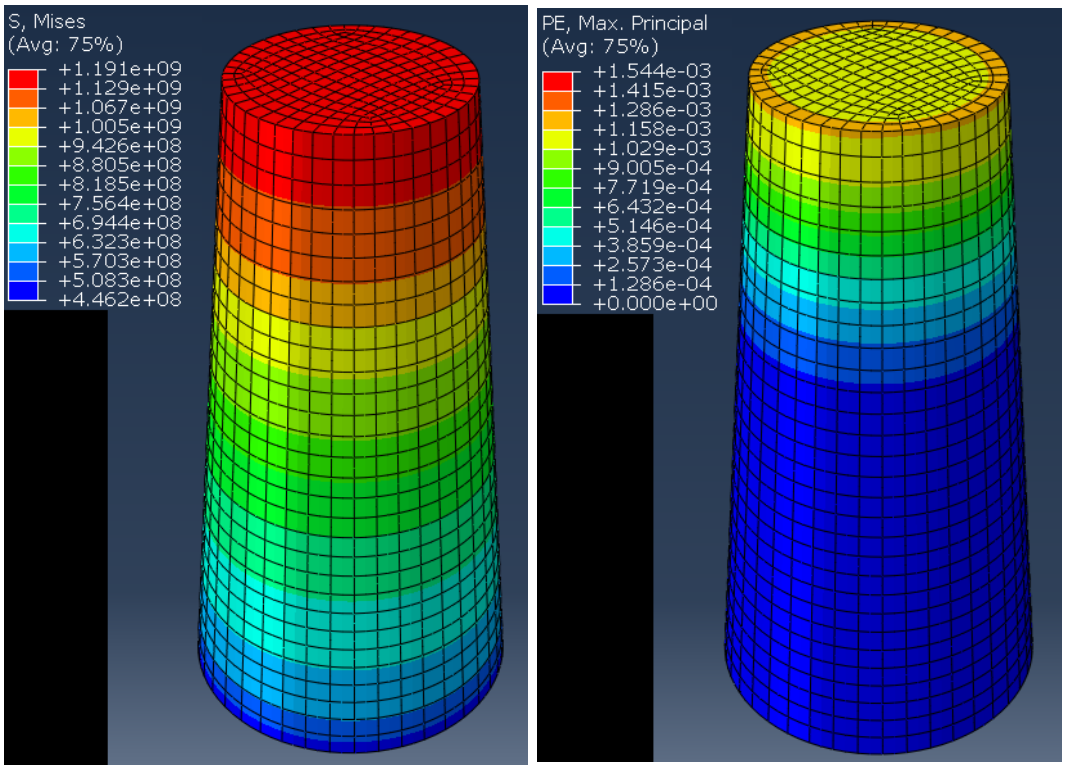

(a) Von Mises stress **(b)** Plastic Strain

Figure 5.19: Finite element model of a pillar with 5° taper showing the stress and plastic strain concentrated at the top of the pillar

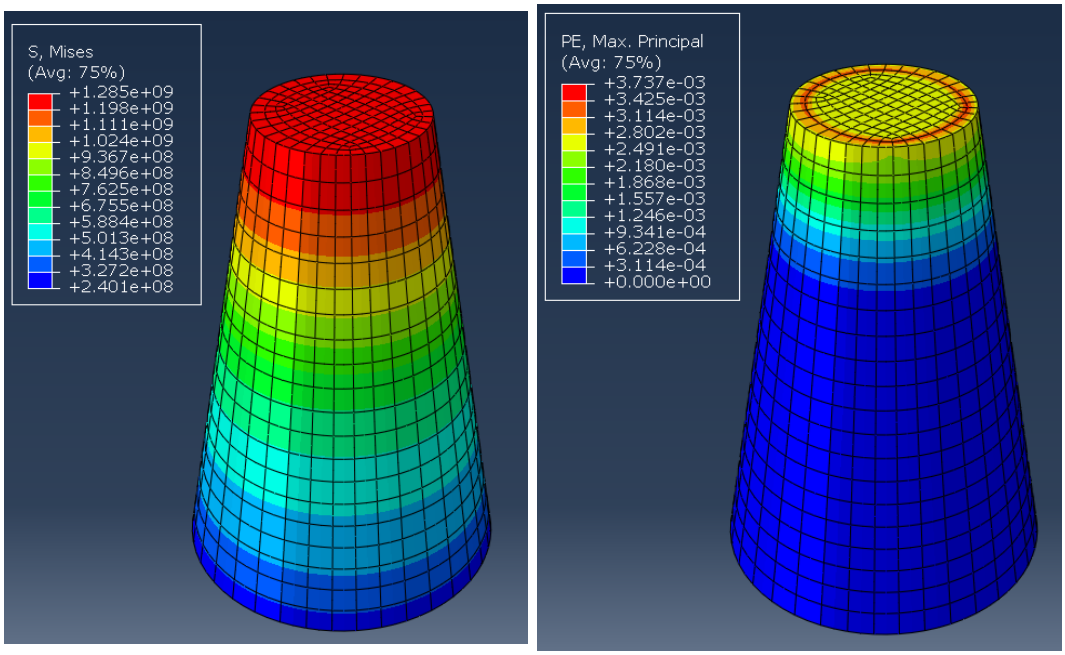

(a) Von Mises stress

(b) Plastic Strain

Figure 5.20: Finite element model of a pillar with 10° taper

5.6 Discussion

5.6.1 Irradiation Depth and Tapered Pillars

One key aspect to investigate in this micro-pillar compression experiment was whether the pillars being of greater length (6 μm) than the depth of the irradiated layer (2 μm) had a significant impact on the key measurements made. There are several pieces of evidence that deformation is localised to the top region of the pillar, and so the irradiated volume is dominating the results.

Firstly, the evidence from the in-situ recording of the pillar compression shows deformation occurring only in the top few microns of the pillars. Slip bands and movement of material is observed in this region and not in the visible sections of the pillar lower down. In W-1.4Re Ion, these slip bands are observed to coincide with large jumps in displacement, suggesting that these are responsible for the majority of the deformation observed.

Secondly, the measured flow stresses are higher in both irradiated materials than the unirradiated. This shows that the irradiation damage is affecting the mechanical properties, which indicates that the irradiated layer is dominating the deformation behaviour.

Finally, the FEM models show the effect of the tapered pillar shape on the stress and strain distributions. With a five degree taper (similar to the lowest measured in the experiment), the Von Mises stress has dropped to a third of its peak value by midway down the pillar. This has a dominant effect on the plastic strain, which is the main property being investigated in this experiment. The plastic strain clearly initiates in the top third of the pillar. With the maximum ten degree taper this effect is even more pronounced. While FEM is not accurate at modelling mechanical properties on this scale, these equation-based predictions for stress and corresponding yield are reflected in observations from in-situ recording and TKD.

5.6.2 Comparison to Work on Unirradiated Tungsten

Kim et al. [125] also measured micro-pillar compression in single crystal tungsten for pillars below 1 μm in diameter orientated along [100]. These pillars showed yield stresses above 1000 MPa and a strong size effect, with yield stress deceasing with increasing pillar size. The size dependent power-law (m = 0.42) determined predicts a flow stress $\approx$ 800 MPa for pillars with diameter of 2 μm. This is significantly higher than the flow stress measured at 3% strain in this work but similar to the flow stress measured at 10% strain.

This difference is likely due to low initial contact between pillar and indenter. As a result the 3% flow stress is not an accurate measure of material property. However, by 10% strain it is likely that the pillar and indenter are now in good contact and accurate measurements are being made. This is verified by the result

agreeing with the work by Kim.

The work by Kim includes one image of a post-test tungsten pillar, which had a diameter ≈ 500 nm. Multiple slip bands are visible, all near the top of the slightly tapered pillar, but one has significantly larger deformation than any others. This is likely caused by the pillar having a diameter below one micron. Their results also showed large strain bursts in the smaller pillars (d ≈ 250 nm). The strain bursts decreased in size with increasing pillar size, to the point where a 823 nm pillar showed also smooth deformation.

This observation matches with the smooth deformation observed in 2 μm diameter pillars in unirradiated W and W-1.4Re. It is also interesting that the irradiated pillars in this work behaved similarly to much smaller pillars in the work by Kim, with large strain jumps and clear slip bands appearing, particularly in irradiated W-1.4Re. This suggests that a similar strengthening mechanism that contributes to the size effect in small pillars is acting in larger pillars in irradiated material.

Schneider et al. [182] also tested tungsten pillars aligned along [100] with diameters ranging from 200 to 5000 nm. They observed much higher flow stresses and a lower size effect (m = 0.21) than Kim et al. The reason for this is unclear. Schneider measured an approximately flat flow stress for 2 μm diameter pillars of around 2000 MPa for 2 to 15 % strain, approximately double the 10% flow stress measured in this work. Their results again show large strain jumps in small pillars and smoother plastic deformation in pillars with d > 1 μm.

These results show that strain bursts are encouraged by smaller pillar sizes. Unirradiated pillars > 1 μm in diameter in tungsten do not show significant strain burst behaviour.

5.6.3 Comparing Pillar Compression with Nanoindentation

The flow stresses from micro-pillar compression are compared to the hardness measurements from chapter 3 in figure 5.21. Hardness is approximately equal to three times the yield stress, so the flow stresses have been multiplied by a factor of three for this figure. It is clear in this figure that 3x the flow stress underestimates the measured hardness. Grieveson et al. [126] also found similarly large difference between flow stress and hardness in pure iron and the size-law from Kim et al. [125] predict a bulk yield stress much lower than the textbook values for tungsten. This suggests that micro-pillar compression may routinely underestimate yield stresses of materials, although the reason why is unclear. There are a couple of possible explanations that apply to this work in particular.

Firstly, the test depth is smaller in the nanoindentation measurements, where hardness values were calculated between 200 and 700 nm depth. By comparison 10% strain in the micro-pillars is at a depth of 600 nm. The hardness measurement decreases by 1 to 2 GPa for each sample between 200 and 600 nm so this may be contributing to the difference. If larger indents could be carried out on these samples, lower hardnesses

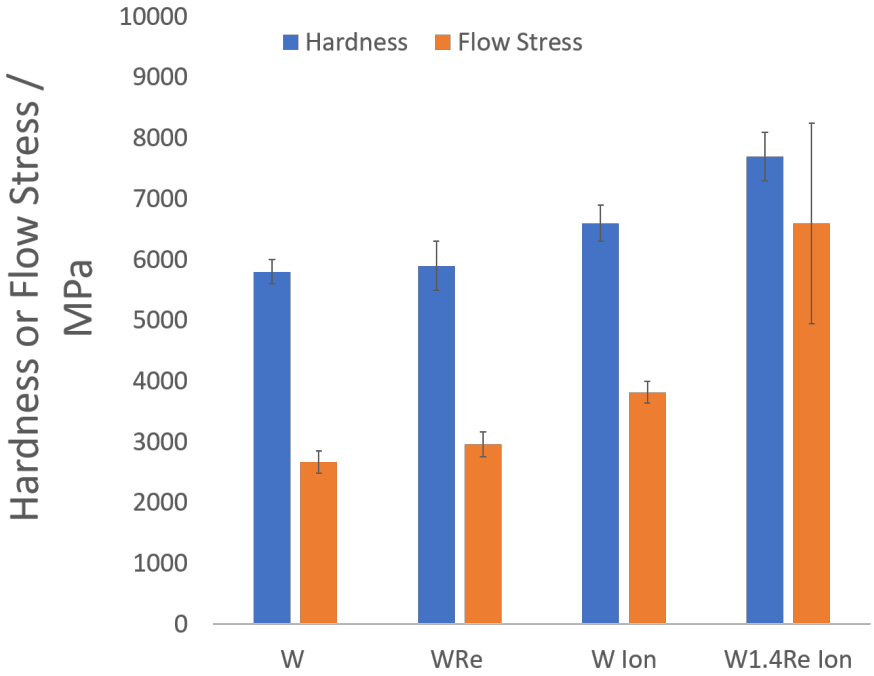

Figure 5.21: Comparing indentation hardness (200 - 700 nm) with 3x the pillar flow stress at 10% strain

would be expected as 700 nm is still well within the size effect region.

Secondly, the contact area between the indenter head and the pillar is clearly increasing as a function of depth due to the flat surface of the indenter not being completely parallel to the slightly-curved top of the pillar. As a result, even with in-situ measurements of the width of the pillar at the depth where slip bands can be observed, there may be significant plastic strain near the indenter head that is being underestimated.

The small height of the pillars (6 μm) results in a large region under the pillar being subjected to low stress. As a result micro-pillars cannot be used to accurate probe elastic properties; estimating the Young's Modulus from unloading curves from pillar compression would give a result of the order of 10 GPa, compared to 410 GPa from nanoindentation.

With these errors in the absolute size of mechanical properties, it is clear that micro-pillars are most appropriate for carrying out comparative and qualitative studies. Due to the interest in comparing unirradiated and irradiated material in this case, and the capability of in-situ testing to give additional insight into deformation mode, there is still much that can be uncovered from these results.

5.6.4 Effect of Ion Irradiated on Pillar Deformation

The damage characterised in chapter 3 is clearly having a strong effect on the flow stress and deformation behaviour of the micro-pillars. The flow stress at 10% strain was observed to increase significantly in both W Single and W-1.4Re following ion irradiation. This is an indicator that the damage induced is making dislocation motion through these materials more difficult.

There is a difference, however, in the behaviour change between W Single and W-1.4Re after irradiation. Both irradiated samples showed increased slip localisation with large, distinct slip bands appearing during the tests. However, the appearance of slips bands in W-1.4Re Ion was sudden and associated with load drops in the stress-strain curve, while they appeared gradually in W Single Ion and no large strain drops were observed. This demonstrates that the rhenium clustering caused by ion irradiation is having a strong effect on dislocation behaviour.

The only other self-ion irradiation micro-pillar compression study was carried out by Grieveson et al. [126]. Grieveson et al. [126] found that ion irradiation of iron inhibited strain bursts using stress-control test. This is the opposite behaviour to the results found in this work where it was found that irradiation damage promoted strain bursts in W-1.4Re. However, the mechanical tests in this work were carried out under strain-control (made clear by load drops during testing). This difference in control mechanism may be affecting the deformation behaviour of the pillars.

For example, Reichart et al. [127] investigated proton beam irradiated 304 stainless steel using similar sized pillars to those used in this work and by Grieveson. This was carried out using strain-control and the results was that strain bursts were encouraged by irradiation damage.

This difference in behaviour depending on loading condition matches work carried out by Cui et al. [128]. Cui observed that irradiation damage has been found to inhibit or promote strain bursts in different materials under different test conditions and explained these differences through molecular dynamics modelling. One of their key observations was that irradiation damage inhibits strain burst under stress-control conditions. Cui found that strain bursts can be promoted or inhibited by irradiation damage in strain-controlled conditions.

The relatively large size of micro-pillars in this work (d $>$ 1 μm) reduces the probability of strain bursts [183], as it is more likely for there to be a dislocation able to move or an active dislocation source when the standard activation stress is reached. In the model developed by Cui, for a strain burst to occur, a higher activation stress (above that usually required for dislocation motion) must be applied without dislocation motion occurring. A dislocation must then become active at some critical stress value. This dislocation will move through the material and leave the pillar. As it moves it will create additional sources that will generate more dislocations until the sources are exhausted by the decreasing stress level. These generated dislocations will also move through the material, resulting in the observed strain burst.

Applying this understanding of the model to this work leads to some interesting conclusions. Firstly, it is clear that the irradiation damage present in W Single Ion (dislocation loops d $\approx$ 5 nm) is not sufficient to increase the activation stress enough to cause large strain bursts in pillars of this size. Carrying out tests on smaller pillars in this material may produce large strain bursts.

Secondly, the irradiation damage present in W-1.4Re Ion is sufficient to drastically reduce dislocation mobility. This then results in high activation stresses that can produce the observed large strain bursts. It is unclear whether it is the higher density of small dislocations or the presence of rhenium precipitates that is causing this behaviour. Some pillars in this sample showed a very high initial flow stress that decreased with increasing strain (work softening). This behaviour is explained by Cui as the effect of dislocations sweeping away damage, making it easier for future dislocations to pass through the material.

Cui models pure materials and the defects present in them (only interstitial loops for BCC materials). As a result that model does not have any consideration of the effects of precipitates, which are clearly present in W-1.4Re Ion. Further dislocation dynamics modelling may provide insight into the effect of the precipitates on the deformation behaviour of this material, and may reveal whether strain bursts and work softening are more likely to be associated with dislocations cutting precipitates or dislocation climb or bowing.

5.7 Summary

Micro-pillars in unirradiated and ion irradiated W Single and W-1.4Re have been tested using in-situ compression. The flow stresses from unirradiated W Single agree with literature values, and a hardening effect associated with irradiation has been measured. This was shown to be significantly greater in the rhenium containing material, which also showed large strain bursts during testing. These factors suggest that irradiation induced rhenium precipitation is causing a significant change in dislocation behaviour within these pillars.

These results show how enhanced information about the effects of radiation damage can be acquired through micro-pillar testing of ion irradiated material. While nanoindentation shows the increased irradiation hardening associated with the presence of rhenium, these pillar compressions have indicated a much more drastic change in dislocation behaviour. This can be used to better inform modelling of deformation in irradiated materials.

6 Conclusions

6.1 Effects of Neutron Irradiation on Single Crystal Tungsten

This work provided valuable data regarding a range of properties following neutron irradiation to 1.67 dpa at 1173 K.

Firstly, the study of transmutation (in section 3.3) through FISPACT modelling, EDS X-ray spectroscopy and gamma spectroscopy showed the accuracy of FISPACT modelling for predicting transmutation in tungsten. This was the first study to have used multiple techniques to analyse the accuracy of FISPACT modelling in tungsten. Critically, an accurate, experiment-specific neutron spectrum was required, as was consideration of self-shielding effects. This is an important verification given the broad use of FISPACT for analysing transmutation under fission neutron irradiation [74] and predicting the behaviour of tungsten in DEMO [35].

Secondly, the analysis of irradiation hardening in chapter 3 added useful information to the existing data set on neutron irradiation in tungsten. It showed that hardening trends previously observed at lower temperatures and under different neutron spectrums [53] continue up to 1173 K in HFR. The results from TEM imaging showed that the size and density of loops may have been underestimated in other works due to the lack of weak-beam dark-field TEM analysis. Additionally, it highlights the need for a consistent, reproducible approach to identifying voids.

The improved imaging of dislocation loops allowed for the hardening model applied by Huang et al. [53] and described in section 3.7 to be refined, with the improved Friedel-Kroupa-Hirsh model applied to hardening from dislocation loops [99]. The combination of atom probe tomography for detecting rhenium clusters, weak-beam

dark-field imaging of dislocation loops, and over-, under-focus imaging of voids was shown to give a good analysis of the post-irradiation microstructure that could be used to accurately predict irradiation hardening.

Finally, the characterisation of the post-irradiation brittle to ductile transition in chapter 4 provides critical information for the design and operation of future fusion devices. These results show that the increase in BDT temperature in single crystal tungsten is > 500 K after irradiation at fusion relevant temperatures. The result of this is that the minimum operating temperature for tungsten in a fusion reactor may be even higher than previously expected [65]. The characterisation of activation volume and energy provides valuable information for modelling changes in BDT following irradiation and demonstrates that our current models for predicting these changes are inaccurate [135].

6.2 Developing Ion Irradiation of Tungsten

The literature review carried out for this work [184] highlighted the dramatic differences in irradiation hardening observed between ion and neutron irradiation. Chapter 3 identifies the origins of these differences. In particular, the importance of accurate transmutation analysis is demonstrated through similar hardening being achieved in W-1.4Re Ion and W Single Neutron. The lack of transmutation analysis in early neutron irradiation studies explains why there was a large discrepancy between ion- and neutron-induced irradiation hardening in pure tungsten.

However, while similar irradiation hardening was achieved, microstructure analysis and modelling showed the different origins of this increase in hardness in W-1.4Re Ion and W Single Neutron. These results illustrated the failure of ion irradiation to match the void formation and rhenium clustering behaviour observed under neutron irradiation. The most likely cause of these differences is the difference in dose-rate and the trends observed suggest that a Mansur temperature shift for ion irradiation [78] may reduce the differences between ion- and neutron-irradiated tungsten.

The analysis of W-1.4Re Ion in chapter 3 illustrated the need for improved understanding of this interaction between dislocations and rhenium clusters. A high density of rhenium clusters were identified in W-1.4Re Ion, but it was clear from the model over-predicting hardening in this material that the low concentration of rhenium in these clusters was reducing their impact on irradiation hardening. This shows that a better understanding of the effects of irradiation defects than can be acquired from nanoindentation is required.

Micro-pillar testing of ion irradiated tungsten and W-1.4Re was described in chapter 5. The results presented here show how this technique can be applied to generate additional mechanical information from ion irradiated tungsten. In particular, the strain burst behaviour was shown to match that predicted by dislocation dynamics (DD) modelling [128]. The results from micro-pillar testing may be used to better inform other

DD models investigating the interactions between dislocations and irradiation-induced defects in tungsten. A clear difference in the behaviour of dislocations interacting with dislocation loops and rhenium clusters was highlighted by the difference in results between W Single Ion and W-1.4Re Ion.

6.3 Moving to Real-World Materials

Single crystal or large grained material was the focus of this work in order to eliminate differences caused by pre-irradiation microstructure as the difference between ion and neutron irradiation was perceived to be very large. This work has closed that difference significantly and provided a solid baseline for information regarding the effects of ion and neutron irradiation on single crystal tungsten.

However, any real-world tungsten components will be manufactured from polycrystalline, potentially nano-grained, tungsten [21]. The preliminary results from this work indicate that this may reduce the increase in BDT temperature, but the full effect is far from clear. It is apparent that grain boundaries are dominating the fracture behaviour of this material and so predicting the performance of tungsten in a fusion environment will be heavily reliant on a better understanding of the effect of neutron irradiation on grain boundaries in these materials.

6.4 Future Work

The first area of future work should be to replicate the four-point bend testing of neutron-irradiated single crystal-tungsten on the neutron-irradiated polycrystalline tungsten that is already available. This would demonstrate the relevance of the results presented in this work are to real-world materials and will help identify the likely failure mode of these materials will be during operation in a fusion environment. These results would confirm or contradict the conclusion that grain boundary weakening of tungsten under neutron irradiation is the critical process. This evidence would be in two forms: firstly more SEM fractographs from various testing conditions that will provide direct evidence for or against intergranular fracture; and secondly the activation energy of the BDT in neutron-irradiated polycrystalline tungsten could be determined, granting insight into the controlling process for ductile behaviour of that material.

These results will be most valuable if combined with microstructural studies of the grain boundaries and surrounding volume in neutron-irradiated polycrystalline tungsten. This work has identified precipitates, voids and dislocation loops in single-crystal tungsten following neutron irradiation using TEM and APT. Replicating this around grain boundaries in polycrystalline tungsten would provide insight into how radiation damage is causing grain boundary embrittlement. In particular APT of a neutron irradiated grain boundary may reveal an increased concentration of impurities. TEM work indicating an increased concentration of rhenium at these grain boundaries

has been carried out by Klimenkov et al. [66] but quantification of the concentration was not possible with this technique.

The second area where further work is needed is improving ion irradiation of tungsten to match neutron irradiation results. The effect of dose rate on the clustering behaviour in tungsten should be investigated, as should the impact of temperature during ion irradiation. In order to establish the differing effects of dynamic and thermal annealing, a post-irradiation annealing experiment could be carried out on ion-irradiated tungsten and tungsten-rhenium in order to establish if precipitates and/or voids will form in these materials given sufficient time and thermal energy.

If ion irradiation can be used to replicate the microstructural changes induced by neutron irradiation, further development of micro-mechanical test techniques will still be required in order to extract mechanical data from this technique. The micro-pillar and micro-cantilever studies carried out here can form the basis of this work in order to develop techniques to analyse the mechanical properties both within grains and at grain boundaries. Replicating the micro-pillar studies on neutron irradiated tungsten will inform the relevance of the change in deformation mode observed in ion-irradiated W-1.4Re. Equally, carrying out micro-cantilever testing on grain boundaries in ion irradiated W-Re alloys will demonstrate whether ion irradiation is capable of replicating the grain boundary embrittlement observed in neutron irradiated tungsten. This may lead to ion irradiation facilitating the study of irradiated-induced embrittlement of tungsten under a far broader range of conditions than those readily available using neutron irradiation.

Finally, there is need to combine irradiation damage results with the full range of challenging conditions in the fusion divertor. For example high-heat flux testing of neutron-irradiated tungsten is necessary to determine the maximum heat load and lifetime of plasma-facing tungsten components in a fusion environment. It is likely to be a combination of fusion conditions (high heat load, plasma exposure and neutron irradiation) that prove the most problematic for fusion materials and tungsten must be tested under this combination before it can be used in a fusion power plant.

References

[1] World Health Organisation, "WHO calls for urgent action to protect health from climate change – Sign the call," 2016.

[2] United Nations, "Paris Agreement," Tech. Rep. December, United Nations, Paris, 2015.

[3] M. Grasso, "Achieving the Paris goals: Consumption-based carbon accounting," *Geoforum*, vol. 79, pp. 93–96, Feb 2017.

[4] S. Kais and H. Sami, "An econometric study of the impact of economic growth and energy use on carbon emissions: Panel data evidence from fifty eight countries," *Renewable and Sustainable Energy Reviews*, vol. 59, pp. 1101–1110, Jun 2016.

[5] European Environment Agency, "Renewable energy in Europe- 2017 Update. Recent growth and knock-on effects," Tech. Rep. 23, European Environment Agency, Copenhagen, 2017.

[6] B. Kroposki, B. Johnson, Y. Zhang, V. Gevorgian, P. Denholm, B.-M. Hodge, and B. Hannegan, "Achieving a 100% Renewable Grid: Operating Electric Power Systems with Extremely High Levels of Variable Renewable Energy," *IEEE Power and Energy Magazine*, vol. 15, pp. 61–73, Mar 2017.

[7] Department for Business Innovation & Skills and Department of Energy & Climate Change, "Nuclear industrial strategy: the UK's nuclear future," tech. rep., UK Government, 2013.

[8] G. Steinhauser, A. Brandl, and T. E. Johnson, "Comparison of the Chernobyl and Fukushima nuclear accidents: A review of the environmental impacts," *Science of The Total Environment*, vol. 470-471, pp. 800–817, Feb 2014.

[9] E. Bloom, R. Conn, J. Davis, R. Gold, R. Little, K. Schultz, D. Smith, and F. Wiffen, "Low activation materials for fusion applications," *Journal of Nuclear Materials*, vol. 122, pp. 17–26, May 1984.

[10] M. Nakamura, K. Tobita, W. Gulden, K. Watanabe, Y. Someya, H. Tanigawa, Y. Sakamoto, T. Araki, H. Matsumiya, K. Ishii, H. Utoh, H. Takase, T. Hayashi, A. Satou, T. Yonomoto, G. Federici, and K. Okano, "Study of safety features and

accident scenarios in a fusion DEMO reactor," *Fusion Engineering and Design*, vol. 89, pp. 2028–2032, Oct 2014.

[11] J. Knaster, A. Moeslang, and T. Muroga, "Materials research for fusion," *Nature Physics*, vol. 12, pp. 424–434, May 2016.

[12] H. Bolt, V. Barabash, W. Krauss, J. Linke, R. Neu, S. Suzuki, and N. Yoshida, "Materials for the plasma-facing components of fusion reactors," *Journal of Nuclear Materials*, vol. 329-333, pp. 66–73, Aug 2004.

[13] A. Gibson and J. Team, "Deuterium–tritium plasmas in the Joint European Torus (JET): Behavior and implications," *Physics of Plasmas*, vol. 5, p. 1839, Apr 1998.

[14] S. J. Zinkle and J. T. Busby, "Structural materials for fission & fusion energy," *Materials Today*, vol. 12, pp. 12–19, Nov 2009.

[15] J. Schlosser, A. Cardella, P. Chappuis, J. Coston, P. Deschamps, and M. Lipa, "Development of High Thermal Flux Components for Continuous Operation in Tokamaks," *14th IEEE / NPSS Symposium : Fusion Engineering, Proceedings, Vols 1 and 2*, pp. 350–356, 1992.

[16] H. Bolt, V. Barabash, G. Federici, J. Linke, A. Loarte, J. Roth, and K. Sato, "Plasma facing and high heat flux materials – needs for ITER and beyond," *Journal of Nuclear Materials*, vol. 307-311, pp. 43–52, Dec 2002.

[17] S. Krat, Y. Gasparyan, A. Pisarev, I. Bykov, M. Mayer, G. de Saint Aubin, M. Balden, C. Lungu, and A. Widdowson, "Erosion at the inner wall of JET during the discharge campaign 2011–2012 in comparison with previous campaigns," *Journal of Nuclear Materials*, vol. 456, pp. 106–110, Jan 2015.

[18] J. Davis, V. Barabash, A. Makhankov, L. Plöchl, and K. Slattery, "Assessment of tungsten for use in the ITER plasma facing components," *Journal of Nuclear Materials*, vol. 258-263, pp. 308–312, Oct 1998.

[19] F. Romanelli, "Overview of the JET results with the ITER-like wall," *Nuclear Fusion*, vol. 53, p. 104002, Oct 2013.

[20] G. Federici, W. Biel, M. Gilbert, R. Kemp, N. Taylor, and R. Wenninger, "European DEMO design strategy and consequences for materials," *Nuclear Fusion*, vol. 57, p. 092002, Sep 2017.

[21] M. Rieth, S. Dudarev, S. Gonzalez de Vicente, J. Aktaa, T. Ahlgren, S. Antusch, D. Armstrong, M. Balden, N. Baluc, M.-F. Barthe, W. Basuki, M. Battabyal, C. Becquart, D. Blagoeva, H. Boldyryeva, J. Brinkmann, M. Celino, L. Ciupinski, J. Correia, A. De Backer, C. Domain, E. Gaganidze, C. Garcia-Rosales, J. Gibson,

M. Gilbert, S. Giusepponi, B. Gludovatz, H. Greuner, K. Heinola, T. Höschen, A. Hoffmann, N. Holstein, F. Koch, W. Krauss, H. Li, S. Lindig, J. Linke, C. Linsmeier, P. Lopez-Ruiz, H. Maier, J. Matejicek, T. Mishra, M. Muhammed, A. Munoz, M. Muzyk, K. Nordlund, D. Nguyen-Manh, J. Opschoor, N. Ordas, T. Palacios, G. Pintsuk, R. Pippan, J. Reiser, J. Riesch, S. Roberts, L. Romaner, M. Rosiński, M. Sanchez, W. Schulmeyer, H. Traxler, A. Urena, J. van der Laan, L. Veleva, S. Wahlberg, M. Walter, T. Weber, T. Weitkamp, S. Wurster, M. Yar, J. You, and A. Zivelonghi, "A brief summary of the progress on the EFDA tungsten materials program," *Journal of Nuclear Materials*, vol. 442, pp. S173–S180, Nov 2013.

[22] A. Giannattasio, Z. Yao, E. Tarleton, and S. Roberts, "Brittle-ductile transitions in polycrystalline tungsten," *Philosophical Magazine*, vol. 90, no. 30, pp. 3947–3959, 2010.

[23] M. Rieth, S. Dudarev, S. Gonzalez de Vicente, J. Aktaa, T. Ahlgren, S. Antusch, D. Armstrong, M. Balden, N. Baluc, M.-F. Barthe, W. Basuki, M. Battabyal, C. Becquart, D. Blagoeva, H. Boldyryeva, J. Brinkmann, M. Celino, L. Ciupinski, J. Correia, A. De Backer, C. Domain, E. Gaganidze, C. García-Rosales, J. Gibson, M. Gilbert, S. Giusepponi, B. Gludovatz, H. Greuner, K. Heinola, T. Höschen, A. Hoffmann, N. Holstein, F. Koch, W. Krauss, H. Li, S. Lindig, J. Linke, C. Linsmeier, P. López-Ruiz, H. Maier, J. Matejicek, T. Mishra, M. Muhammed, A. Muñoz, M. Muzyk, K. Nordlund, D. Nguyen-Manh, J. Opschoor, N. Ordás, T. Palacios, G. Pintsuk, R. Pippan, J. Reiser, J. Riesch, S. Roberts, L. Romaner, M. Rosiński, M. Sanchez, W. Schulmeyer, H. Traxler, A. Ureña, J. van der Laan, L. Veleva, S. Wahlberg, M. Walter, T. Weber, T. Weitkamp, S. Wurster, M. Yar, J. You, and A. Zivelonghi, "Recent progress in research on tungsten materials for nuclear fusion applications in Europe," *Journal of Nuclear Materials*, vol. 432, pp. 482–500, Jan 2012.

[24] J. Marian, C. S. Becquart, C. Domain, S. L. Dudarev, M. R. Gilbert, R. J. Kurtz, D. R. Mason, K. Nordlund, A. E. Sand, L. L. Snead, T. Suzudo, and B. D. Wirth, "Recent advances in modeling and simulation of the exposure and response of tungsten to fusion energy conditions," *Nuclear Fusion*, vol. 57, Sep 2017.

[25] E. Lassner and W.-D. Schubert, *Tungsten: properties, chemistry, technology of the element, alloys, and chemical compunds*. New York: Kluwer Academic / Plenum Publishers, 1999.

[26] J. Reiser, J. Hoffmann, U. Jäntsch, M. Klimenkov, S. Bonk, C. Bonnekoh, A. Hoffmann, T. Mrotzek, and M. Rieth, "Ductilisation of tungsten (W): On the increase of strength AND room-temperature tensile ductility through cold-rolling," *International Journal of Refractory Metals and Hard Materials*, vol. 64, pp. 261–278, Apr 2017.

[27] K. Sasaki, S. Nogami, M. Fukuda, Y. Katakai, and A. Hasegawa, "Effect of heat treatment on bend stress relaxation of pure tungsten," *Fusion Engineering and Design*, vol. 88, pp. 1735–1738, Oct 2013.

[28] D. Hull and D. Bacon, *Introduction to Dislocations*. Oxford: Butterworth-Heinemann, 4th edition ed., 2001.

[29] K. Farrell, A. Schaffhauser, and J. Stiegler, "Recrystallization, grain growth and the ductile-brittle transition in tungsten sheet," *Journal of the Less Common Metals*, vol. 13, pp. 141–155, Aug 1967.

[30] U. M. Ciucani, A. Thum, C. Devos, and W. Pantleon, "Recovery and recrystallization kinetics of differently rolled, thin tungsten plates in the temperature range from 1325 °C to 1400 °C," *Nuclear Materials and Energy*, vol. 20, p. 100701, Aug 2019.

[31] D. Armstrong, X. Yi, E. Marquis, and S. Roberts, "Hardening of self ion implanted tungsten and tungsten 5-wt% rhenium," *Journal of Nuclear Materials*, vol. 432, pp. 428–436, Jan 2013.

[32] T. Hwang, M. Fukuda, S. Nogami, A. Hasegawa, H. Usami, K. Yabuuchi, K. Ozawa, and H. Tanigawa, "Effect of self-ion irradiation on hardening and microstructure of tungsten," *Nuclear Materials and Energy*, vol. 9, pp. 430–435, 2016.

[33] A. Hasegawa, M. Fukuda, T. Tanno, and S. Nogami, "Neutron Irradiation Behavior of Tungsten," *Materials Transactions*, vol. 54, pp. 466–471, Mar 2013.

[34] N. Taylor and R. Pampin, "Activation properties of tungsten as a first wall protection in fusion power plants," *Fusion Engineering and Design*, vol. 81, pp. 1333–1338, Feb 2006.

[35] M. Gilbert and J.-C. Sublet, "Neutron-induced transmutation effects in W and W-alloys in a fusion environment," *Nuclear Fusion*, vol. 51, p. 043005, Apr 2011.

[36] L. Greenwood and F. Garner, "Transmutation of Mo, Re, W, Hf, and V in various irradiation test facilities and STARFIRE," *Journal of Nuclear Materials*, vol. 212-215, pp. 635–639, 1994.

[37] J.-C. C. Sublet, J. W. Eastwood, and J. G. Morgan, *The FISPACT -II User Manual*. No. 6, CCFE, 2014.

[38] C. J. Werner, J. S. Bull, C. J. Solomon, F. B. Brown, G. W. Mckinney, M. E. Rising, D. A. Dixon, R. L. Martz, H. G. Hughes, L. J. Cox, A. J. Zukaitis, J. C. Armstrong, R. A. Forster, and L. Casswell, "MCNP ® Release Notes MCNP Version 6.2 Release Notes," tech. rep., Los Alamos National Lab. (LANL), Los Alamos, NM (United States), 2018.

[39] R. Averback and T. Diaz de la Rubia, "Displacement Damage in Irradiated Metals and Semiconductors," *Solid State Physics*, vol. 51, pp. 281–402, Jan 1998.

[40] T. Troev, N. Nankov, and T. Yoshiie, "Simulation of displacement cascades in tungsten irradiated by fusion neutrons," *Nuclear Instruments and Methods in Physics Research Section B: Beam Interactions with Materials and Atoms*, vol. 269, pp. 566–571, Mar 2011.

[41] M. R. Gilbert, S. L. Dudarev, P. M. Derlet, and D. G. Pettifor, "Structure and metastability of mesoscopic vacancy and interstitial loop defects in iron and tungsten," *Journal of Physics: Condensed Matter*, vol. 20, p. 345214, Aug 2008.

[42] J. B. Wallace, L. B. Bayu Aji, L. Shao, and S. O. Kucheyev, "Dynamic annealing in Ge studied by pulsed ion beams," *Scientific Reports*, vol. 7, no. 1, pp. 1–7, 2017.

[43] B. D. Wirth, "How does radiation damage materials?," *Science*, vol. 318, no. 5858, p. 1866, 2007.

[44] A. Sand, K. Nordlund, and S. Dudarev, "Radiation damage production in massive cascades initiated by fusion neutrons in tungsten," *Journal of Nuclear Materials*, vol. 455, pp. 207–211, Dec 2014.

[45] A. Sand, S. Dudarev, and K. Nordlund, "High-energy collision cascades in tungsten: Dislocation loops structure and clustering scaling laws," *EPL (Europhysics Letters)*, vol. 103, p. 46003, 2013.

[46] H. Xu, R. E. Stoller, Y. N. Osetsky, and D. Terentyev, "Solving the Puzzle of 100 Interstitial Loop Formation in bcc Iron," *Phys. Rev. Lett.*, vol. 110, p. 265503, Jun 2013.

[47] M. Wen, N. M. Ghoniem, and B. N. Singh, "Dislocation decoration and raft formation in irradiated materials," *Philosophical Magazine*, vol. 85, no. 22, pp. 2561–2580, 2005.

[48] O. El-Atwani, E. Aydogan, E. Esquivel, M. Efe, Y. Q. Wang, and S. A. Maloy, "Detailed transmission electron microscopy study on the mechanism of dislocation loop rafting in tungsten," *Acta Materialia*, vol. 147, pp. 277–283, 2018.

[49] P. Okamoto and L. Rehn, "Radiation-induced segregation in binary and ternary alloys," *Journal of Nuclear Materials*, vol. 83, pp. 2–23, Aug 1979.

[50] M. Gilbert, Z. Yao, M. Kirk, M. Jenkins, and S. Dudarev, "Vacancy defects in Fe: Comparison between simulation and experiment," *Journal of Nuclear Materials*, vol. 386-388, pp. 36–40, Apr 2009.

[51] G. S. Was, *Fundamentals of Radiation Materials Science: Metals and Alloys*. Springer Science & Business Media, 2007.

[52] T. Suzudo and A. Hasegawa, "Suppression of radiation-induced point defects by rhenium and osmium interstitials in tungsten," *Scientific Reports*, vol. 6, pp. 1–6, Jul 2016.

[53] C.-H. Huang, M. R. Gilbert, and J. Marian, "Simulating irradiation hardening in tungsten under fast neutron irradiation including Re production by transmutation," *Journal of Nuclear Materials*, vol. 499, pp. 204–215, Feb 2018.

[54] L. Gharaee, J. Marian, and P. Erhart, "The role of interstitial binding in radiation induced segregation in {W}-{Re} alloys," *Journal of Applied Physics*, vol. 120, p. 25901, Jul 2016.

[55] R. K. Williams, F. W. Wiffen, J. Bentley, and J. O. Stiegler, "Irradiation induced precipitation in tungsten based, W-Re alloys," *Metallurgical Transactions A*, vol. 14A, pp. 655 – 666, 1983.

[56] V. K. Sikka, "Superlattice of voids in neutron-irradiated tungsten," *Journal of Applied Physics*, vol. 43, no. 12, p. 4942, 1972.

[57] J. Matolich, H. Nahm, and J. Moteff, "Swelling in neutron irradiated tungsten and tungsten-25 percent rhenium," *Scripta Metallurgica*, vol. 8, pp. 837–841, Jul 1974.

[58] H. Heinisch, "Correlation of mechanical property changes in neutron-irradiated pressure vessel steels on the basis of spectral effects," *Journal of Nuclear Materials*, vol. 178, pp. 19–26, Jan 1991.

[59] Y. Nemoto, A. Hasegawa, M. Satou, and K. Abe, "Microstructural development of neutron irradiated W–Re alloys," *Journal of Nuclear Materials*, vol. 283-287, pp. 1144–1147, Dec 2000.

[60] J. He, G. Tang, A. Hasegawa, and K. Abe, "Microstructural development and irradiation hardening of W and W–(3–26) wt%Re alloys after high-temperature neutron irradiation to 0.15 dpa," *Nuclear Fusion*, vol. 46, pp. 877–883, Nov 2006.

[61] T. Tanno, M. Fukuda, S. Nogami, and A. Hasegawa, "Microstructure Development in Neutron Irradiated Tungsten Alloys," *Materials Transactions*, vol. 52, pp. 1447–1451, Jun 2011.

[62] A. Hasegawa, M. Fukuda, K. Yabuuchi, and S. Nogami, "Neutron irradiation effects on the microstructural development of tungsten and tungsten alloys," *Journal of Nuclear Materials*, vol. 471, pp. 175–183, Oct 2015.

[63] T. Tanno, A. Hasegawa, J.-C. He, M. Fujiwara, S. Nogami, M. Satou, T. Shishido, and K. Abe, "Effects of Transmutation Elements on Neutron Irradiation Hardening of Tungsten," *Materials Transactions*, vol. 48, no. 9, pp. 2399–2402, 2007.

[64] V. Barabash, G. Federici, J. Linke, and C. H. Wu, "Material/plasma surface interaction issues following neutron damage," *Journal of Nuclear Materials*, vol. 313-316, pp. 42–51, 2003.

[65] S. Zinkle and N. Ghoniem, "Operating temperature windows for fusion reactor structural materials," *Fusion Engineering and Design*, vol. 51-52, pp. 55–71, Nov 2000.

[66] M. Klimenkov, U. Jantsch, M. Rieth, H. C. Schneider, D. E. J. Armstrong, J. Gibson, and S. G. Roberts, "Effect of neutron irradiation on the microstructure of tungsten," *Nuclear Materials and Energy*, vol. 9, pp. 480–483, 2016.

[67] M. L. Jenkins and M. Kirk, *Characterization of Radiation Damage by Transmission Electron Microscopy Series in Microscopy in Materials Science*. Bristol and Philadelphia: Institute of Physics Publishing, 2001.

[68] C. D. Hardie, C. A. Williams, S. Xu, and S. G. Roberts, "Effects of irradiation temperature and dose rate on the mechanical properties of self-ion implanted Fe and Fe–Cr alloys," *Journal of Nuclear Materials*, vol. 439, pp. 33–40, Aug 2013.

[69] X. Yi, M. Jenkins, M. Briceno, S. Roberts, Z. Zhou, and M. Kirk, "In situ study of self-ion irradiation damage in W and W–5Re at 500 C," *Philosophical Magazine*, vol. 93, pp. 1715–1738, May 2013.

[70] X. Yi, a. E. Sand, D. R. Mason, M. a. Kirk, S. G. Roberts, K. Nordlund, and S. L. Dudarev, "Direct observation of size scaling and elastic interaction between nano-scale defects in collision cascades," *EPL (Europhysics Letters)*, vol. 110, no. 2013, pp. 1–14, 2015.

[71] X. Yi, M. L. Jenkins, M. A. Kirk, Z. Zhou, and S. G. Roberts, "In-situ TEM studies of 150 keV W+ ion irradiated W and W-alloys: Damage production and microstructural evolution," *Acta Materialia*, vol. 112, pp. 105–120, Jun 2016.

[72] F. Ferroni, X. Yi, K. Arakawa, S. P. Fitzgerald, P. D. Edmondson, and S. G. Roberts, "High temperature annealing of ion irradiated tungsten," *Acta Materialia*, vol. 90, pp. 380–393, May 2015.

[73] R. Herschitz and D. Seidman, "An atomic resolution study of radiation-induced precipitation and solute segregation effects in a neutron-irradiated W-25 at.% Re alloy," *Acta Metallurgica*, vol. 32, pp. 1155–1171, Aug 1984.

[74] T. Hwang, A. Hasegawa, K. Tomura, N. Ebisawa, T. Toyama, Y. Nagai, M. Fukuda, T. Miyazawa, T. Tanaka, and S. Nogami, "Effect of neutron irradiation on rhenium cluster formation in tungsten and tungsten-rhenium alloys," *Journal of Nuclear Materials*, vol. 507, pp. 78–86, Apr 2018.

[75] A. Xu, C. Beck, D. E. Armstrong, K. Rajan, G. D. Smith, P. A. Bagot, and S. G. Roberts, "Ion-irradiation-induced clustering in W–Re and W–Re–Os alloys: A comparative study using atom probe tomography and nanoindentation measurements," *Acta Materialia*, vol. 87, pp. 121–127, Apr 2015.

[76] M. Shimada, G. Cao, T. Otsuka, M. Hara, M. Kobayashi, Y. Oya, and Y. Hatano, "Irradiation effect on deuterium behaviour in low-dose HFIR neutron-irradiated tungsten," *Nuclear Fusion*, vol. 55, no. 1, 2015.

[77] A. Hasegawa, M. Fukuda, S. Nogami, and K. Yabuuchi, "Neutron irradiation effects on tungsten materials," *Fusion Engineering and Design*, vol. 89, pp. 1568–1572, Oct 2014.

[78] L. Mansur, "Correlation of neutron and heavy-ion damage," *Journal of Nuclear Materials*, vol. 78, pp. 156–160, Nov 1978.

[79] C. D. Hardie and S. G. Roberts, "Nanoindentation of model Fe–Cr alloys with self-ion irradiation," *Journal of Nuclear Materials*, vol. 433, pp. 174–179, Feb 2013.

[80] G. Was and T. Allen, "Intercomparison of microchemical evolution under various types of particle irradiation," *Journal of Nuclear Materials*, vol. 205, pp. 332–338, Oct 1993.

[81] M. P. Short, D. R. Gaston, M. Jin, L. Shao, and F. A. Garner, "Modeling injected interstitial effects on void swelling in self-ion irradiation experiments," *Journal of Nuclear Materials*, vol. 471, pp. 200–207, 2016.

[82] T. Lauritzen, A. Withop, and U. Wolff, "Swelling of austenitic stainless steels under fast neutron irradiation at elevated temperatures," *Nuclear Engineering and Design*, vol. 9, pp. 265–268, Feb 1969.

[83] K. Farrell, "Experimental effects of helium on cavity formation during irradiation—a review," *Radiation Effects*, vol. 53, no. 3-4, pp. 175–194, 1980.

[84] X. Hu, T. Koyanagi, M. Fukuda, Y. Katoh, L. L. Snead, and B. D. Wirth, "Defect evolution in single crystalline tungsten following low temperature and low dose neutron irradiation," *Journal of Nuclear Materials*, vol. 470, pp. 278–289, Mar 2016.

[85] J. He, A. Hasegawa, and K. Abe, "Effects of transmutation elements on the defect structure development of W irradiated by protons and neutrons," *Journal of Nuclear Materials*, vol. 377, pp. 348–351, Jul 2008.

[86] A. Hasegawa, T. Tanno, S. Nogami, and M. Satou, "Property change mechanism in tungsten under neutron irradiation in various reactors," *Journal of Nuclear Materials*, vol. 417, pp. 491–494, Oct 2011.

[87] M. Fukuda, T. Tanno, S. Nogami, and A. Hasegawa, "Effects of Re Content and Fabrication Process on Microstructural Changes and Hardening in Neutron Irradiated Tungsten," *Materials Transactions*, vol. 53, pp. 2145–2150, Nov 2012.

[88] M. Fukuda, A. Hasegawa, T. Tanno, S. Nogami, and H. Kurishita, "Property change of advanced tungsten alloys due to neutron irradiation," *Journal of Nuclear Materials*, vol. 442, pp. S273–S276, Nov 2013.

[89] M. Fukuda, N. Kiran Kumar, T. Koyanagi, L. M. Garrison, L. L. Snead, Y. Katoh, and A. Hasegawa, "Neutron energy spectrum influence on irradiation hardening and microstructural development of tungsten," *Journal of Nuclear Materials*, vol. 479, pp. 249–254, 2016.

[90] W. D. Nix and H. Gao, "Indentation size effects in crystalline materials: A law for strain gradient plasticity," *Journal of the Mechanics and Physics of Solids*, vol. 46, pp. 411–425, Mar 1998.

[91] P. Hosemann, D. Kiener, Y. Wang, and S. A. Maloy, "Issues to consider using nano indentation on shallow ion beam irradiated materials," *Journal of Nuclear Materials*, vol. 425, pp. 136–139, Jun 2012.

[92] Z. Zhang, D. Chen, W. Han, and A. Kimura, "Irradiation hardening in pure tungsten before and after recrystallization," *Fusion Engineering and Design*, vol. 98-99, pp. 2103–2107, Oct 2015.

[93] A. Khan, R. Elliman, C. Corr, J. J. Lim, A. Forrest, P. Mummery, and L. M. Evans, "Effect of rhenium irradiations on the mechanical properties of tungsten for nuclear fusion applications," *Journal of Nuclear Materials*, vol. 477, pp. 42–49, Aug 2016.

[94] D. Armstrong, C. Hardie, J. Gibson, A. Bushby, P. Edmondson, and S. Roberts, "Small-scale characterisation of irradiated nuclear materials: Part II nanoindentation and micro-cantilever testing of ion irradiated nuclear materials," *Journal of Nuclear Materials*, vol. 462, pp. 374–381, Jul 2015.

[95] D. E. Armstrong and T. B. Britton, "Effect of dislocation density on improved radiation hardening resistance of nano-structured tungsten-rhenium," *Materials Science and Engineering A*, vol. 611, pp. 388–393, 2014.

[96] J. Reiser, S. Wurster, J. Hoffmann, S. Bonk, C. Bonnekoh, D. Kiener, R. Pippan, A. Hoffmann, and M. Rieth, "Ductilisation of tungsten (W) through cold-rolling: R-curve behaviour," *International Journal of Refractory Metals and Hard Materials*, vol. 58, pp. 22–33, Aug 2016.

[97] T. Tanno, A. Hasegawa, J. He, M. Fujiwara, M. Satou, S. Nogami, K. Abe, and T. Shishido, "Effects of transmutation elements on the microstructural evolution and electrical resistivity of neutron-irradiated tungsten," *Journal of Nuclear Materials*, vol. 386-388, pp. 218–221, Apr 2009.

[98] X. Hu, T. Koyanagi, M. Fukuda, N. K. Kumar, L. L. Snead, B. D. Wirth, and Y. Katoh, "Irradiation hardening of pure tungsten exposed to neutron irradiation," *Journal of Nuclear Materials*, vol. 480, pp. 235–243, Nov 2016.

[99] S. Zinkle and Y. Matsukawa, "Observation and analysis of defect cluster production and interactions with dislocations," *Journal of Nuclear Materials*, vol. 329-333, pp. 88–96, Aug 2004.

[100] S. Queyreau, G. Monnet, and B. Devincre, "Orowan strengthening and forest hardening superposition examined by dislocation dynamics simulations," *Acta Materialia*, vol. 58, pp. 5586–5595, Oct 2010.

[101] F. Kroupa and P. B. Hirsch, "Elastic interaction between prismatic dislocation loops and straight dislocations," *Discussions of the Faraday Society*, vol. 38, pp. 49–55, 1964.

[102] J. T. Busby, M. C. Hash, and G. S. Was, "The relationship between hardness and yield stress in irradiated austenitic and ferritic steels," *Journal of Nuclear Materials*, vol. 336, no. 2-3, pp. 267–278, 2005.

[103] R. E. Stoller and S. J. Zinkle, "On the relationship between uniaxial yield strength and resolved shear stress in polycrystalline materials," *Journal of Nuclear Materials*, vol. 283-287, no. PART I, pp. 349–352, 2000.

[104] G. Bonny, D. Terentyev, J. Elena, A. Zinovev, B. Minov, and E. Zhurkin, "Assessment of hardening due to dislocation loops in bcc iron: Overview and analysis of atomistic simulations for edge dislocations," *Journal of Nuclear Materials*, vol. 473, pp. 283–289, May 2016.

[105] G. M. Pharr and W. C. Oliver, "Measurement of Thin Film Mechanical Properties Using Nanoindentation," *MRS Bulletin*, vol. 17, no. 7, pp. 28–33, 1992.

[106] W. Oliver and G. Pharr, "Measurement of hardness and elastic modulus by instrumented indentation: Advances in understanding and refinements to methodology," *Journal of Materials Research*, vol. 19, pp. 3–20, Jan 2004.

[107] N. Stelmashenko, M. Walls, L. Brown, and Y. Milman, "Microindentations on W and Mo oriented single crystals: An STM study," *Acta Metallurgica et Materialia*, vol. 41, pp. 2855–2865, Oct 1993.

[108] M. Shell De Guzman, G. Neubauer, P. Flinn, and W. D. Nix, "The Role of Indentation Depth on the Measured Hardness of Materials," *MRS Proceedings*, vol. 308, p. 613, Jan 1993.

[109] X. Li and B. Bhushan, "A review of nanoindentation continuous stiffness measurement technique and its applications," *Materials Characterization*, vol. 48, pp. 11–36, Feb 2002.

[110] R. Schwaiger, B. Moser, M. Dao, N. Chollacoop, and S. Suresh, "Some critical experiments on the strain-rate sensitivity of nanocrystalline nickel," *Acta Materialia*, vol. 51, no. 17, pp. 5159–5172, 2003.

[111] L. Lu, R. Schwaiger, Z. W. Shan, M. Dao, K. Lu, and S. Suresh, "Nano-sized twins induce high rate sensitivity of flow stress in pure copper," *Acta Materialia*, vol. 53, no. 7, pp. 2169–2179, 2005.

[112] Q. Wei, S. Cheng, K. T. Ramesh, and E. Ma, "Effect of nanocrystalline and ultrafine grain sizes on the strain rate sensitivity and activation volume: Fcc versus bcc metals," *Materials Science and Engineering A*, vol. 381, no. 1-2, pp. 71–79, 2004.

[113] R. W. Evans and L. A. Simpson, "The strain-rate sensitivity of the plastic properties of α-iron at high temperatures," *Philosophical Magazine*, vol. 19, no. 160, pp. 809–819, 1969.

[114] V. Maier, K. Durst, J. Mueller, B. Backes, H. W. Höppel, and M. Göken, "Nanoindentation strain-rate jump tests for determining the local strain-rate sensitivity in nanocrystalline Ni and ultrafine-grained Al," *Journal of Materials Research*, vol. 26, no. 11, pp. 1421–1430, 2011.

[115] V. Maier, C. Schunk, M. Göken, and K. Durst, "Microstructure-dependent deformation behaviour of bcc-metals - Indentation size effect and strain rate sensitivity," *Philosophical Magazine*, vol. 95, no. 16-18, pp. 1766–1779, 2015.

[116] H. Gao, Y. Huang, W. Nix, and J. Hutchinson, "Mechanism-based strain gradient plasticity - I. Theory," *Journal of the Mechanics and Physics of Solids*, vol. 47, pp. 1239–1263, 1999.

[117] Y. Huang, H. Gao, W. Nix, and J. Hutchinson, "Mechanism-based strain gradient plasticity—II. Analysis," *Journal of the Mechanics and Physics of Solids*, vol. 48, pp. 99–128, Jan 2000.

[118] D. Kiener, A. M. Minor, O. Anderoglu, Y. Wang, S. A. Maloy, and P. Hosemann, "Application of small-scale testing for investigation of ion-beam-irradiated materials," *Journal of Materials Research*, vol. 27, pp. 2724–2736, Nov 2012.

[119] M. Saleh, Z. Zaidi, C. Hurt, M. Ionescu, P. Munroe, and D. Bhattacharyya, "Comparative Study of Two Nanoindentation Approaches for Assessing Mechanical Properties of Ion-Irradiated Stainless Steel 316," *Metals*, vol. 8, no. 9, p. 719, 2018.

[120] J. S. K. Gibson, "Mechanical Behaviour of Irradiated Tungsten for Fusion Power," *DPhil Thesis, University of Oxford*, 2015.

[121] M. T. Lessmann, I. Sudić, S. Fazinić, T. Tadić, A. Calvo, C. D. Hardie, M. Porton, C. García-Rosales, and P. M. Mummery, "The effects of ion irradiation on the micromechanical fracture strength and hardness of a self-passivating tungsten alloy," *Journal of Nuclear Materials*, vol. 486, pp. 34–43, 2017.

[122] M. D. Uchic, P. A. Shade, and D. M. Dimiduk, "Plasticity of Micrometer-Scale Single Crystals in Compression," *Annual Review of Materials Research*, vol. 39, no. 1, pp. 361–386, 2009.

[123] D. Kiener, P. J. Guruprasad, S. M. Keralavarma, G. Dehm, and A. A. Benzerga, "Work hardening in micropillar compression: In situ experiments and modeling," *Acta Materialia*, vol. 59, no. 10, pp. 3825–3840, 2011.

[124] D. Kiener, P. Hosemann, S. A. Maloy, and A. M. Minor, "In situ nanocompression testing of irradiated copper.," *Nature materials*, vol. 10, pp. 608–13, Aug 2011.

[125] J. Y. Kim, D. Jang, and J. R. Greer, "Tensile and compressive behavior of tungsten, molybdenum, tantalum and niobium at the nanoscale," *Acta Materialia*, vol. 58, no. 7, pp. 2355–2363, 2010.

[126] E. Grieveson, D. Armstrong, S. Xu, and S. Roberts, "Compression of self-ion implanted iron micropillars," *Journal of Nuclear Materials*, vol. 430, pp. 119–124, Nov 2012.

[127] A. Reichardt, A. Lupinacci, D. Frazer, N. Bailey, H. Vo, C. Howard, Z. Jiao, A. Minor, P. Chou, and P. Hosemann, "Nanoindentation and in situ microcompression in different dose regimes of proton beam irradiated 304 SS," *Journal of Nuclear Materials*, vol. 486, pp. 323–331, Apr 2017.

[128] Y. Cui, G. Po, and N. Ghoniem, "Does irradiation enhance or inhibit strain bursts at the submicron scale?," *Acta Materialia*, vol. 132, pp. 285–297, 2017.

[129] C. Linsmeier, M. Rieth, J. Aktaa, T. Chikada, A. Hoffmann, J. Hoffmann, A. Houben, H. Kurishita, X. Jin, M. Li, A. Litnovsky, S. Matsuo, A. von Müller, V. Nikolic, T. Palacios, R. Pippan, D. Qu, J. Reiser, J. Riesch, T. Shikama, R. Stieglitz, T. Weber, S. Wurster, J.-H. You, and Z. Zhou, "Development of advanced high heat flux and plasma-facing materials," *Nuclear Fusion*, vol. 57, p. 092007, Sep 2017.

[130] D. Rupp and S. M. Weygand, "Loading rate dependence of the fracture toughness of polycrystalline tungsten," *Journal of Nuclear Materials*, vol. 417, pp. 477–480, Oct 2011.

[131] A. Giannattasio and S. G. Roberts, "Strain-rate dependence of the brittle- to-ductile transition temperature in tungsten," *Philosophical Magazine*, vol. 87, no. 17, pp. 37–41, 2007.

[132] D. Brunner, "Comparison of Flow-Stress Measurements on High-Purity Tungsten Single Crystals with the Kink-Pair Theory," *Materials Transactions, JIM*, vol. 41, no. 1, pp. 152–160, 2000.

[133] E. Tarleton and S. Roberts, "Dislocation dynamic modelling of the brittle–ductile transition in tungsten," *Philosophical Magazine*, vol. 89, no. 31, pp. 2759–2769, 2009.

[134] F. Ackermann, H. Muchrabi, U. Stuttgart, W. Theoretische, and A. Physik, "Temperature- and strain-rate dependence of the flow stress of ultrapure niobium single crystals in cyclic deformation," *Acta Metallurgica*, vol. 31, pp. 1353–1366, Sep 1983.

[135] T. D. Swinburne and S. L. Dudarev, "Kink-limited Orowan strengthening explains the brittle to ductile transition of irradiated and unirradiated bcc metals," *Physical Review Materials*, vol. 2, p. 073608, Jul 2018.

[136] R. C. Rau, J. Moteff, and R. L. Ladd, "Comparison of microstructure with mechanical properties of irradiated tungsten," *Journal of Nuclear Materials*, vol. 24, pp. 164–173, 1967.

[137] I. V. Gorynin, V. A. Ignatov, V. V. Rybin, S. A. Fabritsiev, V. A. Kazakov, V. P. Chakin, V. A. Tsykanov, V. R. Barabash, and Y. G. Prokofyev, "Effects of neutron irradiation on properties of refractory metals," *Journal of Nuclear Materials*, vol. 191-194, pp. 421–425, 1992.

[138] J. M. Steichen, "Tensile properties of neutron irradiated TZM and tungsten," *Journal of Nuclear Materials*, vol. 60, pp. 13–19, Apr 1976.

[139] P. Krautwasser, H. Derz, and E. Kny, "Influence of fast neutron fluence on the DBTT of tungsten, W-10Re and W-3.4Ni-1.6Fe," *High Temperatures-High Pressures*, vol. 22, no. 1, pp. 25–32, 1976.

[140] V. Barabash, G. Federici, M. Rödig, L. L. Snead, and C. H. Wu, "Neutron irradiation effects on plasma facing materials," *Journal of Nuclear Materials*, vol. 283-287, no. PART I, pp. 138–146, 2000.

[141] J. Riesch, M. Aumann, J. W. Coenen, H. Gietl, G. Holzner, T. Höschen, P. Huber, M. Li, C. Linsmeier, and R. Neu, "Chemically deposited tungsten fibre-reinforced tungsten - The way to a mock-up for divertor applications," *Nuclear Materials and Energy*, vol. 9, pp. 75–83, 2016.

[142] Y. Li and C. Robertson, "Irradiation defect dispersions and effective dislocation mobility in strained ferritic grains: A statistical analysis based on 3D dislocation dynamics simulations," *Journal of Nuclear Materials*, vol. 504, pp. 84–93, Jun 2018.

[143] R. E. Stoller, M. B. Toloczko, G. S. Was, A. G. Certain, S. Dwaraknath, and F. A. Garner, "On the use of SRIM for computing radiation damage exposure," *Nuclear Instruments and Methods in Physics Research Section B: Beam Interactions with Materials and Atoms*, vol. 310, pp. 75–80, Sep 2013.

[144] S. L. Dudarev, "Private Communication," tech. rep., UK Atomic Energy Authority, Abingdon, Oxfordshire, UK, 2018.

[145] D. Saxey, J. Cairney, D. McGrouther, T. Honma, and S. Ringer, "Atom probe specimen fabrication methods using a dual FIB/SEM," *Ultramicroscopy*, vol. 107, pp. 756–760, Sep 2007.

[146] D. B. Williams and C. B. Carter, *Transmission Electron Microscopy: a Textbook for Materials Science*. Springer, 2009.

[147] M. R. Ruehle, "Transmission Electron Microscopy of Radiation-Induced Defects," tech. rep., Argonne National Laboratory, Argonne, 1971.

[148] J. Schindelin, I. Arganda-Carreras, E. Frise, V. Kaynig, M. Longair, T. Pietzsch, S. Preibisch, C. Rueden, S. Saalfeld, B. Schmid, J.-Y. Tinevez, D. J. White, V. Hartenstein, K. Eliceiri, P. Tomancak, and A. Cardona, "Fiji: an open-source platform for biological-image analysis," *Nature Methods*, vol. 9, pp. 676–682, Jul 2012.

[149] J. C. Haley, "TEM of neutron, proton and self-ion irradiation damage in FeCr alloys," *DPhil Thesis, University of Oxford*, 2018.

[150] X. Yi, M. L. Jenkins, K. Hattar, P. D. Edmondson, and S. G. Roberts, "Characterisation of radiation damage in W and W-based alloys from 2 MeV self-ion near-bulk implantations," *Acta Materialia*, vol. 92, pp. 163–177, 2015.

[151] X. Yi, "Electron Microscopy Study of Radiation Damage in Tungsten and Alloys," *DPhil Thesis, University of Oxford*, 2014.

[152] W. Van Renterghem and I. Uytdenhouwen, "Investigation of the combined effect of neutron irradiation and electron beam exposure on pure tungsten," *Journal of Nuclear Materials*, vol. 477, pp. 77–84, 2016.

[153] N. Castin, G. Bonny, A. Bakaev, C. J. Ortiz, A. E. Sand, and D. Terentyev, "Object kinetic Monte Carlo model for neutron and ion irradiation in tungsten: Impact of transmutation and carbon impurities," *Journal of Nuclear Materials*, vol. 500, pp. 15–25, 2018.

[154] D. Tabor, "The physical meaning of indentation hardness," *Sheet Metal Industries*, vol. 31, no. 329, pp. 749–757, 1954.

[155] Z. Zhang, K. Yabuuchi, and A. Kimura, "Defect distribution in ion-irradiated pure tungsten at different temperatures," *Journal of Nuclear Materials*, vol. 480, pp. 207–215, Nov 2016.

[156] E. Hasenhuetl, Z. Zhang, K. Yabuuchi, and A. Kimura, "Effect of displacement damage level on the ion-irradiation affected zone evolution in W single crystals," *Journal of Nuclear Materials*, vol. 495, pp. 314–321, Nov 2017.

[157] M. Fukuda, K. Yabuuchi, S. Nogami, A. Hasegawa, and T. Tanaka, "Microstructural development of tungsten and tungsten–rhenium alloys due to neutron irradiation in HFIR," *Journal of Nuclear Materials*, vol. 455, pp. 460–463, Dec 2014.

[158] J. Fikar, R. Schäublin, D. R. Mason, and D. Nguyen-Manh, "Nano-sized prismatic vacancy dislocation loops and vacancy clusters in tungsten," *Nuclear Materials and Energy*, vol. 16, pp. 60–65, Aug 2018.

[159] A. Xu, D. E. Armstrong, C. Beck, M. P. Moody, G. D. Smith, P. A. Bagot, and S. G. Roberts, "Ion-irradiation induced clustering in W-Re-Ta, W-Re and W-Ta alloys: An atom probe tomography and nanoindentation study," *Acta Materialia*, vol. 124, pp. 71–78, Feb 2017.

[160] G. Monnet, "Multiscale modeling of irradiation hardening: Application to important nuclear materials," *Journal of Nuclear Materials*, vol. 508, pp. 609–627, Sep 2018.

[161] J. D. Campbell and W. G. Ferguson, "The temperature and strain-rate dependence of the shear strength of mild steel," *Philosophical Magazine*, vol. 21, no. 169, pp. 63–82, 1970.

[162] Q. Wei and L. J. Kecskes, "Effect of low-temperature rolling on the tensile behavior of commercially pure tungsten," *Materials Science and Engineering A*, vol. 491, no. 1-2, pp. 62–69, 2008.

[163] D. Armstrong, "Measuring Elastic , Plastic and Fracture Properties using Micro-Cantilever Testing," *DPhil Thesis, University of Oxford*, 2009.

[164] Q. Wei, T. Jiao, K. T. Ramesh, E. Ma, L. J. Kecskes, L. Magness, R. Dowding, V. U. Kazykhanov, and R. Z. Valiev, "Mechanical behavior and dynamic failure of high-strength ultrafine grained tungsten under uniaxial compression," *Acta Materialia*, vol. 54, no. 1, pp. 77–87, 2006.

[165] D. Brunner and V. Glebovsky, "Analysis of flow-stress measurements of high-purity tungsten single crystals," *Materials Letters*, vol. 44, no. 3, pp. 144–152, 2000.

[166] L. Romaner, C. Ambrosch-Draxl, and R. Pippan, "Effect of rhenium on the dislocation core structure in tungsten," *Physical Review Letters*, vol. 104, no. 19, pp. 1–4, 2010.

[167] P. L. Raffo, "Tungsten-Rhenium Alloys," *Nasa Technical Note*, vol. NASA TN D-, 1968.

[168] Y. Mutoh, K. Ichikawa, K. Nagata, and M. Takeuchi, "Effect of rhenium addition on fracture toughness of tungsten at elevated temperatures," *Journal of Materials Science*, vol. 30, no. 3, pp. 770–775, 1995.

[169] D. Madyira, "Effect of Wire EDM on Microstructure and Fracture Toughness of 7075-T6511 Aluminum Alloy," in *Proceedings of the World Congress on Engineering*, (London), 2015.

[170] D. M. Madyira and E. T. Akinlabi, "Effects of wire electrical discharge machining on fracture toughness of grade 5 titanium alloy," *Lecture Notes in Engineering and Computer Science*, vol. 2, pp. 1393–1398, 2014.

[171] J. D. Murphy, A. J. Wilkinson, and S. G. Roberts, "Characterisation of plastic zones around crack-tips in pure single-crystal tungsten using electron backscatter diffraction," *IOP Conference Series: Materials Science and Engineering*, vol. 3, 2009.

[172] J. Toribio, "Role of crack-tip residual stresses in stress corrosion behaviour of prestressing steel," *Construction and Building Materials*, vol. 12, pp. 283–287, Jul 1998.

[173] G. Odette, G. Lucas, E. Donahue, and J. Sheckherd, "Fracture toughness and micromechanics in a V-4Cr-4Ti alloy," *Journal of Nuclear Materials*, vol. 233-237, pp. 502–506, Oct 1996.

[174] E. Gaganidze, H. C. Schneider, B. Dafferner, and J. Aktaa, "High-dose neutron irradiation embrittlement of RAFM steels," *Journal of Nuclear Materials*, vol. 355, no. 1-3, pp. 83–88, 2006.

[175] B. V. Cockeram, T. S. Byun, K. J. Leonard, J. L. Hollenbeck, and L. L. Snead, "Post-irradiation fracture toughness of unalloyed molybdenum, ODS molybdenum, and TZM molybdenum following irradiation at 244 C to 507 C," *Journal of Nuclear Materials*, vol. 440, no. 1-3, pp. 382–413, 2013.

[176] I. Belianov and P. Marmy, "The effect of low dose irradiation on the impact fracture energy and tensile properties of pure iron and two ferritic martensitic steels," *Journal of Nuclear Materials*, vol. 258-263, pp. 1259–1263, 1998.

[177] L. Dezerald, L. Proville, L. Ventelon, F. Willaime, and D. Rodney, "First-principles prediction of kink-pair activation enthalpy on screw dislocations in bcc transition metals: V, Nb, Ta, Mo, W, and Fe," *Physical Review B - Condensed Matter and Materials Physics*, vol. 91, no. 9, pp. 1–7, 2015.

[178] J. Ast, M. Göken, and K. Durst, "Size-dependent fracture toughness of tungsten," *Acta Materialia*, vol. 138, pp. 198–211, Oct 2017.

[179] R. R. Keller and R. H. Geiss, "Transmission EBSD from 10 nm domains in a scanning electron microscope," *Journal of Microscopy*, vol. 245, no. 3, pp. 245–251, 2012.

[180] F. Bachmann, R. Hielscher, and H. Schaeben, "Texture Analysis with MTEX – Free and Open Source Software Toolbox," *Solid State Phenomena*, vol. 160, pp. 63–68, 2010.

[181] A. J. Wilkinson and T. B. Britton, "Strains, planes, and EBSD in materials science," *Materials Today*, vol. 15, no. 9, pp. 366–376, 2012.

[182] A. S. Schneider, D. Kaufmann, B. G. Clark, C. P. Frick, P. A. Gruber, R. Mönig, O. Kraft, and E. Arzt, "Correlation between critical temperature and strength of small-scale bcc pillars," *Physical Review Letters*, vol. 103, no. 10, pp. 1–4, 2009.

[183] Y. Cui, G. Po, and N. Ghoniem, "Temperature insensitivity of the flow stress in body-centered cubic micropillar crystals," *Acta Materialia*, vol. 108, pp. 128–137, Apr 2016.

[184] R. Abernethy, "Predicting the performance of tungsten in a fusion environment: a literature review," *Materials Science and Technology*, vol. 33, pp. 388–399, 2017.